NGU Report 2006.059

KONTIKI Report 2005-2006
Continental Crust and Heat
Generation In 3D

REPORT

Report no.: 2006.059	ISSN 0800-3416	Grading: Confidential to 17.08.2011

Title:
KONTIKI Report 2005-2006, Continental Crust and Heat Generation In 3D

Authors:
Odleiv Olesen, Niels Balling, Cécile Barrère, Niels Breiner, Børre Davidsen, Jörg Ebbing, Harald Elvebakk, Laurent Gernigon, Janusz Koziel, Kirsti Midttømme, Øystein Nordgulen, Lars Olsen, Christophe Pascal, Randi K. Ramstad, Hans O. Rendall, Jan Steinar Rønning, Jan Reidar Skilbrei, Trond Slagstad and Bjørn Wissing

Client:
Statoil ASA

County:
Akershus, Oppland, Sogn & Fjordane, Møre & Romsdal, Sør-Trøndelag, Nord-Trøndelag, Nordland and Troms

Commune:

Map-sheet name (M=1:250.000):

Number of pages: 185   Price (NOK):
Map enclosures:

Fieldwork carried out:	Date of report:	Project no.:	Person responsible:
May-Oct. 2005	17.08.2006	3066.00	

Summary:

Statoil and NGU have established the Kontiki Project (Continental Crust and Heat Generation In 3D) in 2004 to improve the understanding of heat flow variation in sedimentary basins. The Kontiki 2005-2006 report summarises the results from the second year of the three-year project period. The heat generation of the mainland basement rocks has been calculated from the chemical analyses of the U, Th and K content in c. 3300 samples. We have measured thermal conductivity of 309 samples from 6 different boreholes. The analyses have been calibrated with measurements from the Geological Survey of Finland and the University of Aarhus. A total of 11 deep wells (c. 700-1000 m) have been established for temperature logging and heat flow calculations in mainland Norway: A) Asker and Hamar (Cambro-Silurian rocks), B) Hurdal (Permian intrusives within the Oslo Rift), C) Fredrikstad (Neoproterozoic granite) and D) Skedsmo and Lærdal (Neoproterozoic gneiss). E) Hjerkinn, Meldal and Sulitjelma (Caledonian nappe complexes), F) Tysfjord and Lofoten (Mesoproterozoic, Trans-Scandinavian Igneous Belt, TIB). Tentative palaeoclimatic corrections have been carried out on pre-existing heat flow data from southern Norway. The calculated corrections range from +2 to +9 mW/m² (i.e. 5-20% of original heat flow values). The heat flow in deep wells in Lærdal, Hjerkinn and Løkken has been calculated from temperature logging and thermal conductivity data. We have compiled depth to crystalline basement maps from northern Norway. Crustal models of the Oslo Rift and Mid Norwegian mainland and continental margin have been established from gravity, magnetic, seismic and bedrock mapping data. The crustal models show the influence of 3D geometry on the present thermal structure and observed heat flow. The Central Scandinavia thermal modelling is indicating that granitoids of the TIB are only present in the upper crust or are less heat productive with increasing burial depth. The modelled moderate and short-wavelength variations in surface heat flow within the Oslo Rift are mainly the result of the different lithological units at a relatively shallow depth. Thick sedimentary rocks do not cover the heat-productive rocks and therefore the near-surface bedrock units control the observed heat flow. The influence of deep-seated crustal intrusives is less important The influence of different basement lithology on heat flow on the Mid-Norwegian margin might be overprinted by the basal heat flow. The surface heat flow is strongly controlled by the structure of the crust in the special case of a varying basal heat flow. Plans for the remaining year of the Kontiki Project are summarised at the end of the report.

Keywords: Geofysikk (Geophysics)	Kontinentalsokkel (Continental shelf)	Tolkning (Interpretation)
Berggrunnsgeologi (Bedrock geology)	Magnetometri (Magnetometry)	
Petrofysikk (Petrophysics)	Gravimetri (Gravimetry)	Fagrapport (Scientific report)

CONTENTS

1   INTRODUCTION

Understanding heat flow variation in sedimentary basins is of vital importance for the success of petroleum exploration campaigns. While the industry has invested much in understanding the thermal input related to lithospheric thinning, it appears that comparatively little has been done on the subject of heat flow from different types of basement. Statoil and NGU have therefore decided to establish the Kontiki Project (Continental Crust and Heat Generation In 3D) to improve the knowledge on the varying heat flow on the Norwegian continental shelf. The age and thickness of the continental crust also affects the surface heat flow. We will therefore also study how the heat flow is dependent on the age of basement provinces. Development of a technique to estimate the heat flow in other basins with more limited background data constitutes another objective of the Kontiki Project.

Approximately half of the heat flow in sedimentary basins originates in the crystalline basement while the other half comes from the mantle (Ritter *et al.* 2004). Only 10% of the heat is produced within the sedimentary rocks of the basins. The heat production within the crystalline basement depends on the content of radioactive elements such as potassium, uranium and thorium. The content of these elements shows a wide variation within the mainland crystalline basement of Norway. Partly due to a lack of systematic data compilation, the knowledge of the basement rock composition below the Norwegian continental shelf is very poor or almost non-existing in large areas.

Relatively acidic rocks of the Precambrian gneisses and granites generate more heat than intermediate-mafic rocks within the Caledonian nappes and high-grade metamorphic units (e.g. the Lofoten gneiss complex). The latter rock units are representative for middle and lower crust. While mafic rocks within underplated bodies and other mafic igneous rocks provide an important transient heat pulse, they have a low radioactive heat production. The transient heat flow from these c. 50Ma old intrusives has returned to near-equilibrium today (Ritter *et al.* 2004). Assuming a constant heat production from the continental crust in basin modelling studies offshore Norway will lead to considerable errors in the calculation of the temperature regime in sedimentary basins. Analysis of offshore and onshore well data is a fundamental step to obtain detailed input for heat flow and thermal gradients.

The present project aims at compiling lithogeochemical information on basement rocks along the coast of Norway with emphasis on characterizing the U, Th and K content. Geophysical information such as seismic, aeromagnetic, and gravity data will, together with well penetrations of basement, provide a basis for extending this information below the offshore sedimentary basins. The Geological Survey of Norway (NGU) holds complete gravity and aeromagnetic databases from the whole of the Norwegian mainland and offshore areas in addition to detailed information on the mainland bedrock geology. The onshore-offshore geophysical interpretations will also be constrained by geochemical analysis and age-dating of basement core samples obtained from offshore exploration wells.

Seismic velocity and seismic reflection patterns from offshore basement rocks will help in distinguishing between Caledonian nappe complexes and more massive Precambrian granites and gneisses. Hence a first order distribution of basement-related heat flow will be mapped.

An additional element of relevance to the heat flow in sedimentary basins is the structural relief of the basement; basement highs most likely act as focussing points for fluid that are being driven out from the overlying sediments. An element of the project will hence be to map the basement structure and to combine this with the mapped rock type distribution.

The depth estimation of Curie temperatures by the analysis of aeromagnetic data allows to interpolate the values between different areas and to provide areal interpretations. In addition, measured bottom hole temperatures from selected exploration wells will be calibrated against radiogenic heat production from basement, and will hence provide a test of the basement type distribution.

2 RADIOGENIC HEAT PRODUCTION OF NORWEGIAN BEDROCK

Trond Slagstad, NGU

One of the main tasks of the Kontiki Project is to characterise Norwegian bedrock in terms of radiogenic heat production (heat produced by decay of the radioactive isotopes ^{238}U, ^{232}Th and ^{40}K). The heat production (A, $[\mu W/m^3]$) of a rock is calculated from its U, Th and K concentrations and density (δ) according to (Rybach 1988):

$$A = \delta*(9.52C_U + 2.56C_{Th} + 3.48C_K)*10^{-5}$$

where C_U and C_{Th} represent U and Th concentrations in ppm, respectively, and C_K represents K concentration in wt.%. The U, Th and K concentrations are determined by standard whole-rock chemical analysis (more rarely by γ-ray spectrometry). Densities are determined using Archimedes' principle by weighing the samples in air and immersed in water, or, if geometrically simple samples are available (e.g., drill cores), weighing the samples and dividing by the calculated volume. If density data are unavailable, the density is estimated based on lithology. The error in the calculated heat production introduced by estimating a density is negligible.

2.1 Available heat production data

At present, the heat production database contains U, Th, K and density data from 3318 samples, mainly from southeastern Norway (Oslo area) and central to north-central Norway (Trøndelag and Nordland). The database will be supplemented with an additional 616 samples from northwestern and north-central Norway by fall 2006. The locations and sources of data are summarised in Table 2.1 and Fig. 2.1.

Table 2.1. Sources and number of analyses in the radiogenic heat production database

Source	No. samp.	Method	Label Fig. 1	Comments	Quality
LITO-project	997	XRF, LA–ICP–MS	LITO 1		1
LITO-project	616	XRF, LA–ICP–MS	LITO 2	Available fall 2006	1
Various NGU samples	623	XRF, LA–ICP–MS	NGU 1		2
Killeen & Heier (1975)	629	γ-ray spectrometry	KH 1975		3
Raade (1973)	967	γ-ray spectrometry	RAA 1973		3
Ormaasen (1976)	102	γ-ray spectrometry	ORM 1976		4

Abbreviations: XRF: x-ray fluorescence; LA–ICP–MS: laser ablation–inductively coupled–mass spectrometry. Quality rated according to analytical method and degree of geological and geographical control.
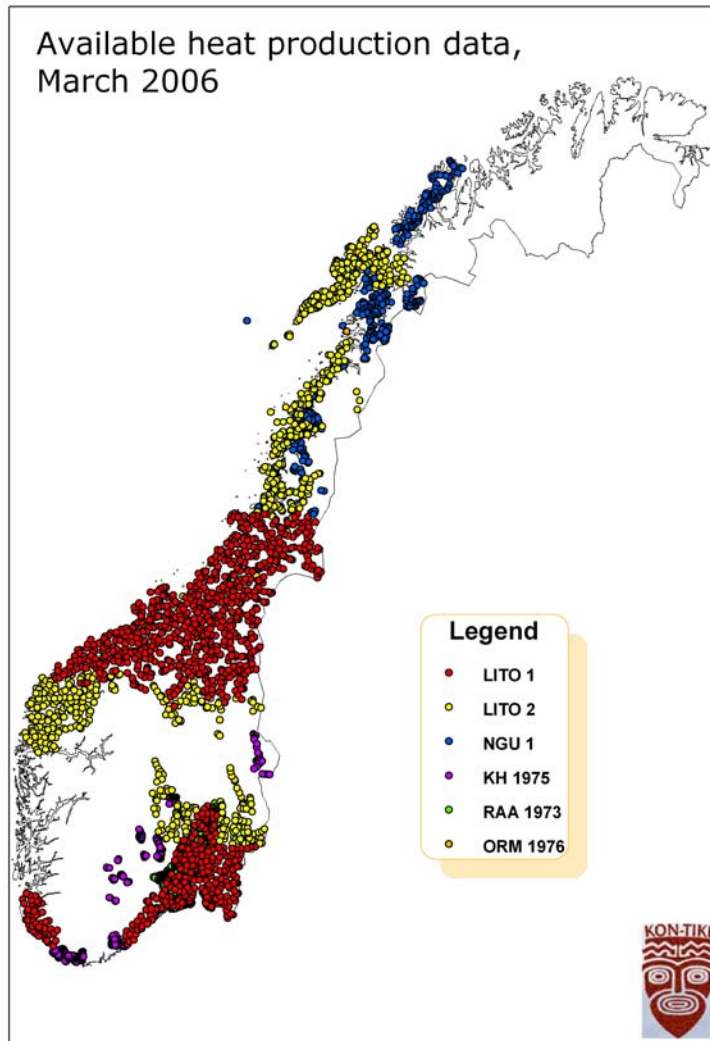
Figure 2.1. ***Map showing the distribution of available heat production data as of March 2006. See Table 2.1 for explanation of legend.***

2.2 Heat production of Norwegian bedrock

The geological basis for the discussion on heat production of Norwegian bedrock is the 1:4 million geological map 'Geological Map, Land and Sea Areas of Northern Europe', by Sigmond (2002). A simplified version of the geological map is shown in Fig. 2.2. The heat production rates presented in Fig. 2.3 are calculated by averaging the heat production rates of samples plotting within individual polygons. This means that an average value is calculated for samples from the Iddefjord granite, another average value is calculated for samples from the Flå granite, and so on. This method is useful for determining variation within and between units (e.g., what is the variation within the Iddefjord and Flå granites, and what is the difference between the two bodies). In order to relate heat production to the larger-scale geological units on the simplified map in Fig. 2.2, area-weighted averages and standard deviations are calculated for subunits classified in the same large-scale geological unit. The data are summarised in Table 2.2, and the units are discussed starting with the least heat-producing unit (numbers in italics refer to units on the simplified geological map in Fig. 2.2).

Simplified geological map of Norway.
modifed after Sigmond (2002)

Legend

1. Oslo rift, magmatic rocks
2. Cambrosilurian sediments, Oslo rift
3. Devonian sedimentary rocks
4. Caledonian intrusive rocks, mainly trondhjemite, tonalite, granodiorite and diorite
5. Caledonian intrusive rocks, mainly granite and granodiorite
6. Seiland Igneous Province, mainly gabbroic rocks
7. Caledonian thrust-sheets, mainly Neoproterozoic metasedimentary rocks
8. Caledonian thrust-sheets, mainly Precambrian gneisses
9. Caledonian, mainly metasedimentary and metamafic rocks
10. Egersund anorthosite
11. Post-Sveconorwegian granites
12. Precambrian gneisses, affected by Caledonian orogeny
13. Precambrian gneisses, TIB affinity
14. Precambrian gneisses, undifferentiated
15. Lofoten AMCG suite
16. Archean

Figure 2.2.   Simplified geological map of Norway, modified after Sigmond (2002).

Radiogenic heat production of Norwegian bedrock

Heat production rates

< 0.10
0.1 - 1.0
1.0 - 1.5
1.5 - 2.0
2.0 - 2.5
2.5 - 3.0
3.0 - 3.5
3.5 - 4.0
4.0 - 5.0
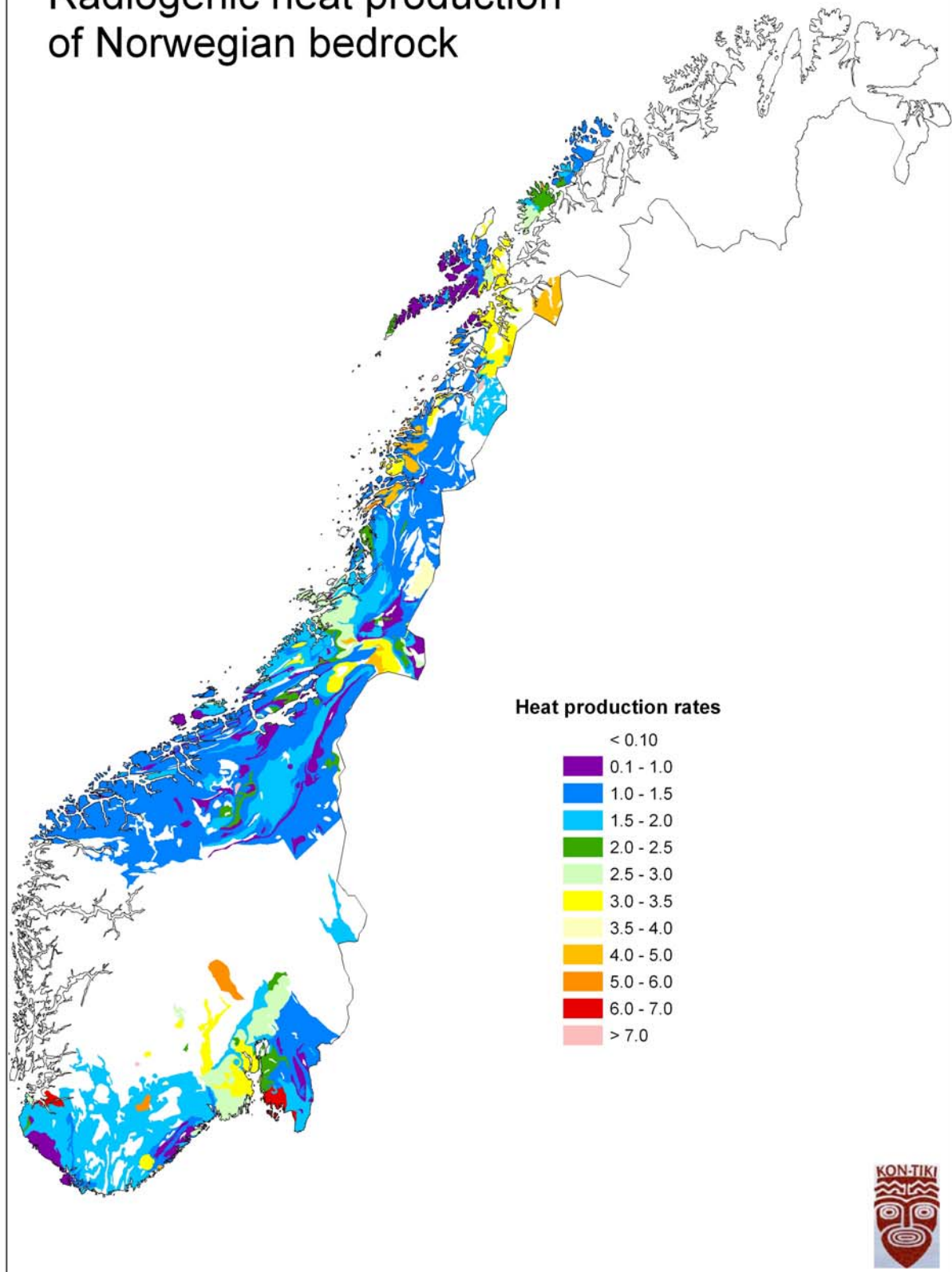5.0 - 6.0
6.0 - 7.0
> 7.0

KON-TIKI

Figure 2.3. Heat production rates determined using the data presented in Fig. 2.1 and Table 2.1. Geological base map modifed after Sigmond (2002).

Table 2.2. Heat production rates ($\mu W/m^{3)}$ of large-scale geological units as defined in Fig. 2b.

Unit	Average	St.dev.	No. samples	No. subunits
1. Oslo Rift	2.9	0.6	1040	17
2. Cambro-Silurian sediments	1.7	0.5	22	2
3. Devonian sediments	1.0	0.1	6	2
4. Caledonian intrusives, misc.	1.2	0.3	25	10
5. Caledonian granites	2.2	1.2	105	21
6. Seiland Igneous Province	No data	No data	No data	No data
7. Neoprot. sediments	1.3	0.6	23	9
8. Cal. thrust-sheets, Precambrian	2.3	1.1	35	10
9. Caledonian thrust-sheets	1.4	0.8	384	81
10. Egersund anorthosite	0.5	0.1	47	2
11. Post-Sveconorwegian granites	4.6	2.5	468	12
12. Western gneiss region	1.4	1.0	221	16
13. Transscandinavian Ign. Belt	3.1	1.7	482	23
14. Precambrian gneisses	1.8	1.3	312	56
15. Lofoten AMCG suite	0.7	0.5	97	2
16. Archaean rocks	1.1	0.3	53	4

The lowest heat production rates are found in the Egersund anorthosite massif (*10*), with an average of 0.5 ± 0.1 ($\pm$ 1 stdv) $\mu W/m^3$, and the Lofoten anorthosite-mangerite-charnockite-granite (AMCG) suite (*15*), with an average of 0.7 ± 0.5 $\mu W/m^3$. The Archaean rocks in Lofoten–Vesterålen and Troms (*16*) also yield low heat production rates, averaging 1.1 ± 0.3 $\mu W/m^3$, which is similar to that found for Archaean rocks in Finland (1.1 ± 1.3 $\mu W/m^3$) (Kukkonen & Lahtinen 2001). Caledonian intrusive rocks of Palaeozoic age (*4*), ranging in composition from trondhjemite, tonalite, granodiorite, diorite to quartz diorite, have low heat production rates averaging 1.2 ± 0.3 $\mu W/m^3$. Neoproterozoic sedimentary rocks (*7*), mostly metasandstones, at tectonostratigraphically low levels, have low heat production rates, averaging 1.3 ± 0.6 $\mu W/m^3$. Undifferentiated Caledonian thrust-sheets (*9*) and gneissic rocks of the Western Gneiss Region (*12*) have similar average heat production rates of 1.4 ± 0.8 and $\pm$ 1.0 $\mu W/m^3$, respectively. The Cambro-Silurian sediments (*2*), downfaulted and preserved within the Oslo rift and consisting of limestomes and shales, yield an average heat production rate of 1.7 ± 0.5 $\mu W/m^3$. Undifferentiated Precambrian gneisses (*14*), dominantly of Meso- to Neoproterozoic age, yield an average heat production rate of 1.8 ± 1.3 $\mu W/m^3$. Most likely, the rocks of the Western Gneiss Region (*12*) represent a northward, caledonised continuation of the Precambrian gneisses in South Norway (*14*). If these two units are considered together, they yield an area weighted average of 1.64 $\mu W/m^3$, nearly identical to the upper crustal average of 1.65 $\mu W/m^3$ (Rudnick & Gao 2003). Granitic intrusions of Palaeozoic age in the Caledonian thrust-sheets (*5*), mainly in Nordland, yield an average heat production of 2.2 ± 1.2 $\mu W/m^3$. Permian magmatic rocks in the Oslo rift (*1*) yield an average heat production rate of 2.9 ± 0.6 $\mu W/m^3$. Precambrian gneisses of late-Palaeoproterozoic age that probably represent the northward continuation of the Transscandinavian Igneous Belt in South Sweden (*13*), yield an average heat production rate of 3.1 ± 1.7 $\mu W/m^3$. The highest heat production rates are found in *c*. 900–1000 Ma post-Sveconorwegian granites (*11*) in South Norway, averaging 4.6 ± 2.5 $\mu W/m^3$. A further discussion of the data and the relationships between heat production rates, lithology, age and tectonic history will be provided when the sampling/analysis is completed in the fall of 2006.

3 BASEMENT SAMPLES FROM THE NORWEGIAN CONTINENTAL MARGIN

Trond Slagstad, Børre Davidsen and Cécile Barrère, NGU

3.1 Introduction

It is generally accepted that crystalline basement (i.e., pre-Devonian) rocks from the Norwegian mainland extend westwards beneath the Mesozoic sedimentary cover in the North Sea and Norwegian Sea. Work on the Norwegian mainland shows that heat production varies by more than an order of magnitude and is closely linked to geological variation; a similar variation can be expected on the continental margin, with obvious effects on its thermal structure. The purpose of this part of the Kontiki Project is to provide constraints on the composition, age and metamorphic history of the basement in the North Sea, Norwegian Sea and Barents Sea in order to improve our understanding of these previously uncharted areas. The results will play an integral role in constraining ongoing 3D thermal modelling of the Norwegian margin and reconstructions of the Caledonian orogenic belt.

3.2 Samples

Thirty samples of basement rocks from 22 wells in the North Sea, Norwegian Sea and Barents Sea were obtained from the Norwegian Petroleum Directorate (Fig. 3.8). Photos and brief descriptions of the samples are provided in Appendix A.

3.3 Analytical work

At present (March, 2006), the samples have undergone petrophysical analysis (density, remanence, magnetic susceptibility and thermal conductivity). The results of the petrophysical analyses are summarised in Table 3.1. By fall 2006, we anticipate that thin sections and major and trace element data will be available (analysed by XRF and LA–ICP–MS at NGU). Ten basement samples, which are thought to be of magmatic origin (intrusive and extrusive rocks and orthogneisses), will be analysed for whole-rock Sm–Nd–Sr isotopic composition. These data will provide important information on petrogenesis and source rocks, and thus the deeper structure of the margin. Geochronological analyses (focussing on U–Pb on zircon to begin with) will be carried out using the LA–ICP–MS at NGU and the NORDSIM ion microprobe in Stockholm (scheduled for late fall, 2006).
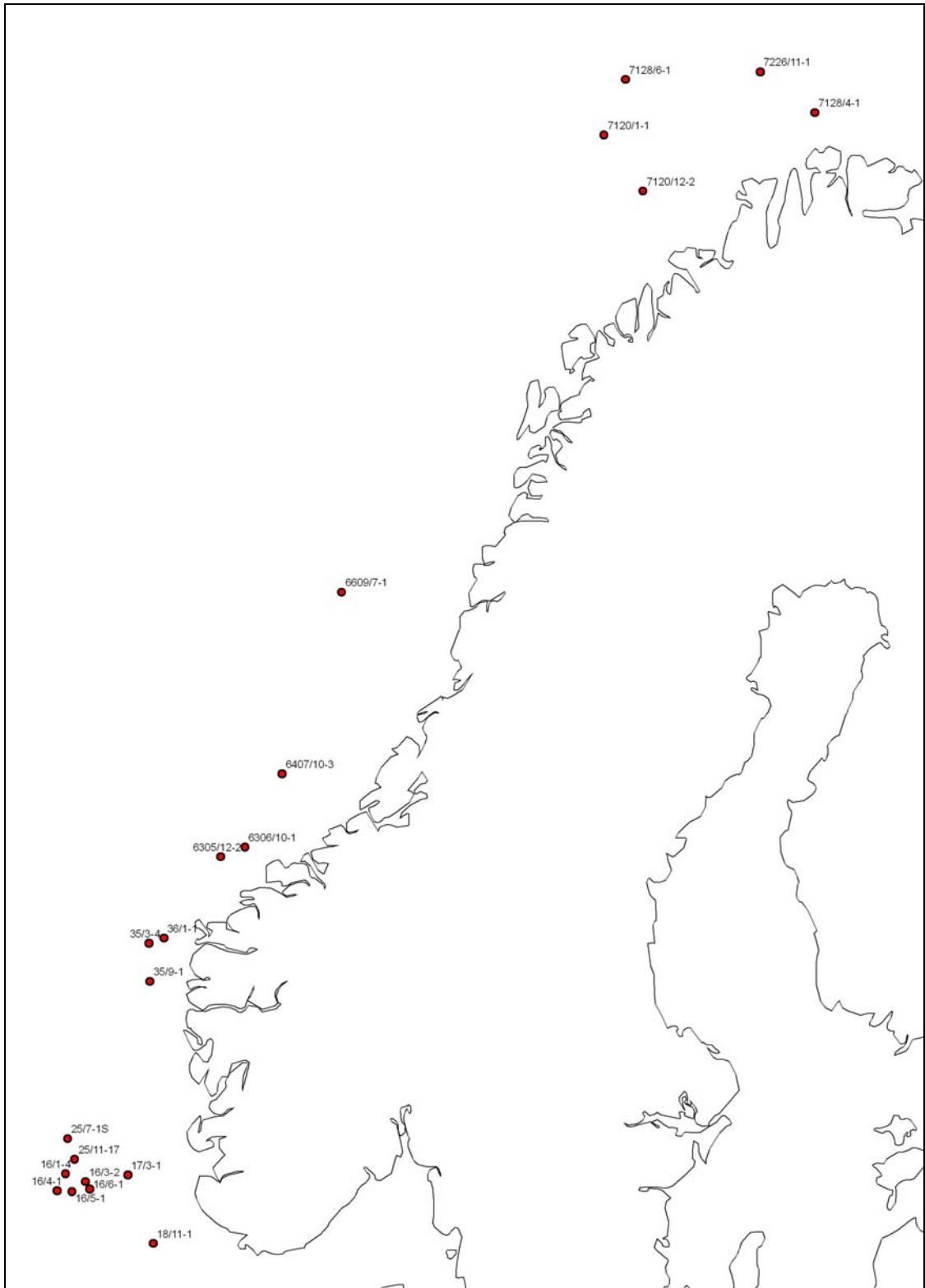
Figure 3.1.   Map showing the locations of wells from which basement samples have been obtained.

Table 3.1. Summary of petrophysical data from samples from the Norwegian continental margin, mainly pre-Devonian basement.

Sample	Depth	UTM E	UTM N	UTM Zone	Litho Code	Rock Name	Density (kg/m^3)	Susceptibility (10^{-6}SI)	Remanence (10^{-3} A/m)
16/1-4	1937	113928	6544566	32	I55	Gabbro	2765	448.4	32.1
16/3-2	2017.7	488031	6516490	31	I02	Granite	2680	949.7	48.8
16/4-1	2907.4	449959	6500262	31	S11	Quartzite	2778	221.3	2.8
16/4-1	2908.6	102089	6520325	32	I02	Granite	2646	88.0	6.9
16/5-1	1929.3	470652	6501144	31	I02	Granite	2662	179.8	11.3
16/6-1	2059.7	494913	6506985	31	V12	Andesite	2591	181.1	9.5
17/3-1	2849.5	201081	6542617	32	M30	Breccia	2750	553.3	10.3
17/3-1	2850.7	201081	6542617	32	M30	Breccia	2661	58.3	0.0
18/11-1	2082.3	236650	6445656	32	M99	Metam. unknown	2639	207.4	22.0
25/11-17	2259.5	126723	6564827	32	S28	Siltstone	2656	291.6	0.0
25/7-1S	3548.2	117155	6594075	32	S28	Siltstone	2883	1406.8	68.7
25/7-1S	3554.3	117155	6594075	32	S13	Sandstone	2722	48.8	9.2
35/3-4	4088.3	230554	6869961	32	M00	Gneiss	2773	234.1	0.0
35/9-1	2313.6	552595	6806290	31	M30	Breccia	2619	286.4	0.0
36/1-1	5212.3	566230	6868811	31	M00	Gneiss	2676	104.3	5.2
6305/12-2	3158.3	331442	6992337	32	S28	Siltstone	2740	456.8	9.6
6306/10-1	3158.5	365416	7006088	32	I55	Gabbro	2767	2836.2	58.6
6306/10-1	3159.2	365416	7006088	32	I55	Gabbro	2732	1001.7	20.0
6407/10-3	2972.1	417314	7109796	32	I02	Granite	2631	1186.7	108.9
6609/7-1	1944.7	500929	7366433	32	S28	Siltstone	2622	14.7	0.0
6609/7-1	1945.8	500929	7366433	32	S28	Siltstone	2580	24.6	11.0
7120/1-1	4002.2	454909	7980020	34	M11	Amphibolite	3085	777.1	27.2
7120/12-2	4675.8	492668	7891571	34	M30	Mylonite	2676	177.8	5.0
7120/12-2	4678.2	923517	7932992	32	M00	Gneiss	2656	181.3	10.1
7120/2-1	2230.65	481923	7987305	34	S00	Polymict conglomerate	2642	241.8	2.8
7120/2-1	2235	481923	7987305	34	S00	Reddish brown, fine-grained conglomerate or ignimbrite???	2656	328.5	8.4
7120/2-1	2239.35	481923	7987305	34	S00	Polymict conglomerate	2738	444.6	10.7
7120/2-1	2242.35	481923	7987305	34	S00	Polymict conglomerate	2495	345.9	0.0
7120/2-1	2641.35	481923	7987305	34	M30	Breccia	2587	421.4	3.9
7120/2-1	2645	481923	7987305	34	S00	Conglomerate, silty and sandy matrix	2556	151.2	0.0
7120/2-1	3478	481923	7987305	34	V20	Diabase	2762	42281.0	475.4
7120/2-1	3479	481923	7987305	34	V20	Diabase	2727	34025.5	291.6
7128/4-1	2527	538226	7938285	35	S28	Siltstone	2640	207.0	0.0
7128/4-1	2527.2	1164255	8044041	32	S13	Sandstone	2638	242.8	28.6
7128/4-1	2528.1	1164255	8044041	32	S13	Sandstone	2617	260.4	46.1
7128/6-1	2540.5	898834	8090885	32	S13	Sandstone	2689	124.8	11.0
7128/6-1	2541.73	700178	8060891	33	S13	Sandstone	2622	125.8	0.0
7226/11-1	5198.3	482263	8015817	35	M04	Biotite-rich schist/gneiss	2783	315.8	5.0
7226/11-1	5198.8	482263	8015817	35	M04	Biotite-rich schist/gneiss	2794	337.9	6.5

4 WELL LOGGING 2005

Harald Elvebakk, Øystein Nordgulen and Jan S. Rønning, NGU.

4.1 Introduction

Temperature logging was carried out in 10 boreholes in southern Norway during the summer of 2005. The University of Aarhus, Denmark carried out the logging with assistance of NGU. The results from the logging are presented in the report "Temperature logging in boreholes in Southern Norway 2005 – a data report" by Niels Balling and Niels Breiner and is included in Chapter 5 of the present report. All information for the boreholes, such as coordinates, altitude, depth, dip, time of drilling and logging are presented in Chapter 5. The description of the logging equipment and the performance of the logging are also included in Chapter 5. Photographs of the logging equicpment are included in Appendix B. Further logging will be performed in 2006. The locations of the boreholes are shown on the overview map below.
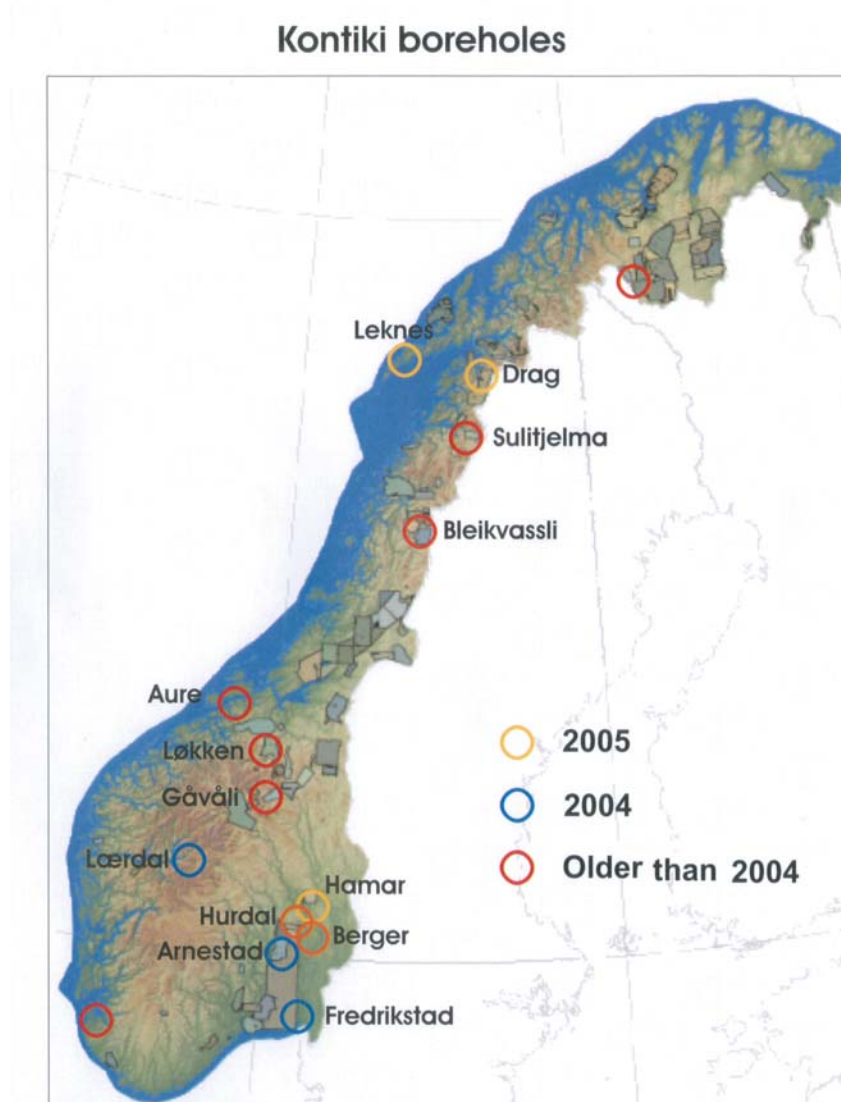
Figure 4.1. Boreholes studied in the Kontiki Project.

4.2 Geophysical logging of Berger borehole (NGU instruments)

NGU has carried out geophysical logging, including temperature logging, in the Berger borehole (Skedsmo) because no cores were obtained from the well. The other parameters were electrical conductivity of borehole water, natural total gamma radiation, rock resistivity (including calculation of porosity) and seismic velocity (both C- and S-wave). Inspection with optical televiewer was also carried out. The borehole was only logged to a depth of 480 m (total depth was 647 m) because of the short wire on the winch. All logging were performed according to descriptions made by Robertsson Geologging Ltd..

The temperature probe (Robertson Geologging Ltd.) has an accuracy of +/- 0.5 ^{o}C. This might be too uncertain but the probe has shown stable and repeatable data.

The resistivity probe measures both the Short Normal and Long Normal resistivity due to the electrode spacing (16" and 64"). The spacing between the current electrode and the potential electrode determines the depth of investigations of the measurements. The resulting data are corrected with respect to the borehole water conductivity (Thunhead & Olsson 2004). Using Archie's Law and the corrected resistivity values the porosity of the rock is calculated (Archie 1942). This will be a relative porosity because of some uncertainty in determining the constants in Archie's Law, cementation factor and correction coefficient for effective pore water conductivity ("kornformfaktor").

The sonic velocity probe records the full sonic wave train at two receivers simultaneously and also the velocity of the first arrival. The formation velocities are calculated, both the compressional and shear wave velocity.

The results from the geophysical logging are shown in Fig. 4.2. The temperature gradient is close to the gradient measured by Balling & Breiner. Comments to the temperature gradient can be read in the Balling & Breiner report (Chapter 5). A few comments will be made on the other measured parameters.

The electrical conductivity in the borehole water is quite high (600 – 1000 µS/cm). Changes in the electrical conductivity might indicate water-bearing open fractures. The gamma log indicates changes in the rock mineralogy. Increasing gamma radiation in the Berger borehole refers to pegmatite veins (up to 200 cps), while the main rock type (diorite) is in the order of 30 – 60 cps. The rock resistivity log shows several low resistivity anomalies at different depths indicating fractures or fracture zones. The optical televiewer log confirms these fractures. The average porosity is about 2 % increasing to 3 – 4 % in the fracture zones.

The sonic velocity log shows an average c-velocity (compressional) of 4000 – 4500 m/s and s-wave velocity of 2500 m/s. Low velocity anomalies correspond with the low resistivity zones indicating fractures.

Berger

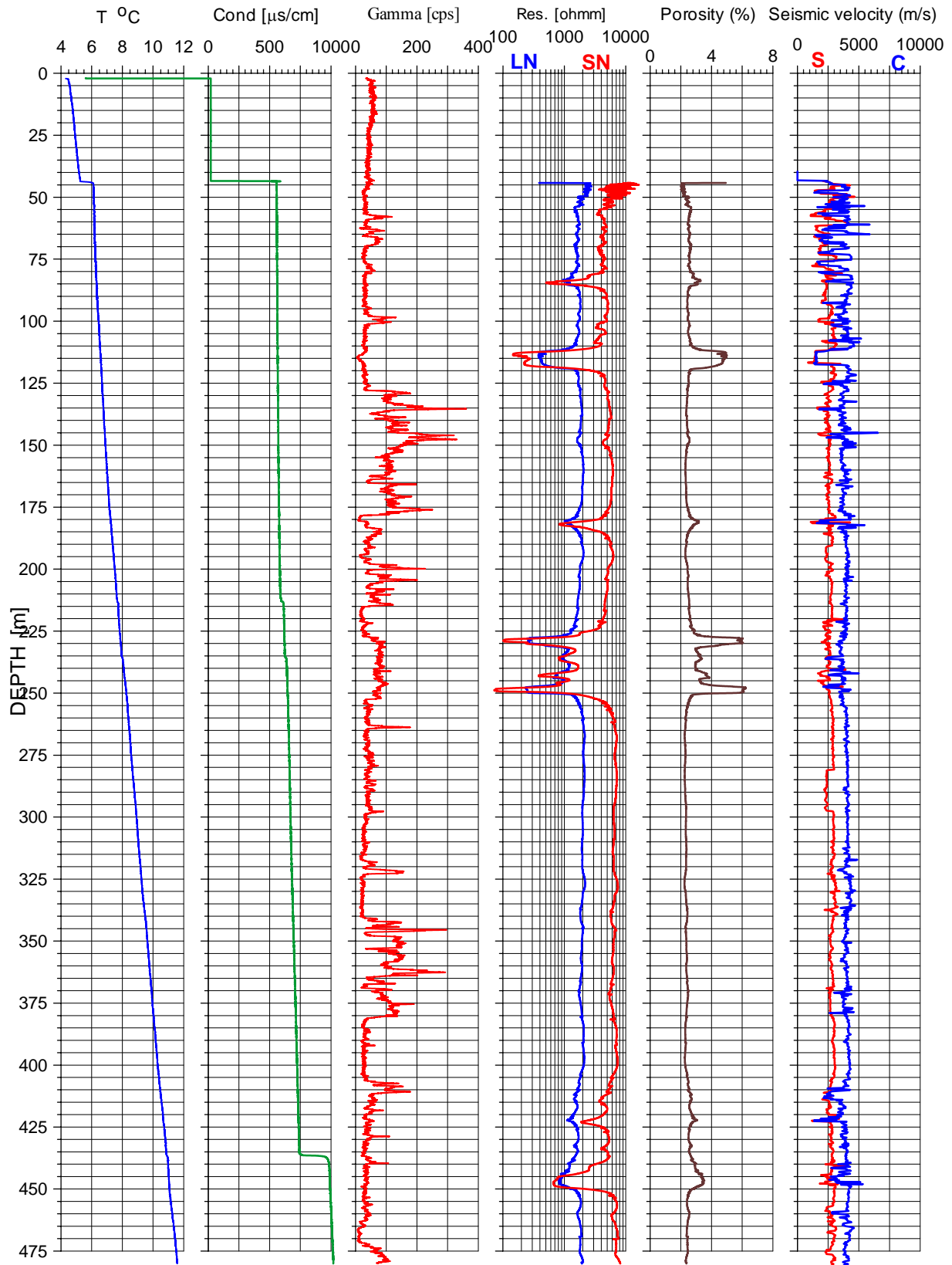UTM   615266 Ø
32V 6654651 N
174 moh.

Figure 4.2.   Geophysical logs from the Berger borehole.

Øystein Nordgulen, NGU made a geological log based on the optical televiewer record.
The main rock type in the Berger borehole constitutes a medium grained, dark intrusive rock, probably a quartz-diorite or diorite. It is difficult to observe foliation in the massive rock. Several coarse-grained pegmatite veins, and sometimes fine-grained granite cut the diorite. Along the boundary between the diorite and the veins, foliation can be observed. Between 255 m and 320 m there is a massive coarse-grained granitoid. In the bottom of the logged part, from 422 m there is a dark, fine-grained rock, probably an amphibolite. Table 4.1 shows a detailed geological log of the Berger borehole down to 480 m.

Table 4.1.   Detailed geological log of Berger borehole (by Øystein Nordgulen).

Depth	Geological description
From water level 45m	Medium-grained diorite
57 – 58 m	Coarse-grained granite/pegmatite.
60 m	Dark inclusion
60,0 – 62,4	Pegmatite
63,9 – 69,1 m	Alternating pegmatite/dark rock, sometimes fine-grained granite
76,6 – 79,8 m	Uniform light granitic rock.
84,5 m	Some fractures.
98 – 100,5 m	Coarse-grained pegmatite. NB Foliation from 96 m.
110,2 – 112 m	Some light thin veins.
113 – 117 m	Pegmatite (poor image), fractures?
126,3 – 177,9 m	Alternating diorite/pegmatite veins and some granite. High gamma radiation.
181,5 – 182,0 m	Open (?) fractures.
183,2 – 186,5 m	Light veins, observed folding
198,2 – 199 m	Coarse-grained pegmatite.
201,8 – 205,4 m	Pegmatite and mixed pegmatite/diorite.
219,8 m	Pegmatite.
225,2	Thin light veins (pegmatite).
228,5 m – ca 250 m	Some lighter rock, sometimes with light veins/spots leading to high gamma response. Low resistivity – no observed cause (fractures) on the OPTV log.
255 m – ca 320 m	Uniform granitoid. More coarse-grained than in the upper part of the borehole. Stable and high resistivity.
320,8 – 326 m	Pegmatite veins in diorite.
337 – 340 m	Pegmatite veins in diorite.
344 – 364 m	Alternating diorite and pegmatite (diffuse).
369,5 – 373,5 m	Light rock with varying amount of irregular veins.
378 – 380,5 m	Light veins.
406 m	Light veins.
412 – 421,4 m	Some light veins.
422,2 m	Light vein in dark, fine-grained rock (amphibolite?).
431,5 m	Light veins (diffuse).
445 – 450 m	Some irregular light veins with no gamma response. Some lower resistivity, no observed fractures on the OPTV log.

Strike and dip calculations from several levels and structures are shown in Table 4.2. The data are produced using the OPTV processing software. In general it was difficult to find structures for measuring the foliation. The best areas in the borehole were observed at the depth of 67–68 m and 97–98 m. At 67-68 m the strike is SW-NE dipping 12-16º to NW. At 97-98 m the strike is N-S dipping 22-29º to W. Measurements have been done at deeper levels, on veins, but it is difficult to state if they represent the real strike and dip of the rock.

Table 4.2.   Measured strike and dip in Berger borehole.

Depth	Azimuth	Strike	Dip	Description			
62.339	N271	N181	20.9	Vein	Planar	Mineralized	Lithological-banding
67.02	**N297**	**N207**	**12.7**	Primary-structure	Planar	Lithological-banding	
67.254	**N319**	**N229**	**16.6**	Primary-structure	Planar	Lithological-banding	
67.535	**N321**	**N231**	**14.1**	Primary-structure	Planar	Lithological-banding	
76.676	N260	N170	48.9	Vein	Planar	Mineralized	
79.856	N202	N112	34.4	Vein	Planar	Mineralized	Granitic pegmatite
97.222	**N284**	**N194**	**23.6**	Primary-structure	Planar	Mineralized	Lithological-banding
98.041	**N264**	**N174**	**29.6**	Vein	Planar	Mineralized	Granitic pegmatite
98.357	**N265**	**N175**	**22.6**	Vein	Planar	Mineralized	Granitic pegmatite
127.776	N135	N045	7.3	Vein	Planar	Mineralized	Granitic pegmatite
132.183	N026	N296	7.8	Vein	Planar	Mineralized	Granitic pegmatite
132.777	N321	N231	8.1	Vein	Planar	Mineralized	Granitic pegmatite
147.581	N343	N253	65.2	FracturePlanar	Fresh	Open-fracture	
147.688	N349	N259	65.9	FracturePlanar	Fresh	Open-fracture	
147.792	N259	N169	33.6	FracturePlanar	Fresh	Open-fracture	
149.577	N274	N184	20.1	Vein	Planar	Mineralized	Granitic pegmatite
157.924	N338	N248	16.5	Primary-structure	Planar	Lithological-banding	
167.296	N337	N247	22.3	Primary-structure	Planar	Lithological-banding	
169.654	N282	N192	20.1	FracturePlanar	Fresh	Open-fracture	
198.327	N324	N234	51.7	Vein	Irregular	Mineralized	Granitic pegmatite
221.381	N003	N273	17.5	Primary-structure	Planar	Lithological-banding	
315.311	N357	N267	32.5	Primary-structure	Planar	Lithological-banding	
315.363	N357	N267	27.5	Primary-structure	Planar	Lithological-banding	
368.495	N289	N199	28.5	Vein	Planar	Mineralized	Lithological-banding
439.185	N195	N105	17.9	Primary-structure	Planar	Lithological-ban**ding**

4.3   Temperature logs from all boreholes (except Lærdal)

Fig. 4.3 shows the temperature logs from all boreholes, except the two short Lærdal drill holes. The Aarhus data presented here represent raw data without any fitering (see Section 5.2). NGU has carried out temperature logging in three of the holes, Arnestad, Berger and Kjøsnesbogen. It is a good correlation between the NGU gradients and the Aarhus gradients. However the NGU temperature values are consequently 0.2 – 0.3 ºC below the Aarhus temperature curves. This is most likely due to the lower accuracy of the NGU temperature probe.

The gradient numbers annotated on the temperature curves in Fig. 4.3 do not correspond quite to the gradients in Table 5. The gradients in Fig. 4.3 are the average gradients along entire boreholes below a depth of c. 100 m, while the Balling gradient is calculated below 300 m.

The Arnestad and Hurdal boreholes reveal the highest gradients, but it should be noticed that the gradient at Arnestad decreases strongly below a depth of 450 m.
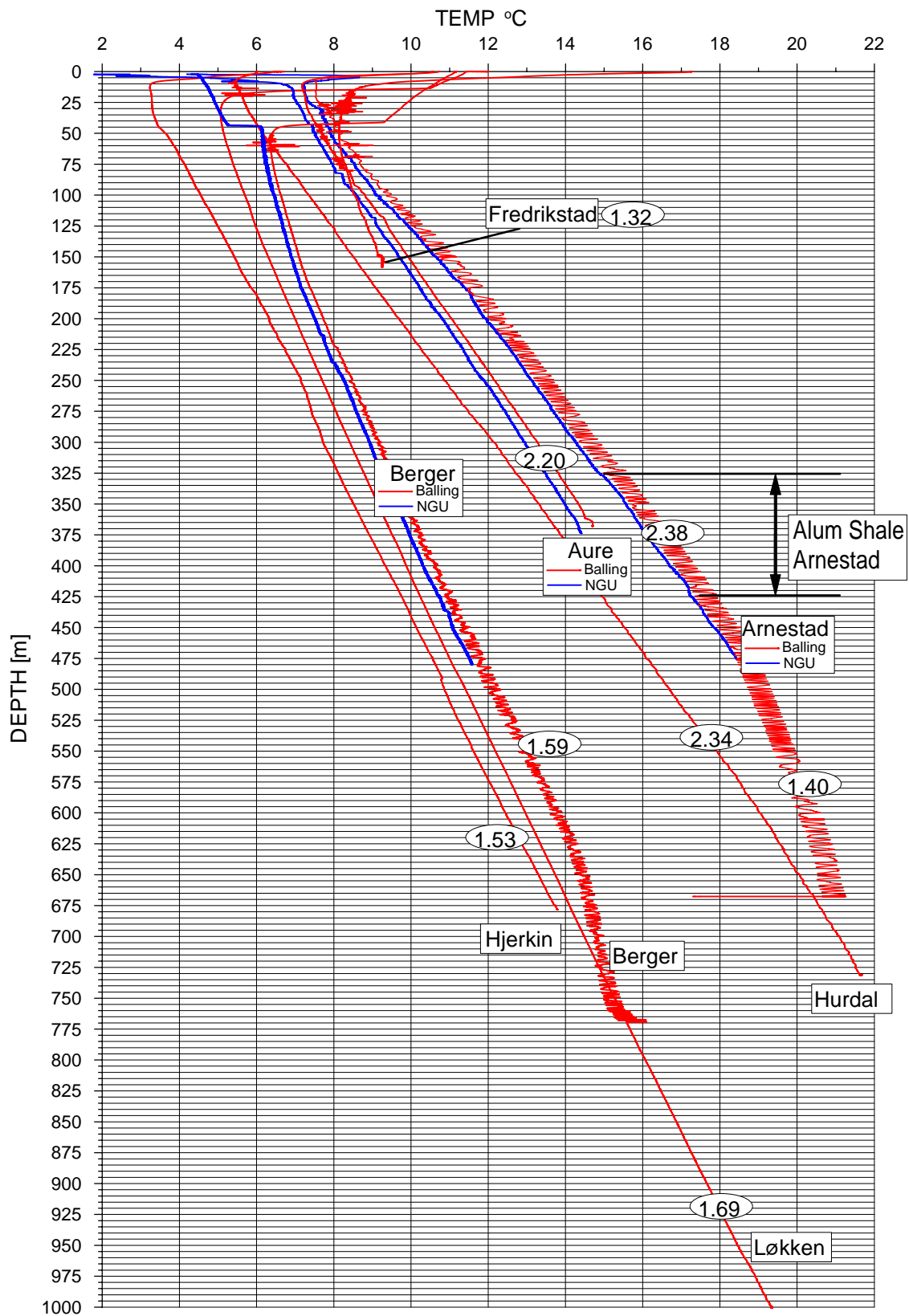

Figure 4.3. Temperature logs from boreholes in southern Norway by NGU and the University of Aarhus (Balling & Breiner).

4.4 Boreholes prepared for logging in 2006

4.4.1 Sulitjelma

Considerable efforts were made to check the conditions in a deep borehole in Sulitjelma. The borehole is situated to the west of the Jakobsbakken mining area in Sulitjelma. The depth of borehole is 1040 m and was drilled for sulphide prospecting in the eighties. The borehole is open and will be logged during 2006. Helicopter transport is necessary to bring the logging equipment into the area. Permission is necessary for helicopter landing (national park). Fig. 4.4 shows a map of the Jakobsbakken area in Sulitjelma.

Sulitjelma
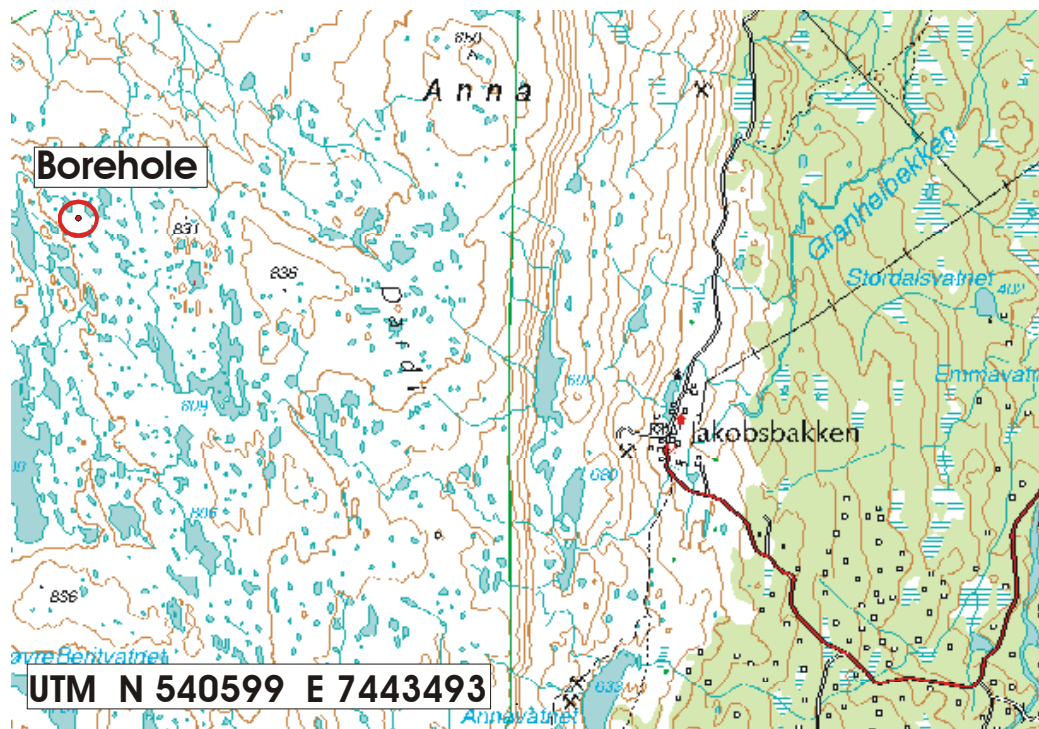
Figure 4.4. Map of the Jakobsbakken area in Sulitjelma showing the borehole location.

4.4.2 Bleikvassli

An old borehole (core) in Bleikvassli has been checked and found to be open. The borehole is 690 m long and is dipping at an angle of 68 º from the horizontal. The borehole is situated close to the Bleivassli sulphide mine and can be reached by car. The mining activity has been terminated. The temperature will be logged during the summer of 2006. Fig. 4.5 shows the location of the Bleikvassli borehole.

Bh 13-98 Bleikvassli

Figure 4.5. Location of the Bleikvassli borehole in Bleikvassli.

4.4.3 Hamar

A core hole was drilled in Hamar (Hamar Airport) within the frame of the Kontiki Project (during September 2005). The hole is vertical and drilled to a depth of 816 m and will be logged during the autumn of 2006. Fig. 4.6 shows the location of the Hamar borehole close to Hamar Airport.
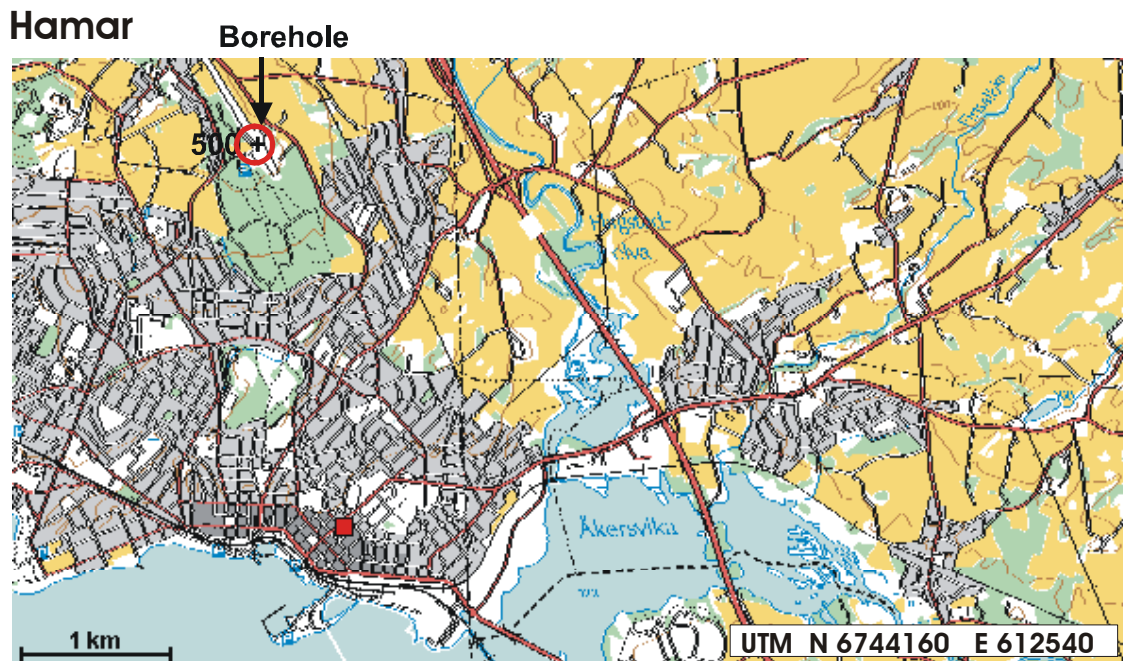
Figure 4.6. Location of the Hamar borehole.

4.4.4 Leknes, Lofoten

A 800 m deep bore hole (core) was drilled at Leknes in Lofoten during November 2005. Temperature logging will be carried out during the summer of 2006. Fig. 4.7 shows the Leknes borehole location.
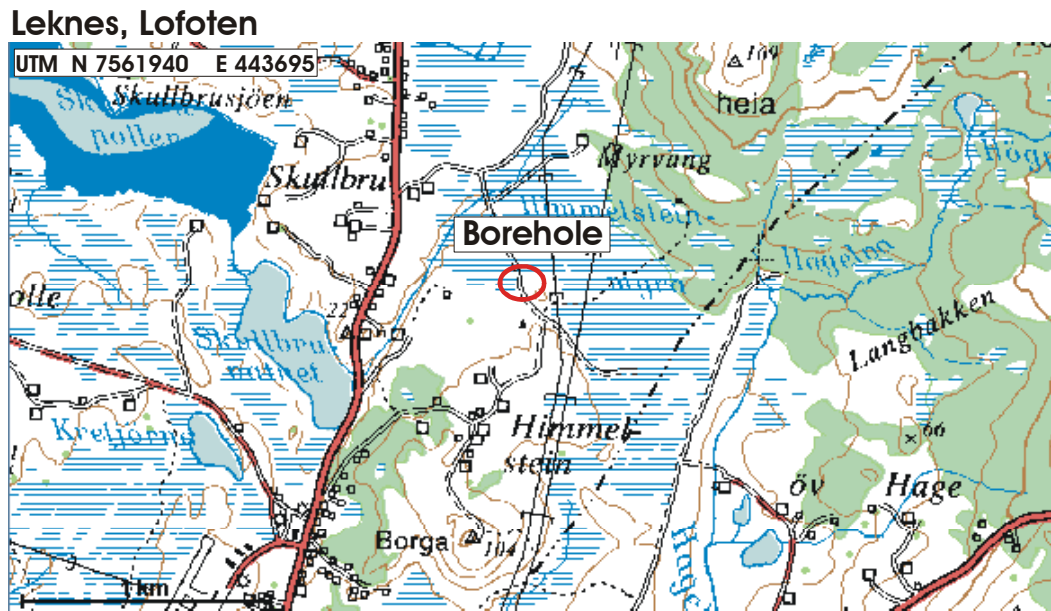
Leknes, Lofoten

Figure 4.7.   Location of the borehole at Leknes, Lofoten.

4.4.5 Drag, Tysfjord

A 779 m depth borehole (core) was drilled in Drag, Tysfjord during October 2005. Temperature logging will be carried out during the summer of 2006. Fig. 4.8 shows the Drag borehole location.

Drag, Tysfjord

Figure 4.8. Location of the Drag borehole in Tysfjord.

4.4.6 Fredrikstad

A part of the Fredrikstad borehole was logged in 2005 by Balling. However the borehole had caved in at a depth of 150 m (drilled to 804 m). The borehole will be opened during the summer of 2006 (redrilled) and a new temperature logging will be carried out.

4.4.7 Hurdal

A mining company (Crew Development) has started prospecting for molybdenum in the Hurdal area. The deposit is situated at a large depth and more drilling is necessary to estimate the tonnage of the deposit. Drilling is planned down to a depth of c. 1000 m and temperature logging will be carried out in at least one of these holes.

4.5   New temperature probe

NGU acquired a new temperature probe and a new winch during the summer of 2006. The new winch has a cable length of 1100 m. We can now carry out our own temperature logging. The new probe will have an accuracy of 0.02 ºC. The probe will in addition measure water parametres such as ph, conductivity, pressure and the content of oxygen and nitrate. The new equipment is delivered by Robertson Geologging Ltd. and will be an add-on to the existing logging equipment at NGU.

5 TEMPERATURE LOGGING IN BOREHOLES IN SOUTHERN NORWAY 2005- A DATA REPORT

Niels Balling and Niels Breiner
Department of Earth Sciences, University of Aarhus, Denmark

5.1 Introduction

In August 2005 temperature logging was carried out in a total of 10 boreholes in Southern Norway. Seven boreholes with accessible (vertical) depths ranging from 154 to 982 m and three shallow holes, about 50 m deep, were measured. Two of the shallow holes were drilled in the Lærdal tunnel (Lærdal 1 and 2) and one at the surface above the tunnel (Lærdal surface). Basic borehole information including location, depth range covered by temperature measurements and time of drilling is summarized in Tables 5.1 and 5.2. Map locations are shown in Fig. 5.1.

The temperature data are to be applied together with new measurements of thermal conductivity in the determination of new values of terrestrial heat flow at the sites of measurements. This report describes the equipment and measuring techniques used for the borehole temperature measurements, the data processing and results of measurements in terms of temperatures and temperature gradients.

The temperature measurements are part of cooperation between the Geological Survey of Norway, Trondheim and the Department of Earth Sciences, University of Aarhus in relation to the Kontiki Project financed by Statoil.

5.2 Equipment and measuring techniques

The applied temperature logging equipment has been developed and constructed by the geophysics group at the University of Aarhus. It consists of a traditional logging winch carrying the logging cable (here 1500 m), a temperature-sensing probe, an electronic recording unit as well as a depth counter, cable weight unit, a tripod and an electrical power generator. The whole system for boreholes down to 1500 m is usually transported in an ordinary department car (Figs B1-B4 in Appendix B). (Equipment for deeper boreholes, up to 5000-7000 m, is available with the winch built on a four-wheel trailer).

The temperature measurement technique is based on the high-precision quartz oscillator principle. A specially cut quartz crystal forms an integral part of an electrical oscillator, the frequency of which is almost linearly related to the ambient temperature. The temperature sensitive quartz crystal is placed in the front tip of the temperature-logging probe together with the associated oscillator electronics. Electrical power for the oscillator and the return oscillator temperature signal are sent between the surface equipment and the down-hole probe through the logging cable.

The system is operated in two-conductor transmission, with one proper conductor, here a single conductor cable (type Rochester, outer diameter 3.16 mm) with amour/borehole water forming the second conducting unit. To avoid unacceptable signal damping, the temperature signal is transmitted at a rather low frequency of about 2 kHz, as compared to the basic frequency of the quartz oscillator of about 9 MHz. The current consumption of the temperature probe is below 10 mA, which ensures signal transmission also under high resistivity conditions ("one proper conductor"). In the surface recording unit the temperature bearing frequency signal is filtered and multiplied (in phase lock loops) up to about 28 MHz. Here 1 Hz corresponds to a temperature resolution of 0.001 °C. The basic construction principles are described in detail by Balling *et al.* (1981).
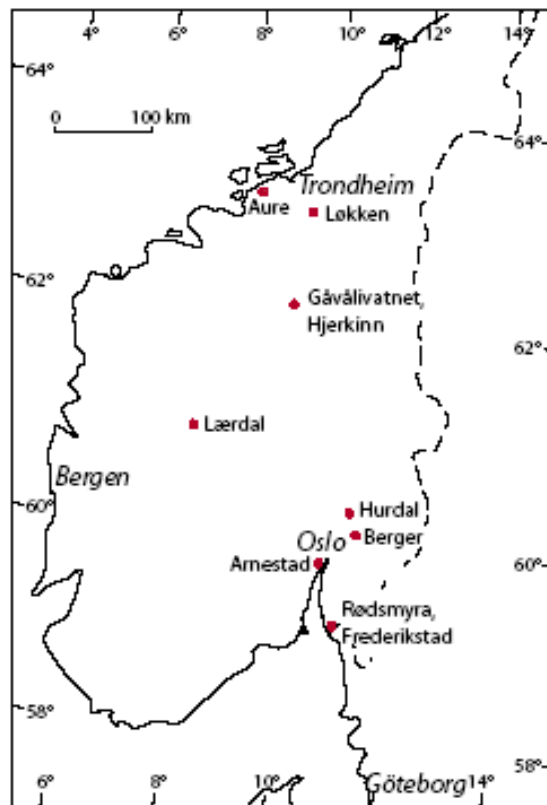

Figure 5.1   Borehole locations indicated by red dots.

Table 5.1.   Basic information for seven borehole localities, (UTM coordinates, zone 32) – including time of logging, dip (average degrees deviation from vertical) and total vertical depth of logged intervals.

Locality	Northing (m)	Easting (m)	Altitude (m)	Date of logging	Dip	Depth (m)	Time og drilling
1 Rødsmyra, Fredrikstad	6563857	610104	28	24.08.05	vertical	154	Dec. 2004
2 Arnestad, Asker	6630237	583546	11	23.08.05	vertical	681	Mar. 2004
3 Berger; Skedsmo	6654660	615271	152	25.08.05	5.8	647	2002/2003
4 Nordli, Hurdal	6707213	610093	276	26.08.05	vertical	750	ca. 1979
5 Gåvålivatnet, Hjerkinn	6904727	532846	ca. 960	17.08.05	20.7	648	ca. 1986
6 Løkken, Meldal	7001453	530797	ca. 310	18.08.05	16.5	985	July 1981
7 Kjøsnesbogen, Aure	7031460	486454	ca. 25	19.08.05	17.1	355	ca. 1990

Table 5.2. **Basis information on time of logging, borehole depth and bottom temperature for the three shallow Lærdal boreholes (one at the surface and two in the Lærdal tunnel).**

Locality	Northing (m)	Easting (m)	Altitude (m)	Date of logging	Depth (m)	Bottom temp (°C)	Time og drilling
Lærdal surface	6761624	410507	1261	31.08.05	49	2.4	Sept. 2004
Lærdal tunnel 1			c. 245	22.08.05	52	17.1	Sept. 2004
Lærdal tunnel 2			c. 245	21.08.05	44	17.0	Sept. 2004

The oscillator frequency signal is calibrated to temperature using a commercial laboratory quartz thermometer as temperature standard. For each logging probe, a fifth-degrees least-squares polynomium is applied to define the relation between frequency and temperature. Under normally good field and local electrical noise conditions, the system has a temperature resolution of 0.001-0.003 °C and an absolute accuracy between 0.01 and 0.05 °C.

The length of cable running into the borehole (depth of probe), is measured by an electronic depth counter. The cable runs over a system of stabilizing wheels including a measuring wheel (Fig. B4 in Appendix B), the angular rotation of which is recorded. The depth counter is calibrated by direct measurement of length of sections of cable run into a borehole. By experience, the reproducibility as well as accuracy of the depth measurement is normally around 0.1 % (+/- 1 m per 1000 m).

The running of the logging system is controlled by a microprocessor, which also transfers data directly to an ordinary PC (via an RS 232 communication port) where they are processed, displayed and recorded to disc files. During logging the following parameters are recorded and stored: time, oscillator frequency and associated temperature, depth of probe, logging speed, weight of probe system and cable in borehole (measured at top tripod). These data are currently visible on screen where also a temperature-depth plot is shown. Thus, recordings are followed in real time during logging (Fig B3 in Appendix B). The stop of depth penetration of the probe at borehole bottom, or at an unexpected local borehole blocking, is easily recognized by observing a combined drop in cable weight and stop in increase of temperature.

Under the special electrical measuring conditions on several present sites in Norway, where the national power system is without a proper electrical zero conductor, our present measuring system with one proper conductor is sensitive to ambient electrical ground currents. This may, as we shall see, induce significant noise in temperature signals, which needs special filtering.

5.3 Borehole logging procedure

The temperature logging is carried out running down-hole in continuous mode at constant speed. Temperature measurements at probe tip running down-hole ensure recordings at undisturbed borehole conditions. The borehole water temperature is measured, which, if no flow of water inside the hole is present, accurately represents the adjacent formation temperature. No attempts were made to accurately measure the temperature within the uppermost few metres of the air-filled part of boreholes above the water table. For most of the present boreholes a nominal logging speed of 10 cm/s was applied and a sample rate of 1 s resulting in a sample density of 10 cm. For the shallow Lærdal-boreholes a logging speed of 5 cm/s was used with a sample density of 5 cm. The procedure of borehole temperature logging is in agreement with international standard procedures (Beck & Balling 1988).

5.4 Data processing

The temperature information is to be presented in terms of temperature versus depth and temperature gradient versus depth. For some borehole sites, as mentioned above, ground electrical noise is induced into the borehole cable transmission systems, which results in equivalent significant temperature noise superimposed on the unperturbed temperature-depth signal. The temperature noise has a character which makes efficient noise filtering possible. Filtered data plots for all sites of measurements are shown in Figs. 5.2-5.11 and unfiltered versions of the same data are shown in Figs. C1- C10 in Appendix C. The induced noise has the character of either rather local noise spikes (e.g. at Lærdal and Rødsmyra, Figs. C1 and C8 in Appendix C) or regular almost harmonic perturbations (e.g. at Arnestad and Berger, Figs. C2 and C3 in Appendix C). Amplitudes of noise vary from 0.01 to 0.1 °C up to locally around 0.5 °C. Little or no significant noise is observed at Gåvålivatnet and Løkken (Figs. C5 and C6 in Appendix C).

The true temperature-depth function around a local depth point may be approximated by a constant temperature-gradient function. This means that filtering using a linear least-squares relation is appropriate. Filtering thus results in removing local temperature deviations (noise) from a local constant-gradient relation. For each borehole, a running constant depth-interval gradient has been applied. For all sites, except the high-noise sites of Arnestad and Berger, a running 5 m interval gradient filter was used. For Arnestad and Berger, a 30 m interval gradient was used.

For boreholes with little or some noise, the 5 m filtering generally results in temperature-depth relation with close to normal local high-precision temperature resolution. The 30 m filter is also very efficient in removing noise, but local potential real gradient variability over depth intervals below the length of filter is, of course, highly smoothed. At shallow depth (around 0-20 m), filtering may have the negative side effect of significantly perturbing local temperature variations such as those associated with the annual temperature wave (e.g. Figs. 5.8, and 5.9 and Figs. C7 and C8 in Appendix C). For the interpretation of data, in particular from the uppermost parts of boreholes, unfiltered and filtered data need to be mutually compared and analysed.

5.5 Results of measurements and a preliminary analysis

Temperature and interval temperature gradients are shown for each borehole. For the deeper and intermediate deep boreholes, running least-squares gradients over depth intervals of 20 m and 100 m are calculated both for the filtered (Figs. 5.2-5.8) and unfiltered data sets (Figs. C1-C7 in Appendix C). For the shallow Lærdal boreholes, interval gradients for 10 and 20 m are calculated. Temperature data sampled at all depth points are applied in the gradient calculations. The gradient plots are based on gradients calculated at depth increments of 1 m.

Borehole temperatures and temperature gradients undisturbed by the process of drilling a borehole and associated (or subsequent) circulation of bore-fluid or other effects related to drilling a hole are referred to as equilibrium temperatures and equilibrium temperature gradients. Such values accurately represent the undisturbed formation temperatures and are used together with the associated values of rock thermal conductivity to calculate heat flow, basically from the product of temperature gradient and thermal conductivity (e.g. Powel *et al.* 1988). The determination of heat flow should, as far as possible, be based on accurate values of equilibrium temperatures. Disturbing effects other than those directly related to the drilling process include ground water circulation inside the hole induced by the presence of the borehole.
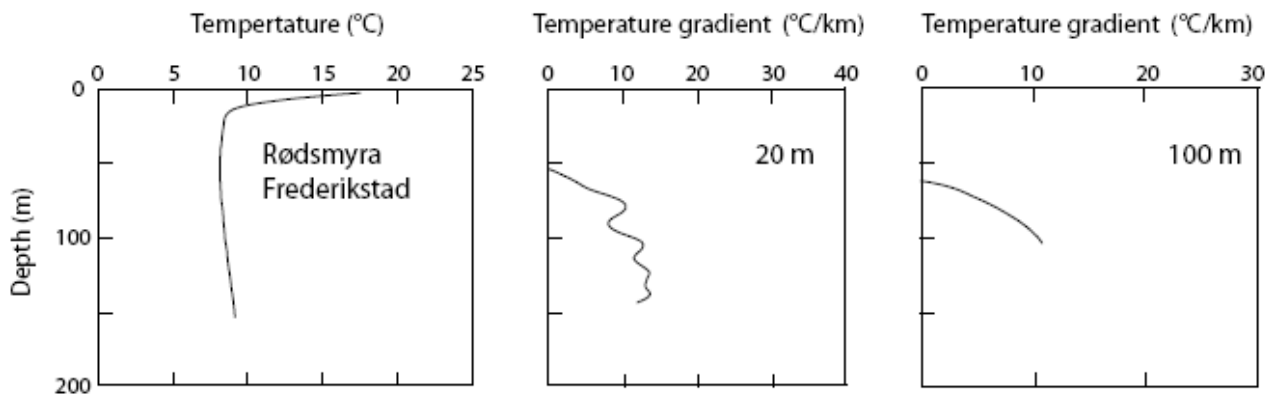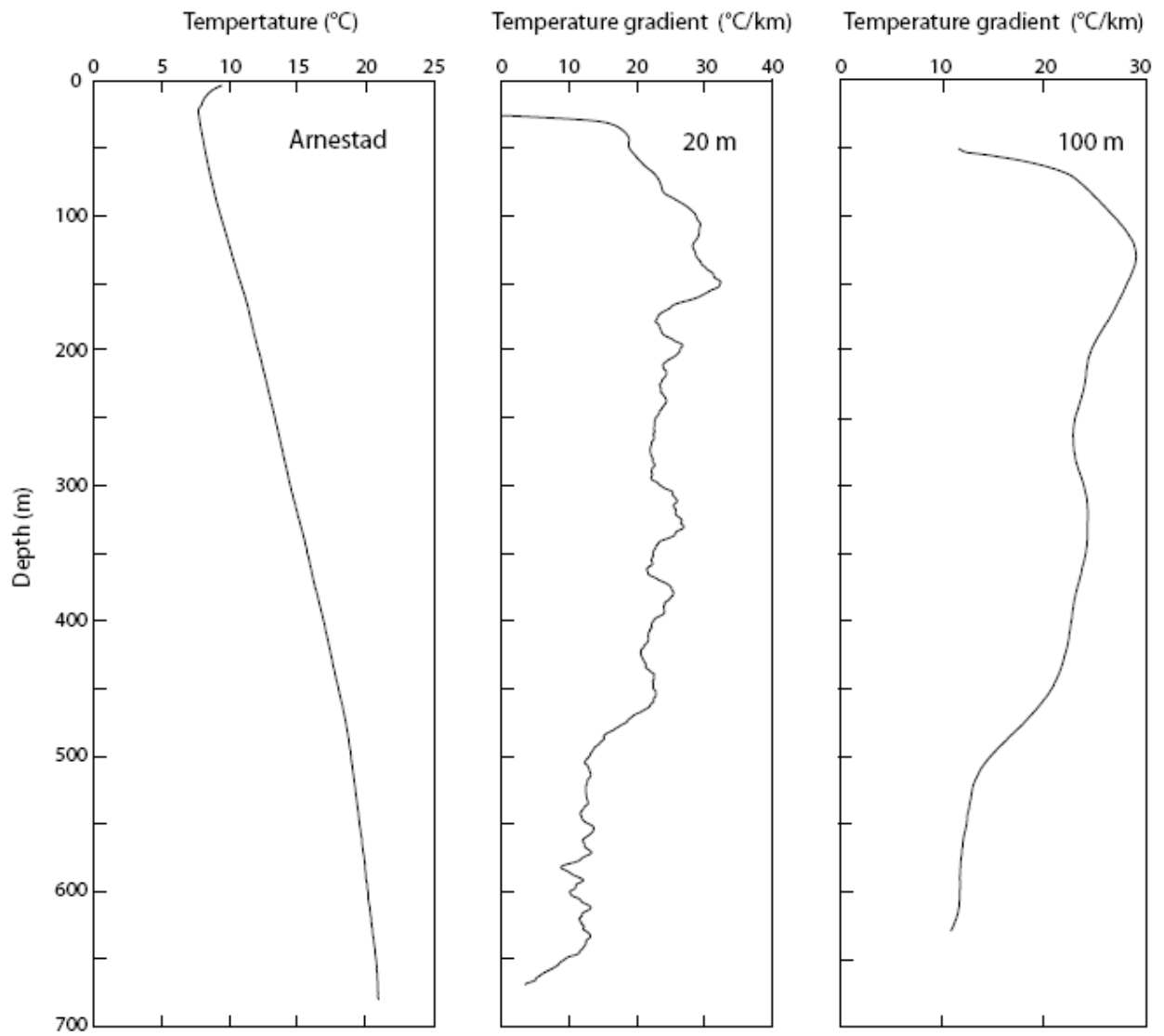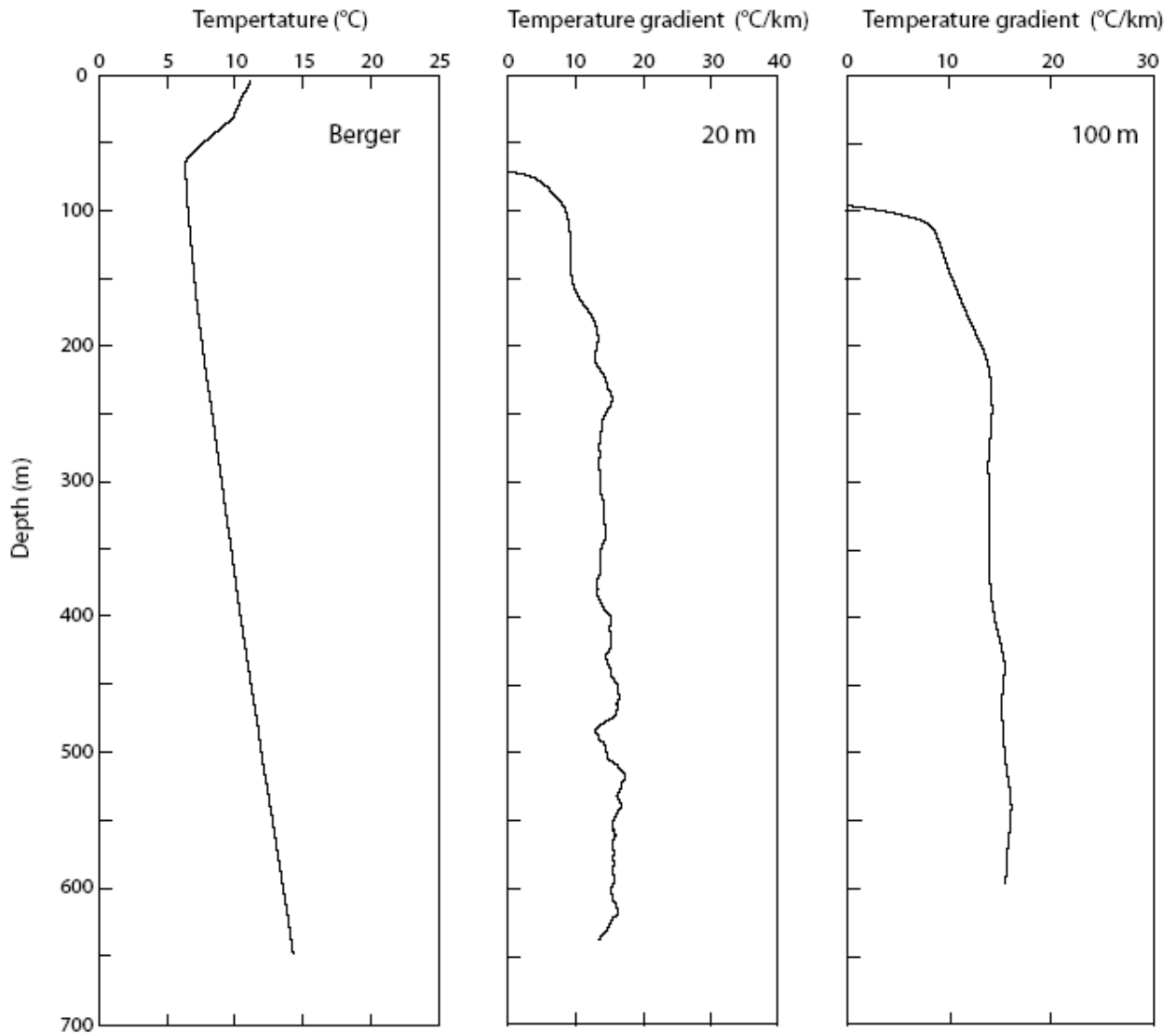

Figure 5.2. Temperature and mean interval temperature gradients as indicated for borehole Rødsmyra, Fredrikstad.

The time needed for a borehole to reach temperature equilibrium depends on several factors including the time used for drilling, type of drilling and the accuracy of temperatures needed. It may be relatively long as compared to the time of drilling in particular if high-precision local temperature gradients are required (Bullard 1947, Beck & Balling 1988). Boreholes drilled before 2002 are unlikely to have any significant disturbances from the drilling. Temperature data from those drilled in 2004 (Tables 5.1 & 5.2) need analysis for potential minor disturbances. Temperature disturbances due to flow of groundwater inside the hole may be present independent of the time since drilling. Such disturbances are typically seen as local significant temperature gradient anomalies at the depths of in- and/or outflow of water.
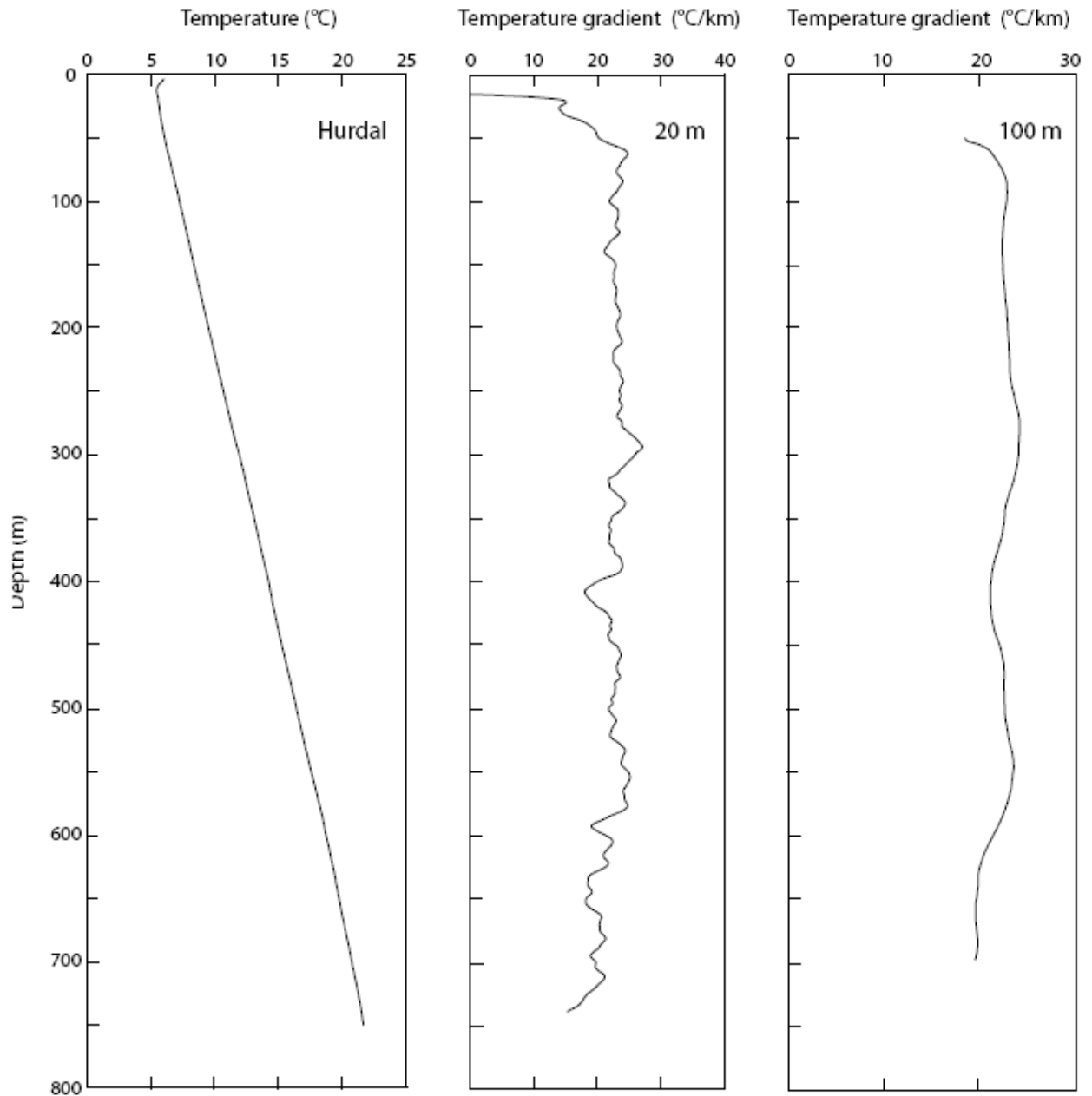
Figure 5.3. Temperature and mean interval temperature gradients as indicated for borehole Arnestad, Asker.

Figure 5.4. Temperature and mean interval temperature gradients as indicated for borehole Berger, Skedsmo.

Local temperature and temperature gradient anomalies may also be due to natural flow of water in cracks, fractures or porous units. Longer wavelength temperature and temperature gradient anomalies may be associated with local topography or transient effects related to short-term as well as long-term surface climatic temperature variations (e.g. Powel *et al.* 1988). Such effects need to be corrected for, as far as possible, before background terrestrial heat flow is calculated.

Figure 5.5. Temperature and mean interval temperature gradients as indicated for borehole Nordli, Hurdal.

The present analysis and comments are preliminary. A more detailed analysis needs to be carried out integrated with an analysis of relations between temperature gradients, rock thermal conductivity and lithology. For several reasons, temperatures in the upper parts of boreholes may include some disturbances (topography, groundwater, palaeoclimate). Therefore, in addition to temperature gradients shown in Figs. 5.2-5.8, average temperature gradients are calculated for the depth intervals below 300 m for the deeper holes (Table 5.3).
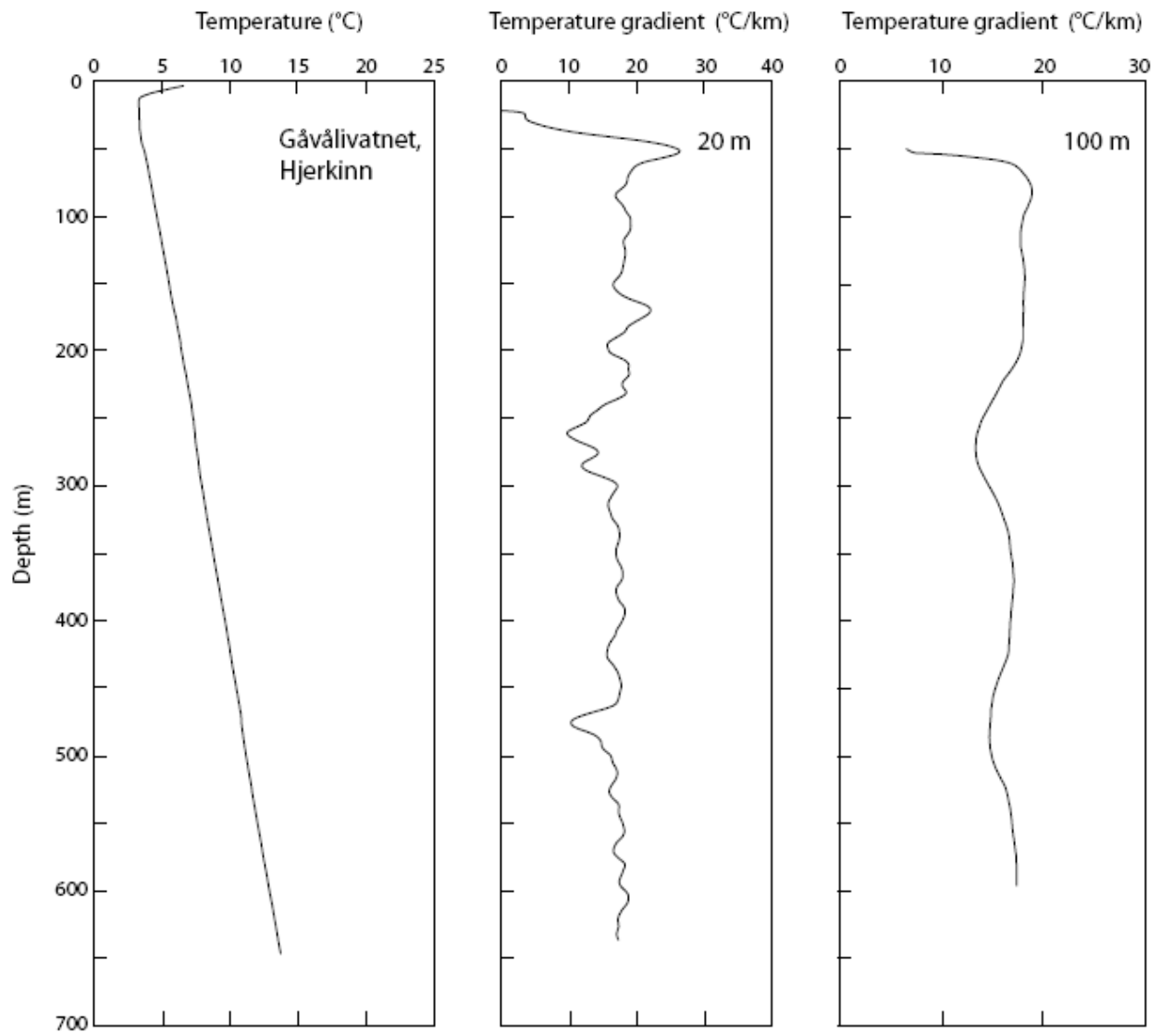
Figure 5.6. Temperature and mean interval temperature gradients as indicated for borehole Gåvålivatnet, Hjerkinn.
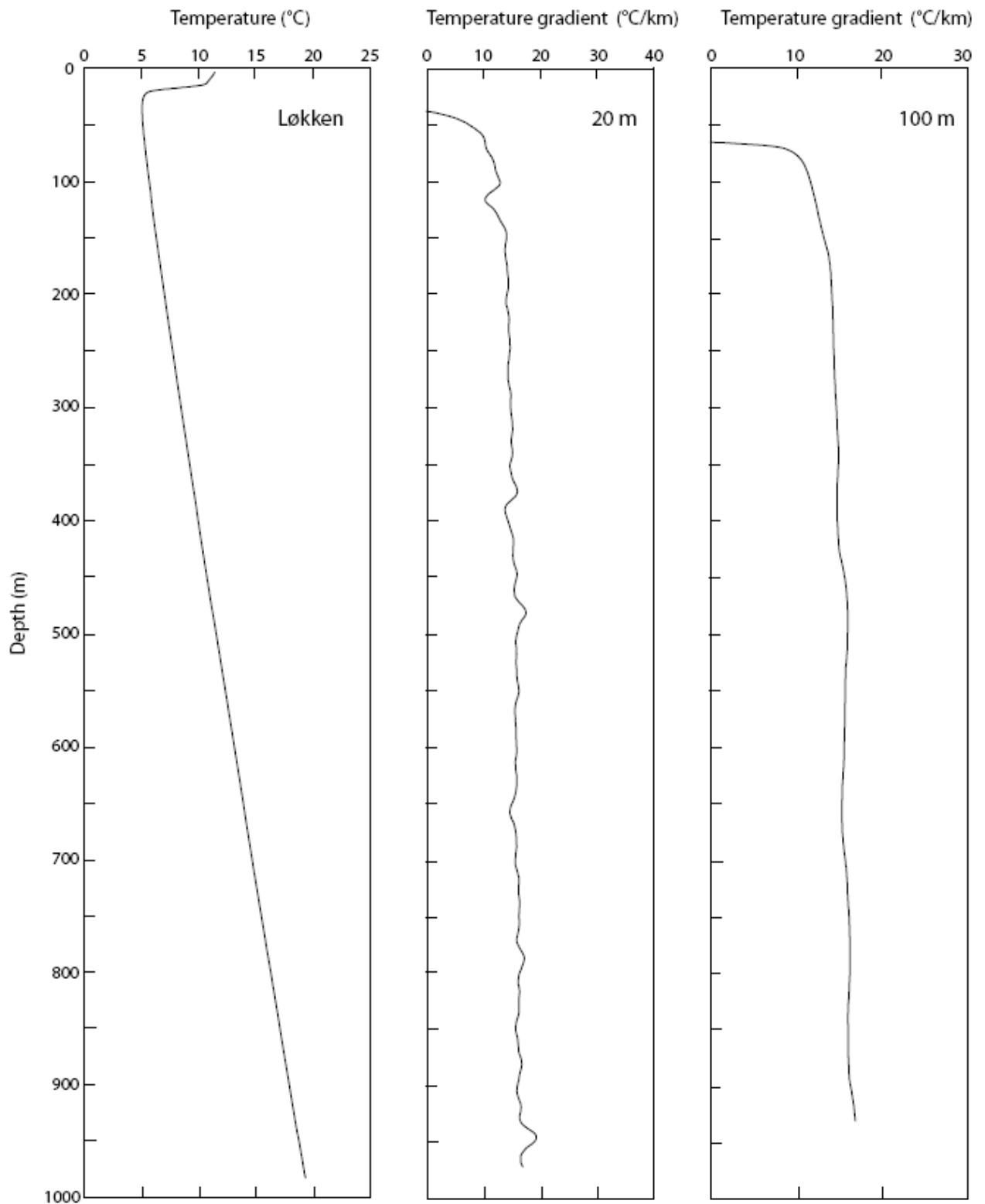
Figure 5.7. Temperature and mean interval temperature gradients as indicated for borehole Løkken.
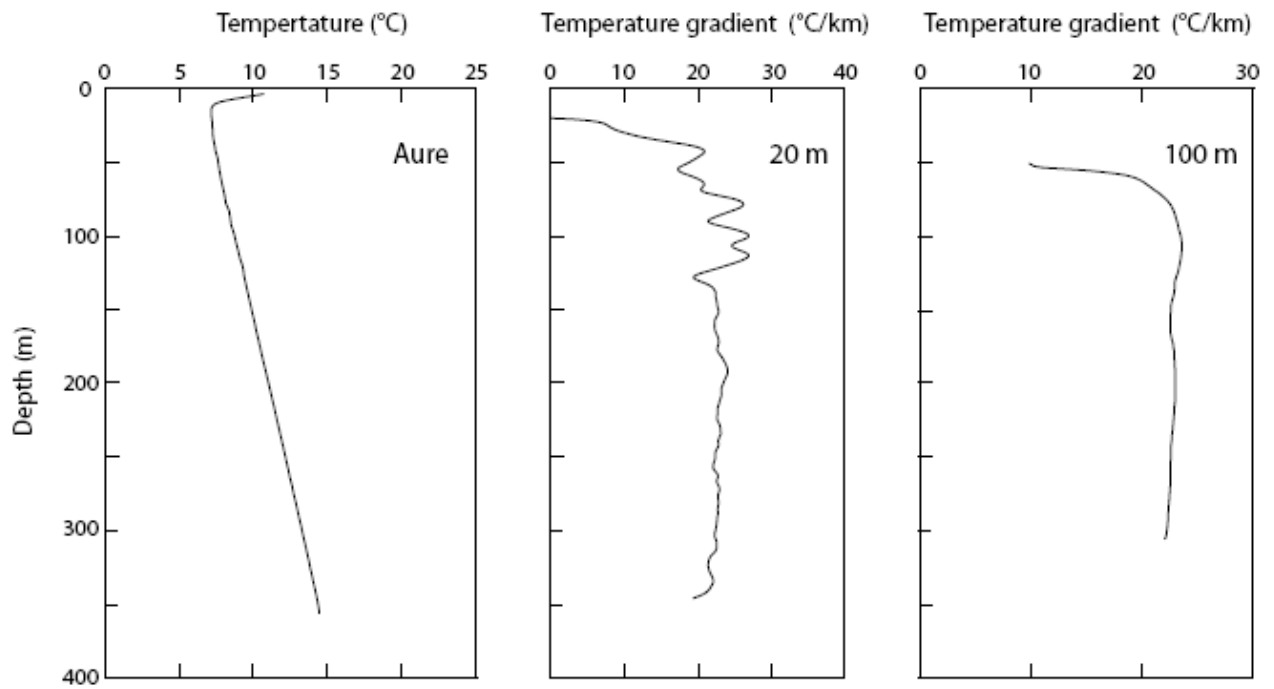
Figure 5.8. Temperature and mean interval temperature gradients as indicated for borehole Kjøsnesbogen, Aure.

Figure 5.9. Temperature and mean interval temperature gradients as indicated for borehole Lærdal surface.

Figure 5.10. Temperature and mean interval temperature gradients as indicated for borehole Lærdal tunnel 1.

Figure 5.11. Temperature and mean interval temperature gradients as indicated for borehole Lærdal tunnel 2.

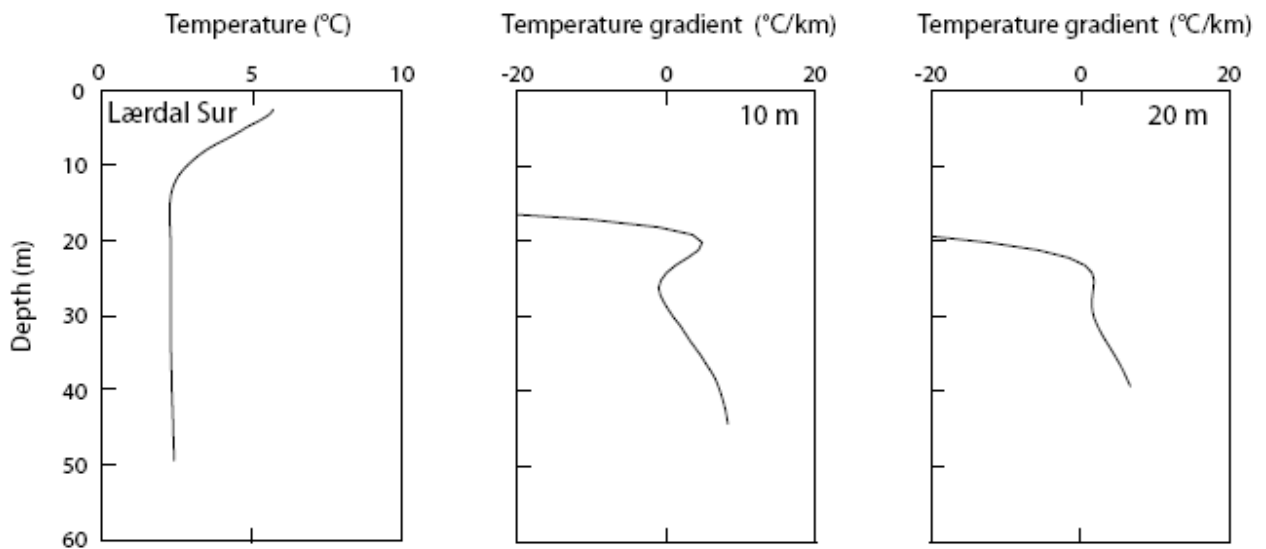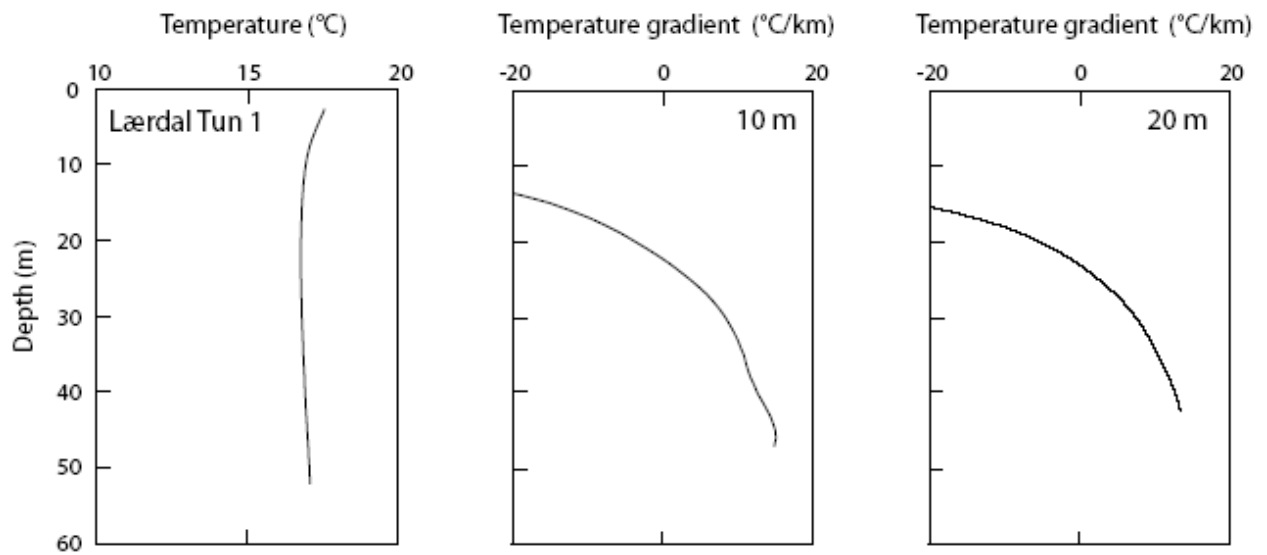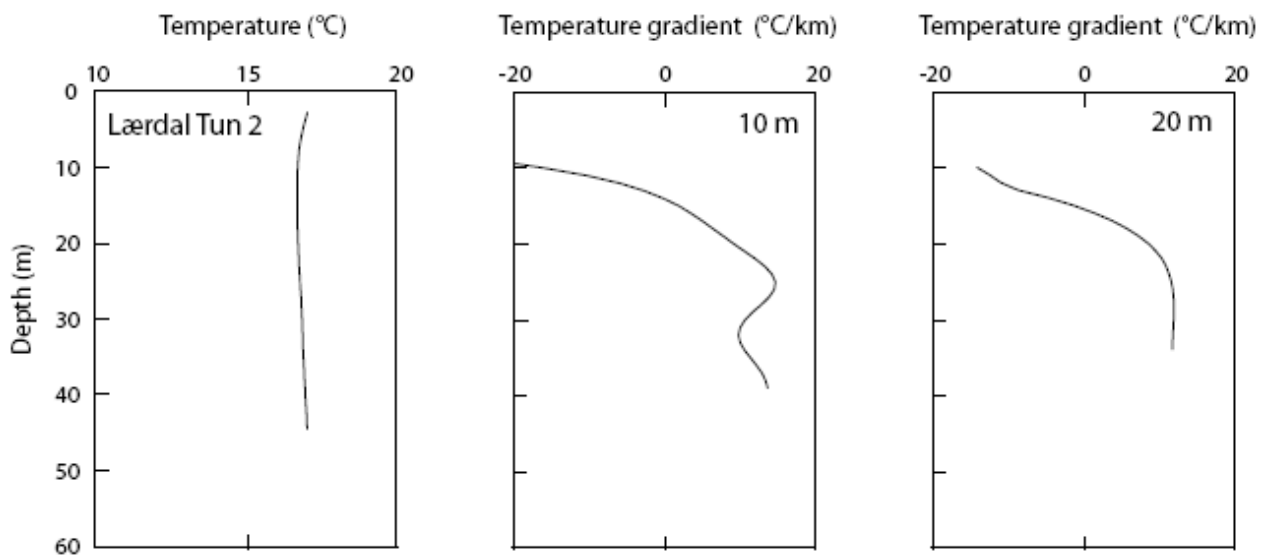**Table 5.3.   Average least-squares temperature gradient from 300 m to bottom, temperatures measured at bottom and the surface intercept temperature using linear extrapolation from the depth interval indicated.**

Locality	Depth Interval (m)	Average temp. gradient (°C/km)	Temp. at bottom (°C)	Surface intercept temp. (°C)
2 Arnestad	300 - 681	17.0	20.9	11.0
3 Berger	300 - 647	15.2	14.3	4.4
4 Hurdal	300- 750	21.9	21.6	5.4
5Gåvålivatnet, Hjerkin	300 - 648	16.5	13.7	3.0
6 Løkken	300 - 982	15.9	19.3	3.6

Most deep mean gradients are around 15-17 °C/km. The mean gradient for Hurdal is significantly higher, 21.9 °C/km. Most boreholes are characterised by having rather constant gradients over large depth sections, sometimes almost the whole measured depth interval. Hurdal has an almost constant gradient around 22 °C/km below 60 m and with some local variability (Fig. 5.5), Løkken has a well defined gradient around 16 °C/km below 150 m with a slightly systematic increase with depth and some local variability, which may be related to local water movements (Fig.5.7). Berger has a rather low gradient, around 13 °C/km between 200 and 400 m and then slightly increasing with depth (Fig. 5.4).

A low gradient at 12-13 °C/km is also observed in the deepest parts (below 500 m) of the Arnestad borehole whereas the upper part (200-460 m) shows a high gradient between 20 and 25 °C/km (Fig 5.3). This difference is likely to be related to a marked shift in thermal conductivity associated with different lithologies. Local gradient variability may be related to effects from drilling the hole in 2004, not yet dissipated. At Gåvålivatnet we observe some gradient variability around a mean value of about 17 °C/km, locally down to 10 °C/km at about 260 and 480 m (Fig. 5.6), which needs further analysis in relation to variations in thermal conductivity and potential water movements. At Kjøsnesbogen we observe a rather well-defined high gradient, 22-23 °C/km between 140 and 350 m (Fig. 5.8).

In the shallow Lærdal tunnel boreholes negative gradients are seen in the upper 15-20 m (Figs. 5.10 and 5.11). This may be related to a minor boundary temperature increase associated with the tunnel. Temperatures in the deeper parts of the holes seem unaffected by the existence of the tunnel. Also the shallow Lærdal surface hole has a negative or near zero gradient above 30 m, which may be related to surface temperature variations (annual and longer term).

The average temperature gradient between the Lærdal surface location and the tunnel boreholes using the data in Table 5.2 is 14.4 °C/km.

The size of temperature gradient variations is in good agreement with those previously observed in Norway (e.g. Grønlie 1977) and in the Fennoscandian region in general (Balling 1995).

As an integrated part of the determination of terrestrial heat flow, temperature gradients are to be analysed in relation to thermal conductivity, which is beyond the scope of this report.

6 THERMAL CONDUCTIVITY MEASUREMENTS

Kirsti Midttømme, Randi K. Ramstad, Janusz Koziel, Hans O. Rendall & Bjørn Wissing, NGU

Thermal conductivity of rock samples is measured with a transient method. Comparable measurements have been carried out at the laboratories of the University of Aarhus and the Geological Survey of Finland. Thermal conductivities are measured on core samples from the boreholes at Hjerkinn, Løkken and in the Lærdal tunnel and on rock samples that are representative for the rocks in the deep borehole at Kjøsnesbogen, Arnestad and Berger.

6.1 Method

Thermal conductivity of rock samples is measured with a transient method. A constant heat flow is induced to the top of the samples. The heat mechanism is radiation and the heat source, with a constant temperature of 300ºC ±2K, is placed 10 mm above the top surface of the sample. The sample is insulated on all other surfaces. The temperature is measured at the base of the sample. Thermal diffusivity (α) is estimated from the temperature – time plot, and the thermal conductivity (k) is calculated from thermal diffusivity, measured density (ρ) and expected specific heat capacity (c_p) of the sample using equation 1:

$$k = \rho c_p \alpha \qquad\qquad (1)$$

The theory of this method is described in Carslaw & Jaeger (1959) and Middleton (1993). Quality controls are carried out by measurements on the standard material Pyroceram 9606. The apparatus at NGU was improved in December 2005 and the error of the thermal diffusivity measurements is now within ± 5%.

6.2 Comparable thermal conductivity measurements at the University of Aarhus and the Geological Survey of Finland, fall 2005

To ensure the validity of the thermal conductivities measured at NGU, samples were sent to the University of Aarhus and the Geological Survey of Finland for comparable measurements.

A total of 14 identical samples was measured with the needle probe method at the University of Aarhus and 8 of the samples of length 20 mm measured at NGU were cut in two samples of length 9 mm and measured with the divided bar apparatus at Geological Survey of Finland (GTK). The results are shown in Fig. 6.1.

A general trend is that NGU measures the lowest thermal conductivity values and University of Aarhus measures the highest values. The deviations between the values measured at University of Aarhus and NGU are within the range of –16.0 % to + 14.8 %. The deviation between GTK and NGU's values are in the range –6.6 % to +8.6 %. The comparable

measurements study will continue with measurements on standard samples and other rock samples.

Comparable thermal conductivity measurements
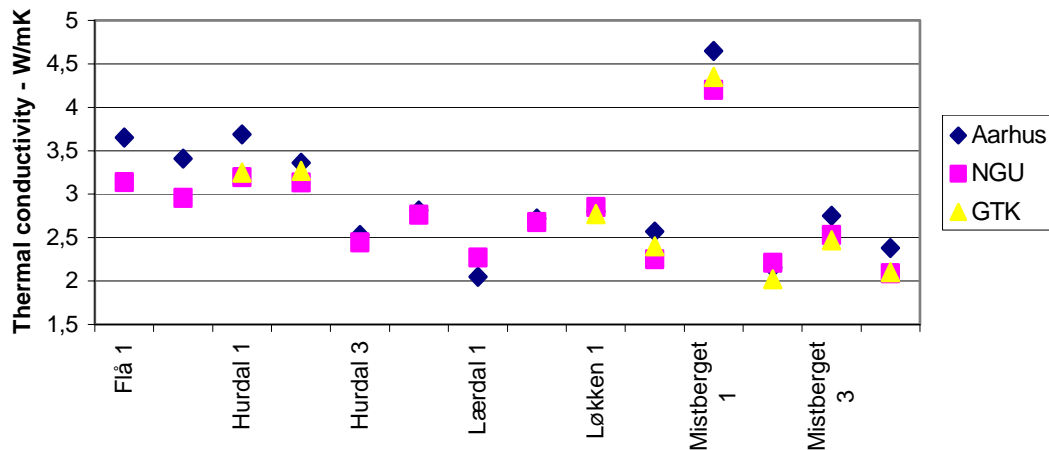
Figure 6.1. *Comparable thermal conductivity measurements at the University of Aarhus, NGU and the Geological Survey of Finland (GTK).*

6.3   Thermal conductivity measurements of rock samples

Thermal conductivities were measured on core samples from boreholes and on samples prepared from a surface rock samples. Standard size of the thermal conductivity samples is disks with diameter of 35 mm and a height of 20 mm.

For rocks with visible layering, the thermal conductivity samples are prepared perpendicular and parallel to the layering of the rock samples. The orientation of the thermal conductivity samples prepared from the cores, are decided from the orientation of the core. The specific heat capacity of the rock samples is assumed to be 850 J/kg·K

6.3.1 Hjerkinn

Thermal conductivity was measured on 62 core samples from the borehole at Gåvålivatnet on Dovrefjell. The length of the borehole is 701.6 m and the deviation of the borehole from the vertical is 20.7º. More information of the borehole is given in Table 5.1. The thermal conductivity measurements are reported in NGU laboratory report 2006-0056. The lithology logged by Folldal Verk (1985) and the locations of thermal conductivity samples in the borehole are shown in Fig. 6.2. The diameter of the core samples is 32 mm.
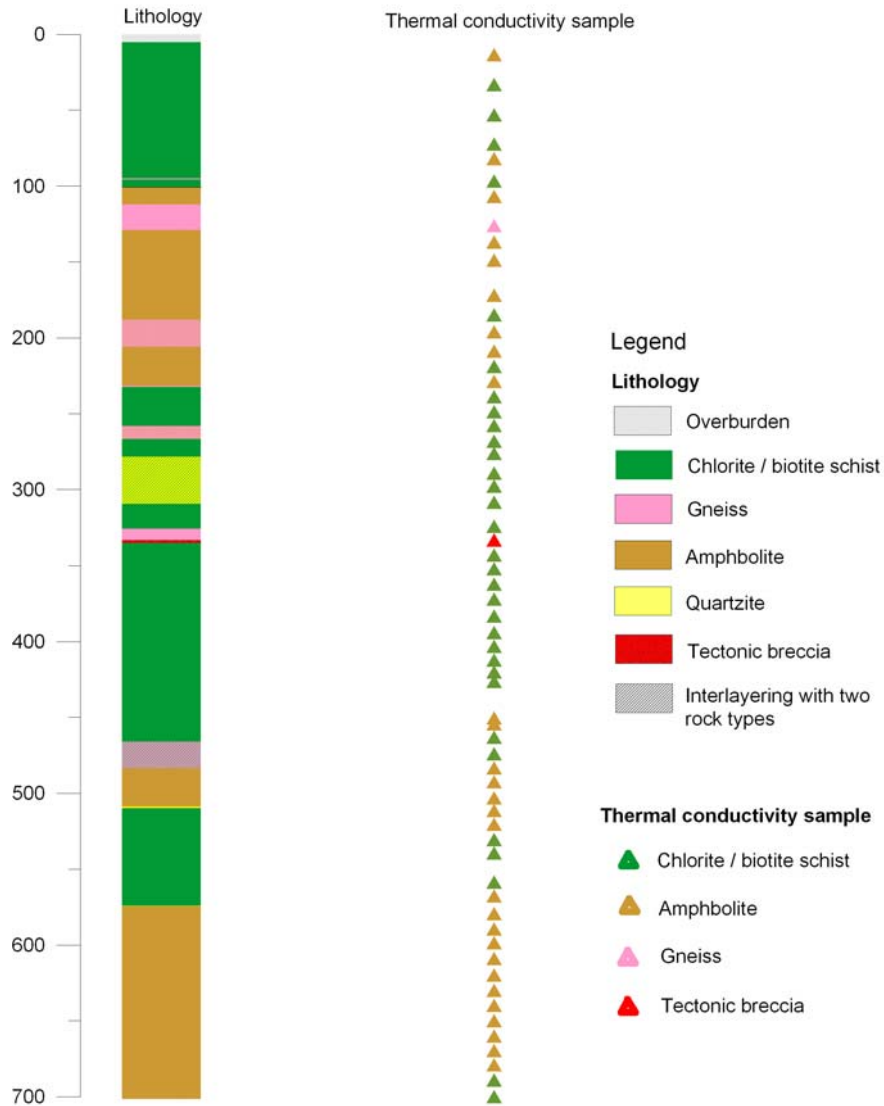
Figure 6.2. Lithology and location of thermal conductivity samples from the borehole at Gåvålivatnet. The borehole length is 701.6 m and the borehole deviation from the vertical is 20.7º. The lithology is based on the log report by Folldal Verk (1985).
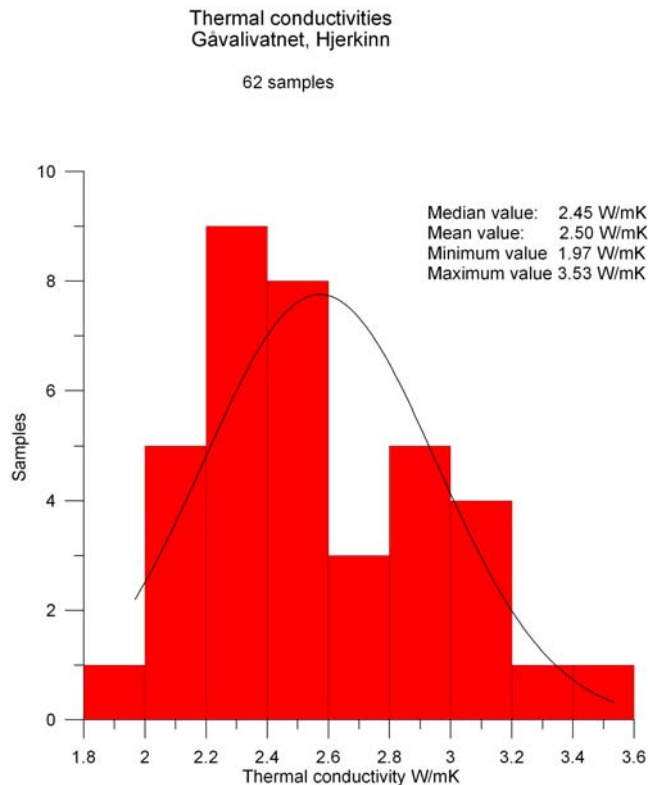
Figure 6.3. *Histogram of thermal conductivities measured on core samples from the borehole at Gåvålivatnet, Dovrefjell. The black line shows the normal distribution line.*

Thermal conductivities of the 62 samples vary from 1.97 W/mK to 3.53 W/mK with a median value of 2.45 W/mK. The measured thermal conductivities of the different rock types are plotted in Fig. 6.4. No samples of quartzite and only one sample of gneiss was measured. Both quartzite and gneiss have higher thermal conductivity than amphibole and schist. Most of the schist samples were prepared angular to the layering. It is therefore difficult to define any anisotropy effect from these thermal conductivity data.

Though only three samples are measured, garnet-biotite-sericite-schist seems to have higher thermal conductivity than the other biotite-chlorite-schist samples.
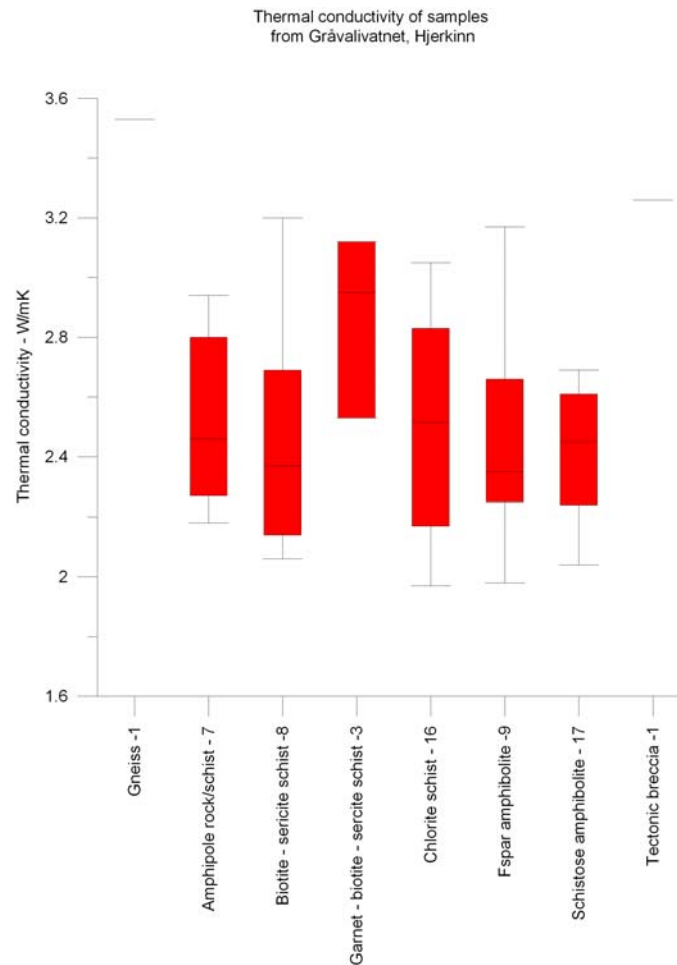
Figure 6.4. Boxplots of thermal conductivities of the different rocks from the borehole at Gåvålivatnet, Dovrefjell. The red box contains the mid 50% of data while the median value is marked with a line inside the box. The brackets above and below the line denote 95 % confidence interval. The digits after the rock name denote the number of thermal conductivity samples.

Thermal conductivity is estimated from the logged lithology and the estimated thermal conductivity is plotted versus borehole length in Fig. 6.5. Thermal conductivity of quartzite and gneiss is assumed from other thermal conductivity measurements at NGU.

The variation in thermal conductivities is inversely correlated with the temperature gradient log reported by Balling & Breiner (see Chapter 5). Lower temperature gradient is measured in the quartzite and gneiss layers than in the amphibole and schist. The temperature gradient vary with a factor of 2.7 from 0.010 K/m to 0.027 K/m, and the thermal conductivity is assumed to vary with a factor of about 2,5 W/m·K (1.8 – 4.5 W/m·K).
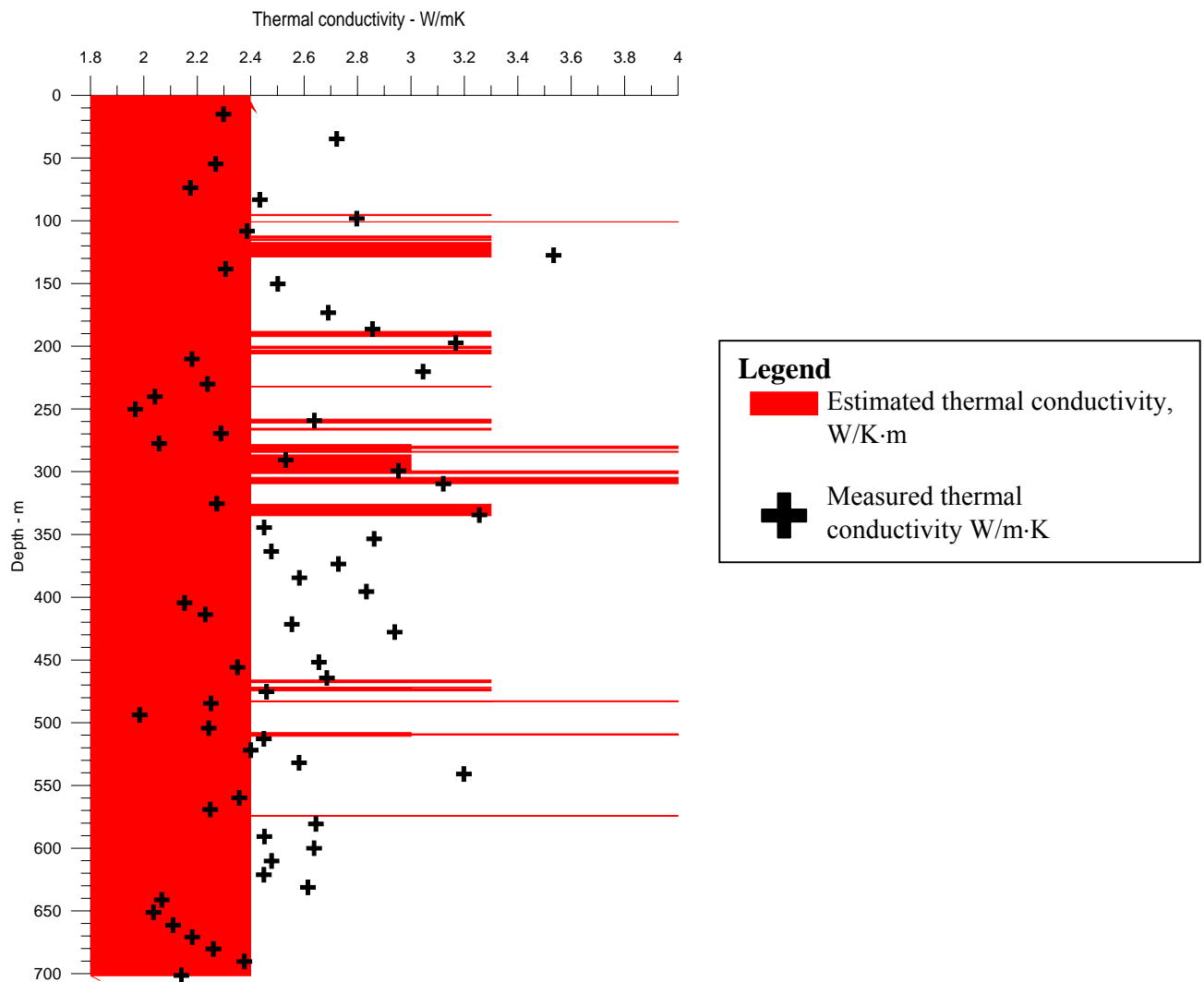
Figure 6.5. Estimated thermal conductivity of the 701 m long borehole at Gåvålivatnet, Dovrefjell. Thermal conductivity values are estimated from the measured thermal conductivities and the lithology.

6.3.2 Løkken

Thermal conductivities were measured on 83 samples from the 1030 long (985 m deep) borehole at Løkken, and reported in NGU laboratory report 2006-0056. More information of the borehole is included in Table 5.1 by Balling & Breiner (Chapter 5). The lithology of the borehole is described in a report from Orkla Industrier. Thermal conductivities of the samples are plotted against the borehole length in Fig. 6.6 and shown in a histogram in Fig. 6.7. Thermal conductivities vary from 2.60 W/mK to 3.56 W/mK with a median value of 3.06 W/mK.

Thermal conductivities
Løkken
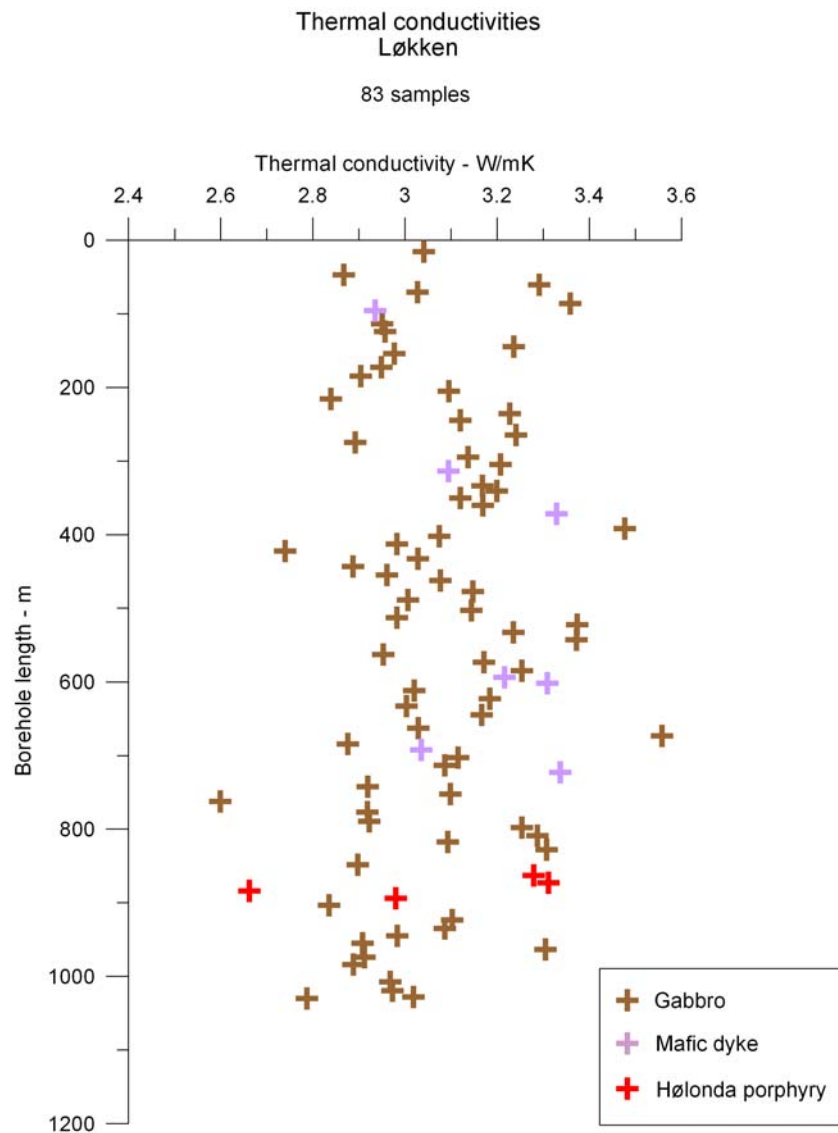
83 samples

Figure 6.6. ***Thermal conductivities of the borehole at Løkken plotted against borehole length. The***
colour of the dots shows the rock type.

The lithology of the samples is classified as gabbro, Hølonda porphyry and mafic dyke.
Thermal conductivities of the different rocks are shown as boxplot in Fig. 6.8. The red box
contains the mid 50% of data. 87 % of the samples are gabbro. All rock types have high
thermal conductivities. But the mafic dyke samples seem to have somewhat higher thermal
conductivity than the gabbro and the Hølonda porphyry samples.
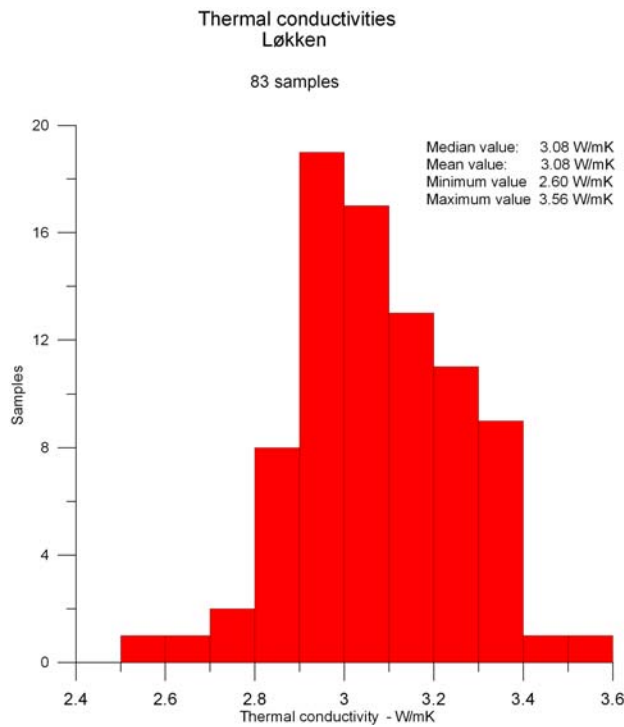
Figure 6.7. Histogram of the 83 thermal conductivites measured on samples from the Løkken borehole.
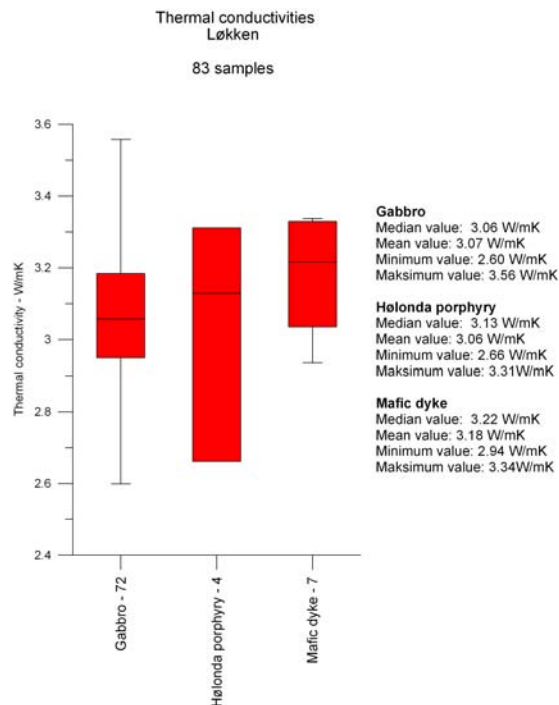
Figure 6.8. Boxplots of the thermal conductivities measured on the core samples from the Løkken borehole.

The variation in the thermal conductivities measured on the gabbro samples is shown in Fig. 6.9. There is no clear correlation between the textural and structural parameters i.e. grain size and the measured thermal conductivities. There is an effect of mineralogy where the samples with high content of pyroxen and magnetite have the highest thermal conductivities. There seems to be a trend where saussurite samples and samples with higher content of epidote have lower thermal conductivity.
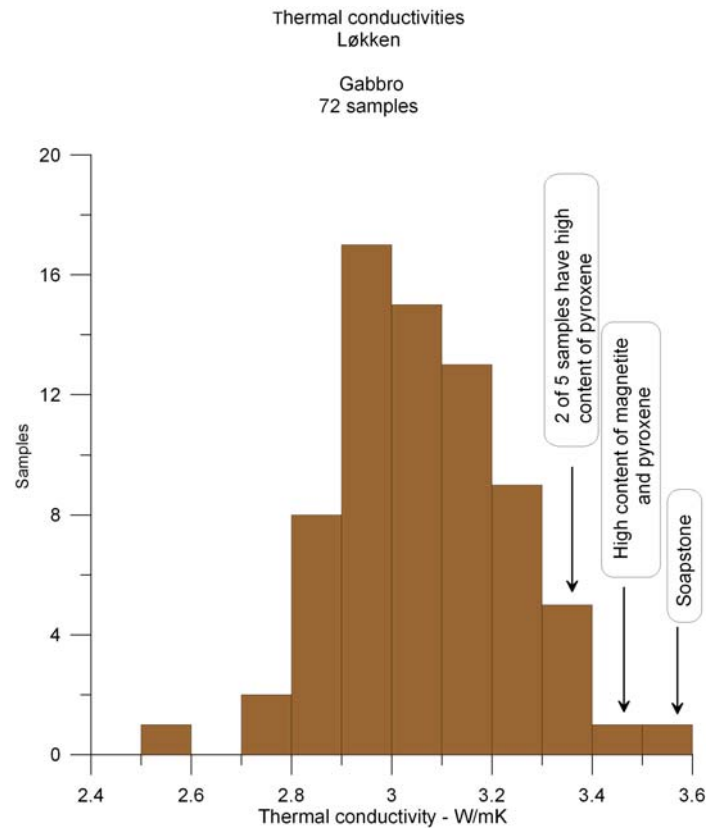
Figure 6.9. *Frequency distribution of measured thermal conductivities on the gabbro samples from the borehole at Løkken.*

The temperature logged in the borehole (Chapter 5) in the Løkken borehole shows a nearly linear trend and the temperature gradient log is low and nearly constant at 15 K/km with the depth. The temperature gradient log fits with the thermal conductivity measurements. The thermal conductivity is high and relative constant with depth.

6.3.3 Kjøsnesbogen

Thermal conductivities were measured on two rock samples taken close to the borehole at Kjøsnesbogen, Aure. More information of the borehole is given in Table 5.1. The samples are dioritic gneiss. Sample 1 is coarse-grained and Sample 2 is fine-grained. Measured thermal conductivities are plotted in Fig. 5.10

49

Thermal conductivity , Aure
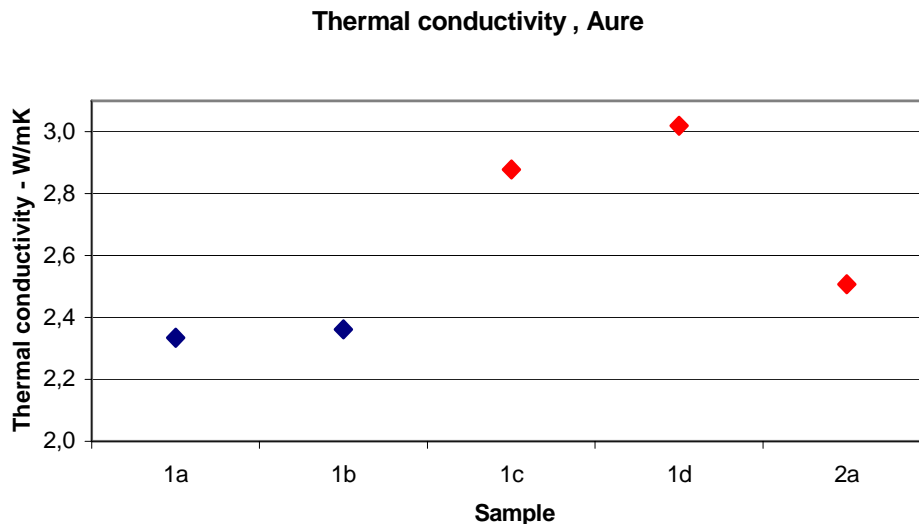
Figure 6.10. Thermal conductivities measured on rock samples from Kjøsnesbogen, Aure. Red dots are measured parallel and blue dots are measured perpendicular to the layering.

The anisotropy effect of the thermal conductivity ($a=k_\parallel / k_\perp$) measured for sample 1 is 1.25. Lower thermal conductivity of sample 2 may be explained by a fine-grained texture and a higher content of dark minerals than in sample 1.

The temperature gradient log reported by Balling & Breiner in Chapter 5 shows variation in the temperature gradient in the upper 130 m of the borehole. The variation is partly dependent on changes in the lithology.

The lithology log will be constructed from the geophysical logs in the borehole, but more thermal conductivity measurements on representative rock samples are needed to produce a better estimate of the heat flow in the borehole.

6.3.4 Lærdal

Two boreholes of about 50 m depth, Lærdal 1 and 2, were drilled in the Lærdal tunnel and located 9.7 km and 11.24 km, respectively, from the Lærdal entrance to the tunnel. Both boreholes are located in gneiss. More information about the boreholes is included in Table 5.2 in Chapter 5. Photographs of the cores and detailed information of the thermal conductivity measurements is reported in the NGU laboratory reports 2005-0311 Lærdal 1 and 2005-0297 Lærdal 2.

Lærdal 1

Thermal conductivities were measured on 69 samples from the Lærdal borehole 1. Thermal conductivities are plotted versus borehole depth in Fig. 6.11. Histogram of the thermal conductivities in Fig. 6.12 shows the distribution of the thermal conductivities. The values range from 2.35 – 5.68 W/mK with a median value of 2.86 W/mK.

The samples are described as granodiorite, granite and mica/granodioritic/dioritic/quartz-rich gneiss. Boxplots of the thermal conductivities of the rocks is shown in Fig. 6.13.
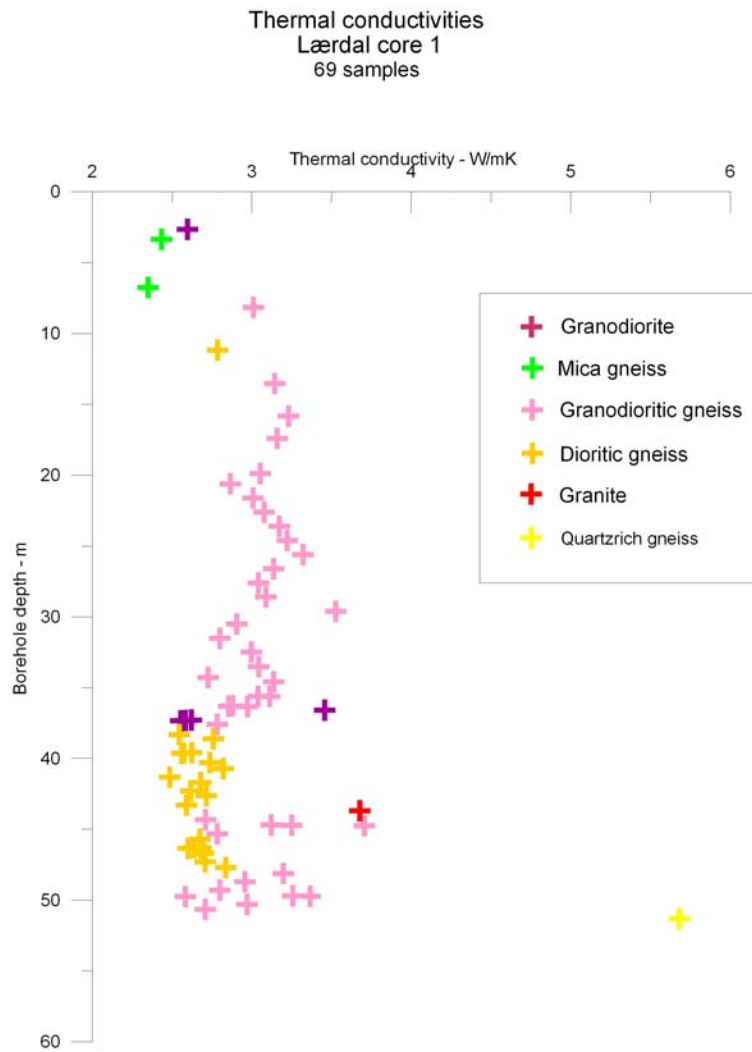
Figure 6.11. Thermal conductivities of the Lærdal 1 borehole in the Lærdal tunnel. The colour of the dots shows the rock type.

Thermal conductivities
Lærdal core 1

69 samples

Lærdal Core1
Median value: 2.86 W/mK
Mean value: 2.94 W/mK
Minimum value: 2.35 W/mK
Maximum value: 5.68 W/mK

Figure 6.12. **Histogram of thermal conductivities measured on samples from the Lærdal borehole 1. The black line shows the normal distribution line.**

Thermal conductivities
Lærdal core 1
69 samples

Dioritic gneiss (20 samples)
Median value: 2.68 W/mK
Mean value: 2.67 W/mK
Minimum value: 2.49 W/mK
Maximum value: 2.84 W/mK

Granodiorite (5 samples)
Median value: 2.60 W/mK
Mean value: 2.76 W/mK
Minimum value: 2.56 W/mK
Maximum value: 3.46 W/mK

Granodioritic gneiss (40 samples)
Median value: 3.04 W/mK
Mean value: 3.04 W/mK
Minimum value: 2.58 W/mK
Maximum value: 3.71 W/mK

Figure 6.13. **Boxplots of thermal conductivities of the different rocks from the Lærdal borehole 1. The red box contains the mid 50% of data while the median value is marked with a line inside the box. The brackets above and below the line denote the 95 % confidence interval.**

52

Fig. 6.13 shows that the thermal conductivity varies with rock type. The sample of quartzrich gneiss has very high thermal conductivity. Of the most common rocks, granodiorite gneiss (median value 3.04 W/mK) has high thermal conductivity while diorite gneiss has (median value 2.68 W/mK) lower thermal conductivity.

The large variation in the thermal conductivities of the five samples of granodiorite is due to the anisotropy effect. The sample prepared parallel to the layering has 34 % higher thermal conductivity than the four samples prepared perpendicular or angular to the layering.

The content of feldspar affects the thermal conductivity of the granodiorite gneiss. The samples with lowest thermal conductivities have veins of feldspar.

Lærdal 2

Thermal conductivities were measured on 75 samples from Lærdal borehole 2, drilled inside the Lærdal tunnel. Thermal conductivities are plotted versus borehole depth in Fig. 6.14. The histogram of thermal conductivities in Fig. 6.15 shows the distribution of the thermal conductivities. The values range from 2.14 to 3.98 W/mK with a median value of 3.25W/mK. The samples are described as mica gneiss, granodioritic gneiss, dioritic gneiss and granite gneiss only by visual inspection of the samples and some inaccuracies may occur. Boxsplots of the thermal conductivities of the rocks are shown in Fig. 6.16.

Figure 6.14. Thermal conductivities of the Lærdal 2 borehole inside the Lærdal tunnel.
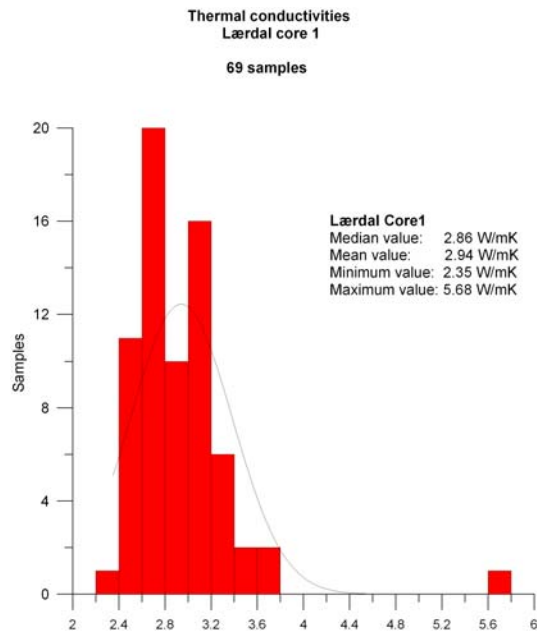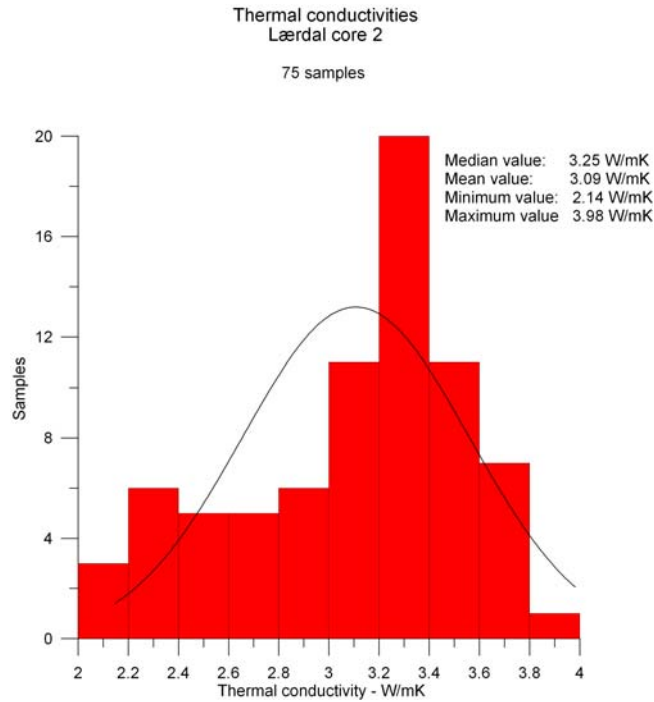
Figure 6.15. *Histogram of thermal conductivities measured on core samples from the Lærdal 2 borehole. The black line shows the normal distribution line.*
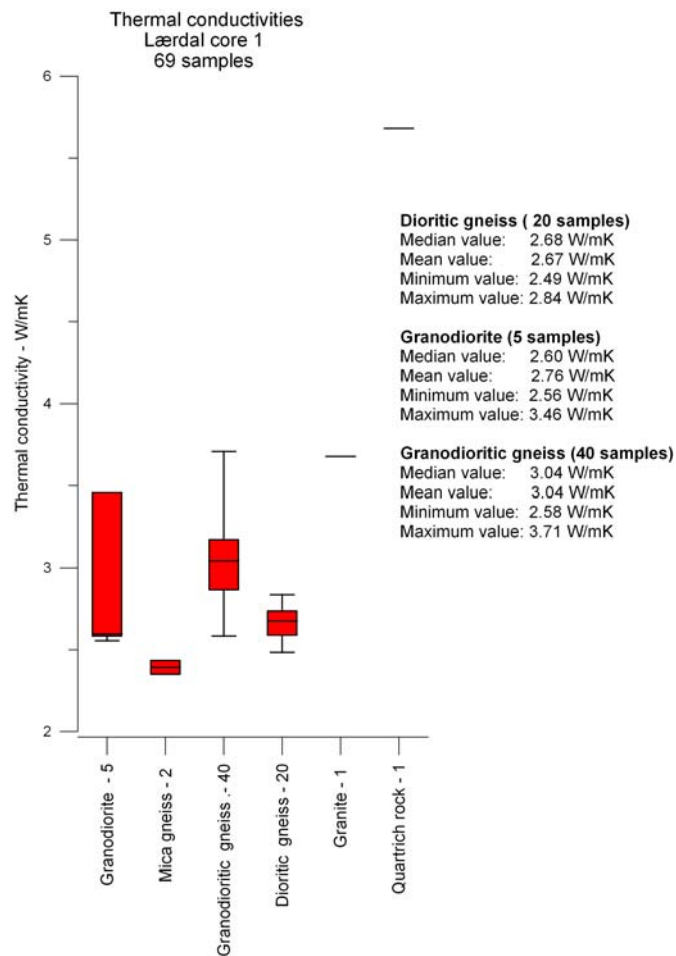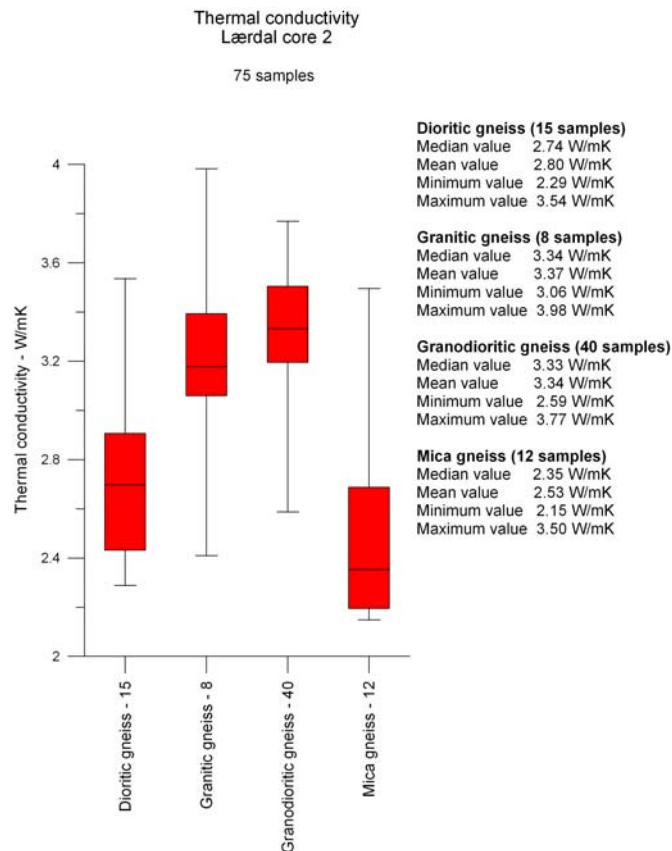

Figure 6.16. *Boxplots of thermal conductivities of the different rocks from the Lærdal 2 borehole. The red box contains the mid 50% of data while the median value is marked with a line inside the box. The brackets above and below the line denote 95 % confidence interval.*
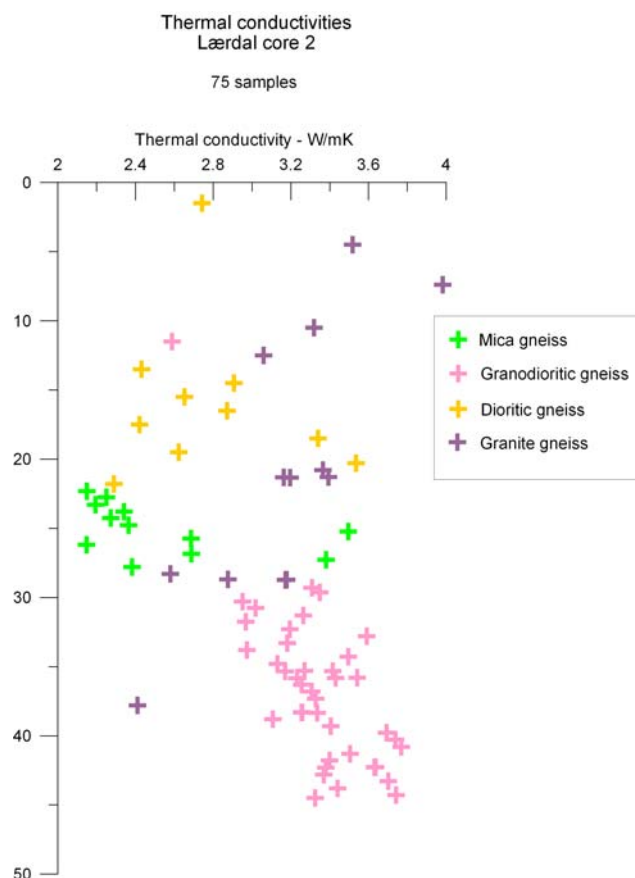
54

The same trend as for the samples from Lærdal 1 borehole is shown in Fig. 6.16 with variation in thermal conductivities with the rock type. Granite gneiss (median value 3.34 W/m·K)- and granodiorite gneiss (median value 3.33 W/m·K) have highest thermal conductivity and micagneiss (median value 2.35 W/m·K) has the lowest thermal conductivities.

The variation in measured thermal conductivity for the different rocks is mainly due to the anisotropy of thermal conductivity. The lowest values is measured perpendicular to the layering and the highest values is measured parallel to the layering. Some variation may also be related to the relatively inaccurate classification of the different rock types.

The temperature gradient log for Lærdal borehole 2 reported in Chapter 5 by Balling & Breiner is inversely correlated to the thermal conductivities. The temperature gradient is highest at a depth of 25-30 m where the bedrock consists of mica gneiss with a low thermal conductivity.

Lærdal 1 and 2 cores

The distribution of the thermal conductivities of all samples from the two boreholes in the Lærdal tunnel is shown in Fig. 6.17. The median value is 3.04 W/mK.
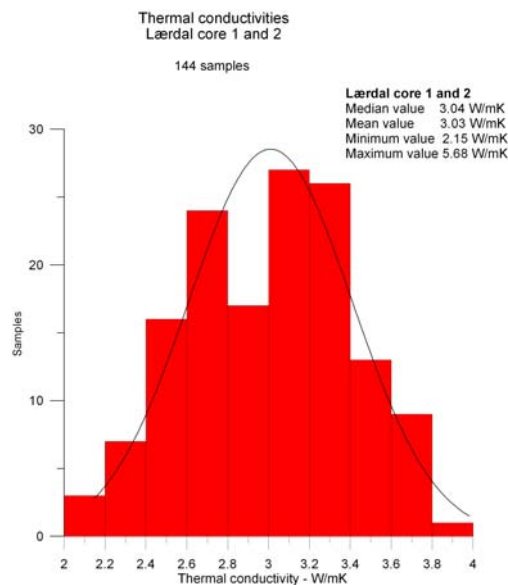
Figure 6.17. Histogram of thermal conductivities measured on samples from Lærdal boreholes 1 and 2. The black line shows the normal distribution line.

Arnestad

A 685 m deep borehole was drilled at Arnestad school, Asker, in 2004. More information of the boreholes is given in Table 5.1. The lithology estimated from optical televiewer and drilling log is shown in Fig. 6.18. The lithology of a 500 m deep borehole located 40 m away from the present Arnestad borehole, is described by Midttømme *et al.* (2004).
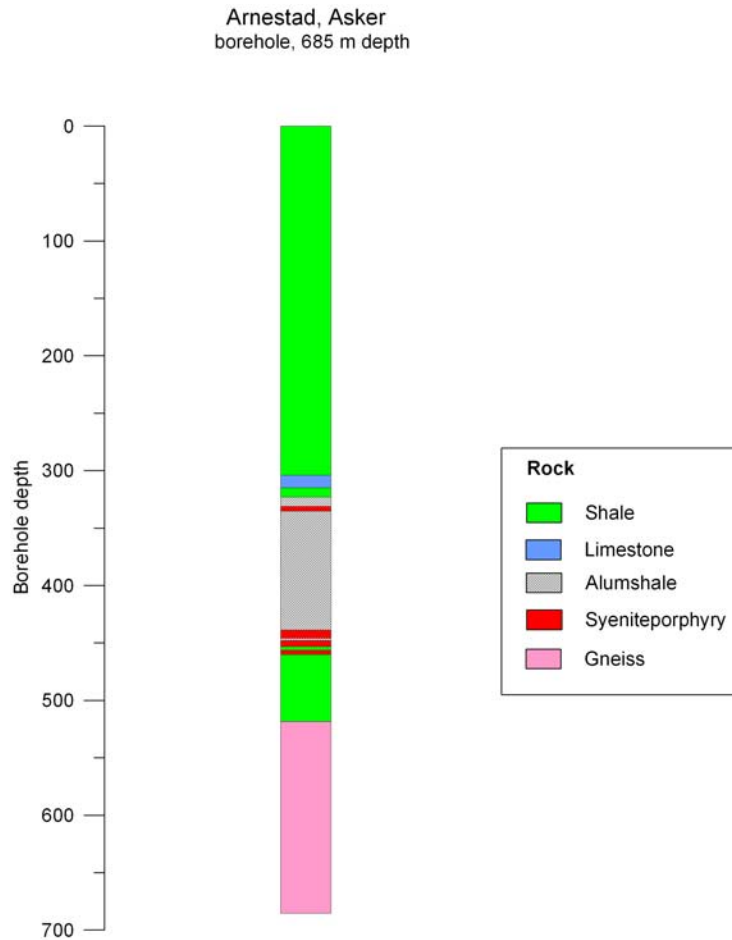
Figure 6.18. Lithology of the 684m deep borehole at Arnestad school, Asker.

Thermal conductivities have been measured on samples from Asker and Bærum and reported by Midttømme *et al.* (2000, 2004). Boxplots of thermal conductivities measured on gneiss, syenite porphyry, claystone and limestone is shown in Fig. 6.19. Based on these measurements, the thermal conductivities of the borehole are estimated (Fig. 6.20). NGU has not measured the thermal conductivity on the alum shale samples.
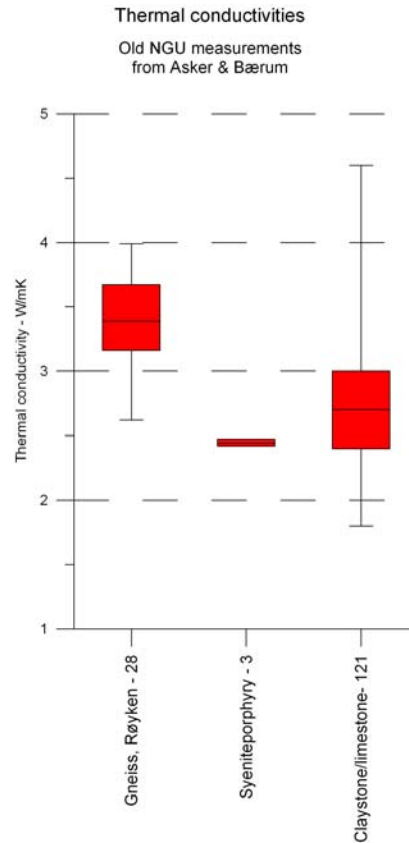
Figure 6.19. *Boxplots of old thermal conductivity measurements of gneiss from the Røyken area, syenite porphyry and claystone /limestone from Asker - Bærum area. The red box contains the mid 50% of data while the median value is marked with a line inside the box. The brackets above and below the line denote 95 % confidence interval. The digits listed after the rocktype represent the number of thermal conductivity samples.*
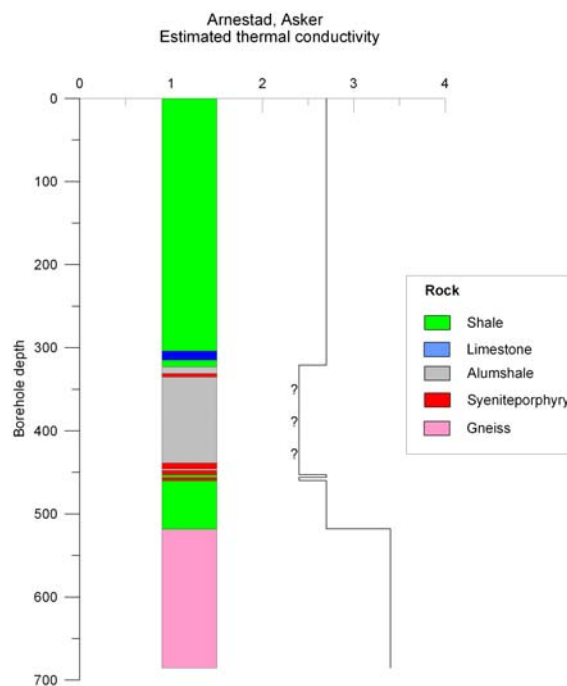
Figure 6.20. Estimated thermal conductivities for the 684 m deep borehole at Arnestad school, Asker.

6.3.5 Berger

The 650 m deep borehole at Berger is drilled in diorite. There are no thermal conductivity samples from the Berger area. Four diorite samples from Lørenskog have previously been measured at NGU. The results are shown in Fig. 6.21. The median value of 18 thermal conductivity measurements is 2.82 W/mK.

Thermal conductivity of diorite, old measurements from Lørenskog
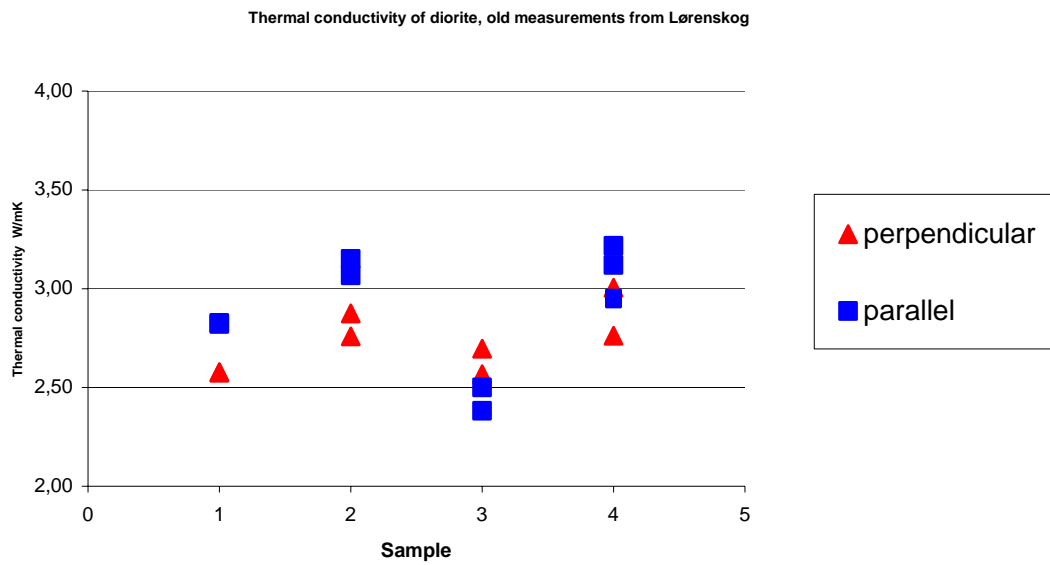
Figure 6.21. Thermal conductivities measured on diorite samples from Lørenskog.

7   PALAEOCLIMATIC CORRECTIONS TO ONSHORE HEAT FLOW DATA

Trond Slagstad and Lars Olsen, NGU

7.1   Palaeoclimatic corrections to heat flow – general considerations

The effects of palaeoclimatic changes on subsurface temperature, and the need to correct for such effects to obtain reliable equilibrium heat flow densities, were recognised a long time ago (Anderson 1934, Benfield 1939). Each temperature disturbance at the surface propagates into the subsurface at a rate determined by the diffusivity of the rock, and the depth of penetration of a measurable disturbance depends on both the amplitude and duration of the disturbance at the surface. Roughly speaking, the effects of Pleistocene ice ages, which lasted several hundred thousand years, extend to depths of several kilometres; climate changes during the Holocene extend to depths of several hundred metres to a few kilometres; and seasonal changes extend to depths of a few tens of metres. The amplitude of the disturbance varies inversely with the elapsed time since the disturbance, which means that the amplitude of a Holocene disturbance will be greater than the amplitude of a similar Pleistocene disturbance. To facilitate discussions of how such corrections can be carried out, we have compiled a detailed palaeoclimatic history for the last 20,000 years, applicable to South Norway. The calculations follow the procedure outlined by Jessop (1990) and assume stepwise temperature changes and a uniform diffusivity. This work is tentative, and further work including more ancient palaeoclimatic changes, starting with the initiation of the last interglacial (Eemian) at *c.* 130 ka, that are applicable to the entire Norwegian mainland will be conducted later in 2006. Furthermore, we only consider heat flow measurements from boreholes, and neglect lake measurements.

The main conclusion of the following section is that it is difficult, if not impossible, to correct many of the existing heat flow data from typically shallow boreholes on the Norwegian mainland with respect to palaeoclimatic history. The reason for this is related both to uncertainties in palaeoclimatic history and lack of details from the heat flow measurements. This is discussed in detail below, and underscores the importance of acquiring new, well-documented heat flow data from deeper boreholes, as is being done in the Kontiki Project.

7.2   Tentative palaeoclimatic history, South Norway, 20 ka to present

Two different records (curves A and B) of the palaeoclimatic history for the last 20 ky have been compiled, summarised in Table 7.1.

A. This annual mean temperature record is based on various palaeoclimatic data (e.g., pollen, insects, frostwedges) compiled in a palaeotemperature curve for NW Europe (including the southern part of Norway) for the last 15.3 ky (Andersen 2000, p. 151). The curve is presented as a range of temperatures between a minimum and a maximum estimate for each year, and we have used these extremes to produce two sets of data. Both sets are based on a subdivision in time intervals given by characteristics in the vegetational history. One data set is based on minimum temperature estimates (*A cold*) and the other on maximum temperature estimates (*A*

warm). For the interval 15.3–22 ka (*LGM, Last Glacial Maximum*) we have used –17 K and – 12.5 K lower than present, as reasonable minimum and maximum temperature estimates, i.e., curves *A cold* and *A warm*, respectively.

B. The second annual mean temperature record used is also based on various palaeoclimatic data (Hartmann 1994), and represents mid-latitude (including southernmost Norway) air temperature for the last 23 ky (Iversen 2000). The record is subdivided in time intervals based on the variations in the temperature curve itself, giving typical 'colder' and 'warmer' temperatures than the general trend. Also in this approach we have produced two data sets. The data sets are equal for the last 13.5 ky, but different for the 13.5–22 ka interval. One set, *'the minimum LGM temperature'* version, includes a temperature estimate for this age interval of –15 K lower than present (*B cold*), whereas the other set, *'the maximum LGM temperature'* version, uses –5 K lower than present (*B warm*) for the same interval.

Table 7.1.   **Temperature-time intervals used for the palaeoclimatic corrections of heat flow data from boreholes in South Norway. Explanation and references in text.**

A cold				A warm			
t_start (yr ago)	t_end (yr ago)	duration (yr)	Temp. relative present (K)	t_start (yr ago)	t_end (yr ago)	duration (yr)	Temp. relative present (K)
2500	100	2400	0.5	2500	100	2400	2.5
6800	2500	4300	1	6800	2500	4300	3
8200	6800	1400	0.5	8200	6800	1400	3
9000	8200	800	-1	9000	8200	800	1.6
10000	9000	1000	-3.5	10000	9000	1000	0
10700	10000	700	-6	10700	10000	700	0
11500	10700	800	-9	11500	10700	800	-3.5
12000	11500	500	-12.5	12000	11500	500	-8.5
12600	12000	600	-11	12600	12000	600	-8
13300	12600	700	-6.75	13300	12600	700	-4.75
13900	13300	600	-6.25	13900	13300	600	-3
14200	13900	300	-8	14200	13900	300	-2.75
14400	14200	200	-8.5	14400	14200	200	-1.5
15300	14400	900	-12	15300	14400	900	-6.5
22000	15300	6700	-17	22000	15300	6700	-12.5

B cold				B warm			
t_start (yr ago)	t_end (yr ago)	Duration (yr)	Temp. relative present (K)	t_start (yr ago)	t_end (yr ago)	duration (yr)	Temp. relative present (K)
150	100	50	-0.5	150	100	50	-0.5
250	150	100	-1	250	150	100	-1
400	250	150	-1.5	400	250	150	-1.5
500	400	100	-0.75	500	400	100	-0.75
600	500	100	-1.25	600	500	100	-1.25
1200	600	600	-0.6	1200	600	600	-0.6
1400	1200	200	-1	1400	1200	200	-1
3500	1400	2100	1	3500	1400	2100	1
3800	3500	300	-1.5	3800	3500	300	-1.5
6000	3800	2200	1.5	6000	3800	2200	1.5
6200	6000	200	-0.75	6200	6000	200	-0.75
8000	6200	1800	1.5	8000	6200	1800	1.5
11500	8000	3500	0	11500	8000	3500	0
13500	11500	2000	-2.5	13500	11500	2000	-2.5
22000	13500	8500	-15	22000	13500	8500	-5

t_start and t_end denote the start and end, respectively, of the various time intervals in the palaeoclimatic model. Temperatures are given relative to the present day temperature.
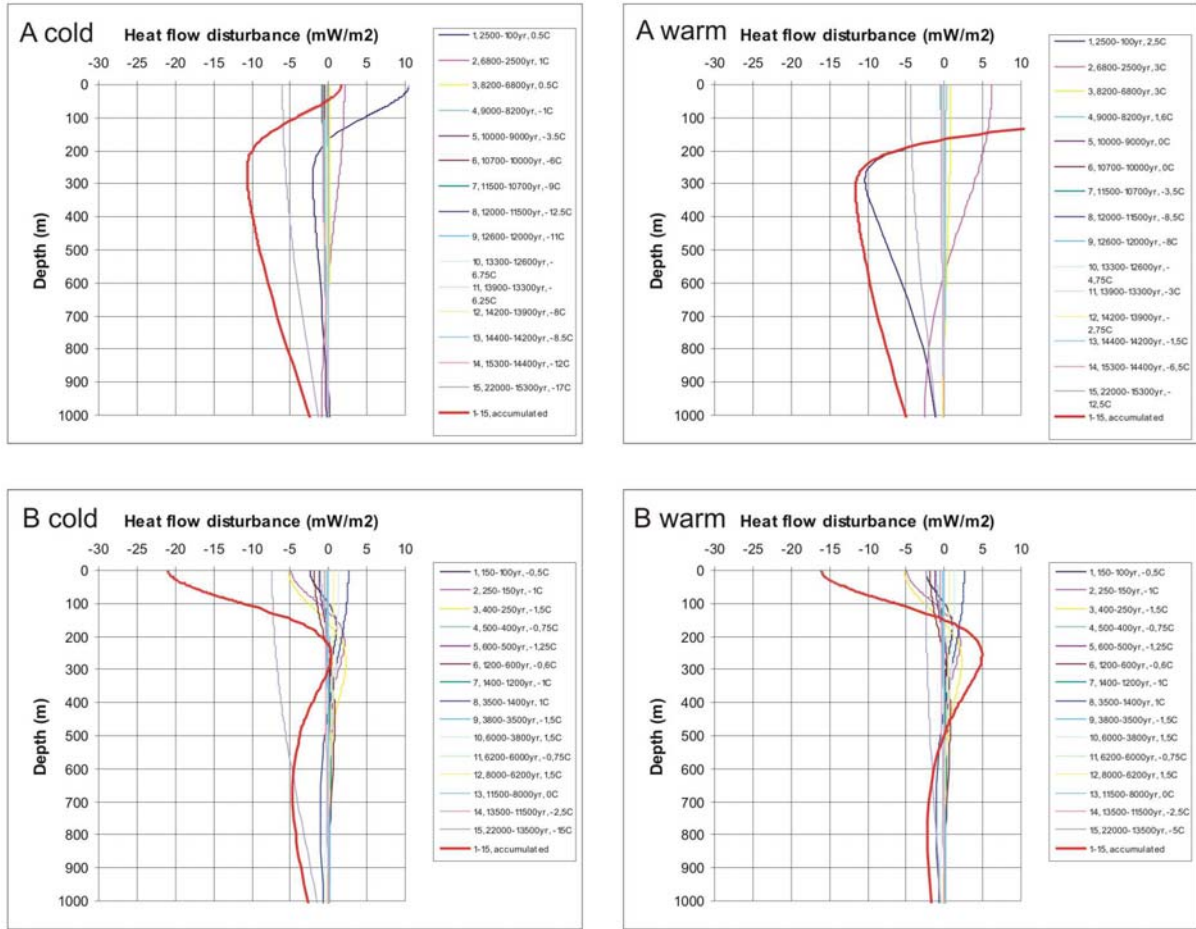
Figure 7.1. *Influence of the palaeoclimatic histories outlined in Table 7.1 on measured heat flow to 1000 m depth. The calculation assumes a diffusivity of 1.31*10⁻⁶ m²/s, which corresponds to a thermal conductivity of 3.0 W/m*K, a specific heat of 850 J/kg*K and a density of 2700 kg/m³.*

Based on these interpretations of climate change over the last 20 ky, we have calculated the influence on temperature, thermal gradient and heat flow at different depths. The effects of individual time intervals as well as the accumulated effect of the whole period are calculated. The latter is used to correct old and new heat flow measurements, whereas the former can be used to identify the time intervals that contribute most to the accumulated effect and therefore may require special attention in future reassessments of the palaeoclimatic history. Fig. 7.1 shows the influence of the four curves on the heat flow measurements down to 1000 m depth.

7.3 Palaeoclimatic corrections to existing heat flow data from South Norway

It is clear from Fig. 7.1 that for heat flow measurements at relatively shallow depths (i.e., <200–300 m), the invoked palaeoclimatic histories yield large and highly variable effects. For example, the required correction for a measurement at 200 m depth is +10 (*A cold*), +6 (*A warm*), +1 (*B cold*), and –4 (*B warm*) mW/m². By comparison, the required correction at 800 m depth is +5 (*A cold*), +8 (*A warm*), +4 (*B cold*), and +2 (*B warm*) mW/m², i.e., a much

narrower range than at 200 m depth. Corrections at still greater depth are even less sensitive to uncertainties in the palaeoclimatic history. Complicating things even more are the large gradients in required correction at shallow depths. For example, *B cold* requires a correction of +11 mW/m^2 at 100 m depth and +1 mW/m^2 at 200 m depth. The most extreme curve is *A warm*, which requires corrections of –24 and +6 mW/m^2 at 100 and 200 m depth, respectively.

Taking one heat flow measurement in Hurdal, *c*. 40 km north of Oslo, to represent the northernmost measurement in "South Norway", the available heat flow data come from measurements at depths <300 m (typically 100–250 m) with depth-intervals typically in the range 100–200 m. As discussed above, there are large discrepancies between the corrections imposed by the different palaeoclimatic curves at these shallow depths. In addition, since we only have information about the average heat flow from each borehole, we are unable to assign different corrections at different depths. As seen above, the corrections may vary by 10–30 mW/m^2 over a 100 m depth-interval for the same palaeoclimatic history. This shows that correcting the existing (old) heat flow data, derived from shallow boreholes, with regard to palaeoclimatic effects is hampered by both uncertainties in palaeoclimatic history and lack of details from the heat flow measurements. For the sake of argument, such a correction is, nevertheless, attempted below.

Most workers agree that the shallow heat flow measurements in South Norway require a positive correction of at least 5–15 mW/m^2 due to the cooling during the Pleistocene ice ages (Cermák *et al.* 1993, Balling 1995). Table 7.1 presents corrected heat flow values from South Norway based on the four palaeoclimatic curves described above. The correction is calculated for the median depth of the measurement interval, i.e., at 150 m for a depth-interval of 100 to 200 m. Two of the palaeoclimatic curves (*A cold* and *B cold*) yield consistent positive heat flow corrections in the range 0 to 11 mW/m^2, whereas curve *B warm* yields mostly positive but some negative corrections in the range –4 to 9 mW/m^2. The *A warm* palaeoclimatic curve dominantly yields rather large, negative corrections (up to –32 mW/m^2) that appear unrealistic. The correction at each site is, therefore, calculated as the average of the corrections suggested by the three curves *A cold*, *B cold* and *B warm*. The calculated corrections range from 2 to 9 mW/m^2, and the corrected heat flow densities range from 50 to 61 mW/m^2, in addition, the site at Hurdal has a very low, unexplained value of 36 mW/m^2.

The palaeoclimatic corrections reported here must be regarded as tentative, and further work will be undertaken to define more rigid palaeoclimatic curves for South Norway and elsewhere. The main conclusion, however, is that even with very well constrained palaeoclimatic curves, large uncertainties will remain in the existing, shallow heat flow data from the Norwegian mainland. This underscores the importance of obtaining new data from deep wells where palaeoclimatic corrections are smaller and can be applied with more confidence. Combining the new heat flow data from the Kontiki Project with new knowledge of variation in radiogenic heat production and thermal modelling, described elsewhere in this report, will help identify prioritised areas for follow-up work.

Table 7.2. Corrected heat flow values from boreholes in South Norway.

No	Site Name	ID	Depth (m)		Gradient	STD	Cond	HF	Heat flow correction (mW/m^2)				Heat flow corrected (mW/m^2)				Cor	HFcor
			Min	Max	C/km		Wm^{-1}K^{-1}	uncor	A cold	*A warm*	B cold	B warm	A cold	*A warm*	B cold	B warm	(mW/m^2)	(mW/m^2)
NOR8	Hurum	1	100	250	13.9	0.1	3.4	**47**	9	-1	4	-2	57	46	51	46	4	**51**
NOR9	Lier	FUG	30	150	15.6	0.1	3.4	**52**	3	-32	14	9	55	20	66	61	9	**61**
NOR10	Hurdal	2	100	300	17.2	0.0	2.0	**35**	9	8	0	-4	43	43	35	31	2	**36**
NOR11	Knaben	7.1	80	260	15.3	0.1	3.1	**48**	9	0	3	-2	57	48	51	46	4	**52**
NOR12	Iveland	5	80	160	14.6	0.2	3.4	**49**	6	-19	10	5	55	30	59	54	7	**56**
NOR17	Lassedal							**50**										**56**
		14	69	182	11.5	1.4	2.9	34	6	-12	7	3	40	22	41	37	5	39
		12	80	169	13.3	0.4	3.5	46	6	-17	9	5	52	29	55	50	7	52
		10	79	177	13.5	0.9	3.1	42	7	-13	8	3	49	29	50	45	6	48
		8	77	192	13.8	0.4	3.7	51	7	-16	9	4	58	35	60	55	7	58
		6	72	171	15.5	0.7	3.8	59	6	-2	11	6	65	57	70	65	8	67
NOR18	Hobbøl		130	280	15.6	0.9	3.4	**53**	10	5	2	-4	63	58	55	50	3	**56**
NOR19	Glamsland		120	250	17.2	0.6	2.8	**47**	9	5	1	-3	57	52	48	44	2	**50**

Depth min/max denotes the depth interval from which the measurement was made. For reasons discussed in the text, the results from curve A warm are kept out of the calculations of average palaeoclimatic corrections. Abbreviations: Cond - thermal conductivity; HF uncor - palaeoclimatically uncorrected heat flow; Cor - average heat flow correction from *A cold, B cold* and *B warm*; HF cor - palaeoclimatically corrected heat flow.

8   NEW, PALAEOCLIMATICALLY UNCORRECTED HEAT FLOW DATA FROM LÆRDAL, HJERKINN AND LØKKEN

Trond Slagstad, NGU

The temperature logging and thermal conductivity data have been discussed elsewhere in this report (Chapters 4-6). Therefore, only the heat flow densities calculated from these data are discussed here. As a first approach to calculating heat flow at Lærdal, Hjerkinn and Løkken, the constant depth-interval thermal gradients determined by Balling, using a linear least-squares relation, were multiplied with thermal conductivities. The thermal conductivity at certain depths in the wells was calculated with a constant depth-interval moving average, the depth intervals corresponding to the depth intervals used by Balling (10 and 20 m for Lærdal; 20 and 100 m for Hjerkinn and Løkken). In addition, the "average" heat flow at each site was determined from the average thermal gradients and average thermal conductivity.

8.1   Lærdal

Fig. 8.1 shows the calculated heat flow as a function of depth for the Lærdal 1 and Lærdal 2 boreholes. In both holes, the heat flow increases with depth. In Lærdal 2, the 10 m depth-interval calculation shows a peak in heat flow at 25 m depth, corresponding to low-conductivity mica gneiss. Apart from this peak, calculations show that the heat flow in the two wells increase monotonically with depth, reaching a maximum value at the bottom of the wells of c. 40 mW/m^2. This increase in heat flow with depth is opposite to what one would observe in a purely conductive, steady-state thermal regime, suggesting that advective heat transport (groundwater), palaeoclimate or the presence of the tunnel plays a role. This is not discussed further here.

Maximum heat flow densities (10 m depth-interval calculation) of 42 and 45 mW/m^2 are observed near the bottom of Lærdal 1 and 2, respectively. The average thermal gradient between the Lærdal surface well and the two Lærdal tunnel wells is 14.4°C/km. Multiplying this gradient with the average thermal conductivity from the two Lærdal wells (3.03 Wm^{-1}K^{-1}) yields an average heat flow of 44 mW/m^2, corresponding rather well to the maximum heat flow densities observed in the wells. A heat flow value of 44 mW/m^2 is therefore suggested as a best, tentative, uncorrected estimate of the heat flow at the Lærdal site.
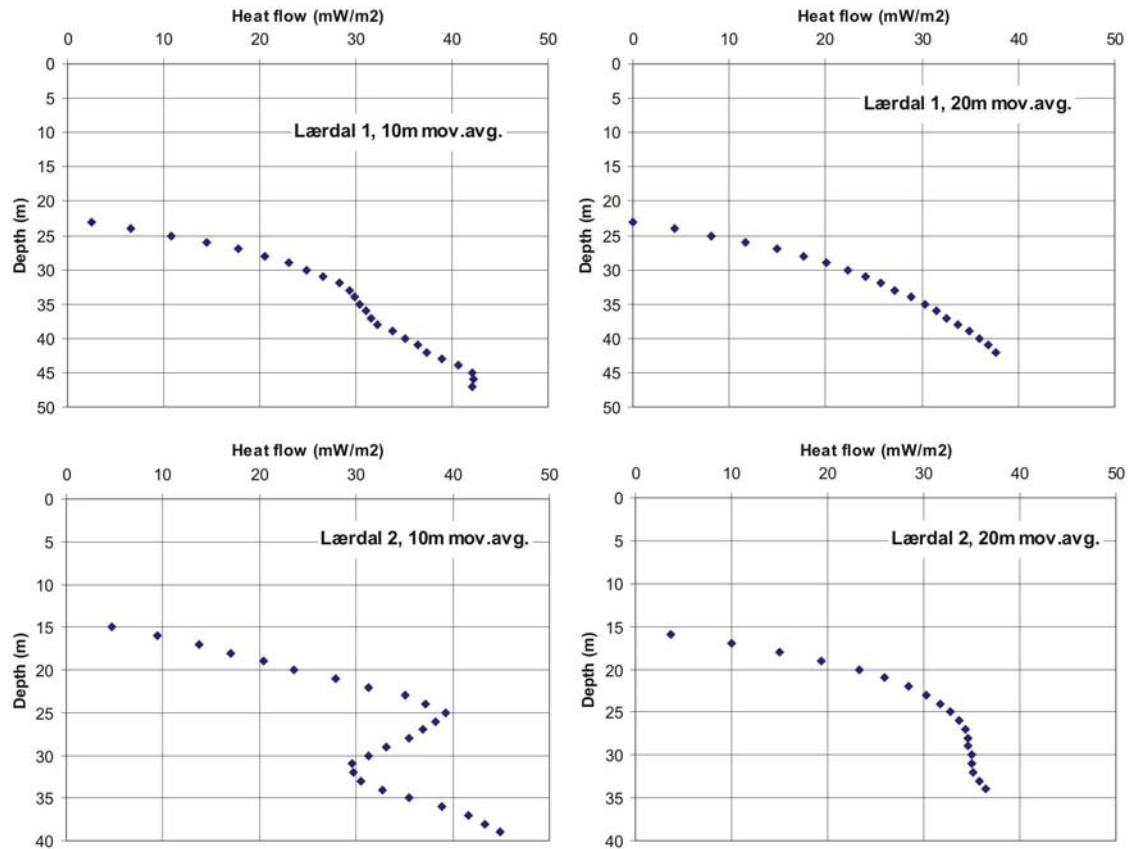
Figure 8.1. Calculated heat flow with depth from two wells in the Lærdal tunnel.

8.2 Hjerkinn (Gåvålivatnet)

Fig. 8.2 shows the calculated heat flow as a function of depth for the well at Hjerkinn (Gåvålivatnet). Despite a better defined thermal gradient than at Lærdal, the large scatter in thermal conductivities produces a large scatter in calculated heat flow. A peak in heat flow (51 mW/m^2) at *c*. 150 m depth corresponds to slightly elevated thermal gradients and conductivities. For the 200 to 648 m depth-interval the 20 m depth-interval calculation yields an average heat flow density of 40 ± 6 mW/m^2 ($\pm$ 1σ), whereas the 100 m depth-interval calculation yields 40 ± 3 mW/m^2. The average thermal gradient for the well at Hjerkinn is 16.5°C/km, which multiplied with the average thermal conductivity of 2.5 Wm^{-1}K^{-1}, yields an "average" heat flow of 41 mW/m^2. This is slightly lower than the average and median (46 and 44 mW/m^2, respectively) heat flow densities measured in six wells between 330 and 560 m depth, drilled from inside a mine at Tverrfjellet, not far from Hjerkinn (Swanberg *et al.* 1974). Here, a heat flow value of 41 mW/m^2 is taken as the best, tentative, palaeoclimatically uncorrected estimate of the heat flow at the Hjerkinn site.

65
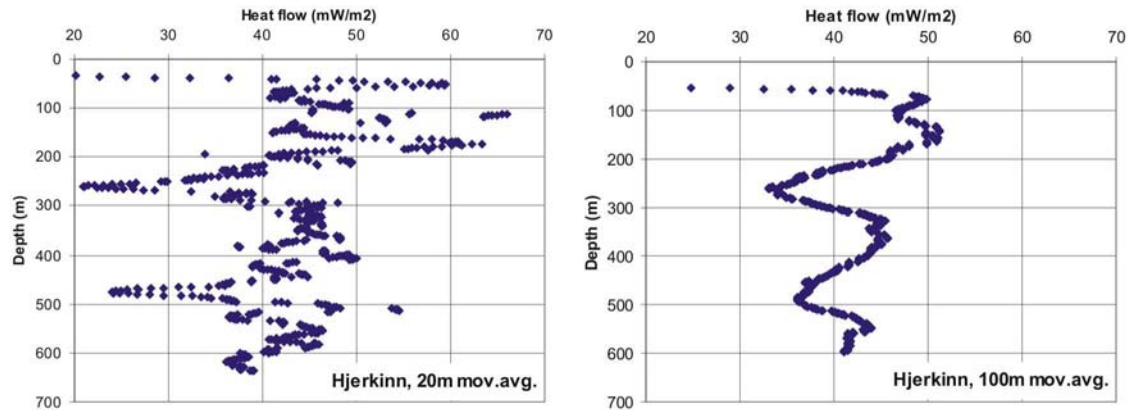
Figure 8.2.   Calculated heat flow variation with depth at Hjerkinn.

8.3   Løkken

Fig. 8.3 shows the calculated heat flow as a function of depth for the well at Løkken. In contrast to the wells in Lærdal and Hjerkinn, the well at Løkken yields a nearly constant heat flow of *c.* 50 mW/m^2 from 500 to the bottom of the well at 980m. In this depth-range, the 20 m depth-interval calculation yields an average heat flow density of 50 ± 3 mW/m^2 ($\pm 1\sigma$), whereas the 100 m depth-interval calculation yields 49 ± 1 mW/m^2. The average gradient is 15.9°C/km, which multiplied by the average conductivity of 3.08 Wm^{-1}K^{-1}, yields an "average" heat flow of 49 mW/m^2, taken here as the best, tentative, palaeoclimatically uncorrected estimate of the heat flow at the Løkken site. This is slightly lower than the average and median (54 and 53 mW/m^2, respectively) heat flow densities measured in four wells between 830 and 1060 m depth, drilled from inside a mine at Løkken (Swanberg *et al.* 1974).
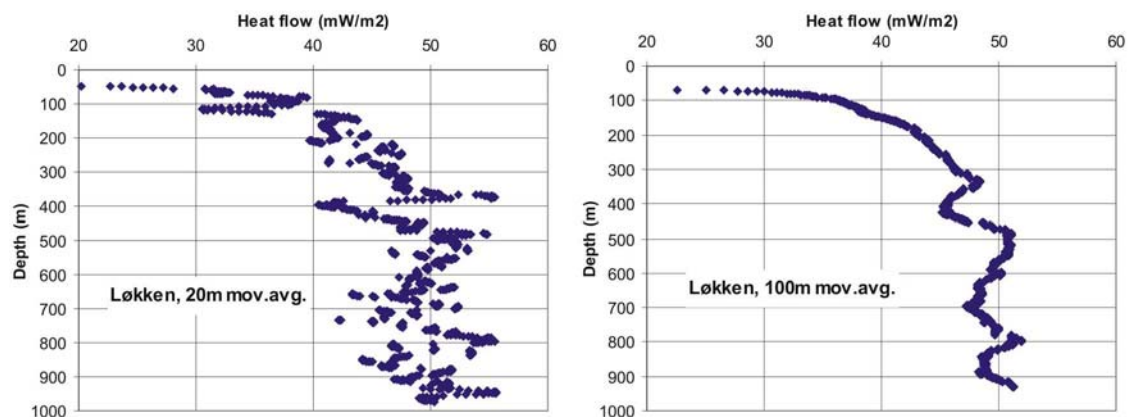

Figure 8.3.   Calculated heat flow variation with depth at Løkken.

9   3D MODELLING: THE MID-NORWEGIAN MARGIN, THE SCANDINAVIAN MOUNTAINS AND THE OSLO RIFT

Jörg Ebbing, Christophe Pascal, Odleiv Olesen and Jan Reidar Skilbrei, NGU

9.1   From structural modelling to temperature modelling

One of the goals in the Kontiki Project was to perform thermal modelling in addition to potential field modelling in order to validate basement and crustal configurations and in order to estimate the influence on basement structures on the observed heat flow. In the following we will describe the density, magnetic and thermal models from 3 areas: (1) the Scandinavian mountains, and especially the Central Scandinavia Profile (2) the Mid-Norwegian margin and (3) the Oslo Rift.

Section 9.2.1 will present a general description of the isostatic state of the Scandinavian mountains and considerations about the crustal structure of the Fennoscandian Shield. In Sections 9.2.2 and 9.2.3 two alternatives 2 ½D model across the central Scandinavian mountains are presented after Skilbrei *et al.* (2002) and modifications. The thermal model and a synthesis of the thermal and density modelling are presented in Section 9.2.4.

The 2D thermal model of the central Scandinavian mountains can be continued in the Mid-Norwegian margin. For the Mid-Norwegian (Møre-Vøring-Lofoten) Margin we present in Section 9.3.1 updates on the previously presented 3D model in the Kontiki Report 2004 (Olesen *et al.* 2005) and Ebbing *et al.* (2006). Additionally, comparison between crustal structures and corrected heat flow values will be given. Along one of the best-studied line we will present a 2D thermal model (Section 9.3.2).

The Oslo Rift is well studied and the wealth of geophysical and geological data makes the area the perfect case example for thermal modelling. The 3D crustal model of the area is described in detail by Ebbing *et al.* (submitted to JGR) and is summarized here (Section 4.1). Thermal modelling is made along one of the central profiles and presented in Section 9.4.2.

Originally, it was also planned to provide a structural model for the northern Viking Graben. However, in the course of the project it was agreed not to carry out the modelling and to concentrate on the three areas introduced above.

9.1.1 Modelling methods

The 3D density and magnetic modelling of the Oslo Graben and Mid-Norwegian margin was done using the interactive forward modelling software IGMAS (Götze & Lahmeyer

1988). The 3D model is based on parallel vertical planes with a polygonal structure. Between the planes a 3D model structure is described by triangulation. For the inverse and forward modeling of the Scandinavian mountains the software package GMSYS-2D and GMSYS-3D haven been used. In GMSYS-3D a 3D structure is described by calculating and adding the gravity effect of layers using the Parker algorithm (Parker 1972).

We used the commercial Finite-Element package Ansys for the thermal modeling of the three areas. The models involve 2D steady-state (i.e. purely conductive) thermal computations. Boundary conditions are setup as constant temperatures at the surface (i.e. 0°C) and constant heat flow at the base of the models. Model geometries are imported from potential field models and heat productions are affected to the different basement units in agreement with values deduced from geochemical analyses. We used 6-noded triangular elements, numerical models contain ~10 000 to ~20 000 elements allowing for accurate and fast computations.

9.2   The Scandinavian mountains and the Central Scandinavia Profile

In this chapter we present the density, magnetic and thermal model along the Central Scandinavia Profile. However, we will first present a general description of the Scandinavian mountains (Section 9.2.1), before the density and magnetic model along the Central Scandinavia Profile is summarized after Skilbrei *et al.* (2002*)* in Section 9.2.2. In Section 9.2.3 we present an alternative model based on the results and in Section 9.2.4 thermal modelling is performed to evaluate the alternative models.

9.2.1 Isostatic state of the Scandinavian mountains

The Scandinavian mountain range is located at the western edge of the Fennoscandian Shield and includes two dome-like areas of high mountains and plateaus, the northern and southern Scandinavian mountains (Fig. 9.1). The Scandinavian mountains extend over more than 1400 km and are not one continuous mountain range, but can be divided into distinct segments according to their topographic shape and gravity signal. Tectonically the Scandinavian landmass has an intracratonic position in close relation to the passive continental margin along the northeast Atlantic. As part of the Fennoscandian Shield the Scandinavian mountains were largely affected by its tectonic evolution. Presently, Fennoscandia is affected by high uplift rates. The rates of present uplift in Fennoscandia range from close to zero along the Norwegian coast to more than 8 mm/yr in central parts of the Gulf of Bothnia. The main cause of the present uplift is related to post-glacial rebound (e.g. Niskanen 1939, Lambeck *et al.* 1998, Milne *et al.* 2001, 2004). But in the
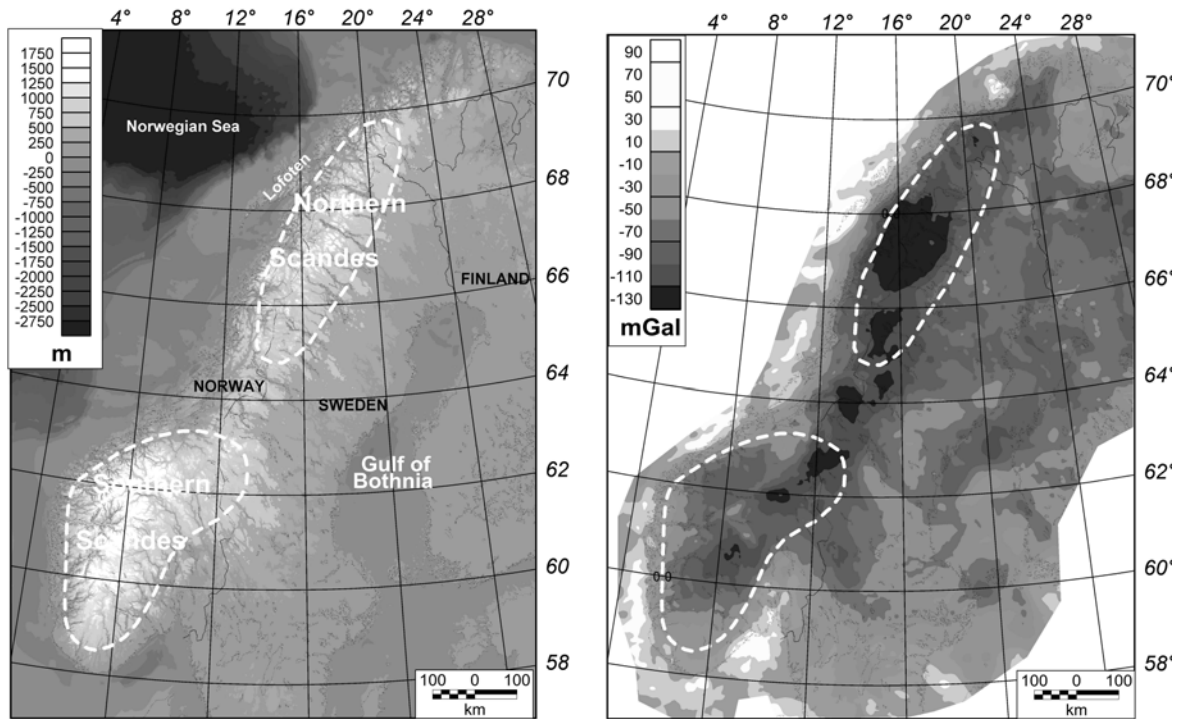
Figure 9.1. *(left) Topography/bathymetry of Fennoscandia (after Dehls et al., 2000). Dotted lines depict the northern and southern Scandinavian mountains and correspond roughly to 500 m above sea level. (right) Bouguer anomaly. See text for details.*

Northern and Southern Scandes two (Cenozoic?) uplift centres have been resolved, mainly by thermochronologic data (e.g. Redfield *et al.* 2005 and references therein). The gravity field provides a means to study the structural differences within the Scandinavian mountains and the mechanism of exhumation of the mountain range. The load imposed by the Scandinavian mountains must be isostatically supported at depth by substantial volumes of low-density material within the crust or the mantle. Thus, the crust-mantle and lithosphere-asthenosphere interfaces are important boundaries with regard to isostatic processes. This study presents an isostatically balanced density model for the Fennoscandian Shield with emphasis on the Scandinavian mountains. First, the data sets are introduced before a description of the 3D density model and the isostatic state of the Scandinavian mountains is given.

Gravity

Fig. 9.1 shows the complete Bouguer anomaly of the Scandinavian mountains and adjacent regions from the compilations by Skilbrei *et al.* (2000) and Korhonen (2002a). The Bouguer anomaly shows a gravity low correlating with the topography of the Scandinavian mountains. In the southern Scandinavian mountains local features can be identified in the Bouguer anomaly and in the northern Scandinavian mountains the maximum axis of the gravity low is slightly shifted with respect to the topography (compare Fig. 9.1 right and left). The correlation between topography and Bouguer gravity anomaly points to the presence of a crustal root. However, in the reminder we will show that such a root cannot be

69

imaged by seismic studies. For the isostatic gravity modelling a lowpass-filtered gravity anomaly is used with a cut-off wavelength of 100 km. The filter removes short-wavelength features that are not a subject of the present study. We will concentrate on the general lithospheric structure.

The seismic image of the Scandinavian mountains

To investigate the crustal structure of the Scandinavian mountain range a variety of reflection and refraction seismic profiles have been carried out in the past (e.g. Kanestrøm & Haugland 1971, Hirschleber *et al.* 1975, Cassell *et al.* 1983, Schmidt 2000). Interpretations combining seismic and gravity data, have enabled compilations of the Moho geometry Kinck *et al.* 1993, Korsman *et al.* 1999, Olesen *et al.* 2002, Mjelde *et al.* 2005). These compilations indicate that the Scandinavian mountains, despite their topographic expression, have no pronounced crustal root (Fig. 9.2). However, the topography has to be isostatically compensated. Candidates might be low-density bodies within the crust or the mantle, or the flexural forces within the elastic lithosphere. We can calculate the gravity effect related to the density contrast at the seismic Moho to study the residual sources in the gravity field and the isostatic loading. The gravity effect of the Moho is calculated using a density contrast at the seismic Moho of 350 kg/m^3. This value is in agreement with densities converted from seismic velocities from regional studies (Kanestrøm & Haugland 1971, Schmidt 2000), which indicate a density contrast between 300 and 400 kg/m^3. Indications of a high-velocity lower crust below the central Fennoscandian Shield can also be found in seismic observations (P-velocities > 7km/s; Korsman *et al.* 1999, Perez-Gussinye *et al.* 2004), providing support for a minor density contrast (200 kg/m^3) between crust and mantle. The insufficient distribution of seismic lines prevents us from clearly defining this structure. Especially, its westwards extension below the Scandinavian mountains is obscure. Mapping the high-density lower crust is, however, an important element when computing the lithospheric loading.

Base of the lithosphere

In addition to the Moho image, a model of the lithosphere-asthenosphere boundary below the Fennoscandian Shield is also available (Calcagnile 1982). The model shows a deepening of the lithospheric base from 110 km below the southern Scandinavian mountains to 170 km below the Bothnian Sea without revealing local patterns below the Northern and southern Scandinavian mountains (Fig. 9.2). The geometry of the lithospheric thickness has to be taken into account to calculate the effect on the gravity (and geoid) from the density distribution at the lithosphere-asthenosphere boundary. The geometry of the lithosphere-asthenosphere boundary has, due to its long-wavelength, a substantial influence on geoid undulations but is less visible in the gravity signal. The gravity effect was calculated with an asthenospheric density contrast of -30 kg/m^3 compared to the lithospheric mantle density. This contrast was previously applied to isostatically balance a lithospheric profile running from the Norwegian shelf to the central Fennoscandian Shield (Bielik *et al.* 1996), and is in agreement with global reference models (e.g. PREM: Dziewonski & Anderson 1981).

Forward modelling

The 3D forward modelling was carried out with the software package GMSYS-3D. The density modelling is relative to a reference lithosphere: upper crust 0-12 km depth: 2670 kg/m^3, middle crust 12-20 km depth: 2800 kg/m^3, lower crust 20-30 km depth: 2900 kg/m^3, lithospheric mantle 30-120 km depth: 3250 kg/m^3; asthenospheric mantle: 120-220 km depth: 3220 kg/m^3. The density of the asthenospheric mantle can only be
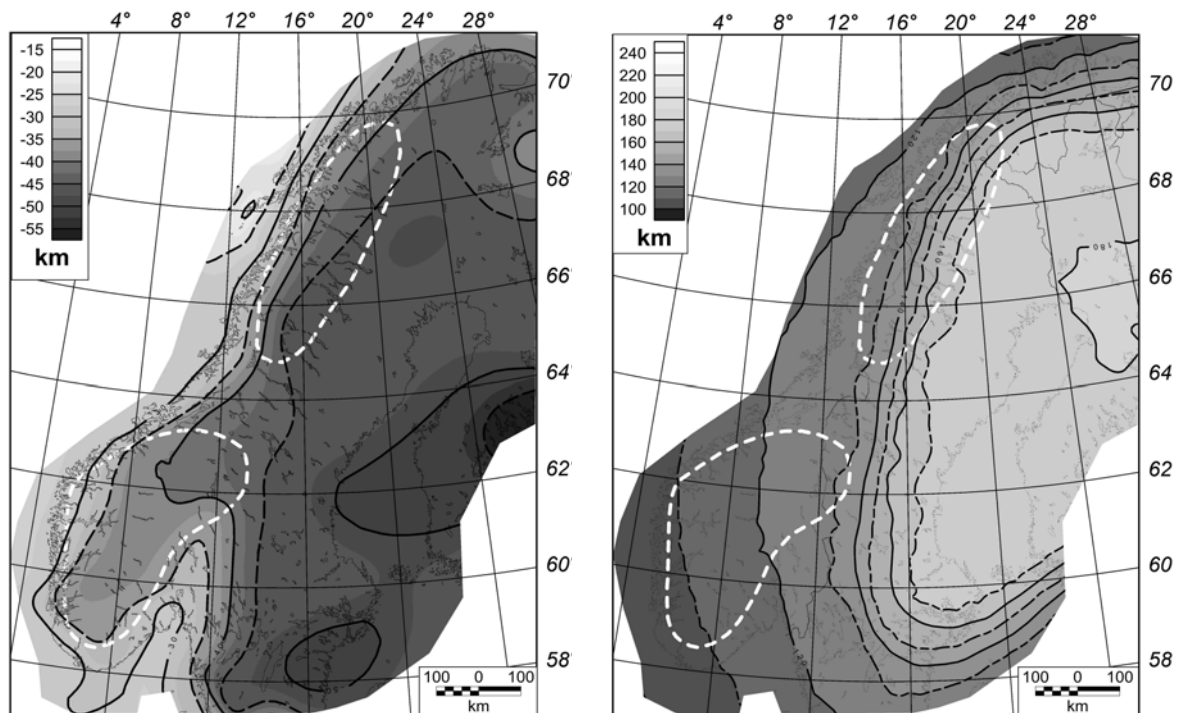
Figure 9.2. (left) Depth to Moho and (right) lithospheric thickness as compiled by seismic/-tomographic studies. The depth to Moho was compiled by a combined analysis of refraction seismic data and gravity studies (see text). The lithosphere-asthenosphere boundary was derived from an analysis of Rayleigh-wave dispersion data (Calcagnile

regarded as a relative density and is chosen to reflect the small density contrast at the base lithosphere as described above. Using a reference model allows us to model the level of the gravity field and not only the shape of the anomaly.

The 3D lithospheric model features a three-layered crust as described above, a crustal base according to the Moho model and the lithospheric base as shown in Fig. 9.2. The simple model provides already a good correlation between the modelled and observed gravity at the Norwegian coastline, but increasingly large negative differences towards the central Fennoscandian Shield. Consequently, high-density material in the lithosphere has to be added and the first candidate is the high-density lower crust as observed in seismic studies. We have to map its distribution by isostatic considerations, because the seismic coverage and resolution is insufficient.

Isostatically balanced gravity model

We calculate the isostatically balanced loading of the lithospheric model described above with:

$$\rho_{Topo}D_{Topo} + \sum_{i=1}^{3}\rho_{ci}D_{ci} + \rho_{mantle}D_{mantle} + \rho_{asth}D_{asth} - \sum_{i=1}^{5}\rho_{refi}D_{refi} = \Delta Load / g$$

with densities ρ and height/thickness D for topography, crust, lithospheric and asthenospheric mantle and reference model as described above. g is the normal gravity field and $\Delta Load$ is giving indication of mass surplus and deficiency. The calculation shows that high-density material is missing especially below the central Fennoscandian Shield. As we know from the seismic studies that such a layer is observed, we convert $\Delta Load$ in a high-density Lower Crustal Body (LCB) with density 3100 kg/m^3 and the isostatic balanced equation becomes:

$$\rho_{Topo}D_{Topo} + \sum_{i=1}^{3}\rho_{ci}(D_{ci}) + \rho_{LCB}D_{LCB} + \rho_{mantle}D_{mantle} + \rho_{asth}D_{asth} = \sum_{i=1}^{5}\rho_{refi}D_{refi}$$

Hereby, we consider mass surplus as not related to the LCB and balance only for the missing masses, as there are no indication for low-density lower crust below the Fennoscandian Shield. This approach results in a LCB (Fig. 9.3) with a thickness up to 25 km in the central Fennoscandian Shield, which is in agreement with estimates from seismic studies (Korsman *et al.* 1999). The next step is to include the LCB into the density model and to calculate the gravity effect. The resulting gravity effect of the isostatic model features a north-south trending band of negative residual from the northern Scandinavian mountains to east of the Oslo Rift. This more than 100 km wide anomaly is coinciding with the Transcandinavian-Igneous-Belt (TIB) with low densities (~2640 kg/m^3) and high heat production, which is also reflected in the heat flow of Fennoscandia (e.g. Olesen *et al.* 2005). Forward modelling in the northern and central Scandinavian mountains indicated that these granites can have a depth-extension up to 20 km (Olesen *et al.* 2002, Skilbrei *et al.* 2002). We introduce a low-density band in the upper crust (2640 kg/m^3) according to the TIB and calculate the gravity effect of the lithospheric model. The residual between the observed and the calculated gravity field is now within 25+/-25 mGal, except in two regions: The southern and northern Scandinavian mountains, where the residual shows two gravity minima (Fig. 9.3).

Discussion and conclusions

The results of the present study show that a crustal root corresponding to the topographic load of the Scandinavian mountains exists. But the crustal root is coinciding with the distribution of high-density lower crust in the central Fennoscandian Shield, which is compensating the deep Moho.

Below the Scandinavian mountains the high-density lower crust thins out (Fig. 9.3). A second structure overprinting the root of the Scandinavian mountains is the TIB. Isostatic

analysis show that the observed root of the Scandinavian mountains cannot explains the gravity low (Ebbing & Olesen 2005). Introduction of low-density granites into the upper crust does, however, explain the gravity low and these granites can be observed at the surface and correlated with magnetic anomalies (Skilbrei *et al.* 2002). The two regions that are not explained by the present model are the areas of Neogene tectonic uplift and the negative gravity residual point to low-density material in the crust or mantle. There is no or only minor evidence from seismic experiments for low-density structures in the middle and lower crust (e.g. Kinck *et al.*1993). Therefore, the presence of light material in the mantle seems more likely. To refine our results subsurface loading, both in the crust and upper mantle, has to be introduced. The information about the depth to the Moho is however ambiguous, due to the quality and resolution of the seismic experiments. (Kinck *et al.* 1993, Korsman *et al.* 1999, Ottemöller & Midzi 2003). A careful review of seismic and seismological investigations shows that new, detailed studies of the deep crust and upper mantle are needed to provide such information (Ebbing & Olesen 2005). If the low-density structure in the upper mantle exists, it is the most likely cause for Cenozoic uplift of the northern and southern Scandinavian mountains. This would imply that models of dynamic topography or related processes in the upper mantle are more valid than recent models suggested by combining AFT analysis and comparison with flexural modelling (Redfield *et al.* 2005).

The general shift between the levels of the presented lithospheric model and the reference model can be explained by a low-velocity/low-density zone in the asthenosphere related to the glacial rebound of Fennoscandia (e.g. Lambeck *et al.* 1998). The results for the base of the lithosphere from Calcagnile (1982) are consistent with a more recent study of the thermal lithospheric thickness by Artemieva & Mooney (2001), but for asthenospheric structures no detailed model is yet available. From theoretical calculations there is also some evidence for an increase in mantle densities from the Norwegian coast towards the central Fennoscandian Shield. However, incorporation of such a density distribution goes beyond the scope of the present study.

9.2.2 Gravity model across the central Scandinavian mountains - Model A

A detailed 2 1/2 D gravity and density model along the central part of the Scandinavian mountains has been presented by Skilbrei *et al.* (2002). We will repeat here the main description of the profile. The modelled profile is located in the central part of the Scandinavian mountain chain and is crossing the Bouguer anomaly low (Fig. 9.4), which is approximately aligned along the axis of the highest elevation of the Scandinavian mountains. Towards the west, the Bouguer gravity is dominated by a pronounced positive coastal gradient, with increasing values towards the shelf. On the residual gravity map (Fig. 9.5), more local gravity lows occur directly correlating to the (Precambrian) basement windows within the Caledonides (e.g. Wolff 1979, Dyrelius 1985). The
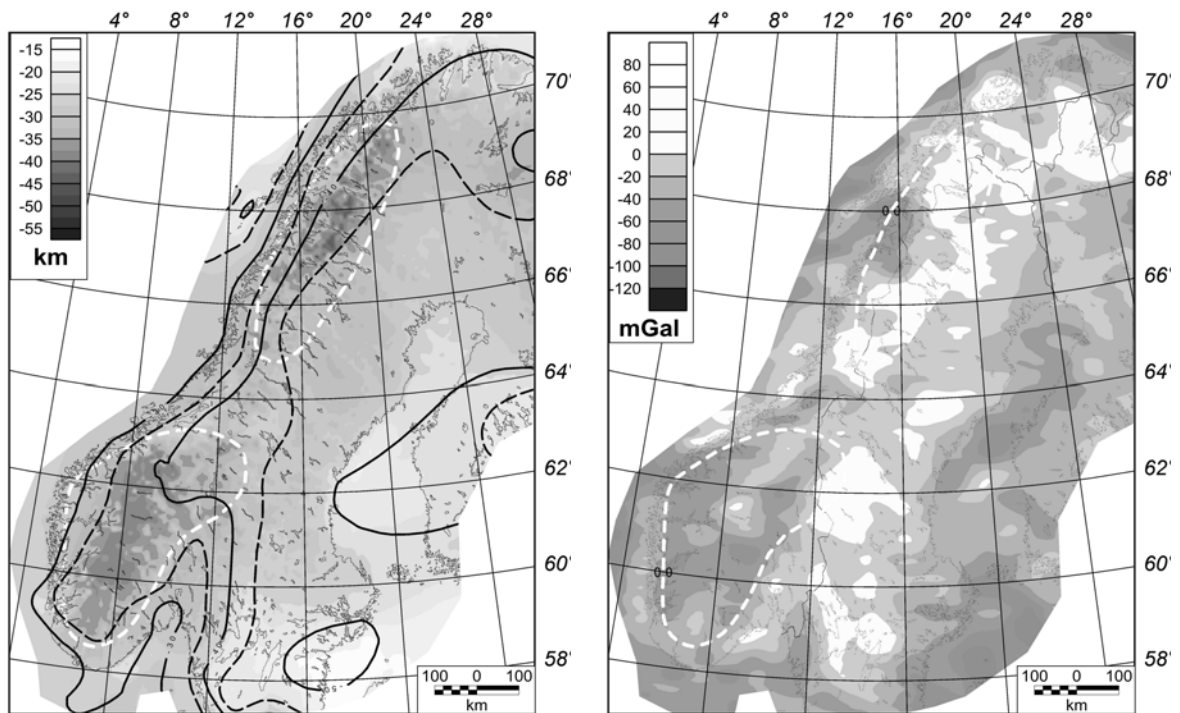
*Figure 9.3. (left) **Depth to top of the high-density lower crust from the isostatic balanced gravity model.** (right) **Residual gravity anomaly: Note the large negative residuals below the Northern and Southern Scandes.***

residual gravity highs correlate to the basic rock units within the different thrust-sheets belonging to the Central Norwegian Caledonides. Quantitative gravity interpretations constrained by density measurements of representative rock units have given nappe thicknesses of about 1 km to 4 km in Sweden (Elming 1980, 1988) and of about 8 km to 10 km as a maximum in Central Norway (Wolff 1984, Skilbrei & Sindre 1991). In eastern Trøndelag (Meråker-Storlien) gravity models demonstrate that the nappes form a half-graben indicating post-Caledonian extensional faulting (Skilbrei & Sindre 1991). A discussion of the gravity field and its relation to the mapped geology in different areas within Central Norway, and to the Moho depth, can be found in Wolff (1984), Dyrelius (1985), and Skilbrei & Sindre (1991). These results were used to constrain the upper part of the model across the central Scandinavian mountains.
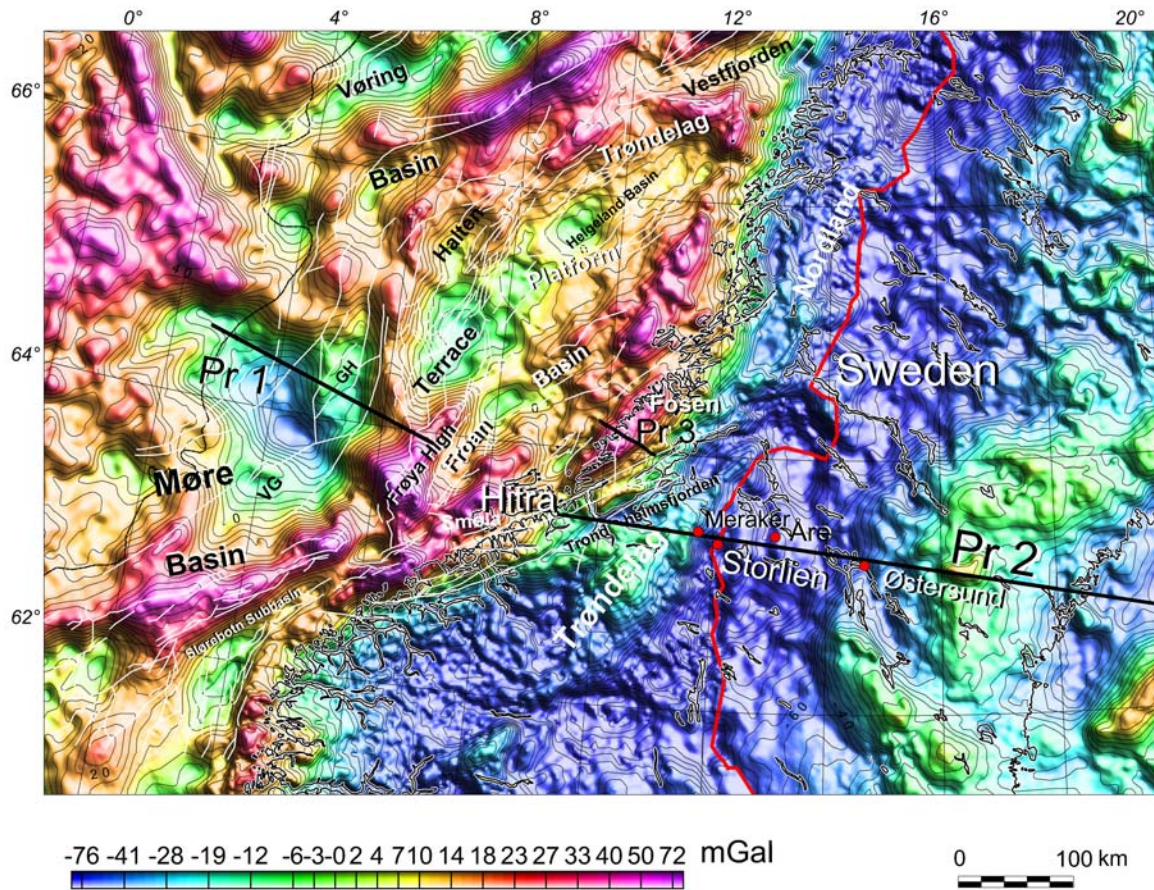
Figure 9.4. Gravity map (Bouguer on land, Free-air at sea). Pr2 shows the location of the modelled profile (Skilbrei et al. 2002).

The model calculations were performed using 2½ D bodies, i.e. bodies of polygonal cross-section with perpendicular end surfaces at variable distance from the profile. The deep interfaces (mantle and lower crust) were extended far away from both ends of the profile in order to avoid edge effects. The location and strike extents of the upper layers were taken from the seismic data and the geological maps (Elming 1988, Juhojuntti *et al.* 2001, Koistinen *et al.* 2001, Wolff 1984). The depth to the Moho and the upper crustal layers were adapted from seismic data interpretations (Juhojuntti *et al.* 2001).
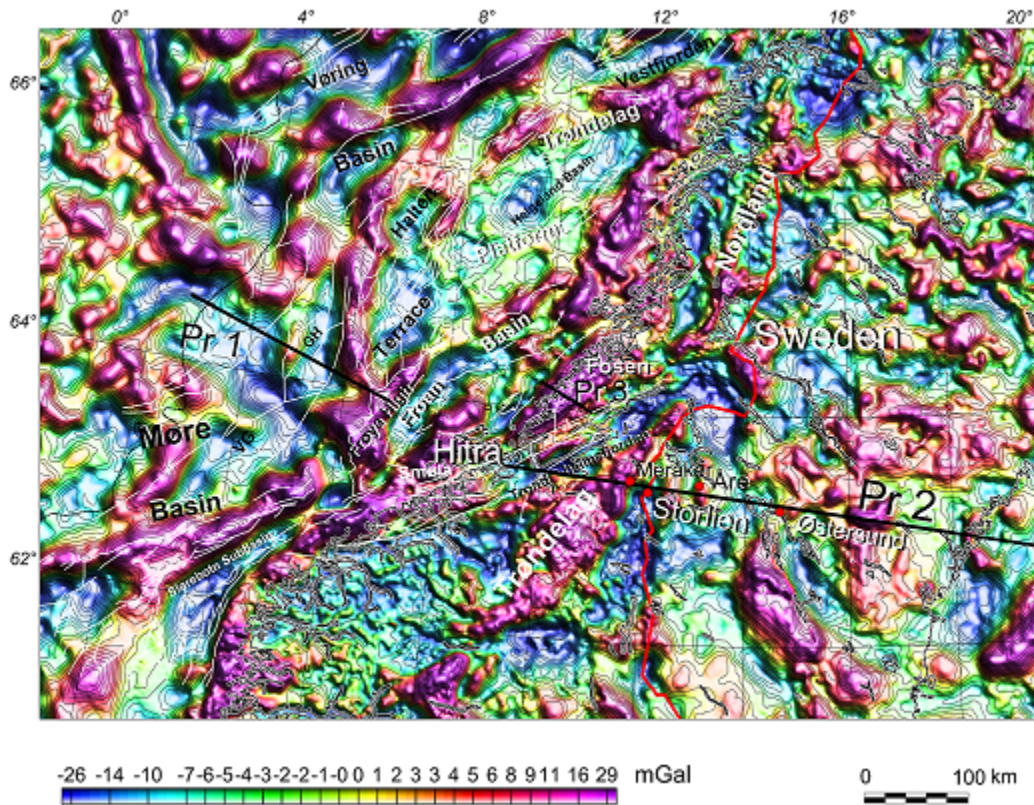
Figure 9.5. Residual, high-pass filtered, gravity map. VG=Vigra High, GH= Grip High. Structural elements in white solid lines. Black solid lines show location of model lines.

Table 9.1.   Densities applied to the Central Scandinavia Profile (Figs.9.6 and 9.7)

Formation	Density (kg/m^3)
Caledonian Nappe Sequence (primarily metasedimentary rocks, weighted mean)	2760
Caledonian Nappe Sequence (primarily metavolcanics, weighted mean)	2840
Seve-Køli	2850
Basement windows (Tømmerås-Grong-Olden)	2650
TIB, granite (Rætan)	2690
Gabbros, dolerite, some granite (Basic rocks in profile)	2850
Jotnian sediments	2610
Rapakivi granite	2640
Lower Crust	2900
Mantle	3250

One of the goals of the modelling was to check whether or not the topography of the Moho surface seen in the depth-converted seismic line of Juhojuntti *et al.* (2001) could be in agreement with the gravity data. In order to improve the model and avoid edge effects along the seismic lines, the profile extends to the coast of Norway (near Hitra) in the west and to Vasa near the coast of Finland in the east. To the east of Østersund, and to the west of Trondheim, the model was kept as simple as possible, using Moho depths close to that of the Moho depth map of (Kinck *et al. 1993*)). In the model by Skilbrei *et al.* (2002, Fig. 9.6a) the shape of the Moho surface mirrors the depth-converted published seismic line of Juhojuntti *et al.* (2001). However, the depths are 2-3 km shallower, because we think that the velocity used in the depth conversion (6.2 km/h) lies on the low side for middle-lower continental crust values. Refraction seismic data along the same transect (Vogel & Lund 1971), and farther to the north (Lund 1979) support this conclusion and Vogel & Lund (1971) applied seismic velocities of 6.2, 6.6 and 7.1 (km/s) for the upper-, middle- and lower crust, respectively. The seismic line from Trondheimsfjorden to Storlien (Hurich *et al.* 1989) did not image the Moho properly. The short wavelength variations of the gravity field correlate with the allochthonous units as explained by Elming (1980), Dyrelius (1985), Wolff (1984) and Skilbrei & Sindre (1991). The main part of the negative gravity and the positive magnetic high is modelled as granitoid units within the Transcandinavian Igneous Belt (TIB). The magnetic modelling indicates that these magnetic batholiths extend to at least 20 km depth, similar to the results of Juhojuntti *et al.* (2001) and Dyrelius (1985).
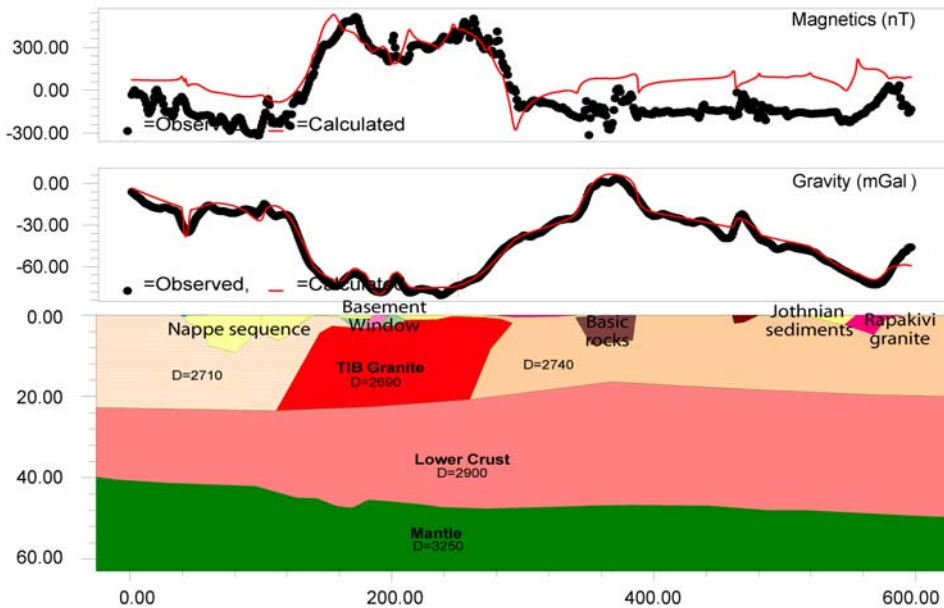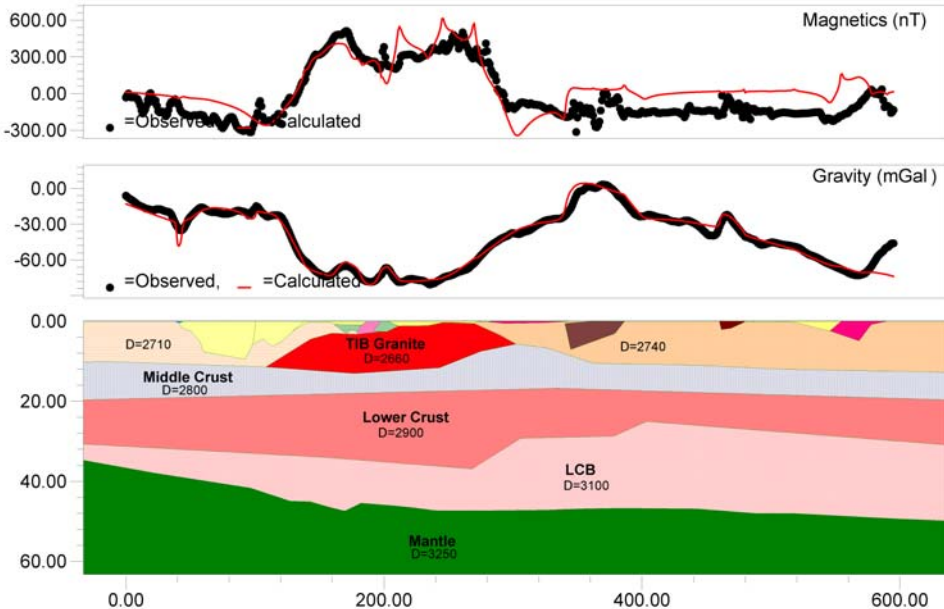
Figure 9.6. *Two alternative models of the density and magnetic structure for the central Scandinavian mountains – Model A: Density structure after Skilbrei et al. (2002). Model B: Density structure with consideration of a high density lower crust. In both model calculations, the asthenosphere-mantle boundary is included at a depth of 120 (west) to 160 km (east) (not shown). Applied near-surface densities and magnetic parameters are shown in Table 9.1. Location of the profile (Pr 2) on Fig. 9.5.*

The density modelling along the deep reflection seismic lines (Fig. 9.6) demonstrates that the paired, high, positive to negative Bouguer gravity anomalies that run parallel to the

coast and the mountains are mainly a complex bulk effect of the following: (1) Moho topography due to extensional events, (2) the extension which has brought lower crustal rocks (relatively high grade and high density) up to, or closer to, the present surface along the coastal zone, (3) the local lows (Bouguer minima) associated with basement culminations and caused by granitoids/batholiths of the Transscandinavian Igneous Belt and an increased Moho depth. The latter is demonstrated by the regional, negative gravity anomaly. The variation of the Bouguer pattern is then partly related to undulations in the 'Moho-surface' both along and across Scandinavia. This may represent the main components of the local Airy isostatic compensation, as discussed also by Olesen *et al.* (2002) based on isostatic corrections. The effect of the present topography (surface uplift minus erosion) and the local geology, is obvious The Caledonian-, Svecofennian- and Sveconorwegian domains represent regional bulk differences in density and thickness of the crust (Pratt compensation +/- regional compensation). Thus, the density model suggests that isostatic balancing of the topographic masses is of combined Airy- and Pratt types.

9.2.3 An alternative model for the Central Scandinavia Profile - Model B

Here, we present an alternative density model for the Central Scandinavia Profile based on the description given in Section. 9.2.2 and the isostatic considerations in Section 9.2.1. The general lithospheric density structure is given by: upper crust 0-12 km depth: 2670 kg/m^3, middle crust 12-20 km depth: 2800 kg/m^3, lower crust 20-30 km depth: 2900 kg/m^3, lithospheric mantle 30-120 km depth: 3250 kg/m^3 and asthenospheric mantle: 120-220 km depth: 3220 kg/m^3. The geometry of the near-surface structures and the Moho geometry are identical to Skilbrei *et al.* (2002). The TIB, however, is modelled with a thickness of 12 km, similar to the isostatic considerations in Section 9.2.1. To isostatically balance the section we have to introduce a high-density lower crust (3100 kg/m^3). The high-density lower crust (LCB) has a thickness of up to 20 km, but is only up to 12 km thick below the TIB granite. The presence of the LCB is constrained by a wide-angle seismic velocity model that shows high-velocities (~6.8-7.2 km/s) at the base of the crust (Schmidt 2000). But, the distribution of areas with high-velocities is not directly correlating to the isostatic gravity model. The resolution of the seismic velocity model makes a clear correlation difficult, as the velocities in the deep crust have a relatively high uncertainty range and biased by the assumed depth to Moho (Schmidt 2000).

9.2.4 Thermal modelling of the Central Scandinavia Profile

For the thermal modelling we considered the two geometries obtained from potential field modelling (i.e. models A and B). Because our current knowledge on surface heat flow values along the Central Scandinavia Profile is relatively poor, we preferred to keep

79

the models simple. Consequently we kept similar conductivities and radioactive heat generations for each unit as well as basal heat flow (i.e. 25 mW/m^2) in the two models (Fig. 9.8).
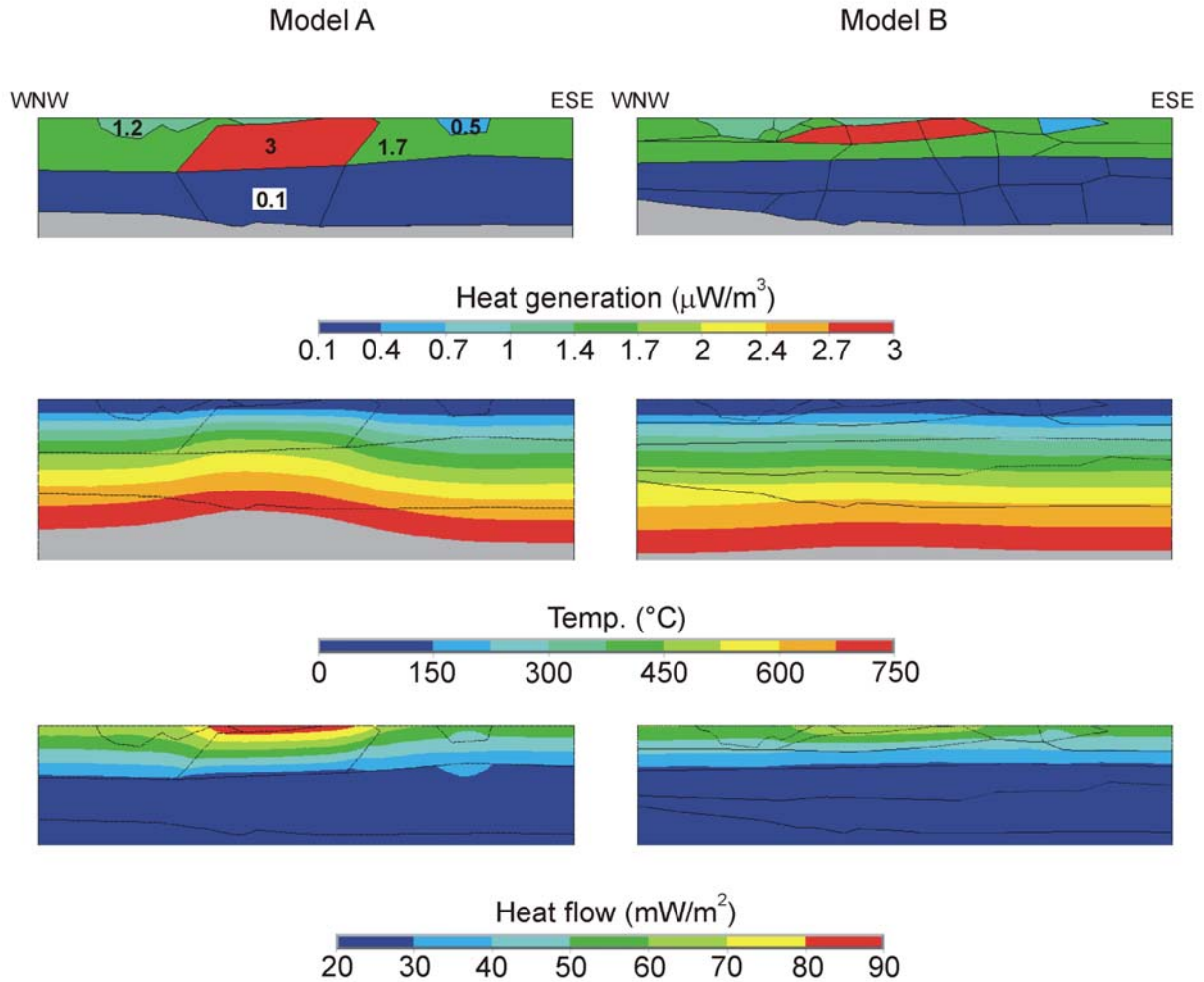
*Figure 9.7. **Input heat generation values and computed temperature and heat flow values for the Central Scandinavia Profile models A (left) and B (right). Used heat generations for each crustal unit are indicated on Model A. Conductivities are 2.5 and 3.5 W/m/K for the crust and the mantle respectively. Boundary conditions are T=0°C at the top and a basal heat flow of 25 mW/m^2 (VE:x2).***

Computed geotherms and heat flow values for both model A and model B are presented in Fig. 9.7. In the case of model A, we note that the modelled thick granite results in a significant increase of the temperature in the lower crust below it. Moho temperatures below the granite are predicted to reach up to ~750°C, exceeding by 100°C Moho temperatures of the surrounding areas (Fig. 9.7) and close to melting temperatures associated to most crustal materials. Modelled surface heat flow values above the granite

reach ~90 mW/m^2, which, if confirmed, would be an anomalously high value for a Precambrian shield.

Computed isotherms for model B (Fig. 9.7 right) show a much more moderate rise below the modelled granite that is thinner than in model A. Moho temperatures remain close to 600°C along the profile decreasing by 100°C west of the Caledonian nappes. Interestingly, predicted surface heat flow values are in the range between 50 to 70 mW/m^2, reaching their maximum above the high heat-producing TIB granite. These computed surface heat flow values appear to be in better agreement with commonly measured values in Proterozoic shields (Artemieva & Mooney 2001).
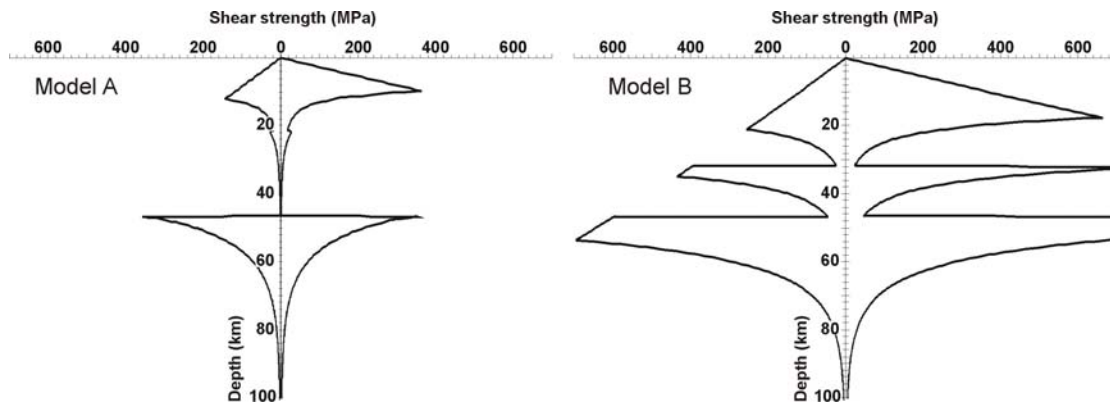
Figure 9.8. ***Lithosphere strength envelopes calculated on the basis of thermal Models A and B at the location of the TIB body. Applied rheological parameters are given in Table 9.2.***

9.2.5 Implications for the thermal and rheological structure of the lithosphere

From our thermal models it is possible to calculate the depth to the thermal base of the lithosphere taken as the 1300 °C isotherm. Model A predicts a base lithosphere plunging from 130 km depth in the west to 136 km in the east, whereas Model B predicts deeper but less variable depths in the order of 140 km. Although the depth difference in between the two models remains well inside the error bars of results from most available methods used to determine the thickness of the lithosphere, base lithosphere depth values as computed for Model B remain in better agreement with values obtained from surface wave studies (140 to 150 km, Calcagnile 1982) and thermal modelling (~150 km, Artemieva 2003). However, much care has to be taken when discussing these previous determinations, because (1) there is no a systematic correlation between seismic and thermal lithosphere and (2) the two studies were conducted at the regional scale providing a crude resolution along the CSP. In particular, short-wavelength variations in the depth to the base of the lithosphere are at the present stage beyond the resolution of the existing data sets.

Table 9.2. **Rheological parameters used for lithosphere strength computations. A strain rate of 10-15 was applied to build the strength envelopes. Creep parameters after Carter & Tsenn (1987).**

Brittle deformation	Friction	Pore pressure ratio	
	0.6	0.35	
Power-law creep	Strain-rate coef. (Pa^{-n}/s)	Stress exponent	Activation energy (J/mol)
TIB: dry granite	$3.16\ 10^{-26}$	3.3	187000
Lower and middle crust: felsic granulite	$2.01\ 10^{-21}$	3.1	243000
LCB: mafic granulite	$8.83\ 10^{-22}$	4.2	445000
Lithospheric mantle: dry dunite	$7.94\ 10^{-18}$	3.6	535000

The thermal state of the lithosphere exerts a strong control on its integrated strength (e.g. Ranalli 1995). We tentatively determined the strength envelopes for the central parts (i.e. at the location of the TIB granitoid) of Models A and B (Fig. 9.8). The parameters used for the construction of the envelopes are listed in Table 9.2. The strength envelopes give a first-order idea of the relative strength of the lithosphere, noteworthy the strength of the lithosphere can be drastically reduced by, for example, the pre-existence of weak fault zones (e.g. Bos and Spiers 2002) or water-saturated rocks (e.g. Ranalli 1995). At the location of the TIB batholith, Model A results in a very weak lithosphere with a brittle-ductile transition at ~10 km depth in the crust and a large viscous channel above the Moho. For Model B, the brittle-ductile transition is predicted to occur at ~20 km depth and the lower crust viscous channel is much less developed.

The Fennoscandian lithosphere is submitted present-day to relatively high tectonic stresses (Stephansson 1989, Pascal *et al.* 2005). Therefore, the extremely weak lithosphere predicted by Model A would reasonably be expected to show signs of high strain-rates. In contrast, the region under interest here (i.e. the region underlain by the TIB granitoid) is practically void of earthquakes (Dehls *et al.* 2000). Moreover, the reconstructed uplift patterns do not show any significant deviation at that location (Dehls *et al.* 2000). These independent observations argue again against a very thick TIB granitoid below the Central Scandinavian mountains.

9.2.6 Discussion and conclusion

About homogeneous heat production through depth
The thermal modelling suggests that an extremely (i.e. ~20 km) thick TIB batholith below the Central Scandinavian mountains is not likely. Our conclusion is mainly based

on the impact of the thickness of the batholith on surface heat flow Moho temperatures and lithosphere strength, assuming a homogeneous heat production inside the body. This later hypothesis has been questioned since the 60s and an exponentially decaying with depth of radioactive heat producing elements is very often adopted (Lachenbruch 1968). It is worth noting that until now none of the two hypotheses has been validated from natural data. Furthermore, recent work on the Sierra Nevada Batholith in California (Brady *et al.* 2006) suggests a much more complex depth-distribution for heat production than previously anticipated, where heat production globally decreases with depth but also significantly increases for some depth intervals. In other words, we strongly suspect that the Sierra Nevada Batholith does not represent a particular case but that similar erratic patterns for the heat production also characterise other plutons including the studied TIB granitoid. In summary, in absence of other firm constraints we preferred to keep the thermal models as simple as possible and concentrate on variations in crustal geometry.

Crustal structure and topography of the Central Scandinavian mountains
The two alternative models for the Central Scandinavian mountains show clearly that the interplay between the TIB and the Scandinavian mountains is influencing the gravity and magnetic field as well as the isostatic state of the lithosphere. The TIB shows a prominent signal in the magnetic anomalies and finds also an expression in the Bouguer gravity. However, estimates of the depth extension of the TIB are dependent on the deep crustal configuration.

In any case, our study shows that the TIB coincides with the main topography and Bouguer gravity low in the northern and central Scandinavian mountains. While the magnetic signal can be associated directly with the TIB granitoids, the Bouguer gravity low is caused by a superposition of the TIB and the deep crustal geometry. Therefore, the Bouguer gravity low can be interpreted to be largely related to the low-density granitoids of the TIB. The low-density rocks of the TIB have to be especially considered to explain the gravity field of the Scandinavian mountains. The distribution near the surface causes a strong signal in the gravity field, even with relatively small density contrast to the surrounding rocks. However, the effect on the isostatic balance of the Scandinavian mountains is less pronounced compared to the influence of deep-seated masses.

Conclusion
From the potential field modelling both presented models are possible for the central Scandinavian mountains. However, isostatic considerations and especially the thermal and rheological modelling make Model B more likely. The key to unveil the structure along the CSP is to do more focussed seismic studies. The results of a new receiver function study along the profile will be available in the near future and combined processing with the wide-angle data will hopefully allow more insights in the deep structure along the transects, that in turn will provide a better background to model the shallow structure of the central Scandinavian mountains.

9.3   3D density and magnetic model of The Oslo Rift

The 3D model of the Oslo Rift is presented by excerpts of Ebbing *et al.* (submitted). Here, we present merely the summary and give a short presentation of their Profile 3, which is here used for the thermal modelling.

9.3.1 Summary

We present a new interpretation of the crustal structure of the Oslo Graben and the northern Skagerrak Graben. Integrated interpretation of seismic, gravity and magnetic field data constrained by petrophysical data and surface geology reveals the location of magmatic intrusions below the Oslo Graben. Source depth estimates by Euler deconvolution of the magnetic field measured at a shallow and a high-altitude flight level show mainly two sets of solutions around <4 km and between 12-16 km depth. 3D modelling of the gravity and magnetic fields gives a depth extent of 1.5-4 km for the exposed magmatic rocks. These are only the cap of a mushroom shaped intrusion that has a depth extent of up to 15 km. Within this structure the magnetization and density are increasing with depth. This leads to a small density contrast to the surrounding, and therefore only magnetic field modelling is able to resolve this deep structure. In addition, the 3D density modelling shows that the gravity high above the Oslo Rift is caused by a combination of crustal thinning and the presence of a high density structure in the upper crust, which is related to the Bamble and Kongsberg Gneiss Complexes. The lower crust below the area shows no significant petrophysical contrast to the surrounding areas; hence no large-volume magmatic underplating is interpreted.The 3D model of the Oslo Graben provides a new volume estimate of the magmatic material in the Oslo Graben system. Our estimate of 63.000 km^3 is only 2/3 of the values estimated in previous studies (>95.000 km^3) as we disregard high-volume magmatic underplating. Thus, our estimate overcomes the discrepancy between the observed extension by upper crustal faulting and magma emplacement. Correlation with structural data and the surface geology as with deep lithospheric features show that differences in the volume of extrusive magmatism within the Oslo Rift can be related to the timing and onset of rifting in the Oslo and Skagerrak Graben.

9.3.2 3D modelling of the Oslo Rift

An integrated interpretation of seismic, petrophysical and gravity and magnetic field data provides the possibility to construct a 3D crustal model of the rift and a more thorough insight into the location of the source for the Permian volcanism in the Oslo Graben.

However, in contrast to the well-defined potential field and petrophysical data sets, the knowledge about the structure of the Oslo Graben from seismic experiments is rather sparse. Therefore, we integrate all the different data sets (two aeromagnetic fields flown at two different altitudes, the gravimetric field, as well as petrophysical data), into one model that fulfils all observed data sets. In total, the 3D model is constructed by 28 vertical sections in the study area (Fig. 9.9). The spacing between the planes varies from 15 km outside the Oslo Graben, to 3-7.5 km within the Oslo Graben depending on the surface geology. Special emphasis was given to the resolution of the volcanic and plutonic structures of the Oslo Graben in the construction of the model.
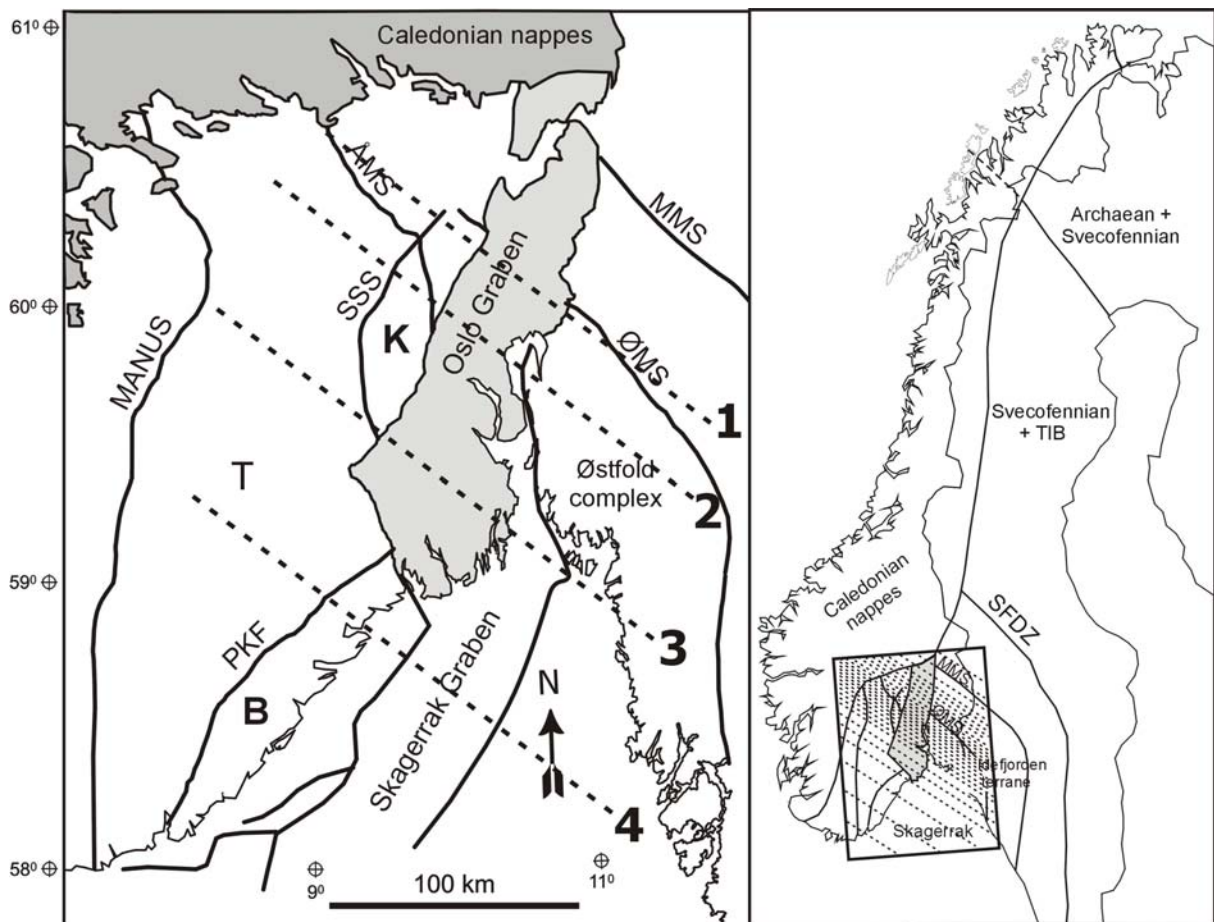
Figure 9.9.   Structural map of the Oslo Rift and surrounding areas. The black dotted lines show the location of the profiles through the 3D density model. The map to the left shows the locations of the profiles presented in Ebbing et al. (subm.) and in Fig 9.11. The overview figure to the right shows all 28 profiles of the 3D model. T: Telemark sector; K: Kongsberg sector; B: Bamble sector; SFDZ: Sveconorwegian frontal deformation zone, SSS: Saggrenda-Sokna shear zone, MMS: Mjøsa-Magnor mylonite zone, ØMS: Ørje mylonite zone, ÅMS: Åmot-Vardefjell shear zone; PKF: Porsgrunn-Kristiansand shear zone; MANUS: Mandal-Ustaoset Fault, TIB: Transcandinavian Igneous Belt.

The interpretation of potential field data is ambiguous and only good constraints minimize the possibilities for the source geometry. The combination of the gravity field and magnetic field (Fig. 9.10) at different flight altitudes helps to constrain the interpretation. The 3D model is presented by a profile crossing the Oslo Rift in the Vestfold Graben (Fig. 9.11). First, the available information on surface geology, petrophysical measurements and seismics was used in order to constrain a density model of the Oslo Rift. The 3D density model of the Oslo Rift explains the regional shape of the Bouguer anomaly as a combined effect of crustal thinning and the presence of a transcrustal ramp related to a mid-crustal layer that reaches the surface in the Kongsberg and Bamble Complexes (Ebbing *et al.* 2005). This is in agreement with the observed high-densities in the over-thrusted high-grade and high-density Kongsberg and Bamble Complexes and the asymmetric shape of the gravity high (Ebbing *et al.* 2005). Comparison of the Bouguer anomaly and the crustal thickness reveals an inverse correlation between the crustal thickness and the gravity lows outside the rift area: thinner crust in the west, but a higher level of gravity signal in the east. This feature is associated to the density distribution and the internal geometry of the crust. Seismic and density data constrain the changes in upper surface densities from west to east in the Oslo Rift region, hereby reflecting the regional bedrock geology of southeastern Norway (Berthelsen *et al.* 1996; Dons & Jorde 1978; Koistinen *et al.* 2001). Based on the seismic velocities (c. 7-7.1 km/s), the lower crust in the model has been assigned a density of 3000 kg/m^3. This value is similar to the values used for the lower crust below the Oslo Graben in the studies of Ramberg (1976), Olsen *et al.* (1987), Wessel & Husebye (1987). The high-density lower crust is not limited to the Oslo Graben but extends through the whole 3D model. The seismic velocities of the middle crustal layer range between 6.5-6.8 km/s and we have assigned it a density of 2830 kg/m^3, consistent with the interpretations of Tryti & Sellevoll (1977) and Sindre (1993). This layer is here interpreted to be upthrusted to the Bamble and Kongsberg Complexes along the western boundary of the Oslo Graben (transcrustal ramp after Lie & Husebye 1993).

The steep gravity gradient to the west of the Oslo Rift can best be explained by a shallow to intermediate crustal source. Our model connects the Bamble Complex with the Kongsberg Complex below the steep gravity gradient along the western margin of the Oslo Rift (Fig. 9.10). However, the 3D density structure alone does not yet give an indication of the source of the Permian volcanism in the Oslo Graben and to identify these, the simultaneous modelling of the magnetic field at two different levels was performed.

The construction of the 3D magnetic model is based on the structure of the density model. Magnetic field anomalies are generally more strongly affected by near surface rocks due to faster decay with the distance to the source rock, and the disappearance of magnetization with temperatures higher than the Curie temperature. Rocks at higher
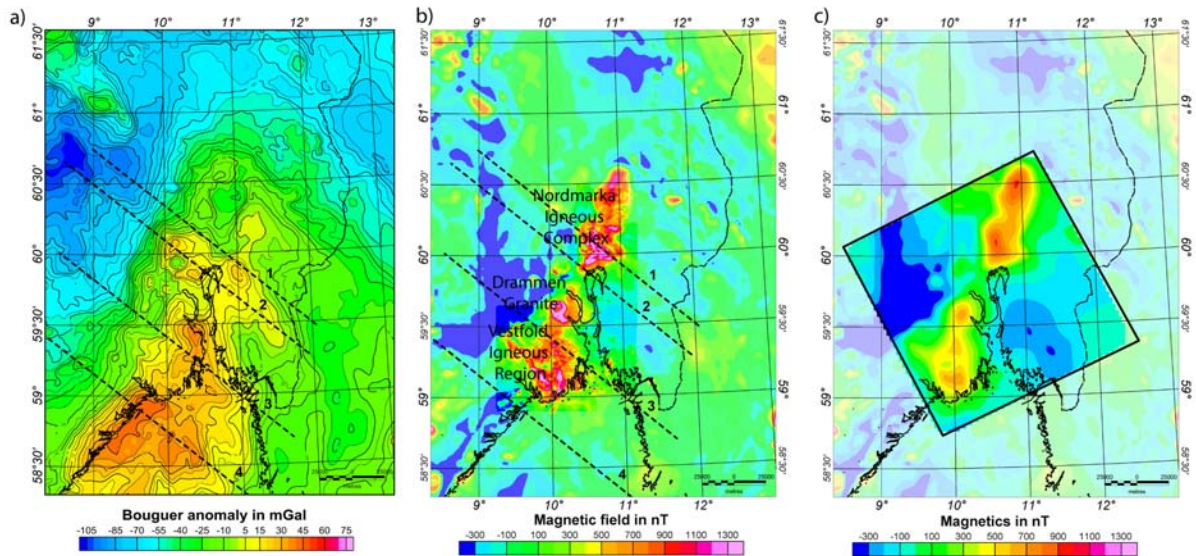
Figure 9.10. Gravity and magnetic fields of the Oslo Rift Region. a) Bouguer anomaly map. The data compilation is based on data sets collected by NGU, SGU, the Norwegian Petroleum Directorate, ExxonMobil, Statoil and the Norwegian Mapping Authority (Skilbrei et al 2000). b) High-resolution aeromagnetic survey (REF) merged with adjacent low-altitude, draped aeromagnetic survey flown in 1973 (Olesen et al. 1997a, Korhonen et al. 2002b). c) The square indicates the data of the high altitude aeromagnetic survey (3000 m flight altitude) as part of the Norwegian Geotraverse project (Aalstad et al. 1977, Heier 1977). Surrounding low-altitude data are shown in transparent colours.

temperatures will not show the ferromagnetic behaviour necessary to generate the discernible magnetic signal. The dominant material is regarded to be magnetite, which has a Curie temperature of 580 ºC (cf. Hunt *et al.* 1995). With typical Moho temperatures in between 500 to 600ºC within continental crust (McKenzie *et al.* 2005), the importance of the crustal geometry in magnetic modelling is obvious. In addition to the magnetic structure, the magnetic anomalies are also affected by the normal magnetic field. During modelling we applied the values as presented in Table 9.2.

The two major magnetic anomalies in the Oslo Graben are located above the Nordmarka Igneous Complex and the Vestfold Igneous Region. The rocks at the surface are heterogeneous and feature a variety of igneous rocks (e.g. syenite, granite, basalt), which have to be included with their magnetic properties in the model.

The Vestfold Igneous Region in the south Oslo Graben is less well sampled by petrophysical measurements than the northern region, but the available data show a distinction between the susceptibilities measured in the lava flows of Vestfold and the larvikites around Larvik. Most of the susceptibility measurements of the lava flows show values less then 0.001 SI, while the larvikites have susceptibilities from 0.025 SI to 0.075 SI with an average around 0.045 SI. Hence, in the south an indication for high magnetic

material at the surface is given, while in the northern part the lava flows have a susceptibility that is only slightly higher than the surrounding rocks. The amplitude of the magnetic anomaly and the average power spectrum analysis give indication of a maximum source depth of more than 17 km (Aalstad *et al.* 1977). But as the surface expression of the mafic rocks and the associated susceptibilities are also larger than in the Nordmarka Region, the most reasonable model represents a broad intrusion with a maximum depth of 14 km (Fig. 9.11). Hereby, the surface rocks are underlain by a broad area of slightly higher susceptibilities (0.055) and Q-rations (1.0) than measured at the surface.

Table 9.2 **Petrophysical parameters and volume of Permo-Carbonifereous magmatic rocks in the Oslo Graben as estimated from the 3D model. a) estimated from the density model by Ramberg (1976).**

	Mean measured Susceptibility (min/max) [SI]	Model Susceptibility SI	Mean measured densities (min/max) [kg/m^3]	Model densities [kg/m^3]	Volume (km^3) this study	Volume (km^3) Neumann *et al.* 1994
Extrusive rocks						
Basaltic lavas	0.05 (0.0005-0.11)	0.035	2950 (2700-3100)	2900	300	300
RP lavas	0.011 (0.0001-0.058)	0.01	2680 (2480-2770)	2700	1250	~1200
Rhyolitic lavas	0.001 0.001-0.002	0.002-0.02	2645 2620-2670	2550	100	50 [a]
Intrusive rocks						
Gabbroic rocks	0.058 (0.0009-0.165)	0.001-0.08	3040 (2760-3300)	3000	50	~5 [a]
Larvikites	0.032 (0.0001-0.109)	0.025-0.04	2700 (2550-3090)	2650	2.000	10.000
Syenites, granites, etc.	0.016 (0.0001-0.136)	0.015-0.035	2610 (2490-2980)	2600	7.600	14.045 [a]
Exposed magmatic rocks, total					**10.500**	**25.600**
Dense, subsurface bodies						
Vestfold		0.045-0.065		2750	25.000	4.610 [a]
Nordmarka		0.020-0.055		2800	17.500	
Magmatic rocks in the deep crust/upper mantle		<0.0001	2950-3100 [a]	3000	<9.000	65.000
TOTAL					**~63.000**	**> 95.200**
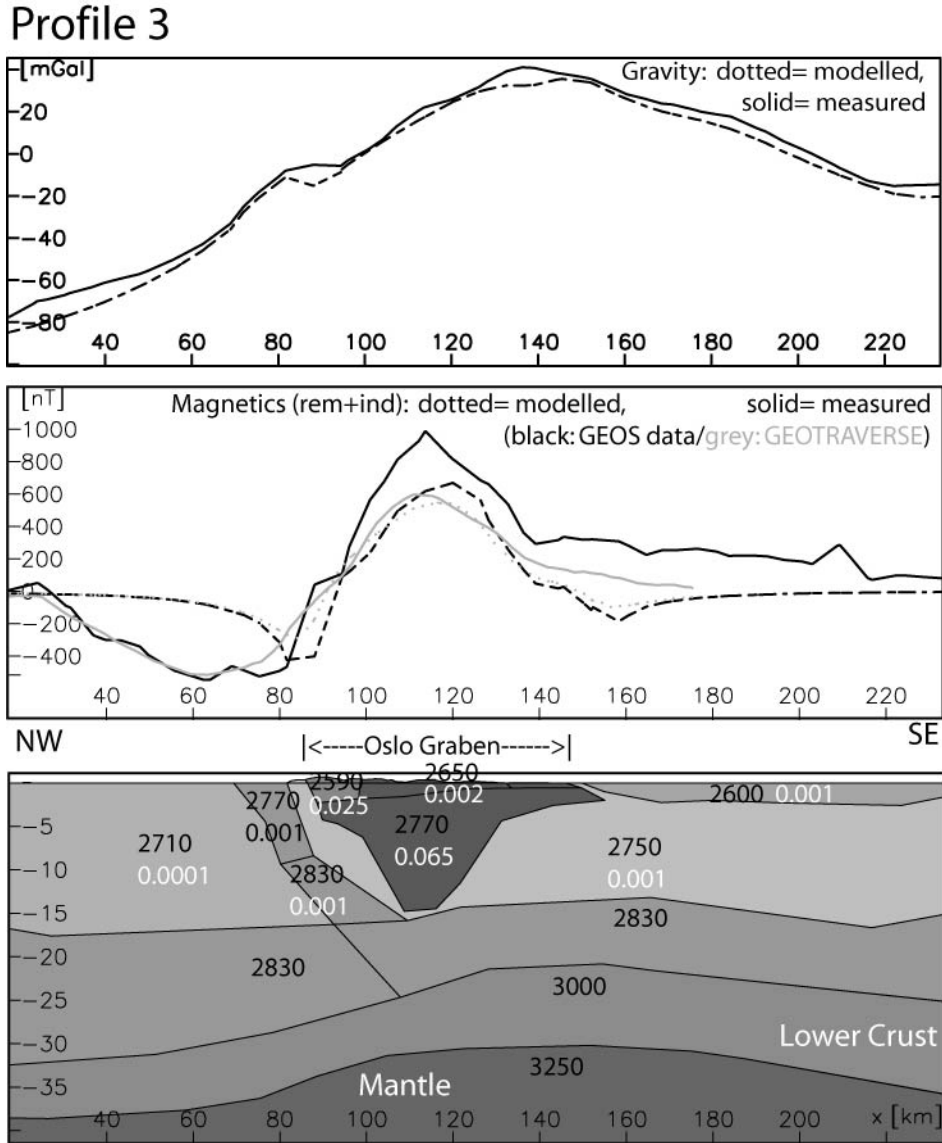
Figure 9.11 Profile 3: Cross-section through the southern Oslo Graben (Vestfold Graben). The upper panel shows observed and modeled Bouguer gravity, in the middle the observed and modeled magnetic anomaly for the GEOS (50 m a. ground) and Geotraverse (3400 m a.s.l.) data are shown. The lower panel shows the crustal density (black numbers in kg/m^3) and magnetic structure (white numbers: susceptibility in SI). The high-magnetic bodies are interpreted to show the magmatic intrusion. For profile location see Fig. 9.9.

9.3.3 Thermal model

Using the geometry given in Profile 3 and heat generation data from NGU's litho database we built and ran a thermal model (Fig. 9.12). Input for each unit is given in Fig. 9.12. In contrast with the Central Scandinavia Profile model (see Section 9.2.4) we fixed

the temperature at the base of the model representing the base of the lithosphere (i.e. 1300°C isotherm). In agreement with results from surface-wave studies (Calcagnile 1982), the base of the lithosphere was modelled at ~120 km depth below the Oslo Graben. Two configurations were modelled: firstly, we assumed that the inferred intrusive material below the Oslo Graben produced as much heat as the country rock (Fig. 9.12, Model 1) and secondly, we assumed that this intrusive body was associated with relatively high heat generation.
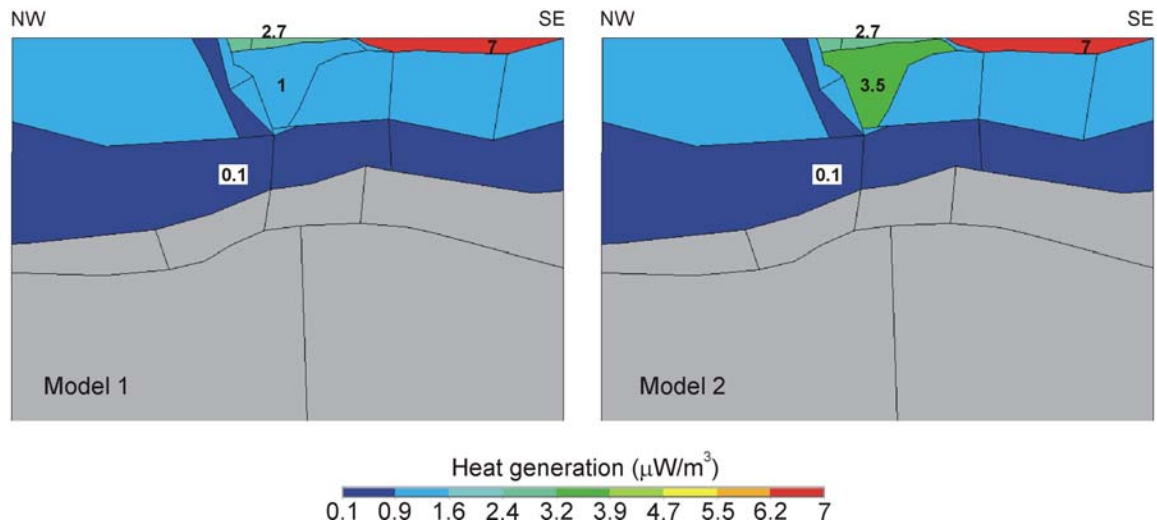
*Figure 9.12. Heat generation values used for thermal Model 1 and thermal Model 2 of the Oslo Graben Profile 3. Used heat generations for each crustal unit are indicated. Conductivities are 2.5 and 3.5 W/m/K for the crust and the mantle respectively. Boundary conditions are T=0°C at the top and T=1300°C at 120 km depth (VE:x3).*

Computed isotherms and heat flow values are given in Fig. 9.13. Moho temperatures are predicted to remain in between 450°C and 550°C for both models 1 and 2. Below the Oslo Graben, a slight increase in Moho temperatures occurs for Model 2 with respect to Model 1. Isotherms are almost flat and variations in Moho temperatures are controlled here mostly by variations in crustal thickness. In particular, minimum Moho temperatures are predicted where the Moho has been previously "arched" during Permian rifting. Noteworthy, the very high heat-producing Iddefjord granite does not affect significantly the shape of the isotherms at deeper crustal levels below it. This is because the granite appears not to show deep roots in the crust. Modelled Moho heat flow in both models is ~30mW/m^2. This value is slightly higher than those commonly inferred for Proterozoic terrains (i.e. ~25 mW/m^2) but can be the result of the last thermo-tectonic event having affected the region (i.e. Permian rifting). It is interesting to note that for Model 1 surface heat flow values scatter along a relatively narrow range of values (i.e. in between ~50 to 60 mW/m^2) and are consistent with values commonly measured in the Oslo region and in Proterozoic terrains. In the case of Model 2 a relatively high heat flow but still in between

reasonable bounds (i.e. ~70mW/m^2) is predicted at the location of the graben. This relatively high heat flow at the surface associated with a pronounced rise of the isotherms at mid-crustal levels below the Oslo Graben. Finally, it is worth noting that the modelled moderate and short-wavelength variations in surface heat flow for both models are the result of the uneven distribution of the different lithological units at relatively shallow depths.
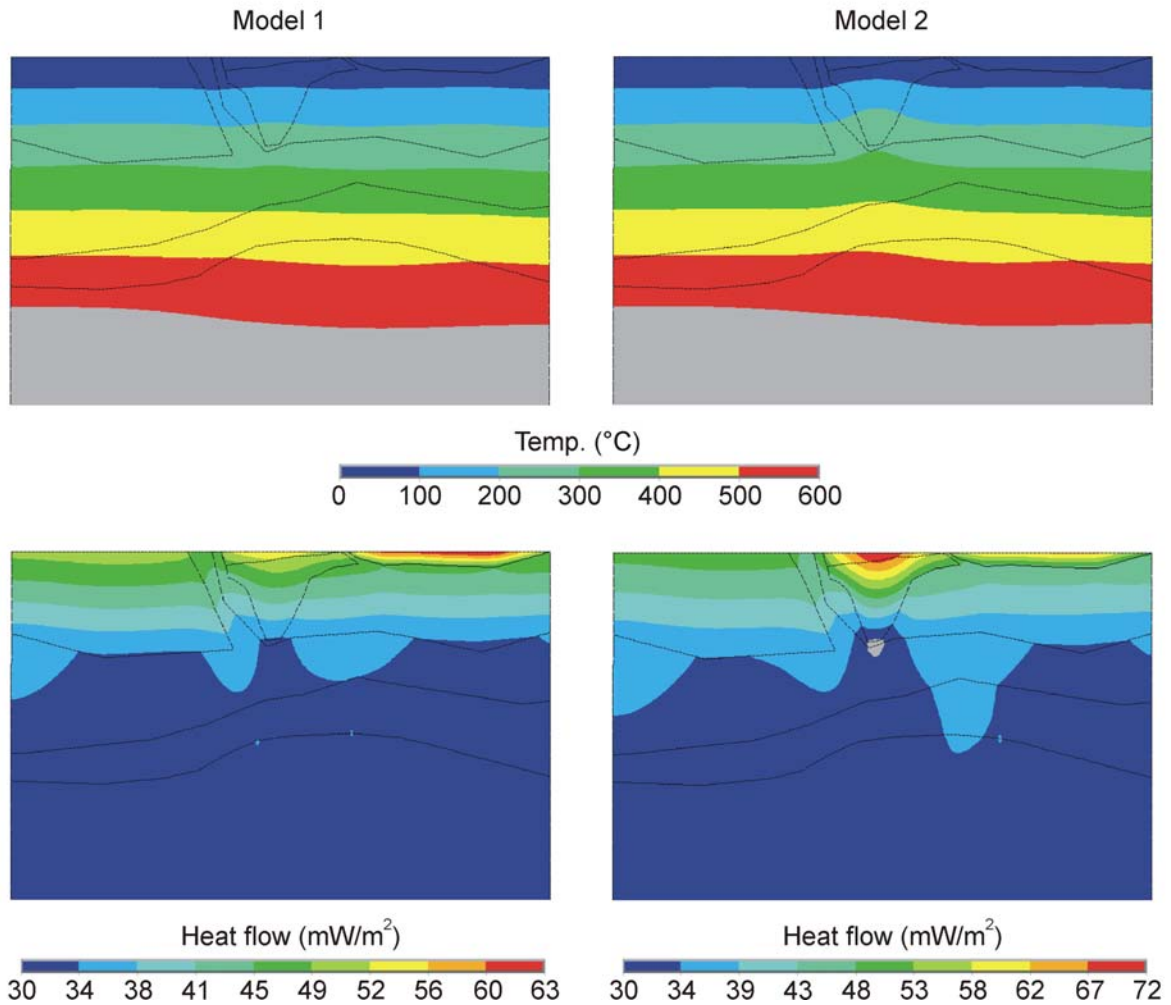
Figure 9.13. Computed temperature and heat flow values for the Oslo Profile 3, models 1 and 2. VE:x3.

9.4   The Mid-Norwegian margin

For the Mid-Norwegian (Møre-Vøring-Lofoten) Margin we will mainly present updates on the previously presented 3D model (Olesen *et al.* 2005, Ebbing *et al.* 2006, Osmundsen *et al.* 2006), before we discuss the thermal structure of the Mid-Norwegian margin.

9.4.1 Gravity and magnetic interpretation of Mid-Norwegian margin

Figure 9.14 shows the gravity field and the magnetic anomaly field of the mid-Norwegian margin and the adjacent mainland. The gravity anomaly field (Skilbrei et al. 2000) is based on measurements from marine gravity profiles collected by the Norwegian Petroleum Directorate, oil companies and the Norwegian Mapping Authorities in addition to gravity data from satellite altimetry in the deep-water areas of the Norwegian Sea (Andersen & Knudsen 1998). Onshore the Bouguer anomaly is shown, which is based on the land measurements carried out by NGU. The magnetic anomaly is based on a NGU compilation of different onshore and offshore surveys (Mauring *et al.* 2003, Olesen *et al.* 2002, 2004). The pattern of flight lines generally provides data along NW-SE trending lines with a spacing of 2-5 km. Further details on the magnetic and gravity data see figure caption. A first comparison of the gravity and magnetic anomalies reveals different structures, probably reflecting sources at different crustal levels. The amplitudes of the magnetic anomalies in the Vøring Basin are very low (around -50±50 nT) and the complex shape of the magnetic anomalies result possibly from changes in bathymetry (distance to near-surface sources), intra-basement variations of magnetic attributes, as well as intrusives (e.g. sills) located at shallower depths within the sediments. Towards the Trøndelag Platform the amplitudes and wavelength of the magnetic anomaly increase, pointing to additional deep-seated, crustal sources.

Previous investigations of the Mid-Norwegian continental margin have largely been based on interpretation of multi-channel reflection seismic data, refraction seismics, commercial and scientific drilling, and analysis of potential field data (e.g. Skogseid *et al.* 1992, Blystad *et al.* 1995, Doré *et al.* 1999, Brekke 2000, Mjelde *et al.* 2001, 2003a, Raum *et al.* 2002, Gomez *et al.* 2004, Fernàndez *et al.* 2004, 2005).

The geometries of the deeper crust and the upper mantle on the mid-Norwegian margin are reasonably well defined by OBS data (see Fig. 9.15a for location). Interpretations of OBS arrays are available from the studies by Mjelde *et al.* (1992, 1993, 1997, 1998, 2001, 2002, 2003a, 2003b, 2005) and Raum *et al.* (2002). In addition, the research group of Rolf Mjelde at UiB provided us with information about the velocity structure along three yet unpublished OBS transects. These three profiles are especially helpful for our interpretation as two cross the Trøndelag Platform and end onshore, and the third one is located across the Møre margin, where few other regional profiles are available (Fig. 9.15). In addition, the Moho compilation by (Kinck *et al 1993*.) and its modifications by (Olesen *et al 2002*) have been used to constrain the model in the onshore area.The estimate of the offshore basement depth is based on the seismic results mentioned above and on studies by Olesen *et al.* (1997b), Doré *et al.* (1999), Brekke (2000), Olesen *et al.* (2002), Osmundsen *et al.* (2002), Skilbrei *et al.* (2002) and Olesen *et al.* (2004). In these

studies also the interpretation to depths of magnetic sources have been applied (e.g. Skilbrei *et al.* 2002, Olesen *et al.* 2004; Skilbrei & Olesen 2005).
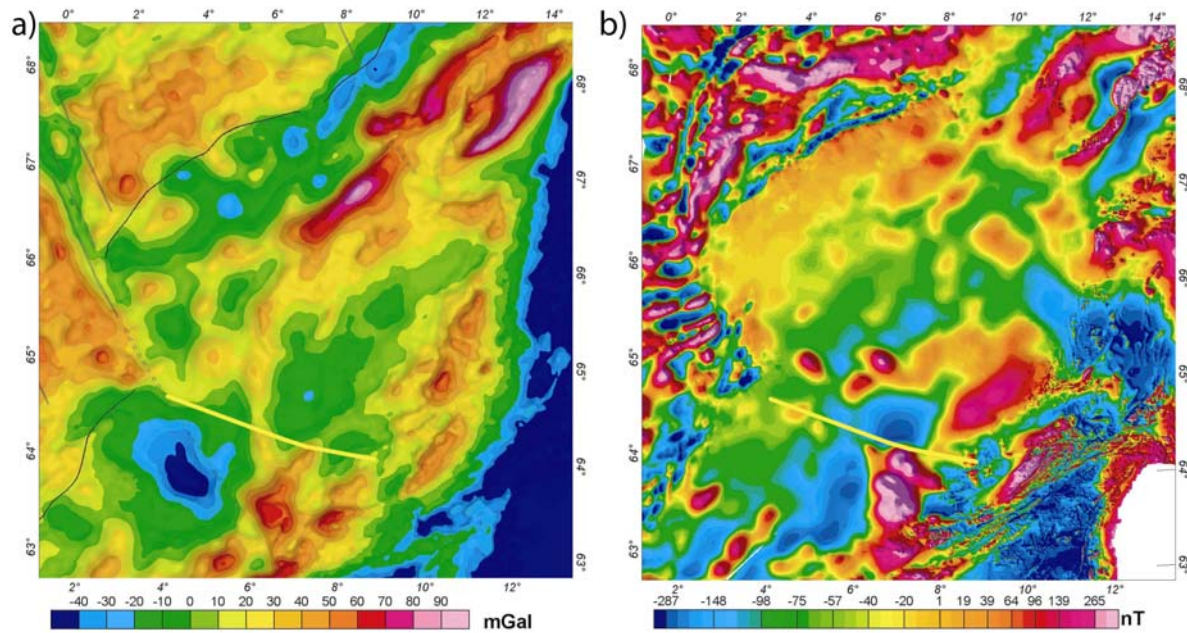

Figure 9.14. (a) Gravity anomaly, (b) Total magnetic field anomaly. (a) The gravity anomaly map is a combination of the free-air anomaly offshore and the Bouguer anomaly onshore (modified from Skilbrei et al. 2000). Offshore measurements of approximately 59,000 km of marine gravity profiles have been acquired by the Norwegian Petroleum Directorate, oil companies, and the Norwegian Mapping Authorities. In addition gravity data from satellite altimetry in the deep-water areas have been used (Andersen & Knudsen 1998). The surveys have been levelled using the International Standardization Net 1971 (I.G.S.N. 71) and the Gravity Formula 1980 for normal gravity. (b) The total magnetic field anomaly is referred to DGRF on the mid-Norwegian continental margin. Eight offshore aeromagnetic surveys have been processed and merged to produce the displayed map (Mauring et al. 2003, Olesen 2002, 2004).

9.4.1.1   3D Density and Magnetic Modelling

The 3D model consists of ~35 cross-sections with a spacing of 10-25 km (Fig. 9.15). The irregular distance between the cross-sections was chosen to provide good coverage of the main geological features and a good overlay with the OBS and seismic reflection profiles.

In addition to the density structure of the crust, which will be described in the reminder, the lithospheric mantle was modelled by assuming a stepwise increase (200K) in temperature from the Moho (c. 500°C) to the asthenosphere with a temperature of c. 1300°C., applying a thermal expansion factor of 3.2×10^{-5} K^{-1} (Breivik *et al.* 1999, Olesen *et al.* 2002, Fernàndez *et al.* 2004).
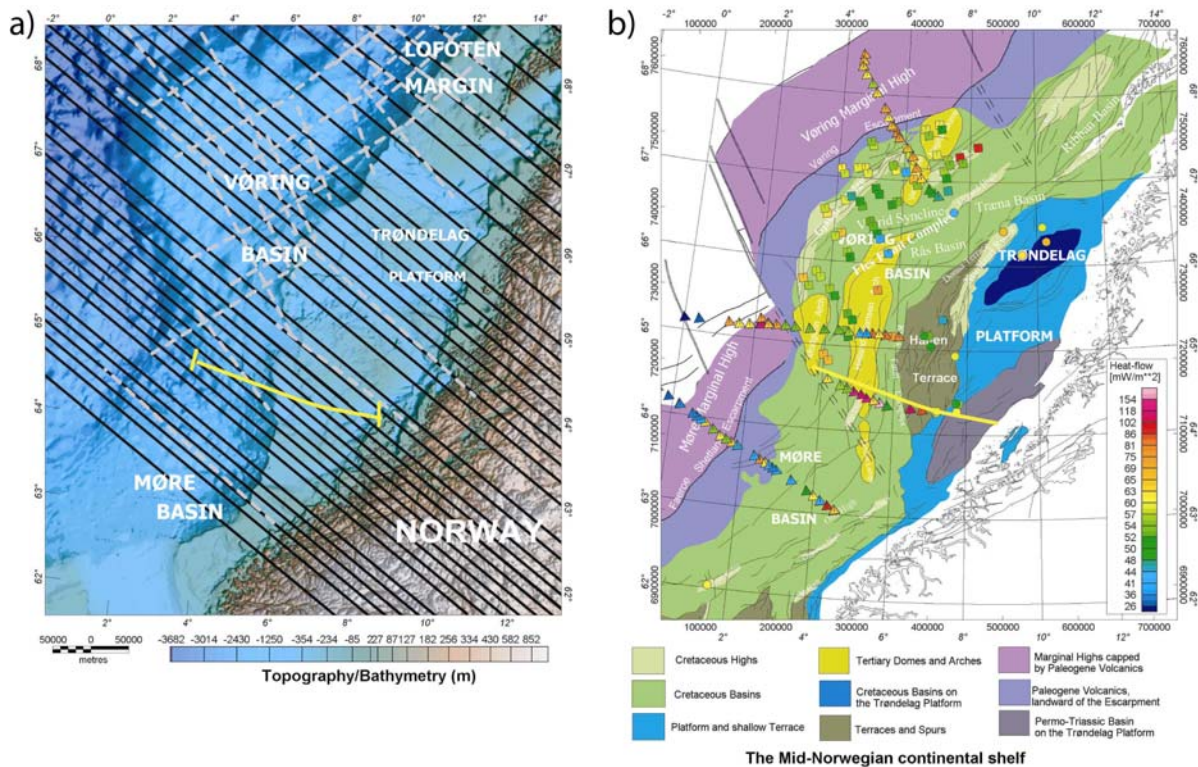
Figure 9.15. *(a) Bathymetry and (b) tectonic setting of the mid-Norwegian margin.(a) The bathymetric data are from a compilation by Dehls et al. (2000), based on satellite altimeter data released for the deep-water part of the study are, and data provided by the Norwegian Mapping Authority, Marine Department Stavanger for the shallow water areas. The black dotted lines in (a) mark the location of the OBS profiles (see Mjelde et al. 2005) for more details), while the thin black lines indicate the cross-sections of the 3D density model. The yellow line shows the location of the density/ magnetic model in Fig. 9.19 (b) Tectonic map after (Blystad et al. 1995) and offshore heat flow measurements.*

The two parameters most important for constructing the 3D density model are the geometry and the density of the structures. The densities used in the model process are based on published values (see Table 9.3), which are based on velocity-density relationships (e.g. Ludwig *et al.* 1970) and on density logs from exploration wells on the Nordland Ridge and Utgard High (e.g. Olesen *et al.* 2002). Table 9.3 provides an overview of the used values. The errors from the velocity-density relations on the applied densities are in the order of ± 0.05 Mg/m^3 and ± 0.1 Mg/m^3 for the upper basement and deep crustal layers, respectively.

Table 9.3   Densities of geological structures in the Norwegian Sea. Density values in Mg/m3. LCB: lower crustal body.

	Raum *et al.* 2002	Mjelde et al. 2001	Mjelde *et al.* 1998	Olesen *et al.* 2002	Fernàndez *et al.* 2004	this study
Water	1.03	1.03	1.03	1.03	1.03	**1.03**
Tertiary	1.95-2.25	1.9-2.15	1.95-2.2	2.2	2.2	**2.1**
Cretaceous Sediments	2.4-2.65		2.45-2.67	2.35-2.5	2.4-2.65	**2.3-2.6**
Upper Cretaceous	2.65			2.35	2.4	**2.3-2.4**
Lower Cretaceous				2.5	2.58	**2.45-2.55**
Pre Cretaceous	2.68-2.76	2.7-2.81	2.83		<2.6	**2.65-2.7**
Lower Volcanics /Sills		2.62-2.8				
Upper Volcanics		2.7-2.77			2.5	
Cont. Crust	2.82-2.84	2.82-2.9	2.7-2.95	2.75-2.95	2.65-2.95	
Basement						**2.7**
Lower Basement						**2.75-2.85**
Lower Crust						**2.95-3.0**
LCB	3.0-3.12	3.11-3.22	3.1-3.23	3.1	3.0	**3.1**
Mantle	3.3-3.34	3.33-3.36	3.33	3.25	3.2	**3.3**

The geometry of the models is based on the studies as described above. These studies constrained the internal geometries of the sedimentary succession, which reduced the uncertainties in the density modelling. Our new interpretation focuses further on the presence of basement structures (e.g. rotated fault blocks) and their correlation with gravity and magnetic signal.

The magnetic anomaly is modelled applying magnetic parameters to the density modelling. Hence, no detailed modelling of the magnetic anomalies has been performed, but rather a regional interpretation. The magnetic parameters we applied to the 3D model are listed in Table 9.4. The parameters are consistent with previous modelling studies in the area (Fichler *et al.* 1999, Skilbrei *et al..* 2002} and petrophysical measurements (Mørk *et al.* 2002).

The magnetic data will only reveal information for the part of the model, which has a present temperature below the Curie temperature. Rocks at higher temperatures will not show the ferromagnetic behaviour necessary to generate the discernible magnetic signal. The dominant magnetic material is regarded to be magnetite, which has a Curie temperature of 580 ºC (cf. (Hunt *et al.* 1995). The depth to the Curie temperature is

Table 9.4. Magnetic parameters applied in the 3D model. For more details see text.

	susceptibility in SI	Q-ratio
Water	0	0
Tertiary Sediments	0.002	0.4
Other Sediments	0.0003	0.5
Basement	0.005	0.5-0.7
Lower Basement	0.01-0.025	1.0-2.5
Lower Crust	0.005	1
LCB	0-0.005	1
Mantle	0	0

consistent with previous studies from the Lofoten area and the Vøring Basin (Fichler *et al.* 1999). The comparison between the Curie depth and the model shows that a contribution from mantle material can be largely excluded. Therefore a contribution to the magnetic anomalies by mantle material is not considered; the same is valid for the part of the lower crust and LCB, which are located at depths below the Curie temperature depth. The main magnetic material is expected to be in the basement (e.g. Fichler *et al.* 1999), while the overlaying sediments have only a small magnetic contribution. Susceptibilities of the basement can range between 0.001 and 0.025 SI (with Königsberg ratios between 1 and 4) while susceptibilities of the overlying sediments are in the order of 0.0003 SI (see also Table 9.4). The upper basement is supposed to be less magnetic than the lower basement, and as will be shown later, especially below the Trøndelag Platform high-magnetic basement at shallow crustal levels is observed related to the prominent gravity and magnetic anomaly. The main magnetic signature is therefore, caused by the changing geometry between the low- and the high-magnetic basement. The inclination and declination of all remanent fields is set to 77.0º and 0.5º, approximately parallel to the present magnetic field.

9.4.1.2   Interpretation of potential field data and structural maps

The gravity and magnetic modelling enables to construct maps of a variety of surfaces, which allow a discussion of some structural elements on the Mid-Norwegian margin.

Top basement
The map of the top crystalline basement (Fig. 9.16a) reveals a deepening from the coastal area towards the continental margin. The Trøndelag Platform features shallow depths (<9 km), while top basement in the Vøring Basin generally is encountered between 11 and 15 km. The top basement map shows a variety of local features, such as basement highs correlating with the Nyk and Utgard Highs. These structural highs reveal positive gravity anomalies. The depth to the crystalline basement is affected by the basin depth and

sediment thickness and the Tertiary domes, especially in the northern Vøring Basin (e.g. Naglfar Dome and Vema Dome). In the southern Vøring Basin the depth to the top basement is similar, but this area lacks prominent basement highs.

The Møre margin to the south also reveals a deep top basement (12-15 km) but the top basement map shows less local features. The East Jan Mayen Fracture Zone marks an approximately 100 km lateral step in the margin. However, the Jan Mayen Lineament is not a well-expressed tectonic feature. Structurally, the transition between the Vøring and Lofoten margins is more pronounced. Northeast of the Bivrost Lineament the top of the crystalline basement is located at a depth less than 10 km, and obviously reaches surface on the Lofoten Ridge and at the northern terminations of the Vestfjorden and Ribban Basins. The Bivrost Lineament is a major tectonic boundary marked by both vertical and horizontal offsets. The Utgard and Nyk Highs are suggested to be the southern continuations of the Lofoten Ridge and Røst High, respectively.
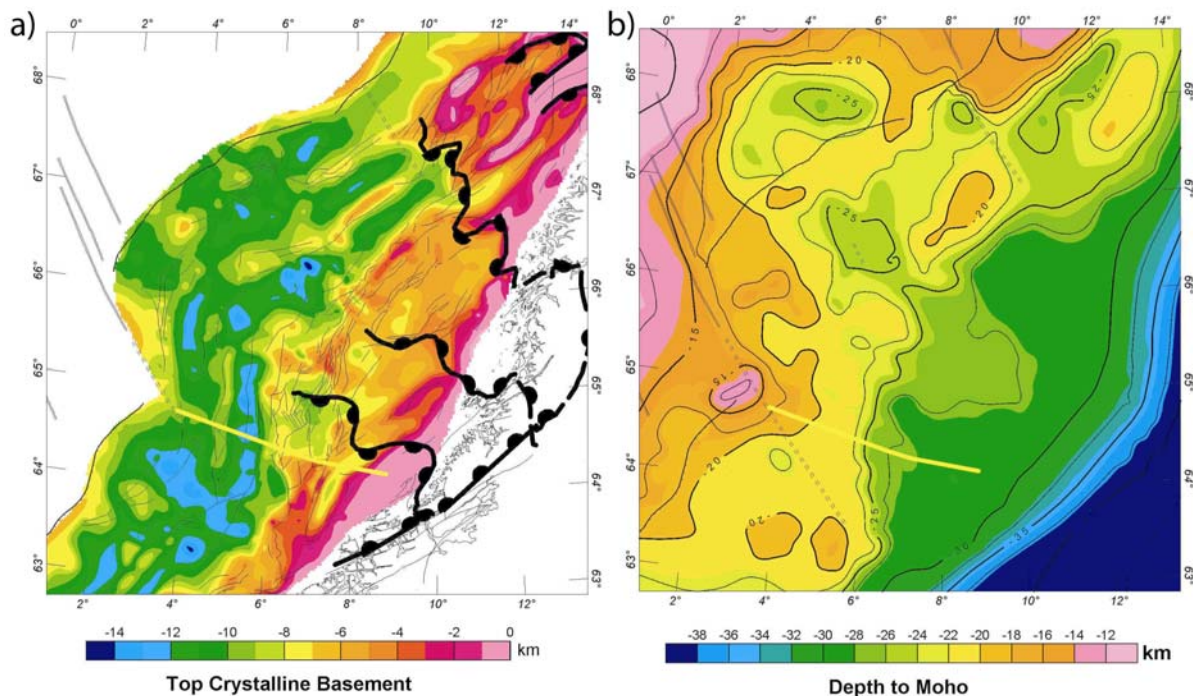
Figure 9.16. (a) Depth to top crystalline basement and (b) Moho Depth. The 3D density model based on seismic experiments and petrophysical data defined the horizons. See text for further details.

Depth to Moho

The depth to the Moho (Fig. 9.16b) is generally between 18 and 28 km. On the Møre margin the depth to the Moho deepens regularly from the coast to the margin, while the Moho depth of the Vøring and Lofoten margins varies more in relationship to local features. Overall the central Vøring margin is characterized by a pronounced deep Moho,

although the Utgard High is underlain by a shallow Moho, correlating to the shallow Moho below the Lofoten Ridge. Because the Lofoten margin is narrower than the Vøring and Møre margins the shallowing of the Moho is more abrupt.
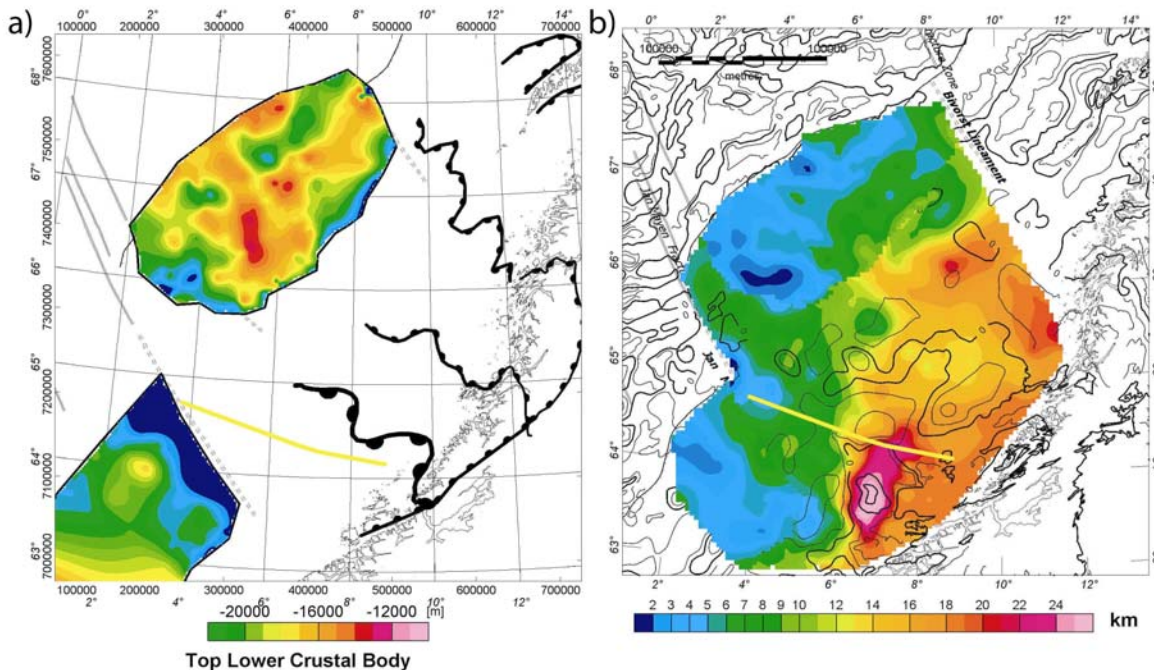
The lower basement

The combined seismic and potential field analysis (see below) shows that the lower basement is a key element in the potential field signals on the Mid-Norwegian margin, and especially on the Trøndelag Platform. The lower basement is defined to have densities >2.75 Mg/m^3 and higher magnetic properties than the uppermost basement. The comparison with the magnetic field anomaly shows that a good correlation exist for the Frøya High between the top of the lower basement and the shape of the main magnetic low (Fig. 9.17a). Also on the remaining part of the Trøndelag Platform a good correlation between the top lower basement and the magnetic anomaly exist. Even more obvious is the connection between the lower basement and the magnetic anomaly and the Trøndelag Platform on the lower basement thickness map (Fig. 9.17b). The area where the lower basement has a thickness of more than 11 km is roughly correlating with the extent of the Trøndelag platform. The thickness of the lower crust and basement is also correlating surprisingly well with the shape of the magnetic anomaly. However, while the shape of the two correlate, the correlation for the amplitudes is less obvious. The Frøya High is clearly connected to a thick basement. However the upper, less magnetic basement is thickening in the north and therefore the lower basement is "only" 12 km thick. However, the shape of the relatively thin lower basement area is correlating with the magnetic high. Here the lowermost basement is thickening and the amplitude of the magnetic anomaly is only up to +100 nT. Consequently, our analysis allows arguing that the relatively magnetic quietness on the outer Vøring margin is mainly related to the missing of lower high-magnetic basement.

The lower crustal body and the lower basement

A high-density and high-velocity body is located at the base of the crust below large portions of the outer parts of the Mid-Norwegian margin. This lower crustal body (LCB) has a density of around 3100 kg/m^3 and velocities > 7 km/s. The extension of the LCB has been mapped in a series of studies (e.g. Mjelde *et al.* 2005; Ebbing *et al.* 2006). While the origin of the LCB remains disputed, its presence is unarguably. For a thorough discussion see Ebbing *et al.* (2006). We consider the LCB to have in general different petrophysical properties than the lower basement. Therefore, we can remove the portion of the LCB (Fig. 9.18a) from the thickness of the lower basement (Fig. 9.17b) to calculate the pure lower basement thickness.
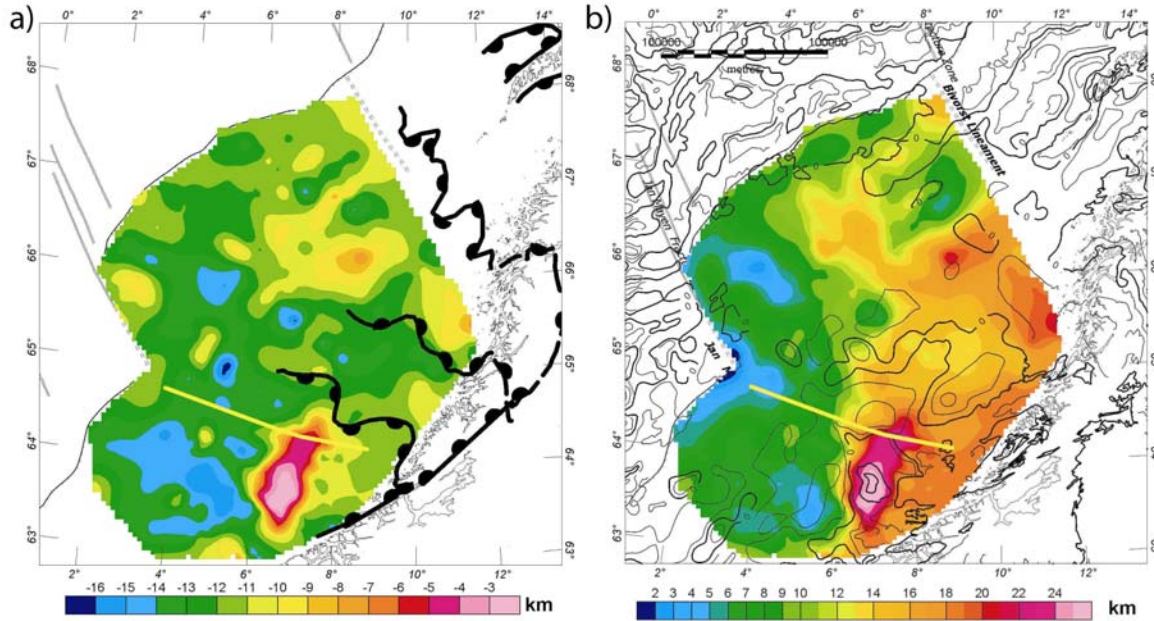
Figure 9.17. *(a)Depth to the lower basement. The lower basement is defined to have densities*
>2.75 Mg/m³, compared to upper basement densities of 2.7 Mg/m³. (b) Thickness
lower basement. The thickness is the difference between the top lower basement and
the Moho. The contour lines show the total magnetic field anomaly from Fig. 9.14
(contour distance 100 nT). The lateral extend of the lower basement is given by the
*extent of the 3D density model.*

Figure 9.18. *(a) Thickness of LCB. (b) Thickness lower basement- LCB. The thickness is the*
difference between the top lower basement and top LCB/ Moho. The contour lines
show the total magnetic field anomaly from Fig. 9.14b (contour distance 100 nT).
The lateral extend of the lower basement is given by the extent of the 3D density
model.

99

The correlation of the thickness of lower basement and the magnetic anomaly is now even clearer. This is indicating that the geometry and thickness of the lower basement is the main element controlling the magnetic anomaly on the Mid-Norwegian margin. The Frøya High is an effect of very shallow lower highly-magnetic basement and the general presence of a thick magnetic basement. The thickness on the outer Vøring margin is significantly reduced and the magnetic anomaly field is relatively quiet.

9.4.1.3   <u>Gravity and magnetic response along a transect crossing the Trøndelag Platform</u>

The transect for the combined density/magnetic and thermal modelling is located on the southernmost part of the Vøring Margin, crossing from the Modgunn Arch over the Helland Hansen Arch and Klakk Fault Complex into the Halten Terrace and Froan Basin. The line location was chosen, as we have good constraints by the seismic lines GMNR94-104 and MNT88- 08 and coverage from offshore heat flow measurements (Fig. 9.15). Additional constraints are given by OBS lines 9 and 14 of (Raum *et al.* 2002) and the western end is near to the OBS line L2003-3. The gravity anomaly along the profile is varying between +/- 20 mGal and is showing no prominent anomalies. Thus, the signal merely reflects the sediment thickness and the geometry of the Moho. The deepening of the Moho is somewhat compensated by thickening of the lower crust (and thinning of the sediments). The geometry of the western extension of the lower crust can be associated with a fault block. This line location takes also advantage of a thin or absent LCB. Therefore, we can directly study the influence of the basement architecture on the thermal structure and do not have to consider mechanisms for the evolution of the LCB.

Seismic interpretation of the top basement is consistent with the source depth estimates using Euler Deconvolution (Osmundsen *et al.* 2006). However, the gravimetric interpretation shows a smoother, shallower surface due to the increased density contrast between the lowermost sediments and the basement. The seismic interpretation further points to a structure in the lower crust below the Cretaceous basin to the east (Osmundsen *et al.* 2006). In the applied velocity model this structure has a velocity of 7.0 km/s, similar to the Lower Crustal Body (LCB) interpreted on the central and northern outer Vøring margin (e.g. Mjelde *et al.* 2005). In the density model and the OBS models this structure has no correlation. The thickness is assumed to be in general in the order of 1-2 km (maximum 4 km). Therefore, the structure might be too small to be clearly observed on the OBS lines and the LCB may extend from the central Vøring to the northern Møre margin. If present, the LCB is a continuous feature on the outer Norwegian margin. Below the Trøndelag platform the lower basement can be observed at a shallow depth, cross-cutting the normal upper basement.
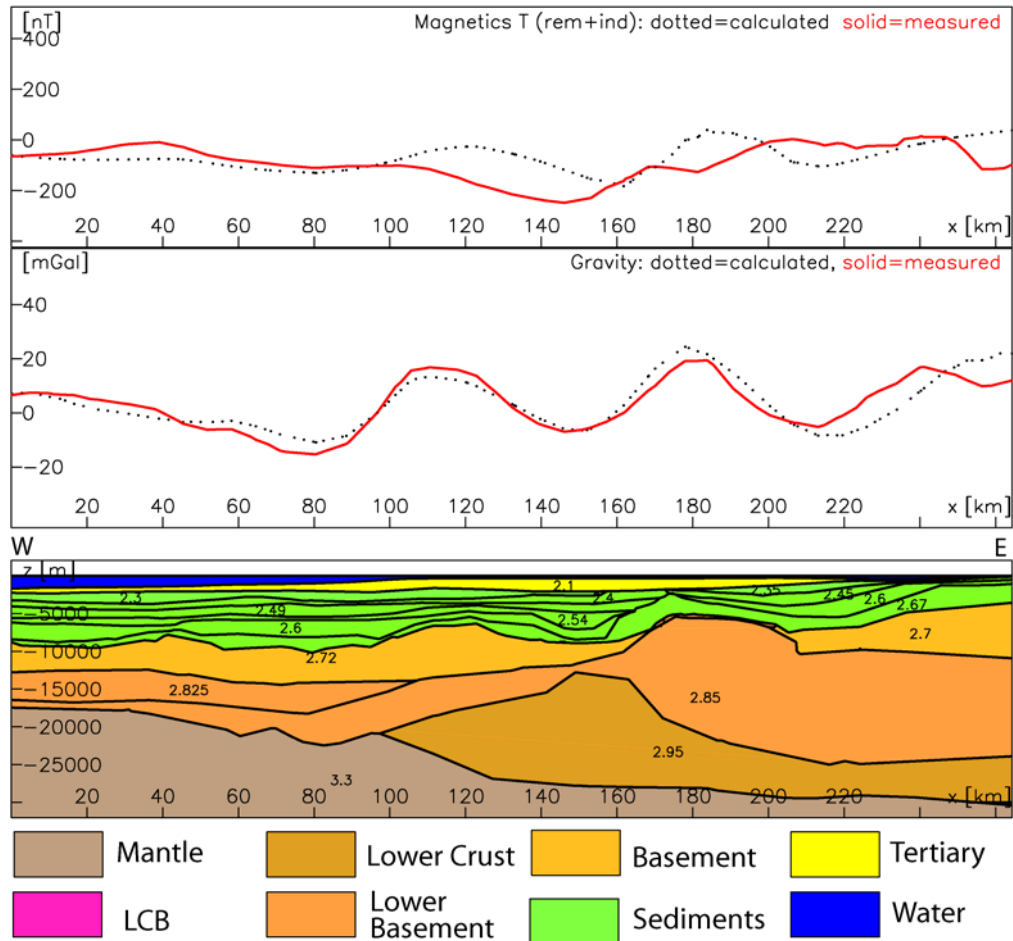
Figure 9.19. ***A transect along the seismic lines GMNR94-104 and MNT88- 08 through the 3D model on the Vøring margin (taken from Osmundsen et al. 2006). The upper panel shows the magnetic anomaly, the middle panel the free-air anomaly. The lower panel shows the modelled density cross-section. Black numbers are density values in Mg/m³ and magnetic properties as explained in Table 9.2 and text. LCB: lower crustal body. See Fig. 9.15 for exact location of the section and text for further details.***

9.4.2 2D thermal modelling

The profile shown in Fig. 9.19 was selected for the thermal modelling. This profile presents the advantage of being the prolongation of the Central Scandinavia Profile (see Section 1.2) on the Norwegian margin. Selected parameters for the modelling and the adopted geometry are given in Fig. 9.20. Heat generation values were inferred from onshore measurements assuming that the high magnetic basement corresponds to Precambrian terrains whereas the low magnetic one is associated to Caledonian nappes.
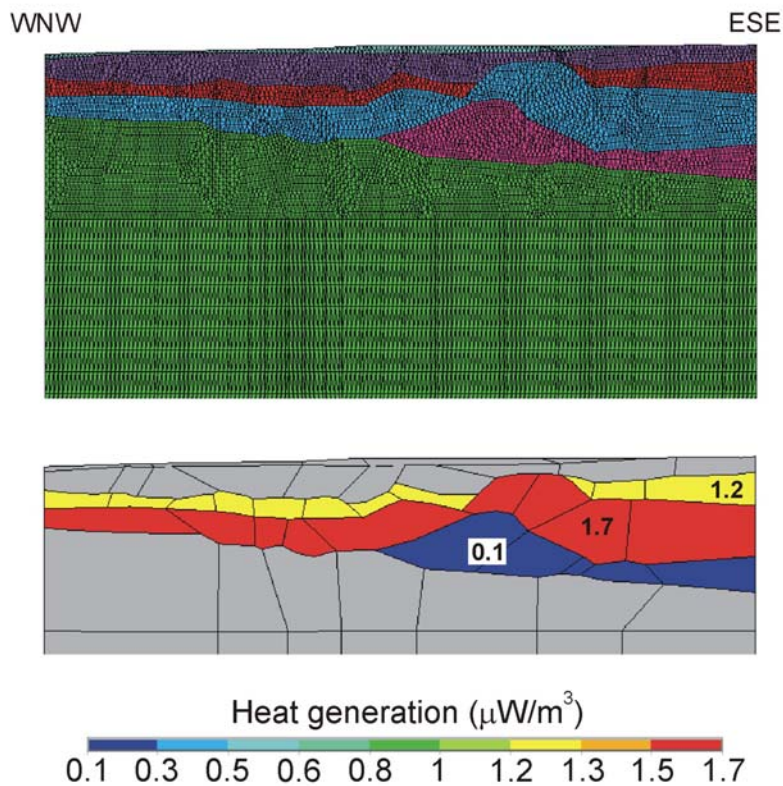
Figure 9.20. Finite element mesh and heat generation values used for the thermal modelling of the Norwegian Margin Profile (see Fig. 9.19). Used heat generations for each crustal unit are indicated. Heat generation in the sediments is assumed to be negligible. Conductivities are 1.5, 2.5 and 3.5 W/m/K for Plio-Pleistocene wedges, the crust and the mantle respectively. Boundary conditions are T=0°C at the top and basal heat flow is varied (see text) (VE:x2).

In the present case, we ran two different models with contrasting boundary conditions at their base. For the first model (Fig. 9.21 left panel), we assumed a flat lithosphere base or alternatively a constant Moho heat flow of 40 mW/m^2. This first model represents the most conservative one in absence of firm constraints on surface heat flow values. The modelling results in high Moho temperatures (i.e. ~700°C) close to the onshore below the Trøndelag Platform and a relatively steep slope for the isotherms dipping towards the ocean. Predicted surface heat flow values range in between ~50 to ~70 mW/m^2, the highest values being computed for the Trøndelag Platform.

For the second model, we assumed that the basal heat flow increases gradually from 25 (i.e. cratonic basal heat flow) to 50 mW/m^2 (i.e. old oceanic basin) when travelling from onshore towards the oceanic domain. This model results in lower Moho temperatures, in particular below the Trøndelag Platform (i.e. 600°C). The computed isotherms are almost flat. Interestingly, surface heat flow values vary now in between ~50 and ~65 mW/m^2 and show an uneven distribution that is strongly controlled by the structure of the crust.
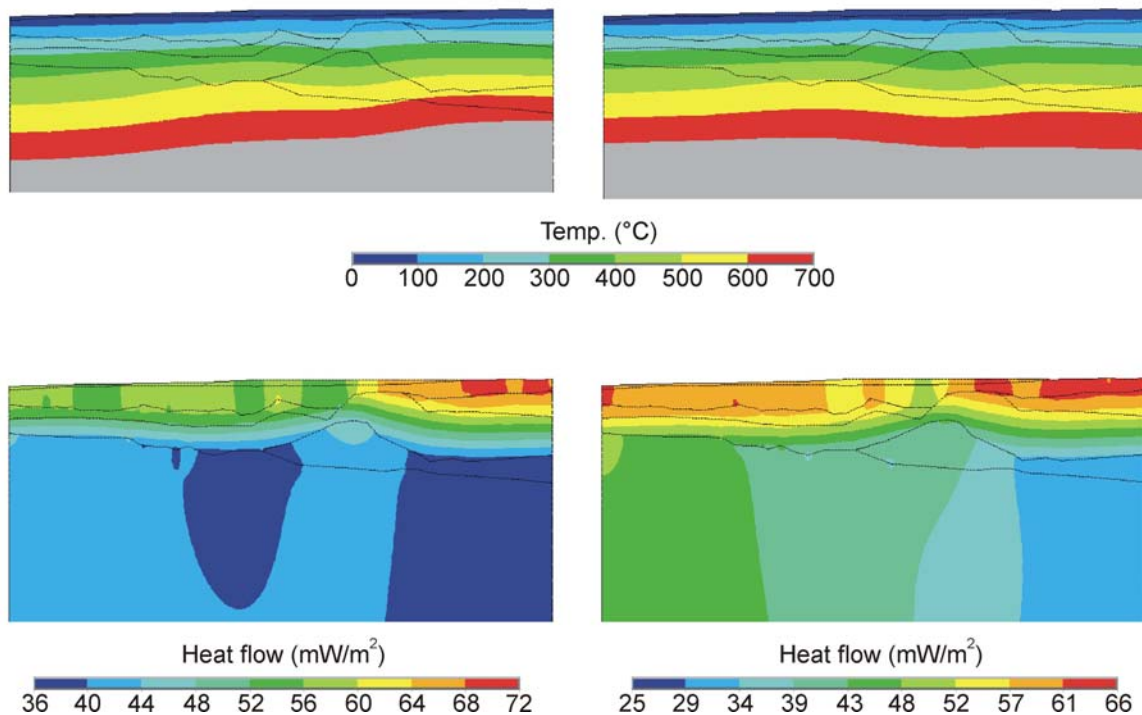
Figure 9.21. Computed temperature and heat flow values for the Norwegian Margin Profile. VE:x2.

9.5   Status - compilation of basement structure map

A basement structure map of mainland Norway and adjacent sea areas represents one of the planned products of the Kontiki Project. The basement depth surface constitutes an important horizon in a complete 3D crustal model. Ebbing & Lundin (2005), Olesen (2005) and Skilbrei (2005) compiled depth to crystalline basement maps from the North Sea, Norwgian Sea and the Barents Sea, respectively for the previous Kontiki Report (Olesen et al. 2005).

Aeromagnetic and gravity data (Figs. 10.6 & 9.22) found a significant basis for mapping crustal structures both on mainland Norway and in the adjacent offshore regions. Fig. 9.22 shows the isostatic residual of the Bouguer gravity data from western Scandinavia based on gravity compilations by Skilbrei *et al.* (2000) and Korhonen *et al.* (2002a). Negative and positive anomalies on the continental shelf reflect to a large extent sedimentary basins and structural highs, respectively. The structural highs on the mid-Norwegian shelf contain high-density and highly magnetised rocks of assumed lower crustal origin and have been interpreted to represent reactivated core complexes (Osmundsen *et al.* 2002, Olesen *et al.* 2002, Skilbrei *et al.* 2002). Fig. 9.23 shows the spatial relationship between core complexes, low-angle detachments and the Transscandinavian Igneous Belt (TIB). The lower crustal rocks were exhumed along the low-angle detachments during a late phase of the Caledonian orogeny (Osmundsen *et al.*

2002). It is important to realise that similar core complexes were formed in northern Fennoscandia in the Proterozoic (Fig. 9.23). They are usually referred to as gneiss domes (e.g. Lindroos & Henkel 1978, Midtun 1988, Henkel 1991, Olesen & Sandstad 1993) and are characterized by positive gravity and aeromagnetic anomalies similar to the younger core complexes in mid-Norway. The gneiss domes in northern Fennoscandia were most likely formed during a gravity collapse of the Proterozoic orogen that formed subsequent to continent-continent collision along the Levajok Granulite Belt (Fig. 9.23).

We have for the present Kontiki report compiled a basement structure map of northern Norway (Fig. 9.24) based on published maps by Henkel (1991), Olesen et al. (1990, 2002) and Osmundsen *et al.* (2002). The basement consists partly of Precambrian rocks, such as granites, gneisses and amphibolites, and partly of Caledonian nappes. The basement depths offshore Finnmark represent mostly Precambrian basement, since the Caledonian nappes on the mainland of Finnmark constitute mostly low-magnetic metasediments. The basement depths in the Norwegian Sea (Nordland area) are on the other hand based on a combined interpretation of magnetic and gravity data and will mostly represent depths to crystalline basement, that is composed of both Precambrian and Caledonian rocks. We plan to compile a basement structure map of southern Norway containing depth to Precambrian basement and the main structural elements such as shear zones and detachment zones. The final Kontiki report will contain a complete compilation of basement structures of mainland Norway and adjacent sea areas south of 71ºN. There will most likely be difficulties in distinguishing depths to crystalline basement from depth to Precambrian basement in parts of the offshore areas. We will have to take this into account when designing the final map layout.
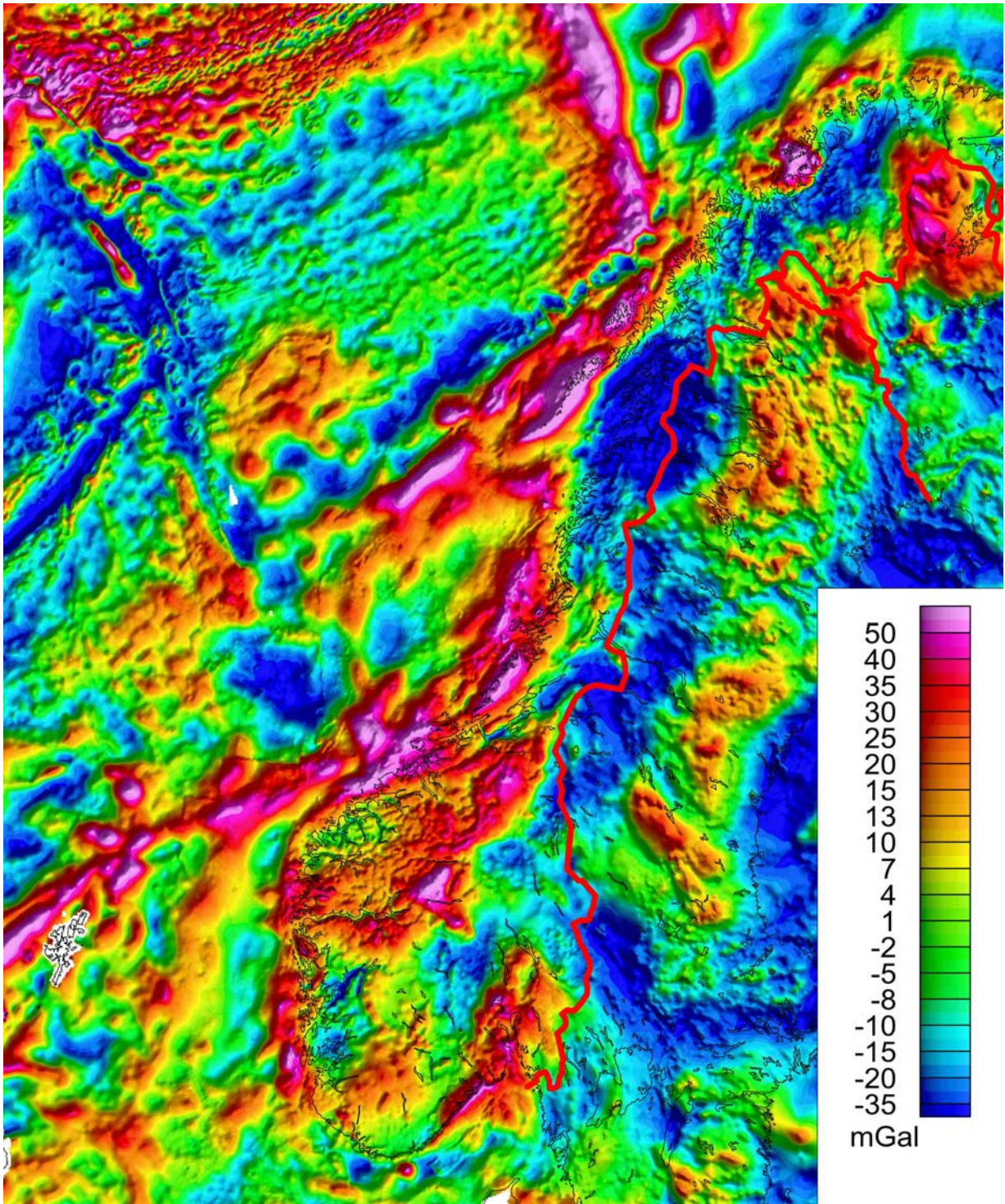
Figure 9.22. Isostatic residual of Bouguer gravity from western Scandinavia - based on gravity compilation by Skilbrei et al. (2000) and Korhonen et al. (2002a).
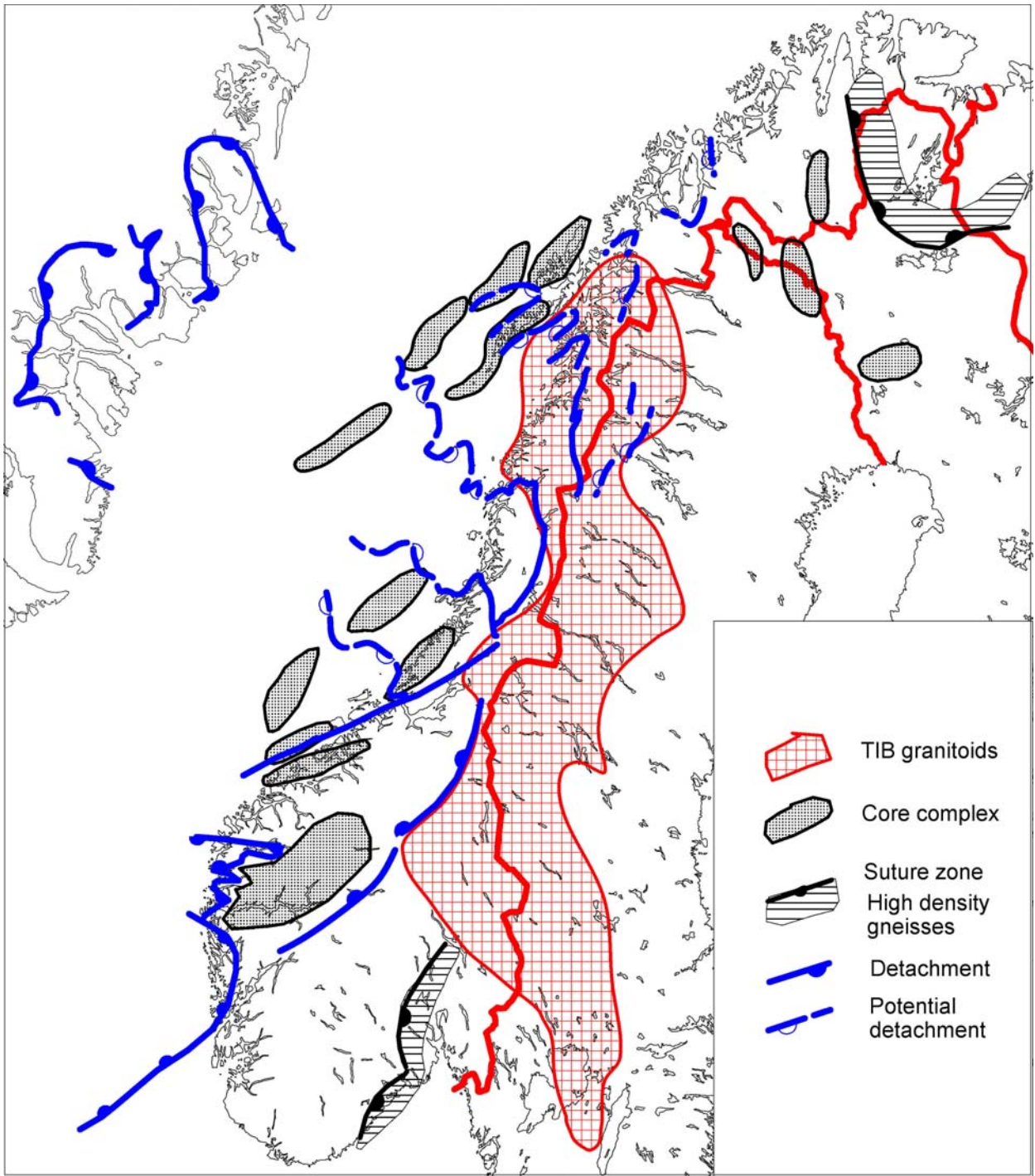
Figure 9.23. Regional structures compiled from interpretations of potential field data and bedrock mapping (Hartz et al. 2002, Olesen et al. 2002, Osmundsen et al. 2002 and Skilbrei et al. 2002). Greenland is rotated back to pre-opening of the Atlantic in the Eocene.
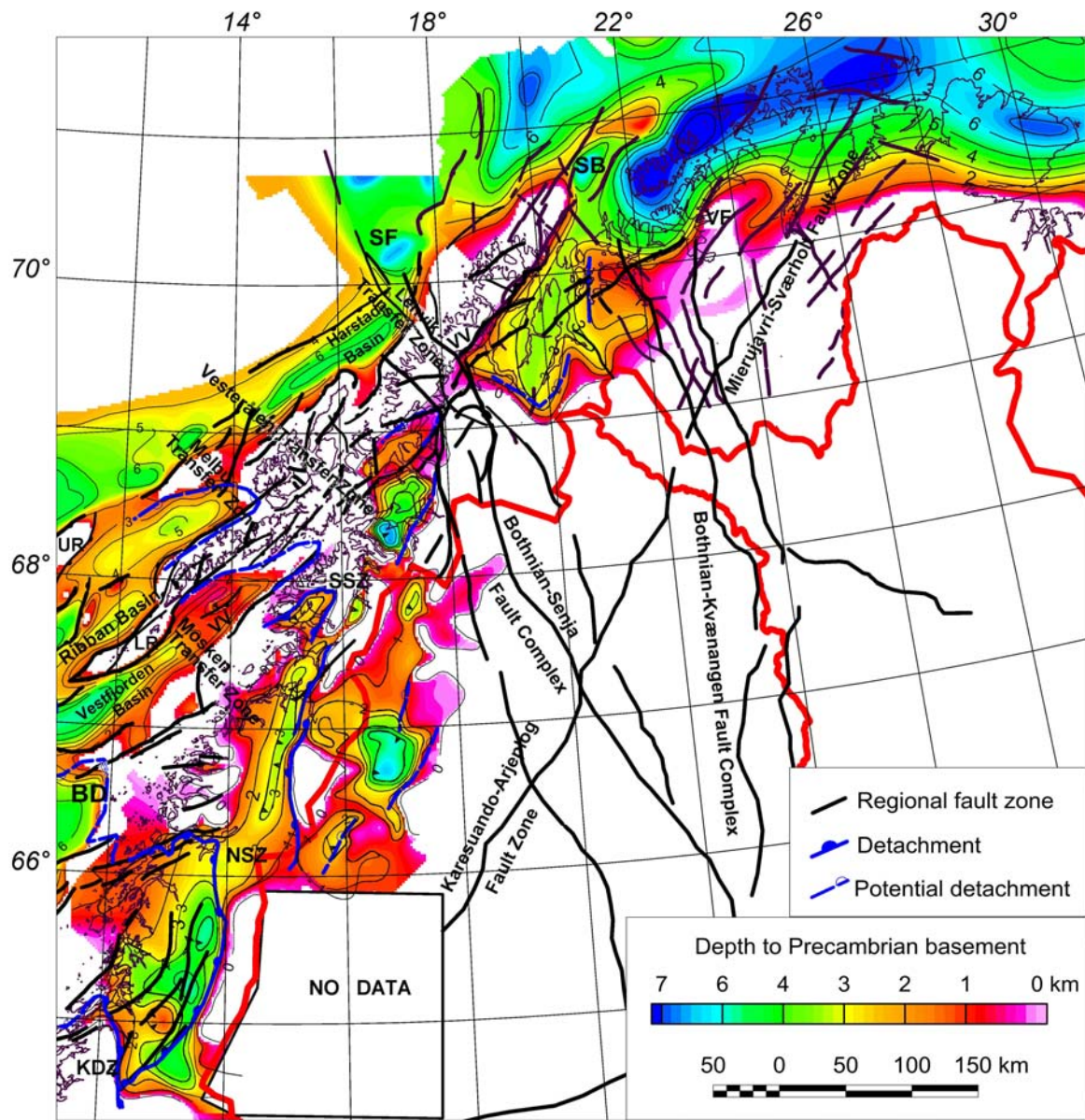
Figure 9.24. Basement structure map from northern Norway compiled from Henkel (1991), Olesen et al. (1990, 2002) and Osmundsen et al. (2002). BD – Bivrost Detachment, KDZ – Kollstraumen Detachment, LR – Lofoten Ridge, NSZ – Nesna Shear Zone, SB – Sørvær Basin, SF – Senja Fracture Zone, SS – Sagfjord Shear Zone; UR – Utrøst Ridge, VF – Vargsund Fault, VV – Vestfjorden-Vanna Fault Compex.

9.6 Discussion and conclusion

The presented 2D models for the central Scandinavian mountains, Mid-Norwegian margin and Oslo Graben show clearly the influence of crustal geometry on the present thermal structure and observed heat flow. For all the areas 3D thermal modelling is beneficial for future studies. However, the feasibility of constrained 3D thermal modelling is not only dependent on the geophysical constraints, but also on surface measurement on heat flow (Slagstad 2005) and radiogenic heat production (Chapter 2 in present report).

For the Central Scandinavia thermal modelling is indicating that the granitoids of the TIB are only present in the upper crust or are less heat-productive with increasing depth. However, the TIB is clearly influencing the isostatic state of the Scandinavian mountains, especially for the northern and central part, and might be related to the Neogene uplift of the Scandinavian mountains. It is important to complete the heat flow database of the Norwegian mainland for correlations with topography and uplift data.

For the Oslo Graben the modelled moderate and short-wavelength variations in surface heat flow are mainly the result of the uneven distribution of the different lithological units at relatively shallow depths. Here, the heat-productive rocks are not buried below thick sediments and therefore the near-surface structures control the observed heat flow. The influence of deep crustal intrusives is less important

Our calculations for the Mid-Norwegian margin show that the influence of different basement lithology might be overprinted by the basal heat flow. Only in the case with a varying basal heat flow the surface heat flow is strongly controlled by the structure of the crust. Here, more effort has to be spent on investigating the change of basal heat flow from the continent-ocean boundary towards the mainland. Correlation with seismic tomography might assist this interpretation as well as detailed analysis of deep crustal structures on the Mid-Norwegian margin (correlation between LCB and basal heat flow?).

10   AN ATTEMPT TO ESTIMATE THE DEPTH TO THE CURIE TEMPERATURE FROM AEROMAGNETIC DATA

Laurent Gernigon, NGU

10.1 Introduction

Estimation of source depths from analysis of crustal magnetic anomalies has always been a tricky problem with ambiguous solutions. The deepest boundary of the Earth's magnetic crust may have two alternate interpretations. It may suggest a crustal interface; generally characteristic of areas with normal or low heat flow. The second possibility may be that at such depths rocks loose their ferromagnetic properties, as in young crust and geothermal regimes where heat flow is large. In the second case, the interface could be interpreted as the Curie isotherm depth. However, the interpretation of the computed depth of the interface as Curie isotherm needs careful data analysis and logical inference from other considerations such as heat flow and history of the concerned area. In this study, we rather refer to the depth of the deepest magnetic source (DDMS) to avoid any controversies.

Several techniques have been used in the past to estimate Curie temperature depth from aeromagnetic survey. One commonly used technique is to estimate the average source depth as half the decay rate of logarithmic power spectrum from gridded data (Bhattacharyya 1964, Spector & Grant 1970, Connard *et al.* 1983, Blakely 1996, Naidu and Mathew 1998). Surprisingly, nobody in the scientific literature has tested this method offshore Norway. In this chapter, we applied the spectral method along the mid-Norwegian margin and adjacent areas in order to test the validity of the technique.

10.2 Curie temperature and crustal nature

The Curie temperature is a term in physics and material science named after the French Pierre Curie (1859-1906), and refers to a characteristic property of a ferromagnetic material. The Curie temperature of a ferromagnetic material, is the temperature where the material looses its characteristic ferromagnetic ability: the ability to possess a net and spontaneous magnetization in the presence of an external magnetic field.

In a geological setting, major sources of magnetic anomalies are often basaltic, mafic or ultramafic igneous rocks. Minerals like titanomagnetite are usually the most common magnetic minerals in mafic igneous rocks. The Curie temperature for this mineral is about 580° C (Shuey *et al.* 1977, Blakely 1996). Byerly & Stold (1977) suggest also that Curie temperatures could be less for felsic plutonic rocks and could range form 400°C to

550°C. The level between the 400 and 600°C isotherms could accordingly represent the Curie windows for most of the crustal rocks

10.3 Power spectrum and filtering sequences: general theory

The general topic of the frequency (or wave-number) domain theory for magnetic field data was developed in detail by Allan Spector in his Doctoral thesis submitted to the University of Toronto titled "Spectral Analysis of Aeromagnetic Data" (Spector & Grant 1970). Much of the formal theories developed afterwards in later publications are taken somewhat directly from his text. Spectral methods to estimate the depth extent of magnetic sources have been used in the last 30 years and have showed both encouraging but as also controversial results. Various papers (Connard *et al.* 1983, Shuey *et al.* 1977, Naidu & Mathew 1998) illustrate geological implication of the spectral methods to define the Curie temperature. They have all used the shape of radially averaged spectra to estimate the depth extent of magnetic sources.

For the purpose of analysing aeromagnetic maps, the ground is assumed to consist of a number of independent anomalies, characterised by a joint frequency distribution in depth width, length and direction cosines of magnetisation. The aim of the spectral methods is to separate the effects of each ensemble in the aeromagnetic map.

No attempt will be made here to present rigorously the equations presented. In fact, we have tried to present a simple synopsis of the theory and workflow use during his study. For more details about the physical and mathematical expressions of the power spectrum analysis we rather refer to (Bhattacharyya 1964, Spector & Grant 1970, Blakely 1996, Naidu & Mathew 1998).

10.4 Database

The spectral methods have been applied to the more recent grid compilation undertaken by NGU (Olesen *et al.* 2006). The more recent surveys SAS-96, VGVB-94, MBAM-97, VAS-97, VBE-AM-00, RAS-03 and JAS-95 are also included in the new data compilation. Specifications for these surveys are shown in Table 10.1. The grid onshore Norway has previously been digitised into a 500x500 m matrix from manually drawn contour maps and the Definite Geomagnetic Reference Field (DGRF) has been subtracted. The mainland area was flown at different flight altitudes and line spacing dependent on the topography. The 5 x 5 km grids were regridded to 500 x 500 m cells before the final merge with the regional compilation, using the minimum curvature GRIDKNIT software from Geosoft (2005).

Table 10.1. Offshore aeromagnetic surveys compiled for the present study (Olesen *et al.* 2006). CGG - Compagnie Générale de Géophysique; GEUS – Geological Survey of Denmark and Greenland; NOO - Naval Oceanographic Office; NGU – Geological Survey of Norway; NPD – Norwegian Petroleum Directorate; NRL - Naval Research Laboratory

| Year	Area	Operator	Survey name	Sensor elevation m	Line spacing km	Length km
1969	SW Barents Sea	NGU	NGU-69	200	4	26.200
1970	SE Barents Sea	NGU	NGU-70	200	4-8	22.800
1971	Viking Graben	Fairey	Fairey-71		2	11.100
1973	Vøring Basin	NGU	NGU-73	500	5	35.000
1972	North Norwegian-Greenland Sea	NRL (Vogt *et al.* 1979)	NRL-72	300	7.5	38.500
1973	South Norwegian-Greenland Sea	NRL (Vogt *et al.* 1979)	NRL-73	300	10 (20)	50.600
1973	Denmark Strait	NOO (Vogt *et al.* 1980)	NOO-73	160	5.5	60.400
1974	Norwegian Sea, east of Iceland	NOO	NOO-74a	160	10	5.500
1974	Norwegian Sea, SE of Iceland	NOO	NOO-74b	160	10	2.000
1974	NE Atlantic, south of Iceland	NOO	NOO-74c	160	5	22.200
1974	Norwegian North Sea	NGU	NGU-74	500	2-7	23.000
1975	Norwegian North Sea	NGU	NGU-75	500	1-6	19.000
1976	Jan Mayen Ridge	CGG/NPD	CGG-76	700	5	11.600
1979	East Greenland shelf	GEUS	GEUS-79	600	8	63.500
1983	Greenland Sea	NRL	NRL-83	300	20	13.000
1984	SW Barents Sea	CCG	TAMS-84	200	2	11.800
1985	SW Barents Sea	CCG	BAMS-85	200	4	16.900
1985	S of Faroe Islands	NOO	NOO-85	230	3	18.100
1986	Trøndelag Platform	Hunting	Hunting-86	200	2	57.000
1987	Vøring Plateau	NOO	NOO-87	230	5	16.900
1987	NW Barents Sea	NGU	BSA-87	250	4-8	34.000
1988	Spitsbergen	NGU	SPA-88	1550	5.5	13.300
1989	Lofoten	NGU	LAS-89	250	2	30.000
1991	Svalbard	Amarok/TGS-Nopec	SVA-91	900	7.5	27.800
1993	N. Viking Graben	NGU	Viking-93	150	0.5-2	28.000
1993	Hel Graben- Nyk High	World Geoscience	SPT-93	80	0.75	19.000
1994	Vøring Basin	Amarok/TGS-Nopec	VGVB-94	140	1-3	31.800
1994	Nordland Ridge-Helgeland Basin	NGU	NAS-94	150	2	36.000
1994	S. Viking Graben	Amarok/TGS-Nopec	VGVG-94	160	0.2	44.800
1996	Skagerrak	NGU	SAS-96	150	2	42.000
1997	Møre Basin	Amarok/TGS-Nopec	MBAM-97	220	1-2	46.600
1998	Vestfjorden	NGU	VAS-98	150	2	6.000
2000	Vøring Basin	TGS-Nopec	VBE-AM-00	130	1-4	17.300
2003	Røst Basin	NGU	RAS-03	230	2	30.000
2005	Jan Mayen FZ	NGU	JAS-05	230	5	32.600

10.5 Calculation of the power spectrum and estimation of the deepest depth of the magnetic source (DDMS)

The first thing that one should do to evaluate the DDMSs is to calculate the power spectrum of a sampled magnetic grid. The following filtering sequences have been led using the Oasis Montaj Magmap filtering toolbox (Geosoft 2005).

The processing sequence includes:

Step 1: The sampling of sub-magnetic grid extracted from the main magnetic compilation. Most of the time we considered square windows as complex shapes introduced filtering artefacts during the processing.

Step 2: The preparation of the initial grid. Before transforming the grid to the wavenumber domain by forward fast Fourier transform (FFT), the grid must be prepared in order to be perfectly square, without dummies and to have the right dimensions acceptable for the FFT (Fig. 10.1). During this preparation, the first order trends from the grid are removed in order to avoid the introduction of large step function and ringing problem during the Fourier domain transformation.
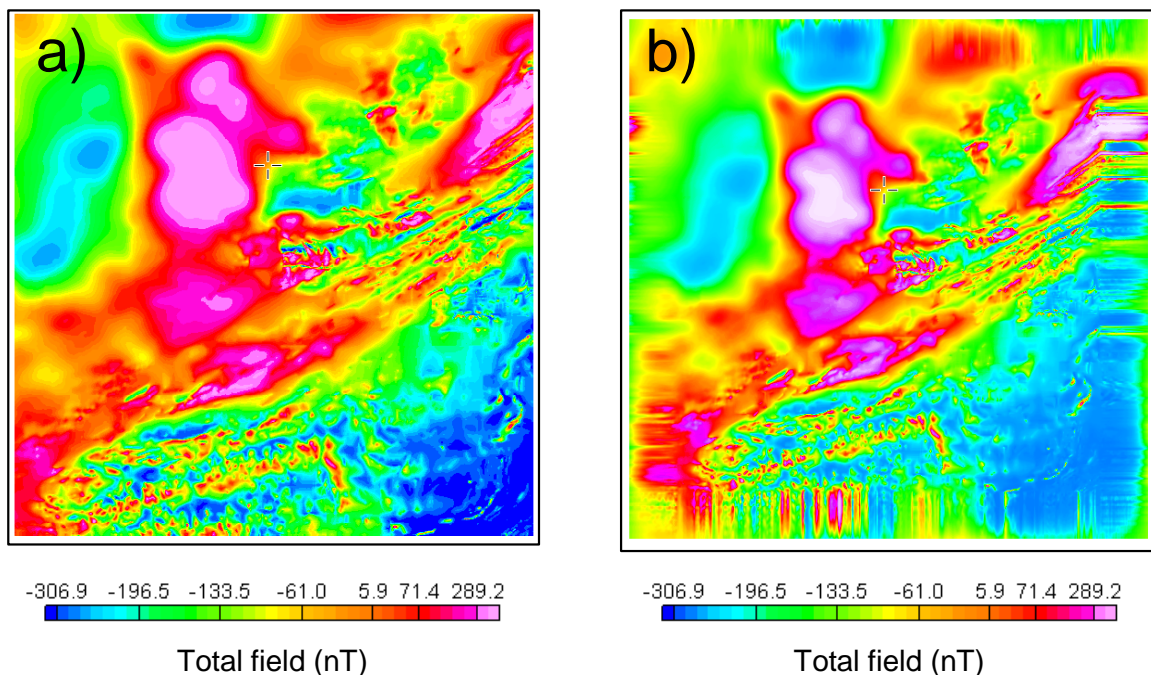
Figure 10.1 a) An example of an initial sampled grid around Trondheim, Norway and b) the same dataset after grid preparation

Step 3: The wave-number domain processing to get the frequency domain representation of the magnetic signal. Fourier theory states that any signal, in our case the magnetic signature, can be expressed as a sum of a series of sinusoids. In the case of the magnetic, these are sinusoidal variations in total field across the sampled grid. This sinusoidal magnetic pattern can be captured in a single Fourier term that encodes: 1) the spatial frequency, 2) the magnitude (positive or negative), and 3) the phase. These three values capture all of the information of the magnetic grid. The spatial frequency is the frequency across space (latitude, longitude in our case) with which the amplitude modulates.

The initial grid in space domain is transformed to a wavenumber domain by the use of a fast Fourier transform (FFT) algorithm. A Fourier transform encodes not just a single sinusoid, but a whole series of sinusoids through a range of spatial frequencies from zero (i.e. no modulation, i.e. the average amplitude of the whole grid) all the way up to the "Nyquist frequency", i.e. the highest spatial frequency that can be encoded in the magnetic grid, which is related to the resolution, or size of the pixels $[(2*\text{cell size})^{-1}]$.

The significant point is that the Fourier image encodes exactly the same information as the initial grid, except expressed in terms of amplitude as a function of spatial frequency, rather than magnetic amplitude as a function of spatial displacement. An inverse Fourier transform of the Fourier image produces an exact replica of the original grid.

Step 4: The calculation of the radially averaged power energy spectrum using a 2D function of the energy relative to wavenumber and direction. The radially averaged energy spectrum is then computed by averaging the power energy (=the square of the Fourier amplitude spectrum) at all direction for the same wavenumber. As it turns out, we can learn something about the contribution of the long and short wavelengths in the spectrum by studying the spectrum itself.

Once the processing is completed, thee power spectrum is usually presented in one of two forms, a radially averaged plot in log-linear space for presentation in graph form or as a grid displayed either as a contour plot or an image. Fig. 10.2a displays the power spectrum as an image and Fig. 10.2b displays the power spectrum as a graph.
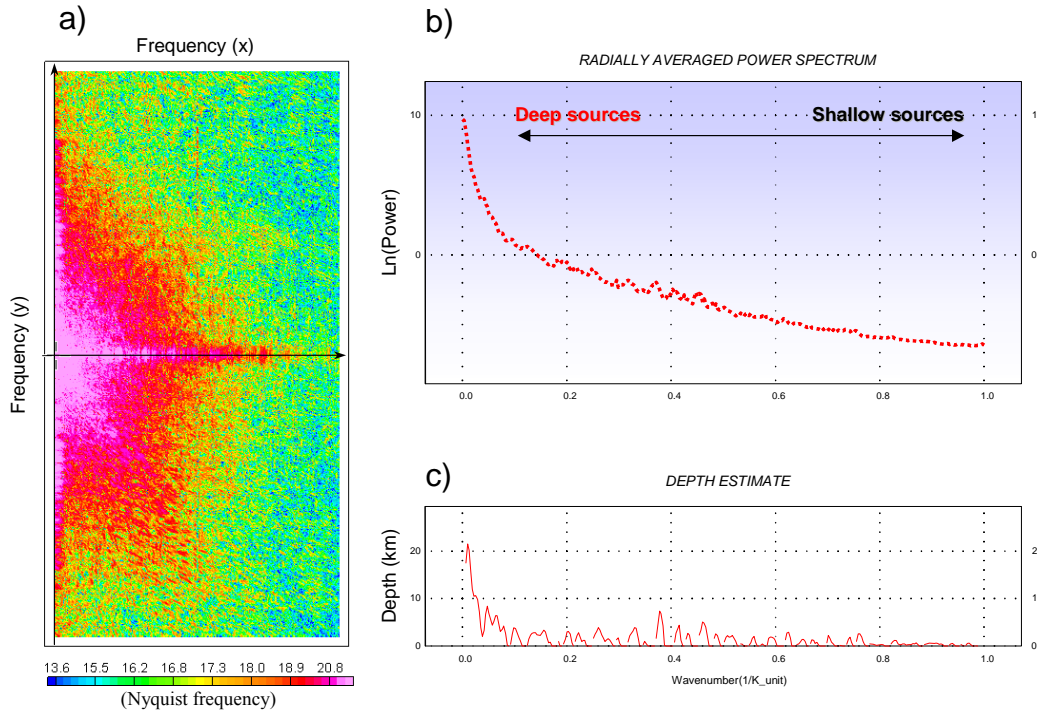
Figure 10.2. (a)Two-dimensional display of the radially power spectrum for the sampled data. (b) Power spectrum with characteristic slopes. Steeper slopes increasing to the left of the plot, coincides with the deep-seated contribution. (c) The depth estimate plot is an automatic 4-5 points slope and depth calculation, derived from the spectrum file.

When considering a grid that is large enough to provide many magnetic sources, the spectrum of this data can be easily interpreted to determine the statistical depth to the tops of the sources using the relationship:

Log E(r)=4πhr

If we examine the shape of a spectrum caused by bottomless bodies (pole sources) at some depth we will see in Fig. 10.2 that the shape is a straight line with a negative slope defining the depth to the top of the bodies. In the real world the bodies are, of course, not all at the same depth so the line defining the spectrum of the deep bodies will represent the average for a considered window.

114
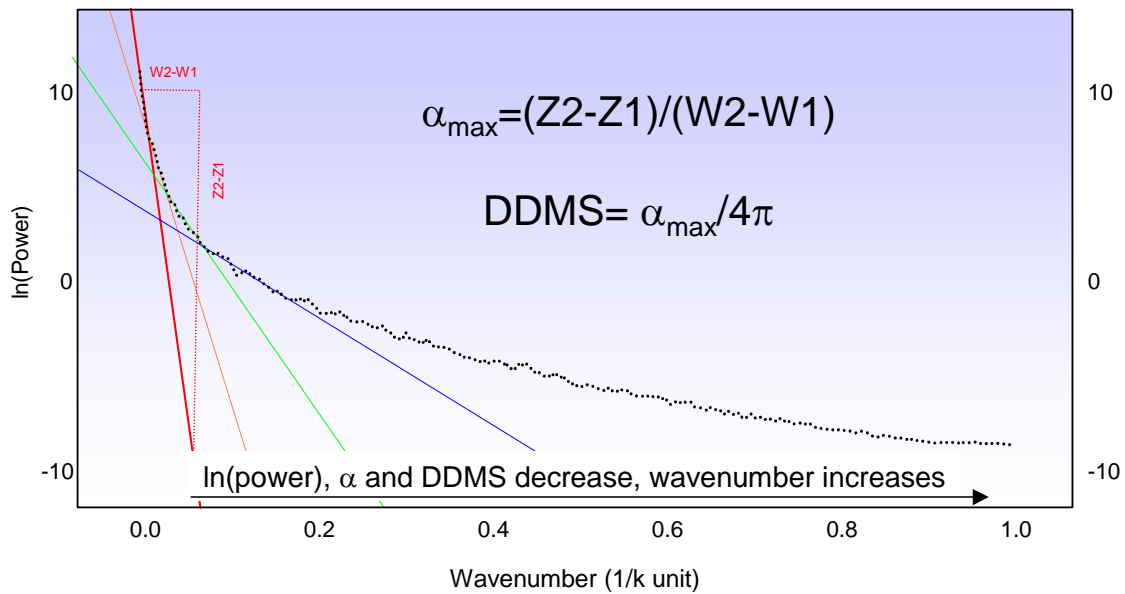
Figure 10.3. Power spectrum analysis of an aeromagnetic map. The steepest slope observed along the spectrum curve, at low wavenumber can be related to the depth of the deepest magnetic source (DDMS).

The statistical average depth for an ensemble of sources can be easily determinated using the value of the slope α along the steepest straight segment observed along the radial spectrum divided by 4π (Fig. 10.3). The steepest slope imaged at low wavenumbers is expected to represent the location of the DDMS (Spector & Grant 1970). From previous papers the DDMS could represent the depth of the Curie temperature.

Oasis Montaj can calculate automatic slopes using a gradient routine along few adjacent points (Fig. 10.2c). Unfortunately, some artefacts at low wavenumbers persist in and sometimes wrongly affect the 4 to 5 points automatic estimation. It should be noted that it is easier and more reasonable to measure the slopes on a printout, as the spectrum is more stretched out. The graphical technique is time-consuming but it makes it easier to identify straight-line segments. Due to graphical uncertainties we estimate an uncertainties of $\pm$ 2km, in average for each depth calculation. All the values presented in this chapter have been manually deduced.

Once a DDMS has been calculated over one window, the same processes are made for new windows. After completion of the depth picking for all windows covering the data grid, we edit the individual data points to make the depth estimation over the grid more consistent internally and with external constraints. It is also recommended to check the regional consistency of the DDMSs and to check with other adjacent windows if one result appears suspicious. Then, it could be useful to recalculate the spectrum and reevaluate the depth if some discrepancies exist.

115

10.6 Windows size and peaks in the spectra

Using the signal processing approach, the size of the sampled windows is relatively important. As a matter of fact, minimum dimension are required in order to solve the depth extends of the average magnetic depths. As a consequence, small windows cannot sometime solve deeper magnetic sources. Connard *et al.* (1983) used the shape of the radially averaged spectra to estimate the maximum depth extend to the bottom of the magnetic layer. In particular, the position of the kmax, characterized by a peak in the spectrum, is expected to better constrain the steeper slope along the graph.
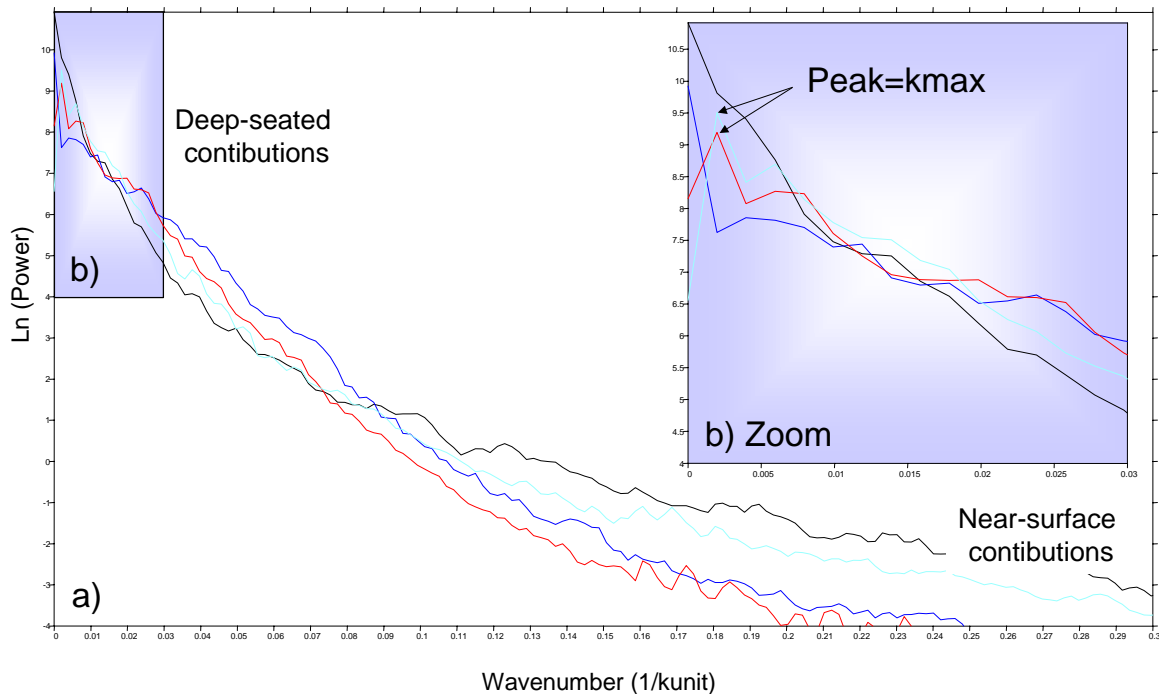
Figure 10.4 a) Power spectrum analysis for different sampled aeromagnetic grids. The graph on Figure 10.4b illustrates the peaks and the location of the kmax locally observed for small wavenumbers.

At low wavenumbers, a peak or a deep null can mean that only the top of a thick magnetic layer is observed (Naidu & Mathew 1998) and the related spectrum can not characterise the bottom of this layer due to inappropriate window size. In such case, we selected a larger window to get a refined spectral representation for the deeper interface.

This part of the spectrum is however susceptible to noise from various sources, particularity from poorly known fields that may be unrelated to the real bottom sources of concern (Blakely 1996). The peak is not detected easily in most of the cases, but we can assume that the steepest slope of the spectrum represents a depth close to this value or a mean depth for the deepest sources (Spector & Grant 1970).

A significant problem linked with the window sizes is the precise location of the DDMSs inside the selected windows themselves. Small windows define relatively small semi-regional areas and the DDMSs results can easily represent an average for specific structural segments along the margin. However, if we are looking for deep sources, the sampled windows and the statistical analysis cover larger areas. Consequently, the location of the estimated DDMS is imprecise compared to smaller windows. The smaller the window is, the better the x,y geographic location of the DDMS point would be (Fig. 10.5). Consequently, if a large window covers several distinct crustal segments, the geodynamic meaning of such a single point could be unreliable and ambiguous.
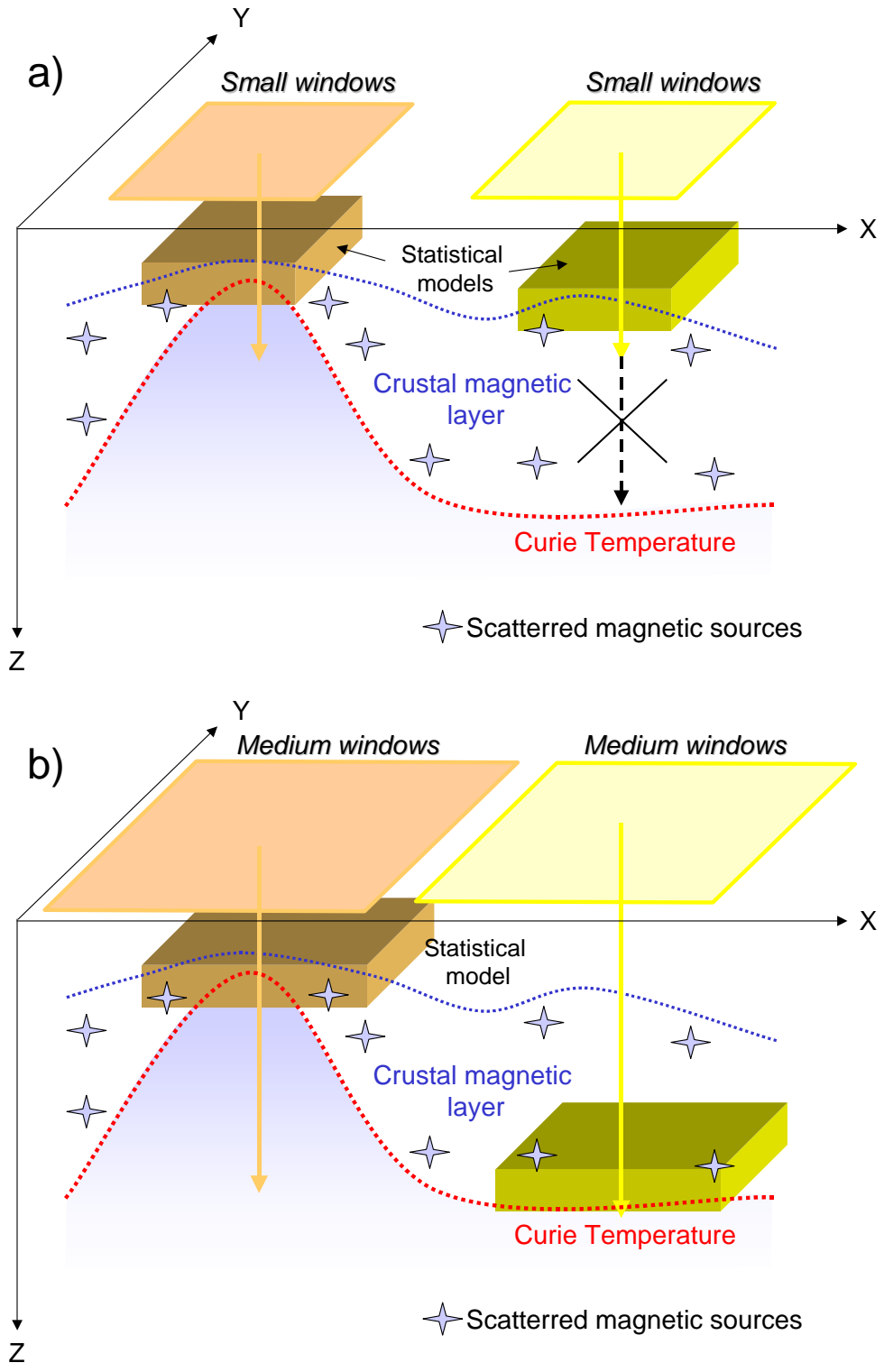
Figure 10.5. *Effects of the window size in estimating deep sources. Some windows do not allow to image deep magnetic sources if their sizes are not large enough. However the bigger the window is, the less accurate the geographic location of the DDMS will be.*

10.7 Application along different segments of the Norwegian shelf

We tested and applied the method in several sampled windows across the main features of the Mid-Norwegian margin and adjacent oceanic domain (Figs. 10.6, 10.7, 10.8, 10.9, 10.10, 10.11). Some windows have been selected along the main segments and structural features of the Mid-Norwegian margin and adjacent oceanic basins (Figs. 10.6, 10.9, 10.11). During the sampling, both large and small windows have been tested.
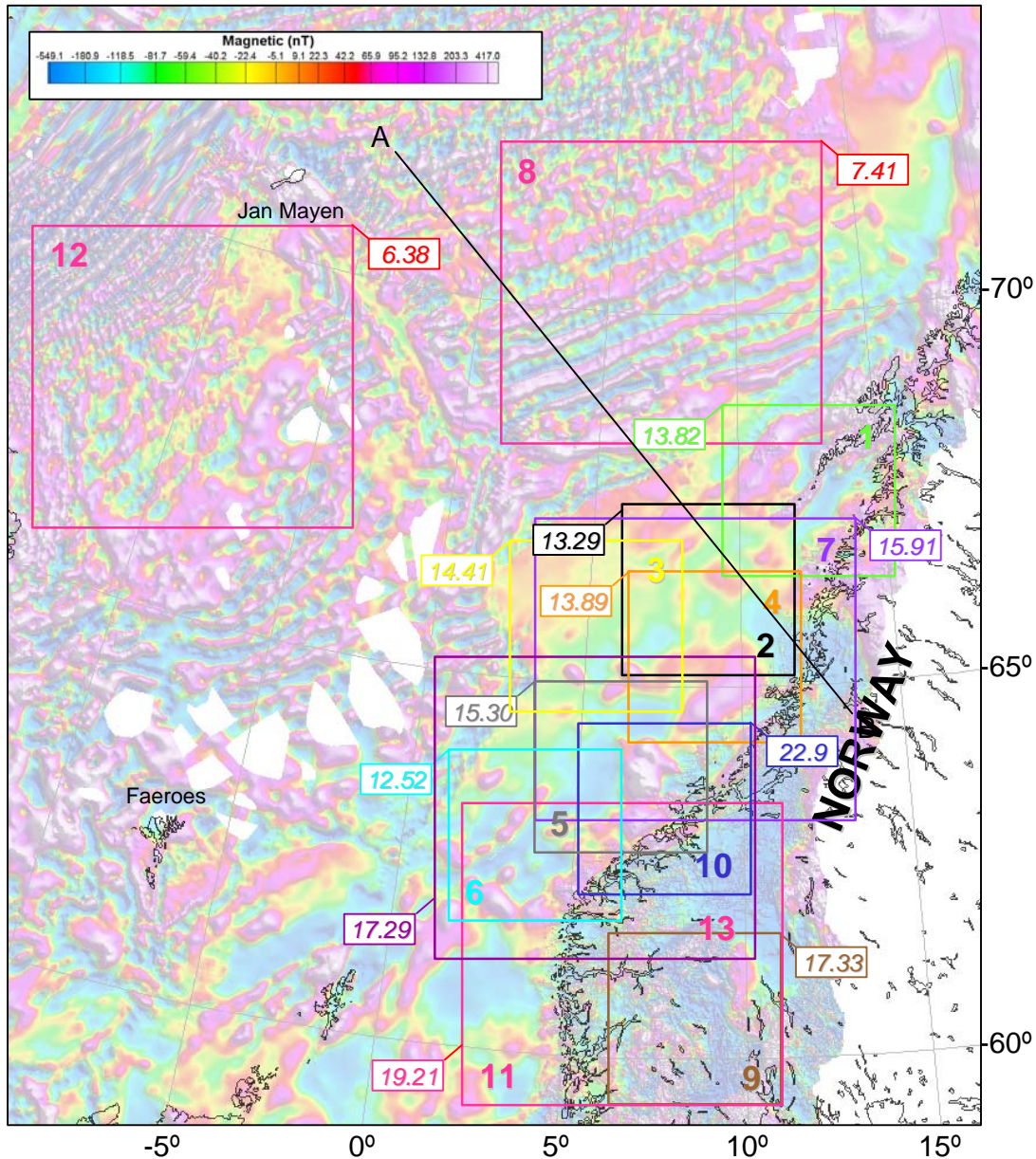
Figure 10.6. Selected windows along the main segments and structural features of the Mid-Norwegian margin and adjacent oceanic basins. Small windows are ~250x250 km wide. Large windows are 475x475 km wide. Numbers indicate the values of the different DDMSs.

Small windows have been selected first across the followings areas:

- Lofoten area (window 1)
- The Nyk-Utgard High area (window 2)
- The Fles-Gjallar area (window 3)
- The Nordland area (window 4)
- The Ormen Lange area (window 5)
- The Møre Basin (window 6)
- The central southern Norway (window 9)
- The Froan Basin-Frøya High (window 10)

Large windows have been tested along:

- The Vøring Basin area (window 7)
- The Lofoten Basin area (window 8)
- The South Norway-Viking Graben area (window 11)
- The Jan Mayen Ridge area (window 12)

Large windows overlap some of the small windows to test the reliability of the measurements estimates.

Using small windows in the continental domain (Fig. 10.6), the DDMSs estimations vary from 22.9 km (deeper values) near Frøya Basin to 12.52 in the central part of the Møre Basin (shallower value) (Figs.10.7 & 10.8). In the Vøring Basin and along the Lofoten margin, the DDMS values ranges from 13.3 km to 14.4 km.

Using large windows the DDMSs vary between 19.25 km in the south Norway-Viking Graben area to 17.29 km in the Møre Basin and 15.91 km in the Vøring Basin area. Intermediate values suggested also deep magnetic material at around 12.4 km in south Norway (windows 11), 4.54 km in the Møre Basin and 8.48 km in the Vøring Basin. The DDMS values along the Møre and Vøring Basin (windows 7 and 13) appeared to be slightly higher than the DDMS indicated by smaller windows sampled along the same areas (windows 2, 3, 4, 5) (Figs. 10.7, 10.8, 10.9). Deeper values are, however, indicated using small windows near the Frøya High (window 10)

In the oceanic domain, windows provide shallower DDMSs (Figs. 10.6 and 10.9). DDMS for the Lofoten Basin is 7.41 km and a value of 6.38 km has been obtained along the Jan Mayen Ridge. Intermediate depths around 3 km are also deduced for the two windows. We point out that any good estimation of the DDMS could not be estimated in the Norway Basin due to poor magnetic coverage and significant gaps in this area.

The DDMS values, in the oceanic domain, appear to be systematically lower that the continental values and clearly reflect the contrast of the magnetic anomalies also observed between the two distinct geophysical and geodynamic domains.
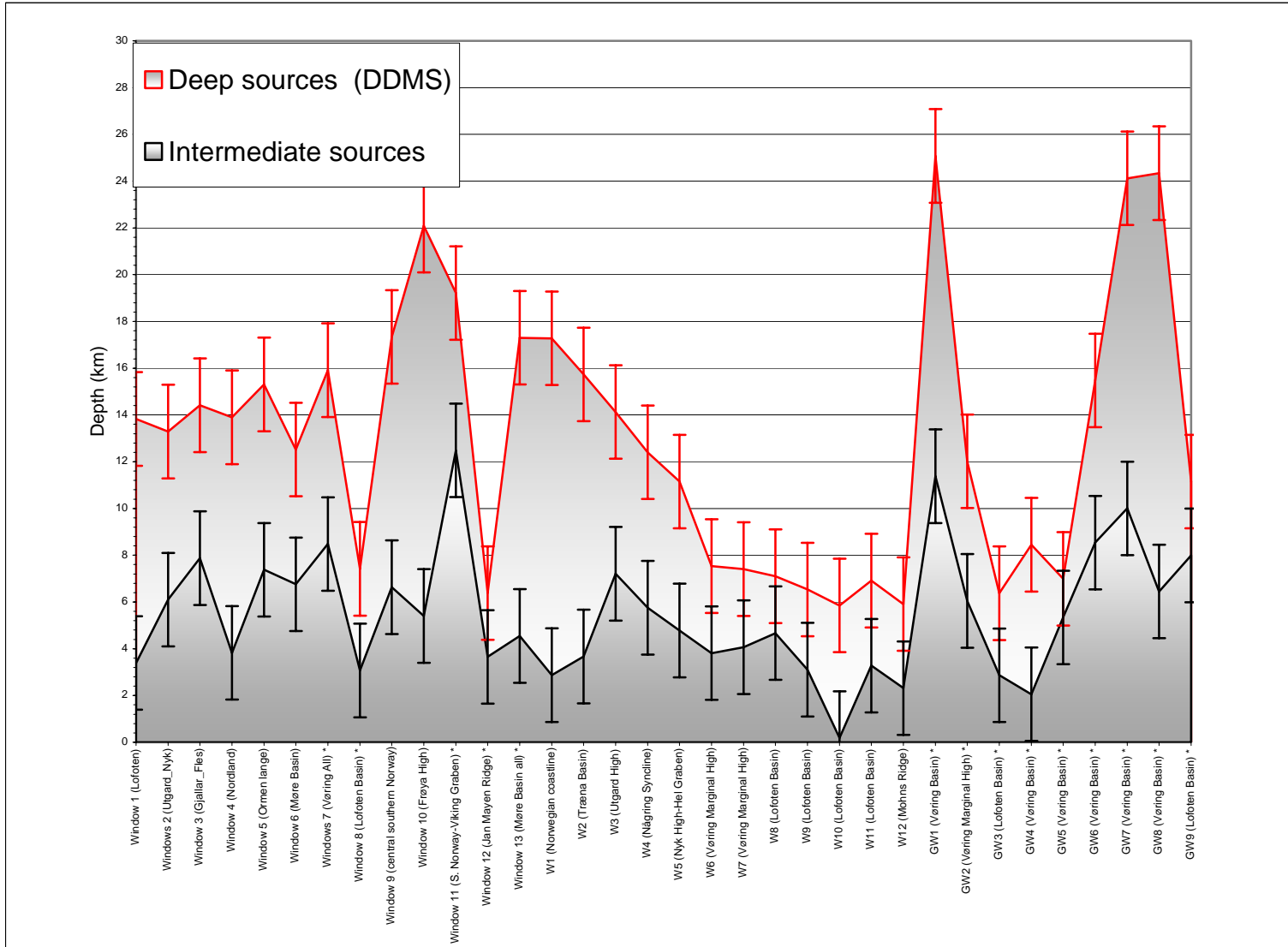
Figure 10.7. Summary of the deep and intermediate magnetic sources measurements obtained from spectrum analysis at different location. * Indicates large windows.
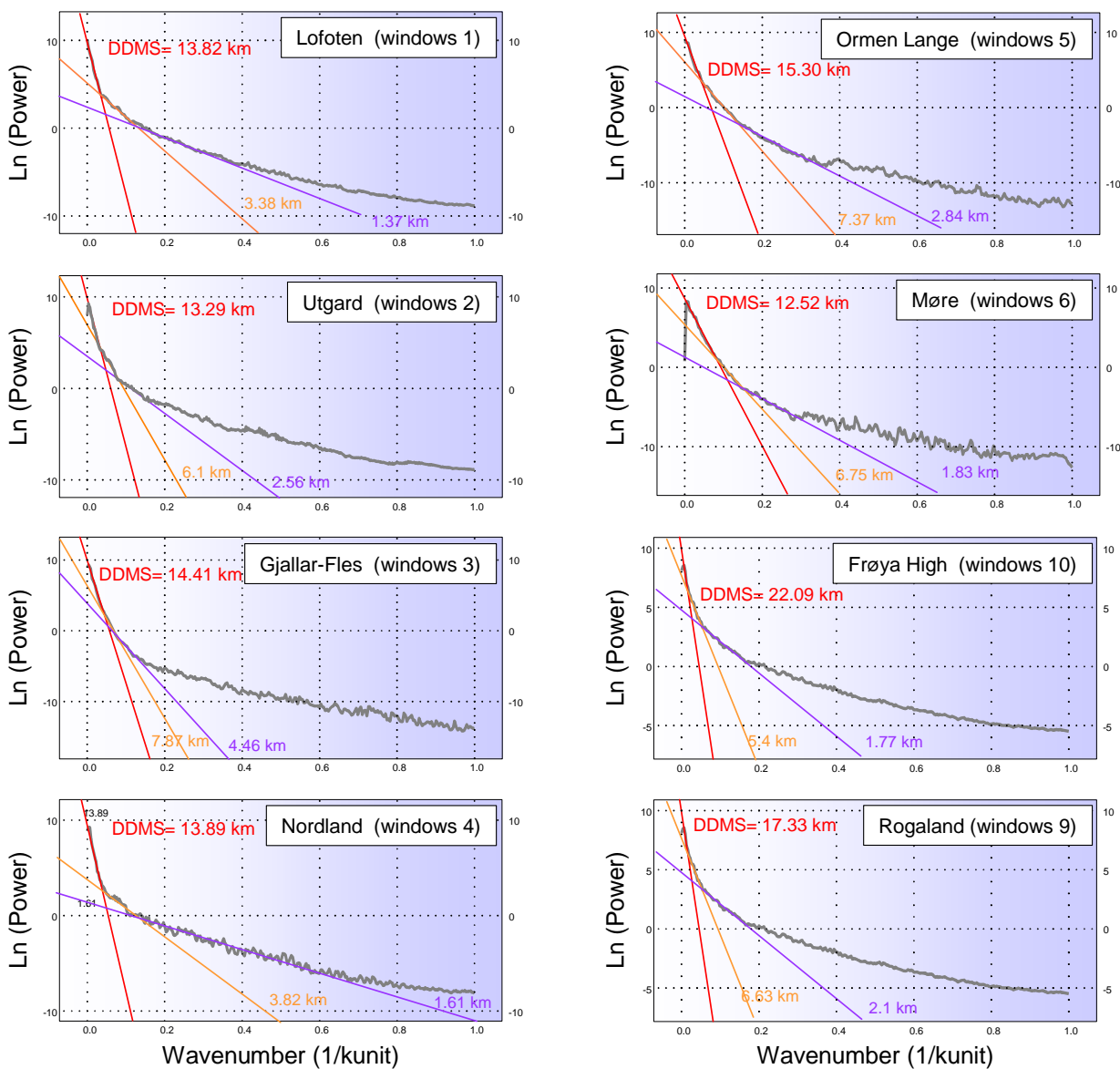
Figure 10.8. Examples of power spectrum analysis along different structural element of the Norwegian shelf and mainland. Location of the windows on Fig. 10.6.
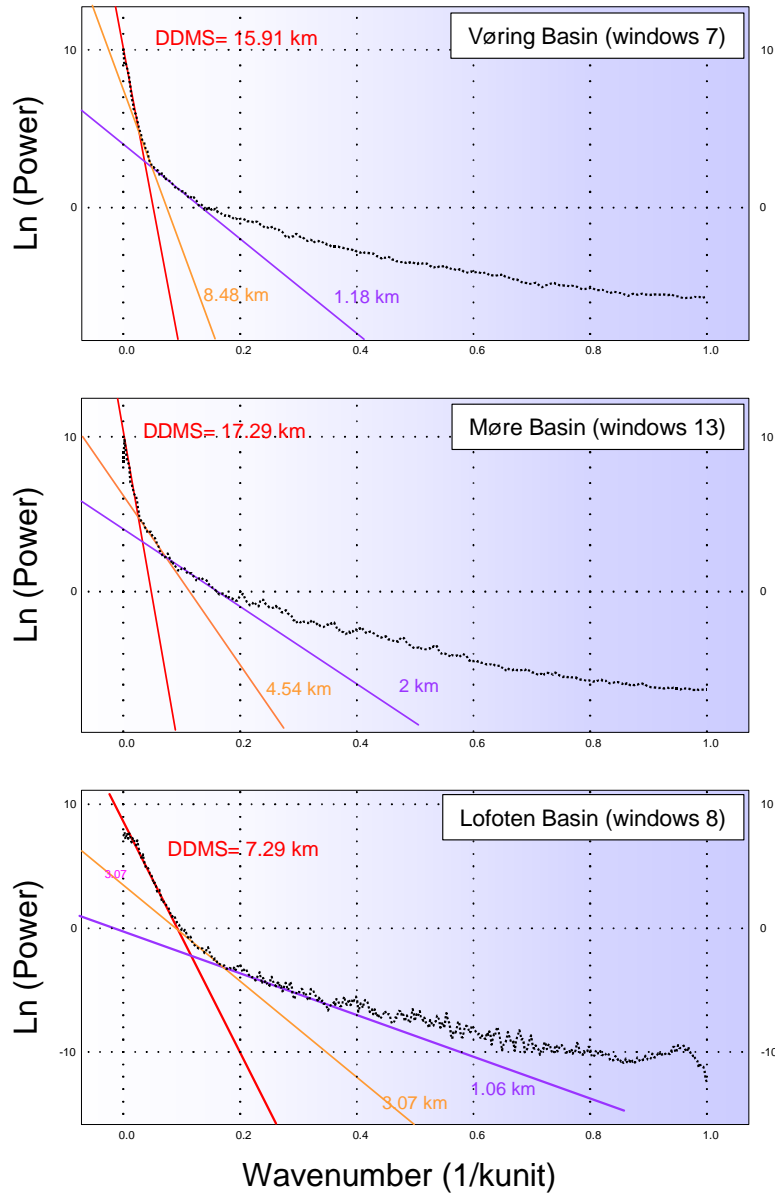
Figure 10.9. Power spectrum analysis of large windows, offshore Norway. The location of the windows are shown in Fig. 10.6

10.8 Application along a NW-SE corridor from the Mid-Norwegian margin to the oceanic spreading ridge.

In a second phase, we sampled some windows along a corridor from the Norwegian mainland to the oceanic spreading axis to the west in order to test the lateral evolution of these values (Fig. 10.10). The main idea was to check the relationships between the depth of Curie temperature and the geodynamic setting of the main magnetic units.
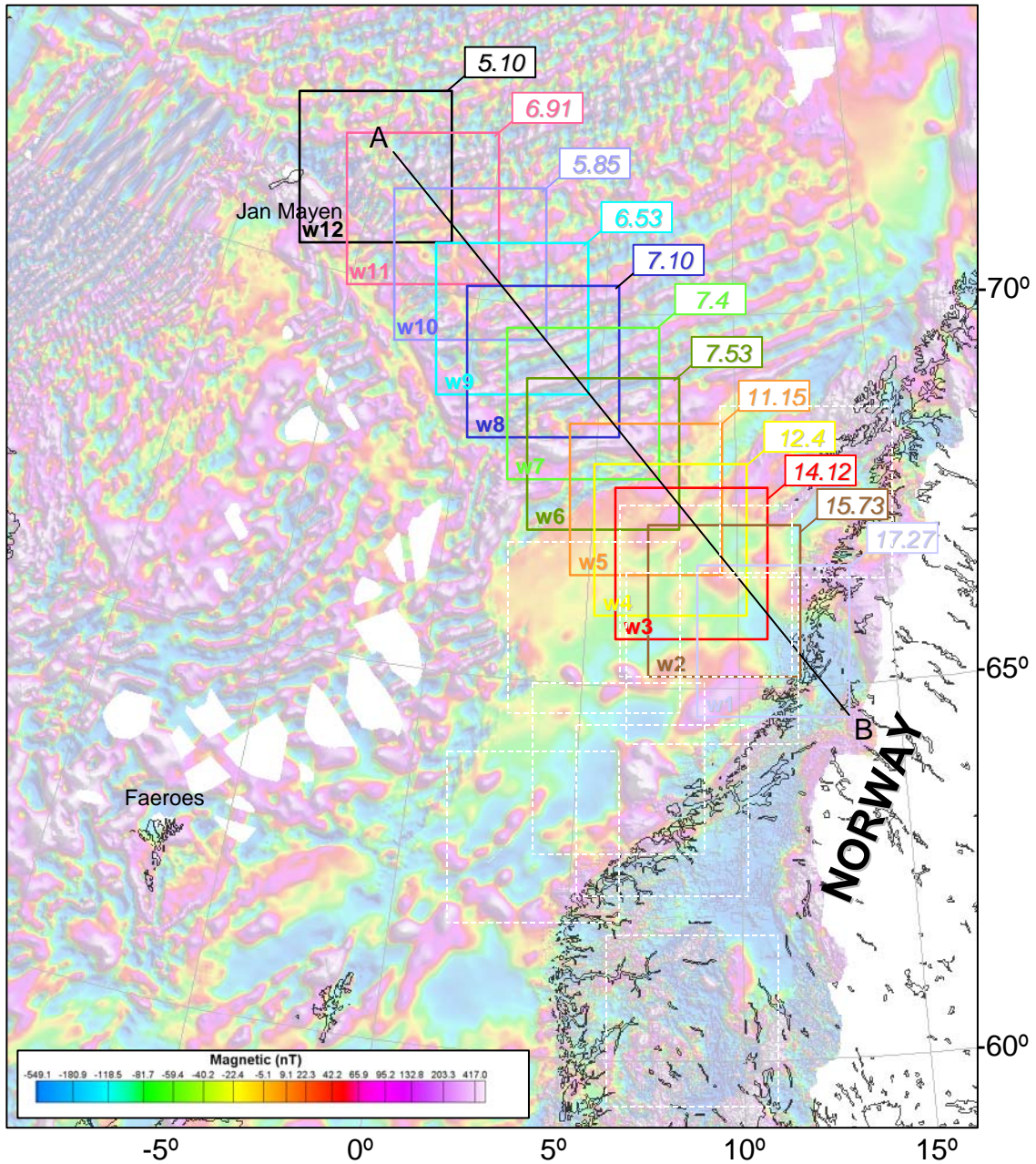
Figure 10.10. *Selected windows along a NW-SE corridor from the Norwegian mainland to oceanic spreading axis. Transect AB is illustrated by Figure 10.12. White dashed lines represent the small windows previously described in Figure 10.6.*

Results for DDMS computation of the main areas are summarised in Tables 10.2 and 10.3 (annexes) and a comparison with the previous DDMS estimations is still possible using Fig. 10.7.

Along the selected corridor, we test different window sizes to test the effect of these parameters (Figs. 10.10 and 10.11).

Across the Vøring Basin the DDMSs progressively decrease from East to West from 15.73 km to 11.15 km along the outer Vøring Basin. A sudden fall of the DDMS is recorded near the Vøring marginal High from 11.15 to 7.5 km (Fig. 10.7). The drop coincides with the continental-oceanic transition zone near the Vøring Marginal High.

West of the Vøring Marginal High (windows W7 to W10), a progressive swallowing of the DDMS is observed from the continental crust toward the oceanic. Along the Lofoten Basin (oceanic domain) the DDMSs do not vary so much and evolve from 7.5 to 5.1 km, close to the Mohns Ridge and Jan Mayen area.
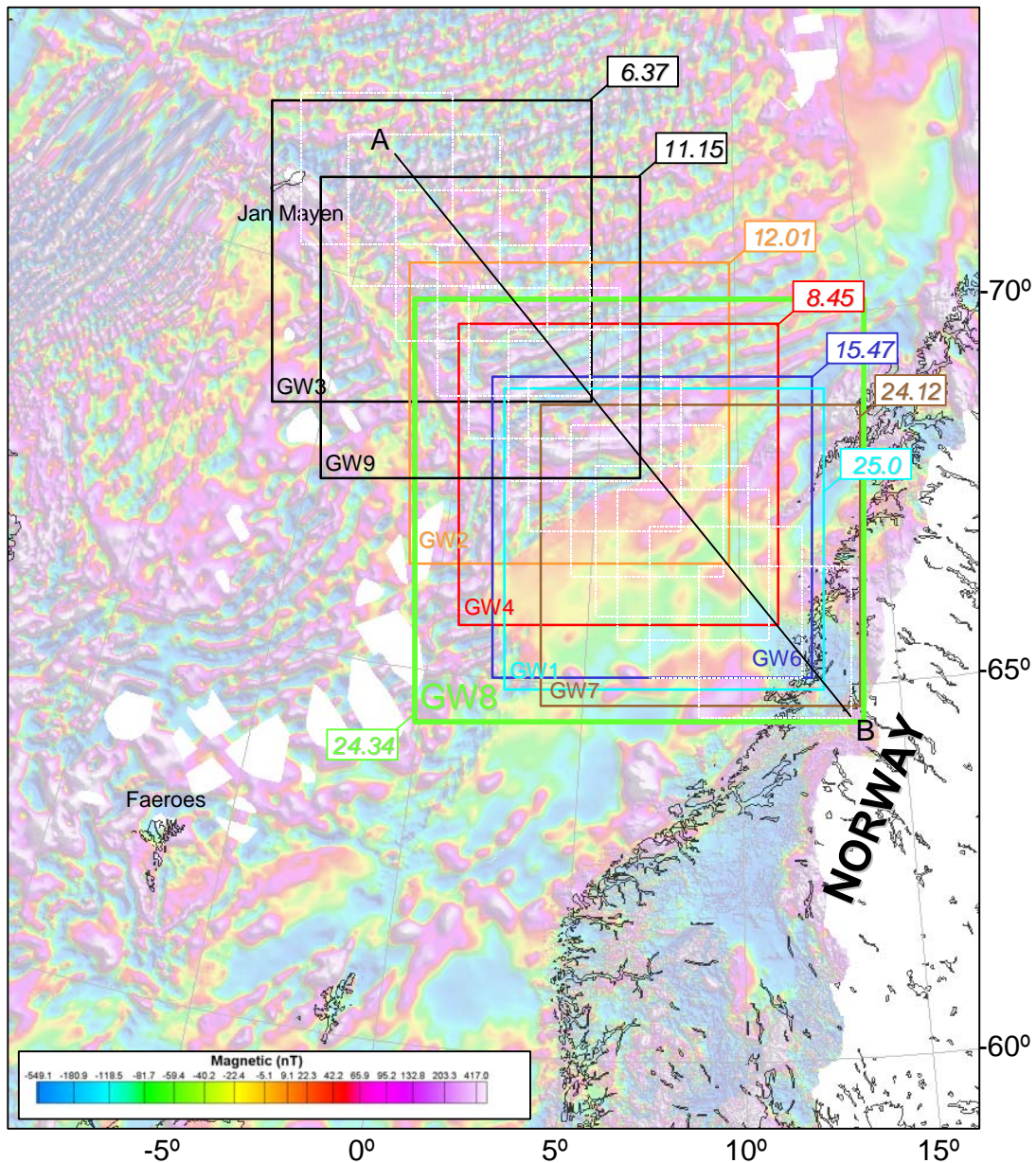

Figure 10.11. Selected large windows along a NW-SE corridor from the Norwegian mainland to oceanic spreading axis.

In the continental domain, the DDMS results obtained using larger windows (~475x475 km), do not vary so much across the Lofoten Basin. The spectrum analysis suggests DDMS values between 6.3 and 12.01 km in the Lofoten Basin (windows GW3 and GW9). Near the coastline and across the Vøring Basin, some windows suggest, however, deeper values of the DDMS (Fig. 10.7). The DDMSs reach 24 to 25 km in windows GW1, GW7, GW8. Compared to the small windows (Figs 10.10 and 10.11) the DDMSs are 5 to 7 km deeper if we use larger windows. Additional intermediate magnetic material are also indicated at the depth s of 11.37 km (GW1), 5 km (GW5), 8.54 km (GW6), 10 km (GW7), 6.44 km (GW8) but are shallower that the DDMS values obtained with small windows along the corridor.

In the oceanic domain, the large window GW3 provides a DDMS of 6.37 km, which is close to the values obtained by the small adjacent windows 10, 11 and 12 (Figs. 10.10 and 10.11). However, large windows GW2 and GW9 provide deeper DDMS values of 11.15 and 12.01 km. These deep DDMSs are also different from the 7.41 km result obtained using the same window size previously described across the Lofoten Basin (cf. window 8, Fig. 10.6). The discrepancies could be explained as a misinterpretation of the spectrum, bad quality of the initial magnetic dataset or by the fact that GW2 and GW9 partly cover the Vøring Spur and the Jan Mayen Fracture Zone. We know from NGU report 2006.018 (Olesen *et al.* 2006) that this area represents an atypical thick oceanic domain that significantly influences the magnetic signal in the area. The deepening of the DDMS could be linked with this lateral variation of the oceanic crust thickness and may reflect the presence of deep gabbroic units in this area. We note also that intermediate magnetic depth values obtained for GW2 (6.04 km) and GW9 (7.99 km) are quite similar to the values obtained using small windows, from windows W8 to W12 (Fig.10.10).

10.9 Does the DDMS represent the Curie temperature?

At this stage of the spectrum approach, a link between the Curie temperature and the values of the DDMS is unfortunately not so obvious and the estimation of source depths from analysis of crustal magnetic sources remains a tricky problem with ambiguous solutions. The DDMS may have two alternate interpretations. It may suggest a lithological interface generally characteristic of areas with normal or low heat flow. The second possibility may be that at such depths, rocks really loose their ferromagnetic properties.

In the oceanic domain, our DDMS values are most of the time shallower than values expected from theoretical models (Fig. 10.12). From the continental-ocean transition zone, the Curie temperature is expected between 30 near the continental ocean transition zone to 5 km near the Mohns ridge assuming the plate model of Parsons & Sclater (1977). Unfortunately, our DDMS values are most of the time shallower that the values expected (Fig. 10.13). Small windows analysis suggests depths from 7.53 km near the COT to 5.10 km near the Mohns Ridge. Even with large windows the depth of the DDMS are still shallower to represent the one of the Curie isotherm. The only exceptions are from the DDMS value estimated near the current spreading

ridge. Here, the DDMS, located at around 6-5km may likely represent the Curie windows. For other DDMS values, the geological meaning of these values rather suggests an interval located between the Moho and the top of the oceanic gabbros.
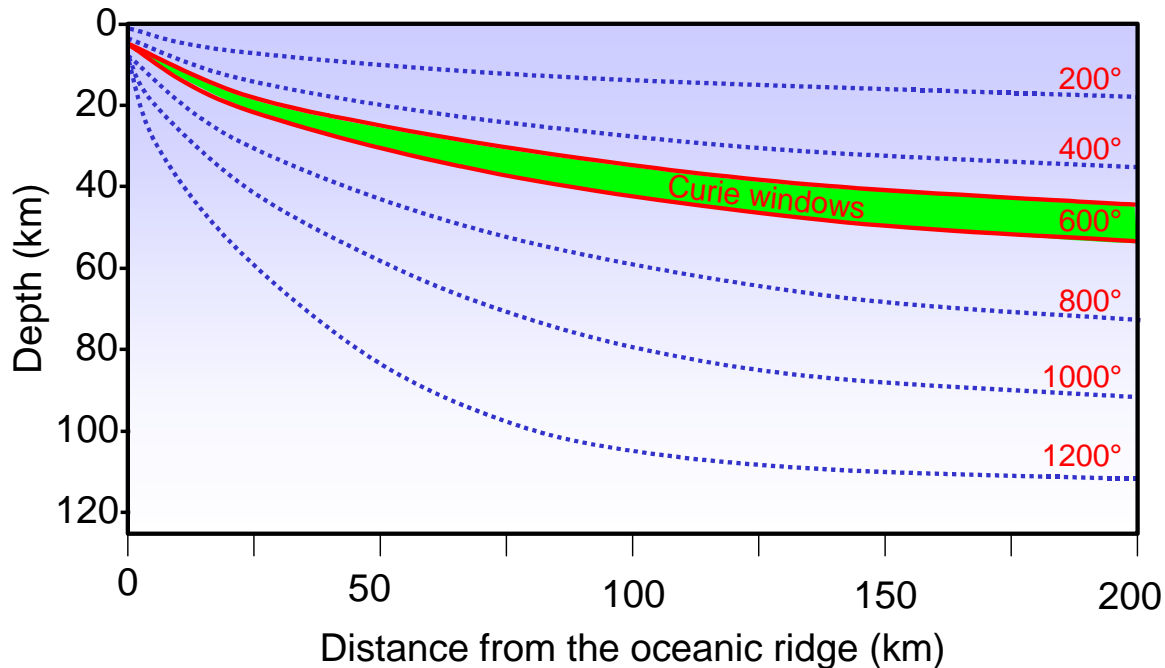
Figure 10.12. Isotherm and Curie temperature evolution along an oceanic spreading system. The graph illustrates the progressive cooling of the oceanic lithospheric plate as a distance (=age) function from the current oceanic ridge. Model from Parsons and Sclater (1977).

In the continental domain, it is even more difficult to estimate and judge the location of the Curie isotherm versus the DDMSs. As a matter of fact, the Curie isotherm does not necessarily represent any strong seismic contrast (like the top basement for example) and/or is locally to deep to be detected with conventional 2D seismic lines. Therefore, it is really difficult to compare our DDMS results with other reliable datasets.

To test the validity of the DDMS, we refer to a recent thermal modelling (Gernigon *et al.* 2006) located near the transect AB described in this chapter (Fig. 10.14). This model provides a recent evaluation of the Curie isotherms expected from the Norwegian mainland to the oceanic crust. Comparing the thermo-kinematical model and the spectral solution, we find that some of the DMMS values between 25 km and 15.47 km (windows GW1, GW7 and GW8) are close to the Curie temperature suggested by this thermal model. Unfortunately, shallower DDMSs between 15 km to 11 km are certainly too shallow to likely represent the actual Curie isotherms. They may represent, at best, crustal features from Moho to top crystalline basement described by wide-angle seismic data (Mjelde *et al.* 2005).
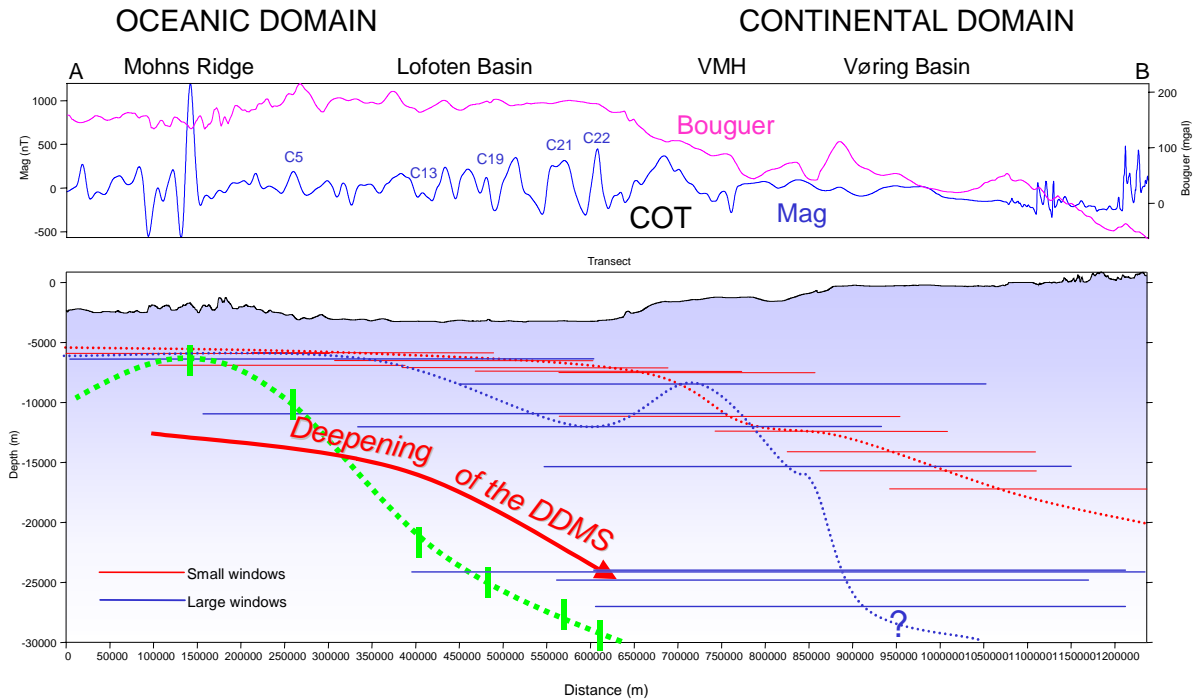
Figure 10.13. Bathymetric transects across the sampled windows. Horizontal bars represent the projection of the sampled windows at the depth of the DDMS obtained by spectral analysis for each of these windows. The red lines represent the projection of the small windows located on Fig. 10, the blue lines represent the large windows, described in Fig. 10.11. The green dashed lines represent the 550°C isotherms calculated assuming the analytic model of Parson & Sclater (1977). Location of the profiles is shown in Fig. 10.10.
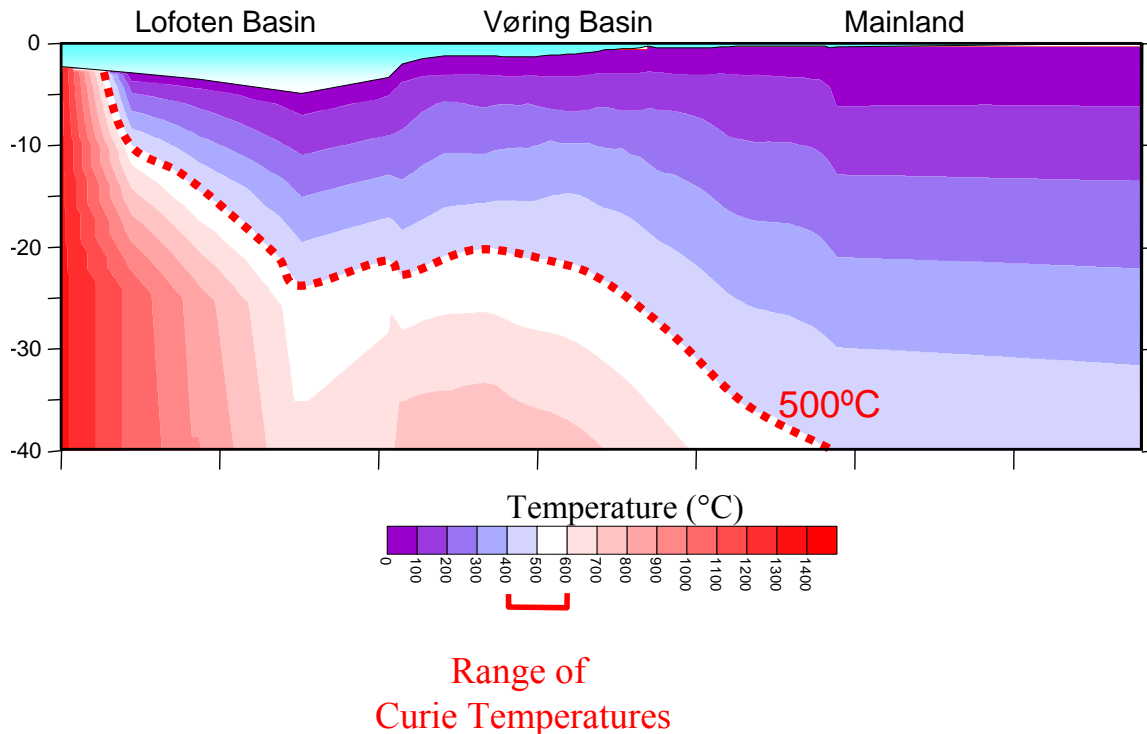
Figure 10.14. Thermal modelling across the Norwegian mainland to the Mohns oceanic spreading ridge, cross-cutting the Vøring Basin (Gernigon et al. 2006). This model provides an independent estimation of the actual Curie isotherm, offshore Norway.

10.10 Conclusions

- In this chapter we estimated depths of the deepest magnetic sources (DDMSs) along the Mid-Norwegian margin and adjacent areas using spectral analysis of aeromagnetic sub-grids. We applied the technique along a wide area and the main magnetic grid was based on a regional compilation of different magnetic datasets with different processing, line spacing and quality. The DDMSs have been deduced from the steepest slopes observed within several grid windows.

- This analysis suggests that the size of the windows is a significant parameter, which limits the depth penetration of the spectrum analysis. Estimation of deep values requires large windows. Therefore, the x,y location of the calculated value remains geographically imprecise.

- At this stage, we cannot postulate that the DDMSs represent the depth to Curie temperatures. The DDMSs values are too scattered to firmly affirm that they represent real Curie depths.

- Even if the spectral methods do not appear successful along the Mid-Norwegian margin, the distribution of the DDMS, suggest however interesting and coherent lateral variations from the oceanic domain to the continental crust even with varying windows size. Lateral

variation is also suggested in the continental domain. This could be useful to determine any structural segmentation along the sedimentary basins even if the real geological meaning of the iso-DDMSs values reminds a complex problem. The DDMSs represent, by definition, statistical values along a certain window and should be considered as an average and rough values of "concrete" magnetic sources existing within the windows. Another problem is probably related to the quality and the non-uniformity of the data.

- From a practical point of view, we believe that the spectral methods could be better applied to provide information about the depth to top basement, using small windows. The interpretation of computed values needs careful data analysis and additional geological and geophysical information should be used to constrain the interpretation of magnetic anomalies. In the future, it seems to be judicious to compare and calibrate the DDMS estimation (and the windows size) with seismic data (not available for this study) to constrain the top basement in order to get the best fit between seismic reflections and the windows size. The technique could also be applied to the gravity dataset and could be compared with other methods (eg. Werner, Euler and deconvolution). The future NGU aeromagnetic survey BAS-06 near the Finnmark platform could be a suitable test area for testing of the methods.

Annexes

Table 10.2. Source depths from spectral analysis of aeromagnetic anomalies along different areas of the Norwegian shelf and mainland.

	ln(power)	wavenumber	slope	depth estimate
Windows 1	**Lofoten**			
deep	9.73	0.056	173.75	**13.82658568**
intermediate	5.11	0.12	42.58333333	3.388673997
shallow	2.42	0.14	17.28571429	1.375553437
Windows 2	**Utgard_Nyk**			
deep	9.52	0.057	167.0175439	**13.29083384**
intermediate	6.9	0.09	76.66666667	6.100939485
shallow	3.55	0.11	32.27272727	2.568182036
Windows 3	**Gjallar Fles**			
deep	9.78	0.054	181.1111111	**14.41236429**
intermediate	7.52	0.076	98.94736842	7.873981395
shallow	3.92	0.09	43.55555556	3.466040983
Windows 4	**Nordland**			
deep	9.43	0.054	174.6296296	**13.89658438**
intermediate	5.86	0.122	48.03278689	3.822327732
shallow	2.3	0.113	20.3539823	1.619718447
Windows 5	**Ormen Lange**			
deep	10	0.052	192.3076923	**15.30335991**
intermediate	6.86	0.074	92.7027027	7.377046687

shallow	2.29	0.064	35.78125	2.847381404
Windows 6	**Møre**			
deep	9.44	0.06	157.3333333	**12.52018886**
intermediate	7.05	0.083	84.93975904	6.759291258
shallow	2.54	0.11	23.09090909	1.837516161
Windows 7	**Vøring Basin all**			
deep	10	0.05	200	**15.91549431**
intermediate	7.78	0.073	106.5753425	8.480996283
shallow	2.05	0.138	14.85507246	1.182129106
Windows 8	**Lofoten Basin**			
deep	8.578	0.092	93.23913043	**7.419734249**
intermediate	3.474	0.09	38.6	3.071690402
shallow	0.94	0.07	13.42857143	1.068611761
Windows 9	**Rogaland**			
deep	10	0.0459	217.8649237	**17.33713977**
intermediate	7.67	0.092	83.36956522	6.634339204
shallow	4.71	0.178	26.46067416	2.105673545
Windows 10	**Frøya High**			
deep	10.55	0.038	277.6315789	**22.09321907**
intermediate	6.45	0.095	67.89473684	5.402891489
shallow	3.16	0.142	22.25352113	1.770878944
Windows 11	***South Norway-Viking Graben***			
deep	9.9	0.041	241.4634146	**19.21504801**
intermediate	8	0.051	156.8627451	12.48274063
shallow	5.05	0.158	31.96202532	2.54345716
Windows 12	***Jan Mayen Ridge***			
deep	8.42	0.105	80.19047619	**6.381355337**
intermediate	5.189	0.113	45.92035398	3.654225662
shallow	2.79	0.111	25.13513514	2.000190501
Windows 13	***Møre Basin all***			
deep	10	0.046	217.3913043	**17.29945034**
intermediate	6.23	0.109	57.1559633	4.548327043
shallow	4.04	0.16	25.25	2.009331157

Table 10.3. Source depths from spectral analysis of aeromagnetic anomalies along a NW-SE transect between the Norwegian mainland and the Mohns Ridge.

	ln(power)	wavenumber	slope	depth estimate
Windows W1				
deep	9.77	0.045	217.1111111	**17.27715327**
intermediate	5.12	0.142	36.05633803	2.869272213
Windows W2				
deep	9.49	0.048	197.7083333	**15.73312927**
intermediate	5.53	0.12	46.08333333	3.667195147
Windows W3				
deep	9.94	0.056	177.5	**14.1250012**
intermediate	6.16	0.068	90.58823529	7.208782717
Windows W4				
deep	9.35	0.06	155.8333333	**12.40082265**
intermediate	7.23	0.1	72.3	5.753451193
Windows W5				
deep	9.25	0.066	140.1515152	**11.15290321**
intermediate	6.01	0.1	60.1	4.78260604
Windows W6				
deep	8.52	0.09	94.66666667	**7.533333973**
intermediate	5.27	0.11	47.90909091	3.812484319
Windows W7				
deep	8.47	0.091	93.07692308	**7.406826198**
intermediate	4.6	0.09	51.11111111	4.06729299
Windows W8				
deep	8.48	0.095	89.26315789	**7.103336407**
intermediate	5.28	0.09	58.66666667	4.668544997
Windows W9				
deep	8.21	0.1	82.1	**6.533310414**
intermediate	3.16	0.081	39.01234568	3.104503828
Windows W10				
deep	8.09	0.11	73.54545455	**5.852561316**
intermediate	1.72	0.74	2.324324324	0.184963853
Windows W11				
deep	8.69	0.1	86.9	**6.915282277**
intermediate	4.53	0.11	41.18181818	3.277144965
Windows W12				
deep	8.17	0.11	74.27272727	**5.910435841**
intermediate	2.33	0.08	29.125	2.317693859

Table 10.4. Source depths from spectral analysis of aeromagnetic anomalies along a NW-SE transect between the Norwegian mainland and the Mohns Ridge.

	ln(power)	wavenumber	slope	depth estimate
Windows GW1				
deep	10.4	0.033	315.1515152	**25.07896073**
intermediate	9.15	0.064	142.96875	11.37709164
shallow	6.68	0.06	111.3333333	8.859625165
shallow	3.7	0.13	28.46153846	2.264897267
Windows GW2				
deep	9.06	0.06	151	**12.0161982**
intermediate	7.6	0.1	76	6.047887837
shallow	3.14	0.08	39.25	3.123415758
shallow	0.98	0.038	25.78947368	2.052261108
Windows GW3				
deep	8.01	0.1	80.1	**6.374155471**
intermediate	3.53	0.098	36.02040816	2.866413006
Windows GW4				
intermediate	8.92	0.084	106.1904762	**8.450369597**
shallow	1.55	0.06	25.83333333	2.055751348
Windows GW5				
intermediate	8.26	0.094	87.87234043	**6.99265867**
shallow	7.38	0.11	67.09090909	5.338924909
Windows GW6				
deep	9.53	0.049	194.4897959	**15.4770062**
intermediate	8.8	0.082	107.3170732	8.540021337
shallow	6.02	0.083	72.53012048	5.771763599
Windows GW7				
deep	9.7	0.032	303.125	**24.12192106**
intermediate	8.8	0.07	125.7142857	10.00402499
shallow	7.73	0.09	85.88888889	6.834820612
Windows GW8				
deep	10.4	0.034	305.8823529	**24.34134424**
intermediate	7.7	0.095	81.05263158	6.449963483
shallow	6.78	0.11	61.63636364	4.904865973
Windows GW9				
deep	9.11	0.065	140.1538462	**11.1530887**
intermediate	9.04	0.09	100.4444444	7.99311492
shallow	7.87	0.1	78.7	6.262747011

11   CONCLUSIONS

11.1 Status 2006

1) Basement rocks in cental and southeastern parts of mainland Norway has been characterised with regard to heat-generating geochemical elements (based on analysed content of K, U and Th in c. 3300 bedrock samples).

2) Existing heat flow data, both offshore and on the mainland of Norway and Sweden have been compiled.

3) 3D models of the Mid Norwegian continental margin and the Oslo Rift have been established from gravity, magnetic, seismic and bedrock mapping data.

4) An updated 2D crustal model through central Scandinavia has been produced.

5) A depth to crystalline basement map from northern Norway has been compiled.

6) Palaeo-climatic corrections have been carried out on 13 pre-existing shallow boreholes (170-300 m deep) from 8 different locations in southern Norway. The calculated corrections range from +2 to +9 mW/m² (i.e. 5-20% of original heat flow values). There is a need for temperature logging in deep boreholes in Norway to obtain improved estimates of palaeo-climatic corrections.

7) A total of 5 deep wells (700-900 m) have been logged by the University of Aarhus with regard to temperature within the mainland basement rocks. Locations: A) Asker (Cambro-silurian rocks), B) Skedsmo and Lærdal (Sveconorwegian greiss) C) Hjerkinn and Meldal (Caledonian nappe complexes). (NGU has recently acquired its own instrumentation and will log 6 wells during the autumn of 2006).

8) New heat flow data have been calculated from temperature logging and thermal conductivity data in Lærdal (44 mW/m²), Hjerkinn (41 mW/m²) and Løkken (49 mW/m²). These data are not climatically corrected yet. The corrections will, however, be small since the boreholes are deep (600-1000m).

9) Crustal models for the central Scandinavian mountains, Mid-Norwegian margin and Oslo Graben show the influence of 3D geometry on the present thermal structure and observed heat flow.

10) The Central Scandinavia thermal modelling is indicating that the granitoids of the TIB are only present in the upper crust or are less heat-productive with increasing burial depth. However, the TIB is clearly influencing the isostatic state of the Scandinavian mountains, especially for the

northern and central part, and might be related to the Neogene uplift of the Scandinavian mountains.

11) The modelled moderate and short-wavelength variations in surface heat flow within the Oslo Rift are mainly the result of the different lithological units at relatively shallow depths. The heat-productive rocks are not buried below thick sediments and therefore the near-surface structures control the observed heat flow. The influence of deep crustal intrusives is less important

12) The influence of different basement lithology on heat flow on the Mid-Norwegian margin might be overprinted by the basal heat flow. Only in the case with a varying basal heat flow the surface heat flow is strongly controlled by the structure of the crust.

13) Depths to the deepest magnetic sources (DDMSs) along the Mid-Norwegian margin and adjacent areas have been calculated using spectral analysis of aeromagnetic sub-grids. A modified technique is needed to calculate the depth to Curie temperature for the final Kontiki report.

11.2 Remaining work

1) Temperature logging of additional 6 deep wells (700-900 m) and measurements of thermal conductivity on samples from cores (or bedrock samples adjacent to the well when cores are missing) to calculate the heat flow within the mainland basement rocks. Locations: A) Fredrikstad (Sveconorwegian granite), B) Hamar (Cambo-Orovician sequence), C) Bleikvassli and Sulitjelma, Nordland (Caledonian nappe complexes) D) Lofoten archipelago (metamorphic core complexe), and E) Tysfjord (granites of the Trans-Scandinavian Igneous Belt, TIB). Drill cores are missing for location A.)

2) Analysis of another 600 bedrock samples (K, U and Th) from the Lito Project. Basement characterisation and calculation of heat production in the Sogn & Fjordane and northern Nordland areas. The total study area will cover the mainland of Norway between 60º and 70ºN (Bergen-Tromsø) in addition to southeastern Norway.

3) Complete basement structure map of Norway south of 71ºN, including offshore basement depths and thickness of Caledonian nappes.

4) Chemical analysis and age-dating of offshore basement drill cores.

5) A review of the tectono-magmatic history. Description of geological terrains including the age, magmatic origin, tectonic and metamorphic history and contact relationships to other terrains.

6) Map thermal conductivity variations and their implications on geothermal gradients and measured/estimated heat flow.

7) Measurements of thermal gradient and thermal conductivity on drill cores (or surface rock samples) in an additional 6-7 deep wells (700-900 m) on mainland Norway and calculation of heat flow.

8) Produce an omproved crustal 3D model for the Mid-Norwegian shelf.

9) Customizing of finite element software for 3D modelling of heat production in basement rocks and heat flow into the sedimentary basin.

10) Calculation of heat flow on the Mid-Norwegian continental shelf from a more detailed crustal models and comparison with observed heat flow. Adjustment of the model. Investigate the change of basal heat flow from the continent-ocean boundary towards the mainland using constraints from seismic tomography and detailed analysis of deep crustal structures (correlation between LCB and basal heat flow?).

11) Analysis of selected exploration wells (c. 30 wells) to calibrate bottom hole temperatures against radiogenic heat production from basement.

12) Calculate depth to Curie temperature using the modified spectral method by Okubo et al. (1985).

12   REFERENCES

Aalstad, I., Åm, K., Håbrekke, H. & Kihle, O. 1977: Aeromagnetic investigations along the Norwegian Geotraverse. In: K.S. Heier (ed.): *The Norwegian Geotraverse Project: A Norwegian contribution to the international upper mantle project and the international geodynamics project.* Geological Survey of Norway (NGU), 77-98.

Andersen, B. G. 2000: *Istider i Norge. Landskap formet av istidens breer*, Oslo, Universitetsforlaget, 216 pp.

Andersen, O.B. & Knudsen, P. 1998: *Gravity anomalies derived from the ERS-1 satellite altimetry*. Kort og Martykelstyrelsen, Kopenhagen (**www.kms.dk**).

Anderson, E. M. 1934: Earth contraction and mountain building. *Beitrage zur Geophysik 42*, 133-159.

Archie, G.E. 1942: The electrical resistivity log as an aid in determining some reservoir characteristics. *Petroleum Technology, 5, 1422 – 1430.*

Artemieva I.M. 2003: Lithospheric structure, composition, and thermal regime of the East European craton: Implications for the subsidence of the Russian Platform. *Earth Planet. Sci. Lett. 213,* 429-444

Artemieva, I.M. & Mooney, W.D. 2001: Thermal thickness and evolution of Precambrian lithosphere: A global study. Journal of Geophysical Research, 106, 16387-16414.

Balling, N. 1995: Heat flow and thermal structure of the lithosphere across the Baltic Shield and northern Tornquist Zone. Tectonophysics 244, 13-50.

Balling, N., Kristiansen, J.I., Breiner, N., Poulsen, K.D., Rasmussen, R. & Saxov, S. 1981: Geothermal Measurements and Subsurface Temperature Modelling in Denmark. GeoSkrifter 16, University of Aarhus. 172 pp.

Beck, A.E. & Balling, N. 1988: Determination of virgin rock temperatures. In: Haenel, R., Rybach, L., and Stegena, L. (eds.), Handbook of Terrestrial Heat-flow Density Determination, 59-85. Kluwer Academic Publ., 486 pp.

Benfield, A. E. 1939: Terrestrial heat flow in Great Britain. *Procedings of the Royal Society of London, Series A 173*, 474-502.

Berthelsen, A., Olerud, S. & Sigmond, E.M.O. 1996: *Geologisk kart over Norge, berggrunnskart OSLO 1:250.000*. Geological Survey of Norway (NGU), Trondheim.

Bhattacharyya B., 1964, Magnetic anomalies due to prism-shaped bodies with arbitrary polarization: Geophysics, v. 29, p. 517-530.

Bielik, M., Dyrelius, D. & Lillie, R.J. 1996: Caledonian lithosphere - gravity structure and comparison with Carpathian lithosphere. *Contributions of the Geophysical Institute of the Slovak Academy of Sciences*, 26, 72-84.

Blakely R. 1996: Potential Theory in Gravity and Magnetic Applications: Cambridge University Press, 461p.

Blystad, P., Brekke, H., Færseth, R.B., Larsen, B.T., Skogseid, J. & Tørudbakken, B. 1995: Structural elements of the Norwegian continental shelf, Part II. The Norwegian Sea Region. Norwegian Petroleum Directorate Bulletin 8.

Bos, B. & Spiers, C.J., 2002, Frictional-viscous flow of phyllosilicate-bearing fault rock: Microphysical model and implications for crustal strength profiles. *Journal of Geophysical Research 107*, doi:10.1029/2001JB000301.

Brady, R.J., Ducea, M.N., Kidder, S.B., & Saleeby, J.B., 2006. The distribution of radiogenic heat production as a function of depth in the Sierra Nevada Batholith, California. *Lithos 86*, 229-244.

Breivik, A.B., Verhoef, J. & Faleide, J.I. 1999: Effects of thermal contrasts on gravity modeling at passive margins: results from the western Barents Sea. *JGR*, 104, 15293-15311.

Brekke, H. 2000: The tectonic evolution of the Norwegian Sea continental margin with emphasis on the Vøring and Møre basins. *In:* Nøttvedt, A. (ed.) *Dynamics of the Norwegian Margin.* Geological Society of London, Special Publication, 167, 327-378.

Bullard, E.C. 1947: The time necessary for a borehole to attain temperature equilibrium. *Mon. Not. R. Astr. Soc., Geophys. Suppl. 5.* 125-130.

Byerly P. & Stolt R. 1977: An attempt to define the Curie point iostherm in northern and central Arizona. *Geophysics 42,* 1394-1400.

Calcagnile, G. 1982: The lithosphere-asthenosphere system in Fennoscandia. *Tectonophysics 90,* 19-35.

Carslaw, H.S & Jaeger, J.C. 1959: Conduction of heat in solids. Oxford Univ. Press, Oxford.

Carter, N.L. & Tsenn, M.C. 1987: Flow properties of continental lithosphere. *Tectonophysics 136,* 27-33.

Cassell, B.R., Mykkeltveit, S., Kanestrøm, R. & Husebye, E.S. 1983: A North Sea southern Norway seismic crustal profile. *Geophys. J. R. Astr. Soc. 72,* 733-753

Cermák, V., Balling, N., Kukkonen, I. T. & Zui, V. I. 1993: Heat flow in the Baltic Shield-results of the lithospheric geothermal modelling. *Precambrian Research 64*, 53-65.

Connard G., Couch R. & Gemperle, M. 1983: Analysis of aeromagnetic measurements from the Cascade Range in central Oregon: *Geophysics 48,* 376-390.

Dehls, J.F., Olesen, O., Bungum, H., Hicks, E., Lindholm, C.D. & Riis, F. 2000: Neotectonic map, Norway and adjacent areas 1:3 mill. Geological Survey of Norway (NGU), Trondheim.

Dons, J. & Jorde, K. 1978: *Geologisk kart over Norge, bergrunnskart SKIEN 1:250.000.* Geological Survey of Norway (NGU), Trondheim.

Doré, A.G., Lundin, E.R., Jensen, L.N., Birkeland, Ø., Eliassen, P.E. & Fichler, C. 1999: Principal tectonic events in the evolution of the northwest European Atlantic margin. *In:* Fleet, A.J. and Boldy, S.A.R. (eds.) *Petroleum Geology of Northwest Europe: Proceedings of the 5th conference*, 41-61. Geological Society, London.

Dyrelius, D. 1985: A geophysical perspective of the Scandinavian Caledonides. *In* Gee, D.G. & Sturt, B. (eds.) *The Caledonide Orogen – Scandinavia and related areas*, 185-194. John Wiley and Sons, Chichester.

Dziewonski, A.M. & Anderson, D.L. 1981: Preliminary reference earth model. *Phys. Earth. Plan. Int. 25,* 297-356.

Ebbing, J. & Lundin, E. 2005: 3D modelling and the Mid-Norwegian Atlantic margin. *In:* Olesen, O. et al. *Kontiki Annual Report 2004, Continental crust and heat generation in 3D.* NGU Report 2005.008, 30-49.

Ebbing, J. & Olesen, O. 2005: The Northern and Southern Scandes - Structural differences revealed by an analysis of gravity anomalies, the geoid and regional isostasy. *Tectonophysics 411,* 73-87.

Ebbing, J., Afework, Y., Olesen, O. & Nordgulen, Ø. 2005: Is there evidence for magmatic underplating beneath the Oslo Rift? *Terra Nova 17,* 129–134.

Ebbing, J., Lundin, E., Olesen, O. & Hansen, E.K 2006: The mid-Norwegian margin: A discussion of crustal lineaments, mafic intrusions, and remnants of the Caledonian root by 3D density modelling and structural interpretation. *Journal of the Geological Society, London 163,* 47-60.

Ebbing, J., Skilbrei, J.R. & Olesen, O. submitted: The magmatic system of the Oslo Graben revealed by forward and inverse modeling of potential fields. Submitted to *JGR - Solid Earth*.

Elming, S.Å. 1980: Density and magnetic properties of rocks in the Caledonides of Jamtland, Sweden. *Geologiska Föreningens i Stockholm Förhandlingar 102*, 439-453.

Elming, S.Å. 1988: Geological modelling based on gravity data from the central parts of the Swedish Caledonides. *Geologiska Föreningens i Stockholm Förhandlingar 108,* 280-283.

Fernàndez, M., Torne, M., Garcia-Castellanos, D., Vergés, J., Wheeler, W. & Karpuz, R. 2004: Deep structure of the Vøring margin: the transition from a continental shield to a young oceanic lithosphere. *Earth and Planetary Science Letters 221*, 131-144.

Fernàndez, M., Ayala, C., Torne, M., Vergés, J., Gómez, M. & Karpuz, R., 2005: Lithospheric structure of the Mid-Norwegian Margin: comparsion between the Møre and Vøring margins. *Geol. Soc. London 162*, 1005-1012.

Fichler, C., Rundhovde, E., Olesen, O., Sæther, B.M., Rueslåtten, H., Lundin, E. & Doré, A.G., 1999: Regional tectonic interpretation of image enhanced gravity and magnetic data covering the Mid-Norwegian shelf and adjacent mainland. *Tectonophysics 306*, 183-197.

Folldal Verk 1985: Logg for borehullet ved Gåvålivatnet, Hjerkinn. Diamond drill hole 2000D. 73 pp.

Geosoft, 2005, Montaj GridKnit, Grid extension for OASIS Montaj v6.1, Tutorial and user guide: Geosoft Incorporated, p. 27.

Gernigon L., Lucazeau F., Brigaud F., Ringenbach J. C., S. P. & Le Gall B. 2006: A moderate melting model for the Vølring margin (Norway) based on structural observations and a thermo-kinematical modelling: Implication for the meaning of the lower crustal bodies: *Tectonophysics 412,* 255-278.

Gomez, M., Verges, J., Fernandez, M., Torne, M., Ayala, C., Wheeler, W. & Karpuz, R. 2004: extensional geometry of the Mid Norwegian margin before early Tertiary continental breakup. *Marine and Petroleum Geology 21*, 177-194.

Grønlie, G., Heier, K.S. & Swanberg, C.A. 1977: Terrestrial heat flow determinations from Norway. *Nor. Geol. Tidsskr. 57.* 153-162.

Götze, H.-J. & Lahmeyer, B. 1988: Application of three-dimensional interactive modeling in gravity and magnetics. *Geophysics 53*, 1096-1108.

Hartmann, D. L. 1994: *Global Physical Climatology*, Academic Press, 411 pp.

Hartz, E.H., Eide, E.A., Andresen, A., Midbøe, P., Hodges, K.V., Kristiansen, S.N., 2002. $^{40}Ar/^{39}Ar$ geochronology and structural analysis: Basin evolution and detrital feedback mechanisms, Hold With Hope region, East Greenland. Nor. Geol. Tidsskr., 82, 341-358.

Heier, K.S. 1977: *The Norwegian Geotraverse Project: A Norwegian contribution to the international upper mantle project and the international geodynamics project.* Geological Survey of Norway (NGU), Trondheim.

Henkel, H. 1991: Magnetic crustal structures in Northern Fennoscandia. *In* Wasilewski, P. & Hood, P. (eds.) Magnetic anomalies - land and sea. *Tectonophysics 192,* 57-79.

Hirschleber, H.B., Lund, C., Meissner, R., Vogel, A. & Weinrebe, W. 1975: Seismic investigations along the Blue Road traverse. *J. Geophys. 41,* 135-148.

Hunt, C., Moskowitz, B.M. & Banerje, S.K. 1995: Magnetic properties of rocks and minerals. In: Rock Physics and Phase Relations. A Handbook of Physical Constraints. *AGU Reference Shelf 3,* 189-204.

Hurich, C.A., Palm, H., Dyrelius, D. & Kristoffersen, Y. 1989: Deformation of the Baltic continental crust during Caledonide intracontinental subduction: Views from seismic reflection data. *Geology 17*, 423-425.

Iversen, T. 2000: Støy, kaos og sirkulasjonsregimer. *Cicerone 3*, 24-28.

Jessop, A. M. 1990: *Thermal geophysics*, Developments in Solid Earth Geophysics 17. Amsterdam, Elsevier Science Publishers B.V., 306 pp.

Juhojuntti, N., Juhlin, C. & Dyrelius, D. 2001: Crustal reflectivity underneath the Central Scandinavian Caledonides. *Tectonophysics 334*, 191-210.

Kanestrøm, R. & Haugland, K. 1971: Crustal structure in Southeastern Norway from Seismic Refraction measurements. *Scientific Report No. 5, Seismological Observatory, University of Bergen, Norway,* 72 pp.

Killeen, P. G. & Heier, K. S. 1975: Radioelement distribution and heat production in Precambrian granitic rocks, southern Norway. *Det Norske Videskaps-Akademi, I. Mat.-Naturv. Klasse. Skrifter, Ny Serie 35*, 1-32.

Kinck, J.J., Husebye, E.S. & Larsson, F.R. 1993: The Moho depth distribution in Fennoscandia and the regional tectonic evolution from Archean to Permian times. *Precambrian Research 64*, 23-51.

Koistinen, T., Stephens, M.B., Bogatchev, V., Nordgulen, Ø., Wennerstrøm, M. & Korhonen, J. 2001: *Geological map of the Fennoscandian Shield, scale 1:2 million.* Geological Surveys of Finland, Norway and Sweden and the Northwest Department of Natural Resources of Russia.

Korhonen, J.,V., Aaro, S., All, T., Elo, S., Haller, L.Å., Kääriäinen, J., Kulinich, A., Skilbrei, J.R., Solheim, D., Säävuori, H., Vaher, R., Zhdanova, L. & Koistinen, T. 2002a: Bouguer anomaly map of the Fennoscandian shield 1: 2 000 000. Geological Surveys of Finland, Norway and Sweden and Ministry of Natural Resources of Russian Federation.

Korhonen, J.,V., Aaro, S., All, T., Nevanlinna, H., Skilbrei, J.R., Säävuori, H., Vaher, R., Zhadanova, L. & Koistinen, T. 2002b: *Magnetic anomaly map of the Fennoscandian shield 1: 2 000 000.* Geological Surveys of Finland, Norway and Sweden and Ministry of Natural Resources of Russian Federation.

Korsman, K., Korja, T., Pajunen, M., Virransalo, P. & GGT/SVEKA Working Group 1999: The GGT/SVEKA Transect: Structure and evolution of the continental crust in the Paleoproterozoic Svecofennian Orogen in Finland. *International Geology Review,* 41, 287-333.

Kukkonen, I. T. & Lahtinen, R. 2001: Variation of radiogenic heat production rate in 2.8-1.8 Ga old rocks in the central Fennoscandian shield. *Physics of the Earth and Planetary Interiors 126*, 279-294.

Lachenbruch, A.H., 1968. Preliminary geothermal model of the Sierra Nevada. *Journal of Geophysical Research 73,* 6977-6989.

Lambeck, K., Smither, C. & Johnston, P. 1998: Sea-level change, glacial rebound and mantle viscosity for northern Europe. *Geophysical Journal International 134,* 102-144.

Lie, J.E. & Husebye, E.S. 1993: Seismic imaging of upper crustal basement faults in the Skagerrak Sea. *Tectonophysics 219,* 119-128.

Lindroos, H. & Henkel, H. 1978: Regional geological and geophysical interpretation of Precambrian structures in Northeastern Sweden. *Sver. geol. unders. C751,* 19 pp.

Ludwig; J.W., Nafe, J.E. and Drake, C.L., 1970: Seismic refraction. In: Maxwell., A. (ed.): *The sea,* Vo.4, Wiley, New York.

Lund, C. 1979: Crustal structure along the Blue Road Profile in northern Scandinavia. *Geologiska Föreningens i Stockholm Förhandlingar 101,* 191-204.

Mauring, E., Mogaard, J.O. & Olesen, O. 2003: Røst Basin Aeromagnetic Survey 2003 (RAS-03). Ra 3 aeromagnetic compilation. Data acquisition and processing report. *NGU Report 2003.070,* 20 pp.

McKenzie, D.P., Jackson, J. & Priestley, K. 2005: Thermal structure of oceanic and continental lithosphere. *Earth and Planetary Science Letters 233*, 337– 349.

Middleton, M. 1993: A transient method of measuring the thermal properties of rocks. *Geophysics 58,* 357-365

Midttømme, K., Hilmo, B.O., Skarphagen, H. & Nissen, A. 2000: Kartlegging av energipotensialet i berggrunn på kartblad Bekkestua, Bærum kommune: Varmeledningsevne til bergarter *NGU Report 2000.036,* 105 pp.

Midttømme, K., Ramstad, R.K., Solli, A., Sørdal, T. & Elvebakk, H. 2004: Grunnvarmekartlegging i Asker og Bærum. *NGU Report 2004.013,* 44 pp.

Midtun, R.D. 1988: Karasjok-grønnsteinsbeltet, Regional geofysisk og geologisk tolkning. *NGU Skrifter 88,* 19 pp.

Milne, G.A., Davis, J.L., Mitrovica, J.X., Scherneck, H.-G., Johansson, J.M., Vermeer, M., & Koivula, H. 2001: Space-geodetic constraints on glacial isostatic adjustment in Fennoscandia. *Science 291*, 2381-2385.

Milne, G.A., Mitrovica, J.X., Scherneck, H.-G., Davis, J.L., Johansson, J.M., Koivula, H., & Vermeer, M. 2004: Continuous GPS measurements of postglacial adjustment in Fennoscandia - 2. Modeling results. *Journal of Geophysical Research 109*, B02412, doi:10.1029/2003JB002619.

Mjelde, R., Sellevoll, M.A., Shimamura, H., Iwasaki, T. & Kanazawa, T. 1992: A crustal study off Lofoten, N. Norway, by use of 3D-component Ocean Bottom Seismographs. *Tectonophysics 212*, 269-288.

Mjelde, R., Sellevoll, M.A., Shimamura, H., Iwasaki, T. & Kanazawa, T. 1993: Crustal structure beneath Lofoten, N. Norway, from vertical incidence and wide-angle seismic data. *Geophysical Journal International 114*, 116-126.

Mjelde, R., Kodaira, S., Shimamura, H., Kanazawa, T., Shiobara, H., Berg, E.W. & Riise, O. 1997: Crustal structure of the central part of the Vøring Basin, mid-Norway margin, from ocean bottom seismographs. *Tectonophysics 277*, 235-257.

Mjelde, R., Digranes, P., Shimamura, H., Shiobara, H., Kodaira, S., Brekke, H., Egebjerg, T., Sørenes, N. & Thorbjørnsen, S. 1998: Crustal structure of the northern part of the Vøring Basin, mid-Norway margin, from wide-angle seismic and gravity data. *Tectonophysics 293*, 175-205.

Mjelde, R., Digranes, P., van Schaack, M., Shimamura, H., Shiobara, H., Kodaira, S. & Næss O. 2001: Crustal structue of the outer Vøring Plateau, offshore Norway, from ocean bottom seismic and gravity data. *Journal of Geophysical Research 106*, 6769-6791.

Mjelde, R., Kasahara, J., Shimamura, H., Kamimura, A., Kanazawa, T., Kodaira, S., Raum, T. & Shiobara, H. 2002: Lower crustal seismic velocity-anomalies; magmatic underplating or serpentinized peridotite? Evidence from the Vøring Margin, NE Atlantic. *Marine Geophysical Research 23*, 169-183.

Mjelde, R., Raum, T., Digranes, P., Shimamura, H., Shiobara, H. & Kodaira, S. 2003a: V_p/V_s ratio along the Vøring Margin, NE Atlantic, derived from OBS data: implications on lithology and stress field. *Tectonophysics 369*, 175-197.

Mjelde, R., Shimamura, H., Kanazawa, T., Kodaira, S., Raum T. & Shiobara, H. 2003b: Crustal lineaments, distribution of lower crustal intrusives and structural evolution of the Vøring Margin, NE Atlantic; new insight from wide-angle seismic models. *Tectonophysics 369*, 199-218.

Mjelde, R., Raum, T., Breivik, A., Shimamura, H., Mural, Y., Takanami, T. & Faleide, J.I. 2005: Crustal structure of the Vøring margin, NE Atlantic: a review of geological implications based on recent OBS data. In: Doré, A.G., Vining, B.A. (Eds.), *Petroleum Geology: North-West Europe and Global Perspectives - Proceedings of the 6th Petroleum Geology Conference.* Geological Society Special Publication. The Geological Society, London, pp. 803– 813.

Mørk, M.B.E., McEnroe, S.A. & Olesen, O. 2002: Magnetic susceptibility of Mesozoic and Cenozoic sediments off Mid Norway and the role of siderite: implications for interpretation of high-resolution aeromagnetic anomalies. *Marine and Petroleum Geology 19,* 1115-1126.

Naidu P. S. & Mathew M. P. 1998: Correlation filtering: a terrain correction method for aeromagnetic maps with application. *Journal of Applied Geophysics 32,* 269-277.

Neumann, E.-R. 1994: The Oslo Rift: P-T relations and lithospheric structure. *Tectonophysics 240,* 159-172.

NGU laboratorie rapport 0297-2005. Varmeledningsevne for prøver fra borehull Lærdal 2, Lærdalstunnelen.

NGU laboratorie rapport 0311-2005. Varmeledningsevne for prøver fra borehull Lærdal 1, Lærdalstunnelen.

NGU laboratorie rapport 0311-2005. Varmeledningsevne for prøver fra Gåvålivatnet Hjerkinn og Løkken.

Niskanen, E. 1939: On the upheavel of land in Fennoscandia. *Ann. Acad. Sci. Fenn., Ser. A 53*, 1-30.

Okubo, Y, Graft, R. J., Hansen, R.O., Ogawas, K. and Tsu, H. 1985: Curie point depths of the Island of Kyushu and surrounding areas, Japan. *Geophysics 53,* 481-494.

Olesen, O. 2005: Crystalline basement in the Norwegian sector of the North Sea. *In:* Olesen, O. et al. *Kontiki Annual Report 2004, Continental crust and heat generation in 3D.* NGU Report 2005.008, 50-55.

Olesen, O. & Sandstad, J.S. 1993: Interpretation of the Proterozoic Kautokeino Greenstone Belt, Finnmark, Norway from combined geophysical and geological data. *Nor. geol. unders. Bull. 425,* 41-62.

Olesen, O., Roberts, D., Henkel, H., Lile, O.B. & Torsvik, T.H. 1990: Aeromagnetic and gravimetric interpretation of regional structural features in the Caledonides of West Finnmark and North Troms, northern Norway. *Norges geologiske undersøkelse Bulletin 419,* 1-24.

Olesen, O., Gellein J., Håbrekke H., Kihle O., Skilbrei J. R., & Smethurst M. 1997a: *Magnetic anomaly map Norway and adjacent ocean areas, scale 1:3 million* Geological Survey of Norway (NGU), Trondheim.

Olesen, O., Torsvik, T.H., Tveten, E., Zwaan, K.B., Løseth H. & Henningsen, T. 1997b: Basement structure of the continental margin in the Lofoten-Lopphavet area, northern Norway: constraints from potential field data, on-land structural mapping and palaeomagnetic data. *Norsk Geologisk Tidsskrift 77,* 15-33.

Olesen, O., Lundin, E., Nordgulen, Ø., Osmundsen, P.T., Skilbrei, J.R., Smethurst, M.A., Solli, A., Bugge, T. & Fichler, C. 2002: Bridging the gap between the onshore and offshore geology in Nordland, northern Norway. *Norwegian Journal of Geology 82*, 243-262.

Olesen, O., Ebbing, J., Lundin, E., Skilbrei, J.R., Smethurst, M.A. & Torsvik, T.H. 2004: Interpretation of the Ra 3 potential field data along the Lofoten-Vøring continental margin, Part 2. NGU Report 2004.027.

Olesen, O., Ebbing, J., Elvebakk, H., Koziel, J., Lundin, E., Midttømme, K., Nordgulen, Ø., Rønning, J.S., Skilbrei, J.R., Slagstad, T., Wissing, B. & Cramer, J. 2005: Kontiki Annual Report 2004, Continental Crust and Heat Generation in 3D. *NGU Report 2005.008,* 70 pp.

Olesen O., Gernigon, L., Ebbing J., Mogaard J., Pascal C. & Wienecke S., 2006, Interpretation of aeromagnetic data along the Jan Mayen Fracture Zone, JAS-05: Geological Survey of Norway. *NGU Report 2006.018*, 161 pp.

Olsen, K.H., Baldridge, W.S., Larsen, B.T., Neumann, E.-R. & Ramberg, I.B. 1987: A lithospheric transect across the Oslo palaeorift. *EOS, Trans. Am. Geophys. Union 68*, 1480.

Orkla Industrier, Grubeseksjonen: Orkla Vest, hull nr 1, 18 s.

Ormaasen, D. E. 1976: *Geochemistry and petrology of the mangeritic rocks in Lofoten−Vesterålen* Cand. real./M.Sc. thesis, Universitetet i Oslo.

Osmundsen, P.T., Sommaruga, A., Skilbrei, J.R. & Olesen, O. 2002: Deep structure of the Mid Norway rifted margin. *Norwegian Journal of Geology 82*, 205-224.

Osmundsen, P.T., Bøe, R., Davidsen, B., Ebbing, J., Eide, E.A., Hendriks, B.W.H., Redfield, T.F. & Smelror, M. 2006: The recycling of an orogen: provenance and routing of detritus from Norway to the Mid-Norwegian margin. *NGU Report 2006.022*.

Ottemöller, L. & Midzi, V. 2003: The crustal structure of Norway from inversion of teleseismic receiver functions. *Journal of Seismology* 7, 35-48.

Parker, R.L. 1972: The rapid calculation of potential anomalies, *Geophys. J. Royal Astr. Society 31*, 447-455.

Parsons B. and Sclater J. 1977: An analysis of the variation of ocean floor bathymetry and heat flow with age, *Journal of Geophysical Research 82,* 803-827.

Perez-Gussinye, M., Lowry, A.R., Watts, A.B. & Velicogna, I. 2004: On the recovery of effective elastic thickness using spectral methods: Examples from synthetic data and from the Fennoscandian shield. *Journal of Geophysical Research 109*, B10409, doi: 10.1029/2003JB002788.

Pascal, C. Roberts, D. & Gabrielsen, R.H. 2005: Quantification of neotectonic stress orientations and magnitudes from field observations in Finnmark, northern Norway. *Journal of Structural Geology* 27, 859-870.

Powell, W.G., Chapman, D.S., Balling, N. and Beck, A.E., 1988: Continental heat-flow density. In: Haenel, R. *et al.* (eds.), Handbook of Terrestrial Heat-flow Density Determination, 167-222. Kluwer Academic Publ. 486 pp.

Ramberg, I.B. 1976: Gravimetry interpretation of the Oslo Graben and associated igneous rocks. *Nor. geol. unders. 325*, 194 pp.

Ranalli, G. 1995: *Rheology of the Earth*, Chapman and Hall, New-York, 413 pp.

Raum, T., Mjelde, R., Digranes, P., Shimamura, H., Shiobara, H., Kodaira, S., Haatvedt, G., Sørenes, N. & Thorbjørnsen, T. 2002: Crustal structure of the southern part of the Vøring Basin, mid-Norway, from wide-angle seismic and gravity data. *Tectonophysics 355*, 99-126.

Redfield, T. F., Osmundsen, P. T. & Hendriks, B. W. H. 2005: The role of fault reactivation and growth in the uplift of western Fennoscandia. *Journal of the Geological Society, London,* 162, 1013-1030.

Ritter, U., Zielinski, G.R., Weiss, H.M., Zielinski, R.L.B., and Sættem, J. 2004: Heat flow in the Vøring Basin, Mid-Norwegian Shelf. *Petroleum Geoscience 10,* 353-365.

Rudnick, R. L. & Gao, S. 2003: The composition of the continental crust. In: Rudnick, R. L. (ed.) *The Crust.* Treatise on Geochemistry 3, Oxford, Elsevier-Pergamon, 1-64.

Rybach, L. 1988: Determination of heat production rate. In: Hänel, R., L. Rybach & L. Stegena eds. *Handbook of Terrestrial Heat-Flow Determination.* Dordrecht, Kluwer Academic Publishers, 125-142.

Raade, G. 1973: *Distribution of radioactive elements in the plutonic rocks of the Oslo region.* Hovedoppgave/M.Sc. thesis, Universitetet i Oslo, 162 pp.

Shuey R., Schlechinger D., Tripp A. & Alley L. 1977: Curie depth determination from aeromagnetic spectra. *Geophys. J. R. Astron. Soc. 50,* 75-102.

Sigmond, E. M. O. 2002: Geological Map, Land and Sea Areas of Northern Europe, Scale 1:4 million, Geological Survey of Norway, Trondheim.

Sindre, A. 1993: *Regional tolkning av geofysiske data, kartblad Arendal.* NGU Report 92.213, 30 pp.

Skilbrei, J.R. 2005: Basement depth map from the Barents Sea and Svalbard. *In:* Olesen, O. et al. *Kontiki Annual Report 2004, Continental crust and heat generation in 3D.* NGU Report 2005.008, 56-61.

Skilbrei, J.R. & Olesen, O. 2005: Deep structure of the Mid-Norwegian shelf and onshore-offshore correlations: Insight from potential field data. In: B.T.G. Wandås, E.A. Eide, F. Gradstein, & J.P. Nystuen (Eds), *Onshore-Offshore relationships on the North Atlantic Margin.* Norwegian Petroleum Society (NPF), Special Publication 12. Elsevier, Amsterdam, 43-68.

Skilbrei, J.R. & Sindre, A. 1991: Tolkning av gravimetri langs ILP-profilet, Hemne-Storlien. *NGU Report 91.171,* 24 pp.

Skilbrei, J.R., Kihle, O., Olesen, O., Gellein, J., Sindre, A., Solheim, D. & Nyland, B., 2000: *Gravity anomaly map Norway and adjacent ocean areas, 1:3 Million.* Geological Survey of Norway (NGU), Trondheim.

Skilbrei, J.R., Olesen, O., Osmundsen, P.T., Kihle, O., Aaro, S. & Fjellanger, E. 2002: A study of basement structures and onshore-offshore correlations in Central Norway. *Norwegian Journal of Geology 82,* 263-279.

Skogseid, J., Pedersen, T., Eldholm, O. & Larsen, B.T. 1992: Tectonism and magmatism during NE Atlantic continental break-up: the Vøring margin. *In:* B.C. Story, T. Alabaster and R.J. Plankhurst (eds.) *Magmatism and the Causes of Continental Break-up.* Geological Society, London, Special Publications, 68, 305-320.

Slagstad, T. 2005: Heat flow. *In:* Olesen, O. et al. *Kontiki Annual Report 2004, Continental crust and heat generation in 3D.* NGU Report 2005.008, 21-24.

Spector A. % Grant 1970: Application of high sensitivity aeromagnetic surveying to offshore petroleum exploration. *Geophysical Prospecting 18,* 474-475.

Stephansson, O. 1989: Stress measurements and modelling of crustal rock mechanics in Fennoscandia. In *Earthquakes at North-Atlantic passive margins: neotectonics and postglacial rebound,* Gregersen, S. & Basham, P.W. (eds.), Kluwer Academic Publishers, Dordrecht, The Netherlands, 213-229.

Swanberg, C. A., Chessman, M. D., Simmons, G., Smithson, S. B., Grønlie, G. & Heier, K. S. 1974: Heat-flow - heat-generation studies in Norway. *Tectonophysics 23*, 31-48.

Schmidt, J. 2000: Deep seismic studies in the western part of the Baltic shield. *Uppsala Dissertations from the Faculty of Science and Technology 24*.

Thunhead, H. & Olsson, O. 2004: Borehole corrections for a thick resistivity probe. *JEEG 9,* 217-224.

Tryti, J. & Sellevoll, M.A. 1977: Seismic crustal study of the Oslo Rift. *Pure and Applied Geophysics 115*, 1061-1085.

Vogel A. & Lund, C.-E. 1971: Profile Section 2-3. *In* Vogel, A. (ed.) *Deep Seismic Sounding in Northern Europe*, 62-75. University of Uppsala, Swedish Natural Science Research Council, Stockholm.

Vogt, P.R., Taylor, P., Kovacs, L.C. & Johnson, G.L. 1979: Detailed aeromagnetic investigations of the Artic Basin. *Journal of Geophysical Research 84,* 1071 – 1079.

Vogt, P.R., Johnson, G.L. & Kristjansson, L. 1980: Morphology and magnetic anomalies north of Iceland. *Joutnal og Geophysics 47,* 67 – 80.

Wessel, P. & Husebye, E.S. 1987: The Oslo Graben gravity high and taphrogenesis. *Tectonophysics 142*, 15-26.

Wolff, F.C. 1979: Beskrivelse til de bergrunngeologiske kart Trondheim og Østersund 1:250,000. *Norges geologiske undersøkelse 353*, 76 pp.

Wolff, F.C. 1984: Regional geophysics in the Central Norwegian Caledonides. *Norges geologiske undersøkelse Bulletin 397,* 1-27.

APPENDIX A

PHOTOGRAPHS OF NPD CORES

Trond Slagstad and Cécile Barrère, NGU

NPD core samples

Well	16/1-4
Depth (m)	1937
UTM_E	459562.76
UTM_N	6525418.88
Zone	31

5 cm

16/1-4, 1937m Utsira High, North Sea
Medium- to coarse-grained rock gabbro made up of orange feldspar and hornblende in subequal amounts, with a magmatic texture. A few small, calcite-filled veins and vugs.

Well	16/3-2
Depth (m)	2017.7
UTM_E	488031.78
UTM_N	6516490.64
Zone	31

5 cm

16/3-2, 2017.7m North Sea

Medium-grained, red granite consisting of fine-grained, whitish-red to red feldspar and coarser (<1 cm) irregular, but generally rounded, grains of quartz. The granite is unfoliated and spotted with 1–4 mm black, unoriented specks of hornblende, homogeneously distributed in the rock.

Well	16/4-1
Depth (m)	2907.4
UTM_E	449959.99
UTM_N	6500262.06
Zone	31

5 cm

16/4-1, 2907.4m Utsira High, North Sea

Compositely layered fine-grained, light grey quartzite and dark grey siltstone. Layer thickness varies from ca. 1 mm up to several cm. The rock is criss-crossed by thin, calcite-filled vein, dominantly subvertical although subhorizontal veins are also found. The subvertical veins appear to form en echelon patterns, and some of the veins are only developed in the quartzite but are not visible in the siltstone. This effect is most likely caused by differences in rheology of the two rock types. Some cm-thick, green to orange layers, slightly oblique to the layering in the rock appear to consist of epidote and albite (?) and are most likely metasomatic.

Well	16/4-1
Depth (m)	2908.6
UTM_E	449959.99
UTM_N	6500262.06
Zone	31

5 cm

16/4-1, 2908.6m Utsira High, North Sea

Fine-grained granite, grey with a reddish hue. The granite is unfoliated and spotted with 1–3 mm black, unoriented specks of hornblende, homogeneously distributed in the rock.

16/5-1, 1929.3m Utsira High, North Sea
Fine-grained, unfoliated, dark red granite with intergrown, irregular (i.e., in matrix) hornblende. There are some cracks in the sample with discontinuous, thin, bleached margins, indicating some alteration.

Well	16/6-1
Depth (m)	2059.7
UTM_E	494913.16
UTM_N	6506985.91
Zone	31

├─────── 5 cm ───────┤

Well	16/6-1
Depth (m)	2059.7
UTM_E	494913.16
UTM_N	6506985.91
Zone	31

├─────── 5 cm ───────┤
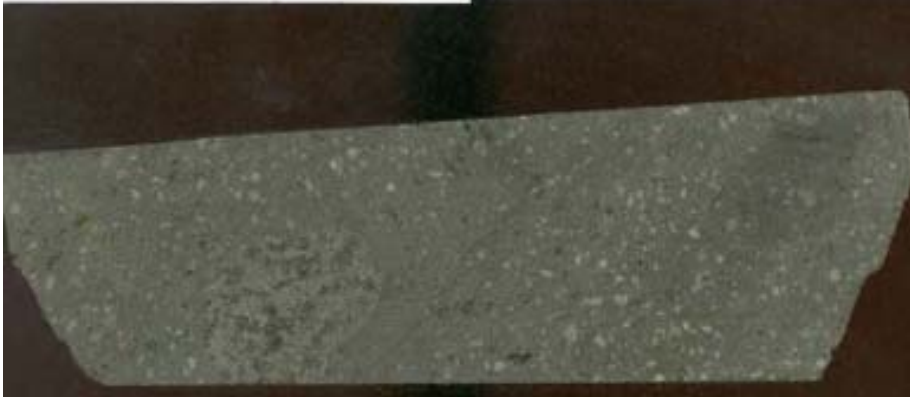
16/6-1, 2059.7m Utsira High, North Sea

Fine-grained, unfoliated, grey rock with abundant small (ca. 1 mm) phenocrysts(?) of plagioclase, specks of hornblende(?), and larger (ca. 2–4 mm) phenocrysts(?) of quartz. The rock also contains a small (ca. 4 cm) inclusion of slightly coarser grey rock, probably a xenolith. The sample is most likely a volcanic rock, possibly an andesite.

Well	17/3-1
Depth (m)	2849.5
UTM_E	546414.75
UTM_N	6531280.15
Zone	31

5 cm

17/3-1, 2849.5m Stord Basin, North Sea

Dark green fault breccia with abundant calcite-filled veins and vugs. The rock appears to contain quite abundant chlorite and possibly epidote, but little quartzofeldspathic material, making it distinct from the other sample from this core (at 2850.7m).

From NPD's Fact-page: "…drilled […] in metamorphic basement rock, dated 410 My".

Well	17/3-1
Depth (m)	2850.7
UTM_E	546414.75
UTM_N	6531280.15
Zone	31

5 cm
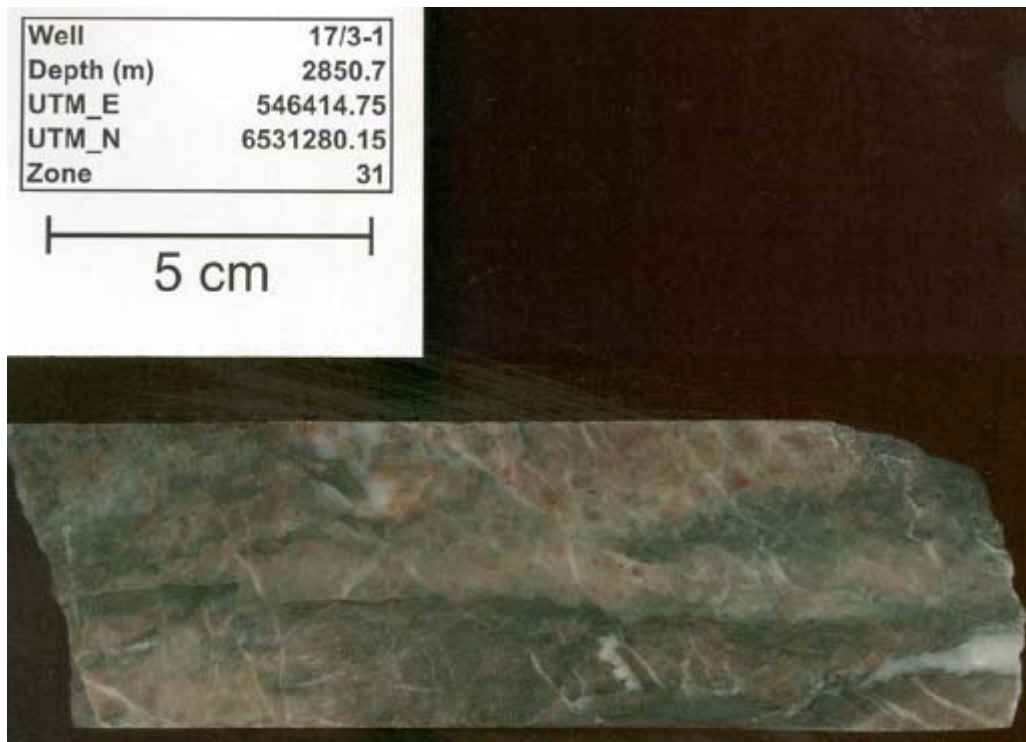
17/3-1, 2850.7m Stord Basin, North Sea

Fault breccia consisting predominantly of medium-grained feldspar, altered feldspar and epidote, as well as layers/inclusions of mafic material. The breccia is cross-cut by numerous calcite-filled veins, some of which offset the breccia, and microveins.

Well	18/11-1
Depth (m)	2082.3
UTM_E	590452.02
UTM_N	6437964.92
Zone	31

5 cm

18/11-1, 2082.3m Stavanger Platform, North Sea

Dark green, microcrystalline rock with rare, scattered plagioclase(?) phenocrysts, typically 1–2 mm across. The rock is criss-crossed by numerous, white, hairline veins that locally are calcite-filled.

25/7-1S, 3548.2m North Sea

Breccia with irregular fragments typically ca. 5 cm long of dark red, microcrystalline calcareous siltstone(?). The fragments have slightly rounded edges. The groundmass consists of some microcrystalline, calcareous, dark green rock, and several irregular patches of microcrystalline, calcareous, dark red rock that appear to transect calcite-filled veins which in turn cut the siltstone fragments. The dark red siltstone and microcrystalline patches are difficult to distinguish, but in general the former appears slightly coarser grained.

Well	25/7-1S
Depth (m)	3554.3
UTM_E	458330.76
UTM_N	6574928.80
Zone	31

5 cm

25/7-1S, 3554.3m North Sea

Faintly banded, fine-grained, grey sandstone. The sandstone is criss-crossed by numerous thin veins, with dark green, white or brown infilling. The brown infilling is calcareous.

Well	25/11-17
Depth (m)	2259.5
UTM_E	470469.44
UTM_N	6546709.03
Zone	31

5 cm
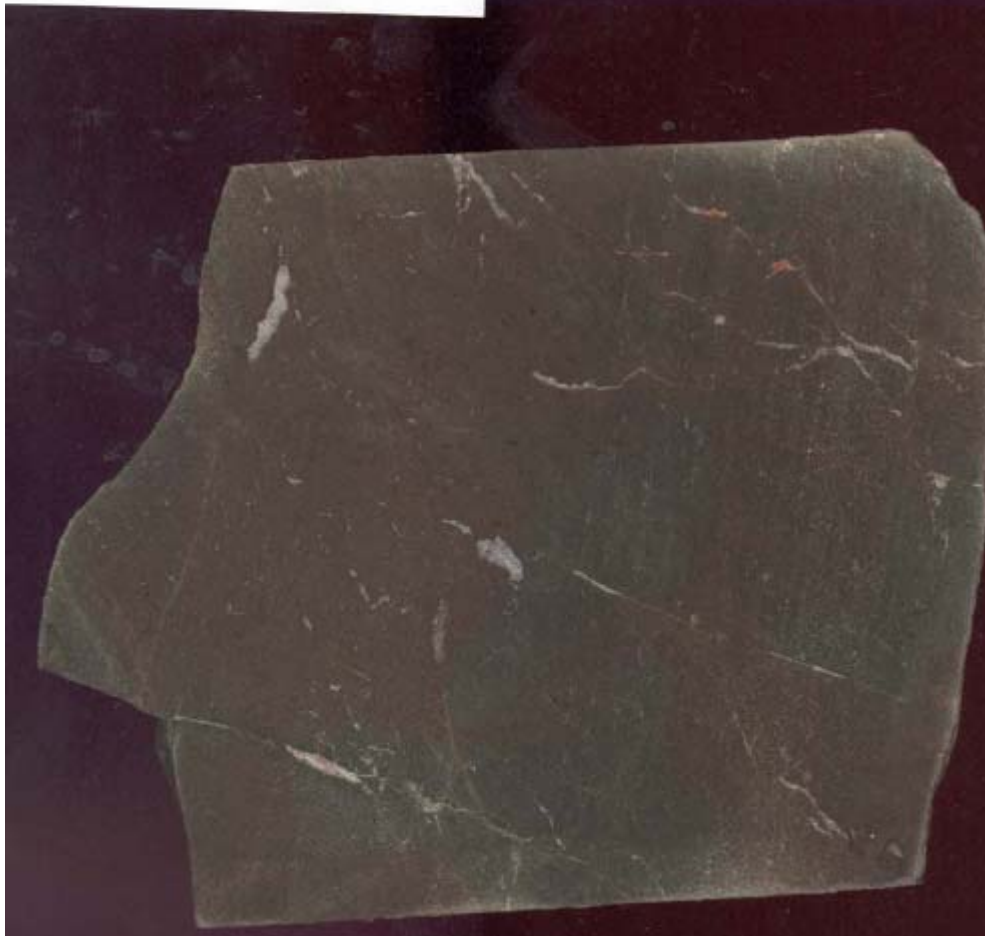
25/11-17, 2259.5m Balder/Grane area, North Sea

Microcrystalline to fine-grained, dark brown to grey siltstone with numerous short (<2 cm), irregular veins and vugs filled with white and more rarely red material, identified as calcite and possibly some zeolite.

Well	35/3-4
Depth (m)	4088.3
UTM_E	545989.90
UTM_N	6859631.80
Zone	31

5 cm
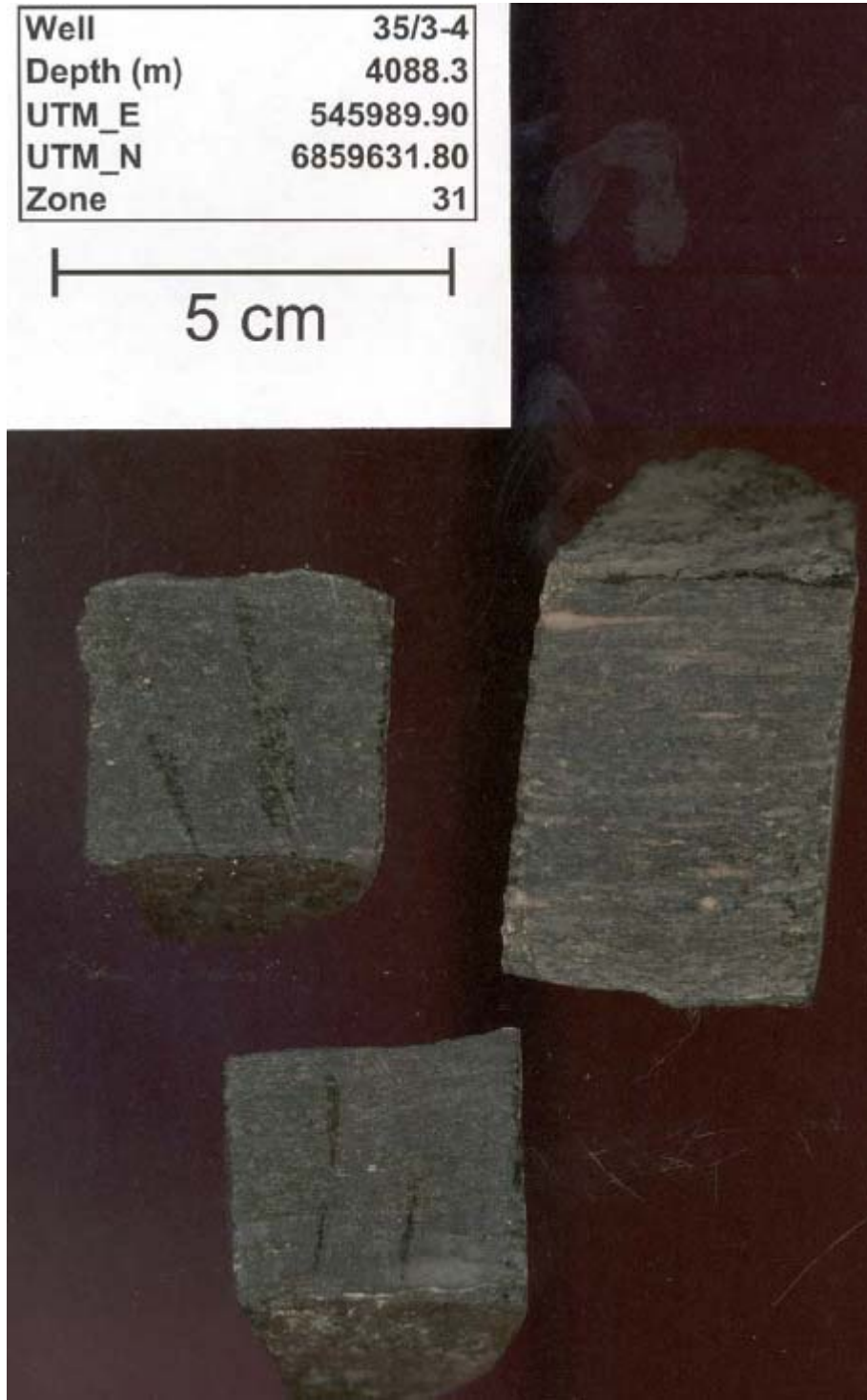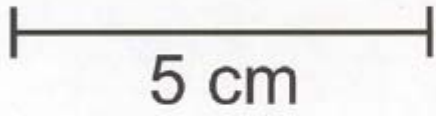
35/3-4, 4088.3m North Sea
Fine-grained, dark grey biotite-rich gneiss with several, concordant mm-sized patches and veins of granitic material. The rock contains a fair amount of pyrite, some with well-developed crystal faces, typically 1–2 mm across but locally up to 5 mm.
From NPD's Fact-page: "…before reaching basement rocks of Caledonian age"

35/9-1, 2313.6m North Sea

Fine-grained, dark green breccia. Colour varies from light grey, green, dark green to dark grey, giving the rock a speckled appearance. The light grey and green material is calcareous. The breccia contains some mm-thick, calcite-filled veins. No larger clasts can be observed.

36/1-1, 5212.3m Block 36/1, North Sea

Fine-grained, grey, biotite-rich, quartzo-feldspathic gneiss. Abundant biotite laths impart the gneiss with a strong foliation.

Well	6305/12-2
Depth (m)	3158.3
UTM_E	635050.51
UTM_N	6990772.25
Zone	31

5 cm

6305/12-2, 3158.3m Norwegian Sea

Grey fault(?) breccia consisting dominantly of angular fragments of siltstone, separated by thin "veins" of dark material. Some fragments of quartz and some calcite that appears to pre-date brecciation. Numerous calcite-filled veins and vugs. The breccia appears to contain abundant chlorite.

Well	6306/10-1
Depth (m)	3158.5
UTM_E	365416.35
UTM_N	7006088.05
Zone	32

5 cm

6306/10-1, 3158.5m Frøya High, Norwegian Sea
Fine- to medium-grained, unfoliated leucogabbro with a few calcite-filled cracks.

Well	6306/10-1
Depth (m)	3159.2
UTM_E	365416.35
UTM_N	7006088.05
Zone	32

5 cm
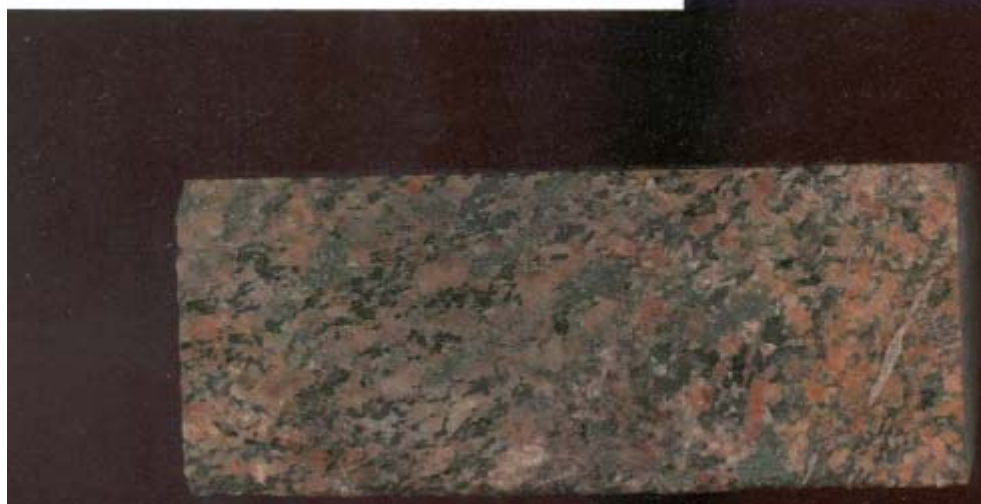
6306/10-1, 3159.2m Frøya High, Norwegian Sea
Fine- to medium-grained, unfoliated leucogabbro with a few calcite-filled cracks.

Well	6407/10-3
Depth (m)	2972.1
UTM_E	417314.23
UTM_N	7109795.67
Zone	32

5 cm

6407/10-3, 2972.1m Norwegian Sea
Fine-grained, unfoliated, dark red granite with small specks (<1 mm) of hornblende.

Well	6609/7-1
Depth (m)	1944.7
UTM_E	500929.07
UTM_N	7366433.20
Zone	32

5 cm
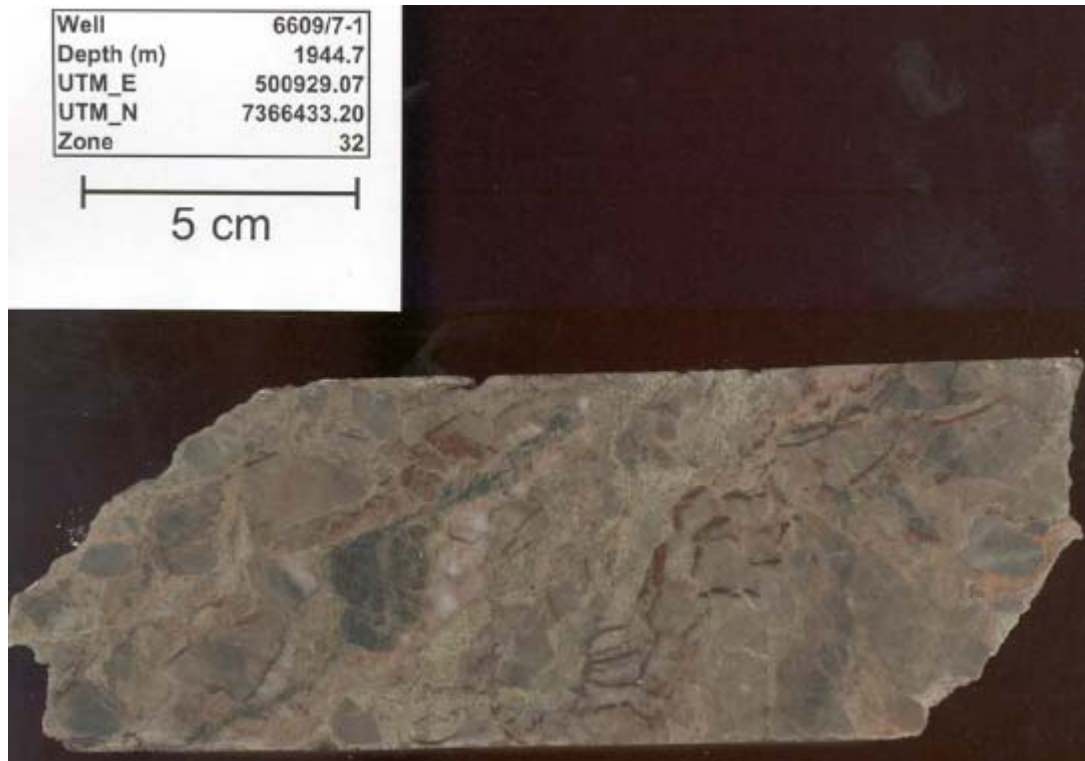
6609/7-1, 1944.7m Norwegian Sea

Breccia with angular fragments of microcrystalline quartzite(?). The quartzite is grey with a reddish hue, and the fragments range in size from a few mm up to several cm. The matrix consists of crumbly, microcrystalline, green material, and minor amounts of red to brown calcareous material.

Well	6609/7-1
Depth (m)	1945.8
UTM_E	500929.07
UTM_N	7366433.20
Zone	32

5 cm
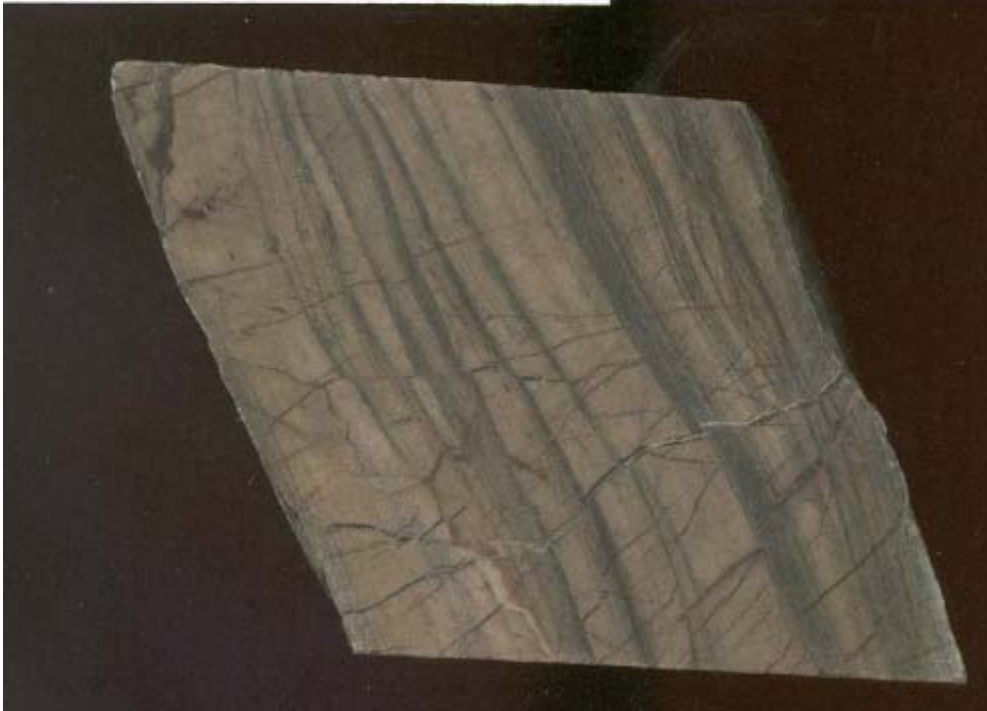
6609/7-1, 1945.8m Norwegian Sea

Laminated metasediment consisting of layers, typically < 1 cm thick, of microcrystalline sandstone/quartzite(?) with a orange hue, and thinner layers of grey, microcrystalline siltstone(?). The rock is extensively cracked with calcite-filled veins. Possible that the sandstone/siltstone is calcareous, but the large number of small calcite-filled veins makes it difficult to discern which part of the rock fizzes when exposed to HCl.

Well	7120/1-1
Depth (m)	4002.2
UTM_E	454909.86
UTM_N	7980020.26
Zone	34

5 cm
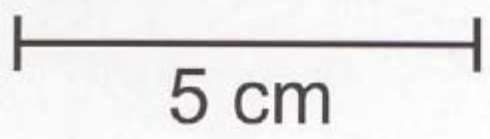
7120/1-1, 4002.2m Loppa High, Norwegian Sea

Fine-grained, foliated, dark grey orthogneiss (?) with 1–2 mm, black amphibole porphyroblasts/phenocrysts(?) scattered homogeneously throughout the rock.

Well	7120/12-2
Depth (m)	4675.8
UTM_E	492668.97
UTM_N	7891571.43
Zone	34

5 cm

7120/12-2, 4675.8m Norwegian Sea

Dark grey mylonite, with numerous thin (<1 mm) and some thicker (<1 cm) leucocratic veins, concordant with the foliation in the rock.

Well	7120/12-2
Depth (m)	4678.2
UTM_E	492668.97
UTM_N	7891571.43
Zone	34

5 cm

7120/12-2, 4678.2m Norwegian Sea

Fine-grained, grey mylonite with diffuse leucocratic bands and rare K-feldspar porphyroclasts. It is conceivable that some of the leucocratic bands represent stretched out porphyroclasts.

Well	7128/4-1
Depth (m)	2527.2
UTM_E	538226.27
UTM_N	7938285.08
Zone	35

5 cm

7128/4-1, 2527.2m Finnmark Øst area, Barents Sea
Laminated shaly sandstone, with apparent upward-fining layers of fine-grained sandstone (at base) through siltstone to shale (at top). Locally the sandstone layers appear to have erosional bases, indicated by what appears to be scour marks filled with relatively coarse sandstone.

Well	7128/4-1
Depth (m)	2528.1
UTM_E	538226.27
UTM_N	7938285.08
Zone	35

5 cm
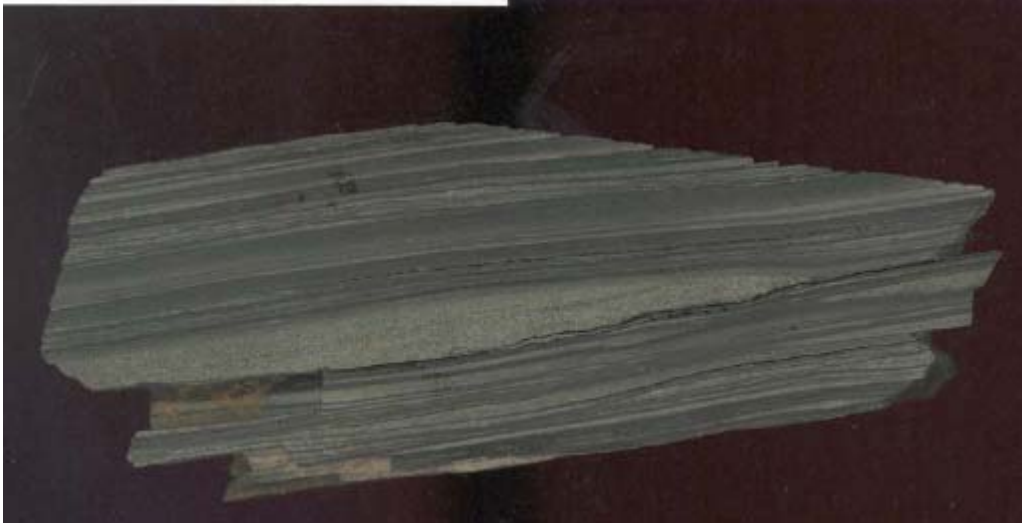
7128/4-1, 2528.1m Finnmark East area, Barents Sea
Laminated fine-grained sandstone and shale, quite similar to 7128/4-1, 2527.2m, but without the apparent sedimentary features.

Well	7128/6-1
Depth (m)	2540.5
UTM_E	700178.77
UTM_N	8060891.68
Zone	33

5 cm

7128/6-1, 2540.5m Finnmark East area, Finnmark Platform, Norwegian Sea

Fine- to medium-grained, layered sandstone, with alternating layers of rusty brown sandstone (0.5–1.5 cm thick) and grey sandstone (0.5–1 cm thick). No differences in grain size or mineralogy between the layers can be observed in hand-sample. The interfaces between the layers are typically sharp but irregular, although locally the contacts appear gradational.

Well	7226/11-1
Depth (m)	5198.8
UTM_E	482263.45
UTM_N	8015817.52
Zone	35

5 cm

7226/11-1, 5198.8m Norsel High, Bjarmeland Platform, Barents Sea

Strongly foliated, medium-grained, biotite-rich schist (amphibolite?) with pods and layers of quartz. The rock also contains sulphides, most likely pyrite, aligned with the foliation.

APPENDIX B

PHOTOGRAPHS OF THE TEMPERATURE LOGGING EQUIPMENT

Niels Balling and Niels Breiner
Department of Earth Sciences, University of Aarhus,
Denmark. (Photos by Jan S. Rønning, NGU)

Figure B1. The temperature logging system in the field, here at Gåvålivatnet, Hjerkinn.

Figure B2. The logging winch is installed inside the logging car together with the electronic steering and recording unit.

Figure B3. The electronic unit. Measured temperatures together with other recorded parameters (depth, weight of probe and cable and logging speed) can be followed in real time on the screen.

Figure B4. The electronic depth counter. An additional mechanical counter is also used (on top of the unit with the small white wheel.

APPENDIX C

PLOTS OF UNFILTERED TEMPERATURES AND TEMPERATURE GRADIENTS

Niels Balling and Niels Breiner
Department of Earth Sciences, University of Aarhus,
Denmark
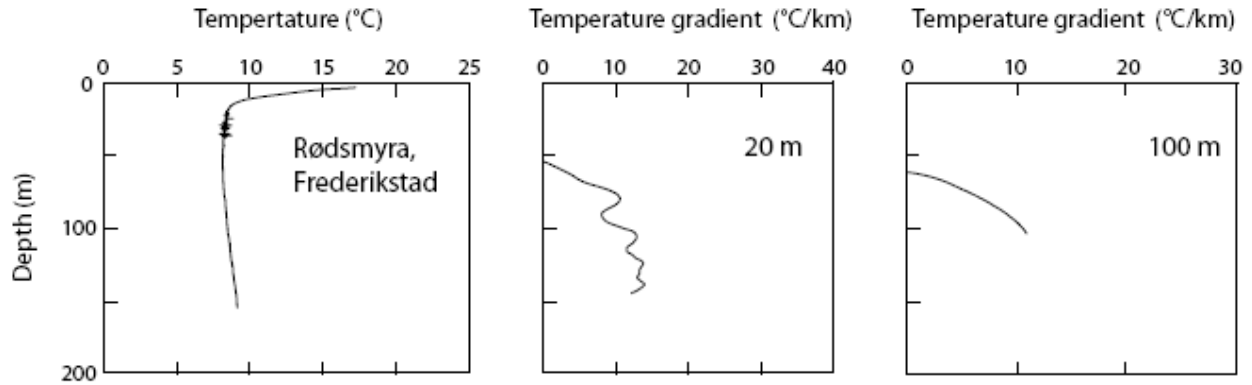
Figure C1. Temperature unfiltered and mean interval temperature gradients as indicated for borehole Rødsmyra, Fredrikstad.
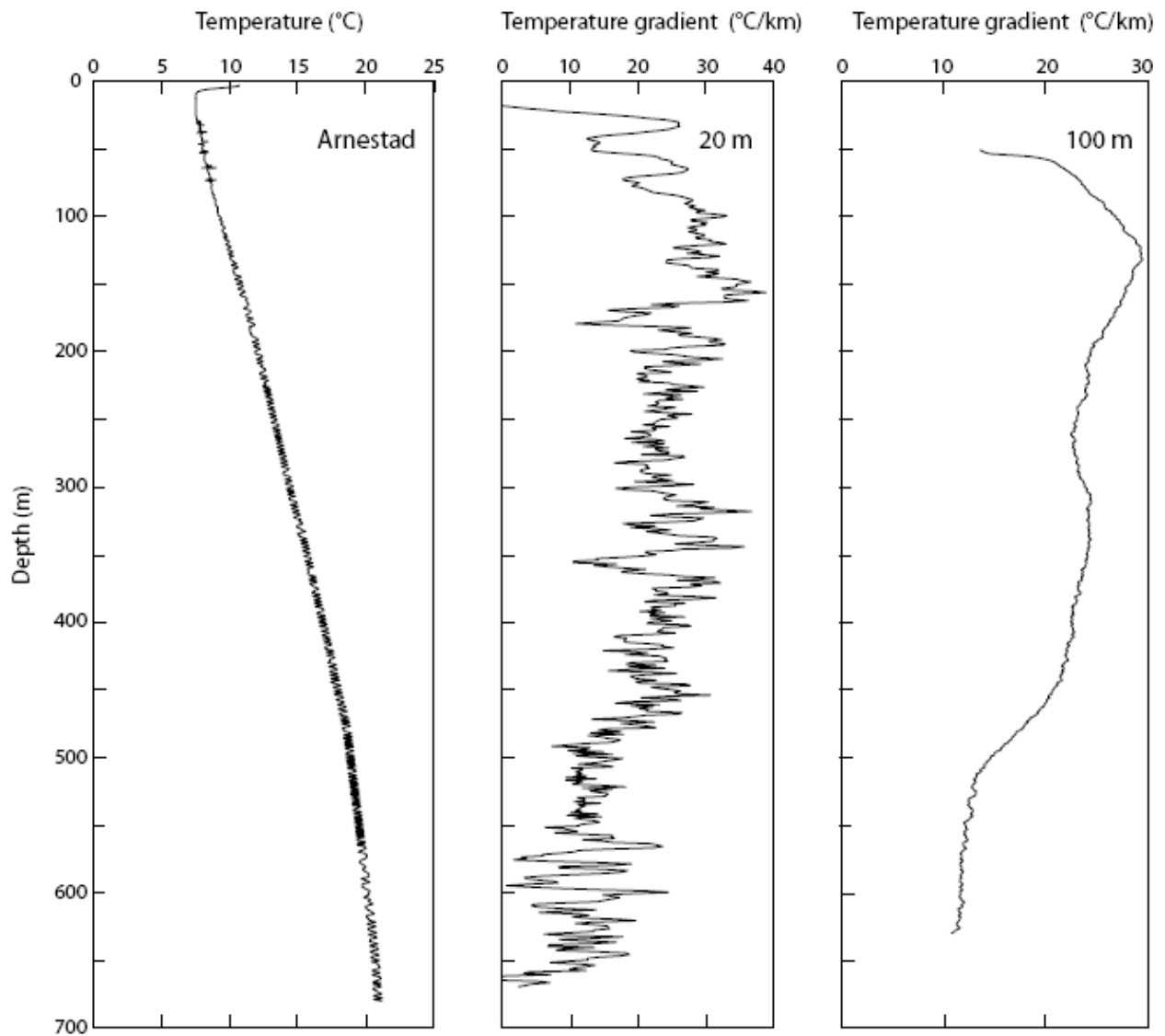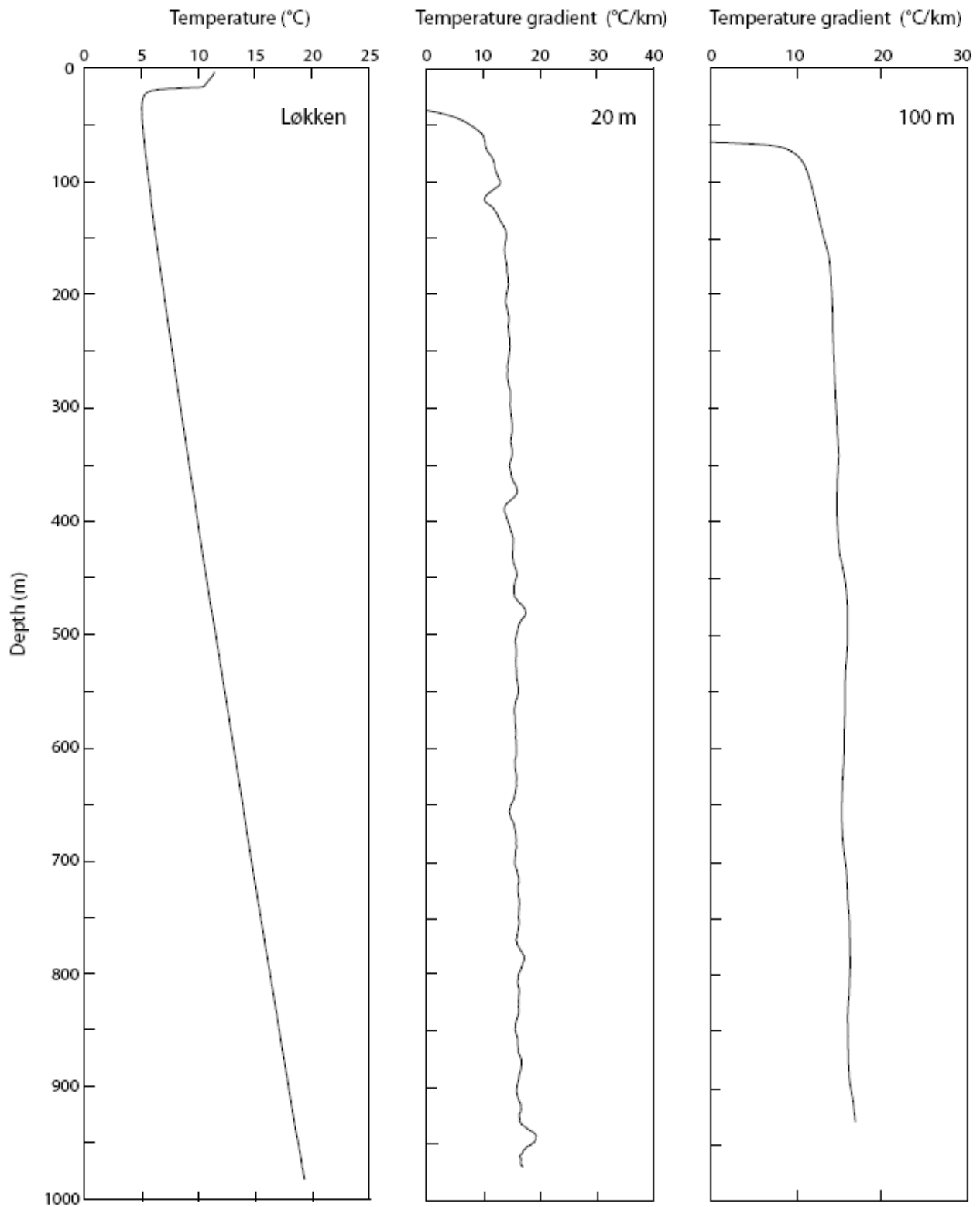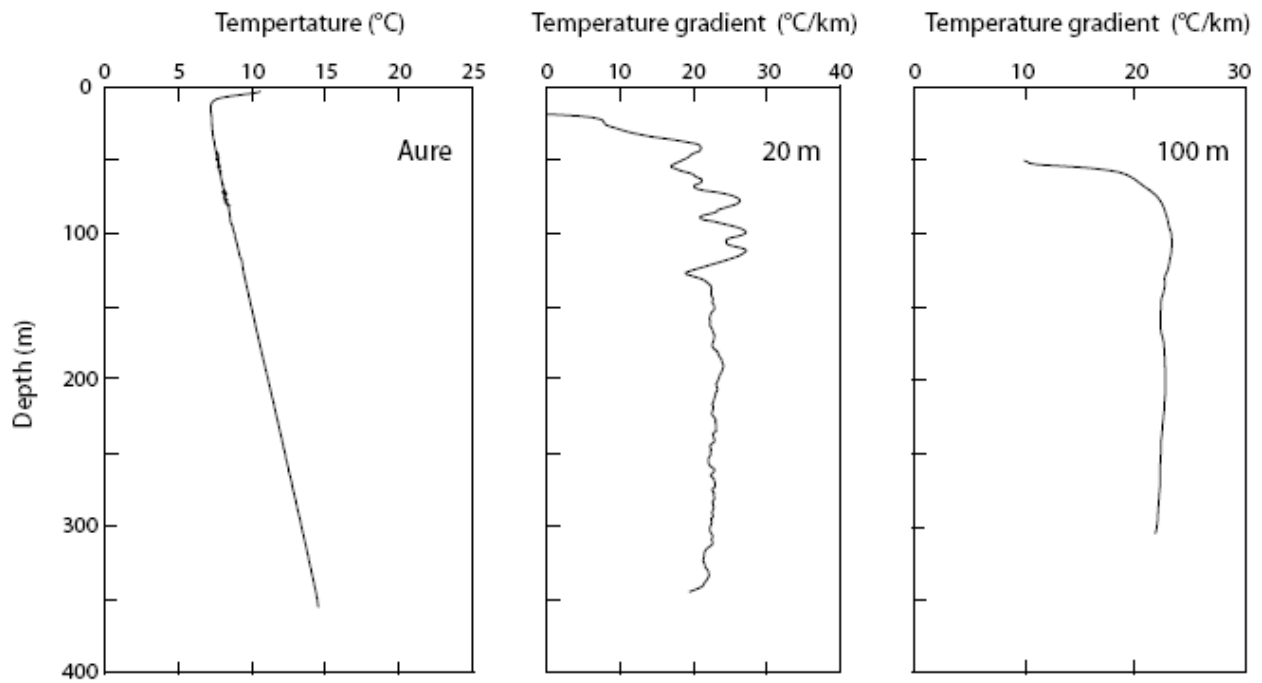
Figure C2. Temperature unfiltered and mean interval temperature gradients as indicated for borehole Arnestad, Asker.
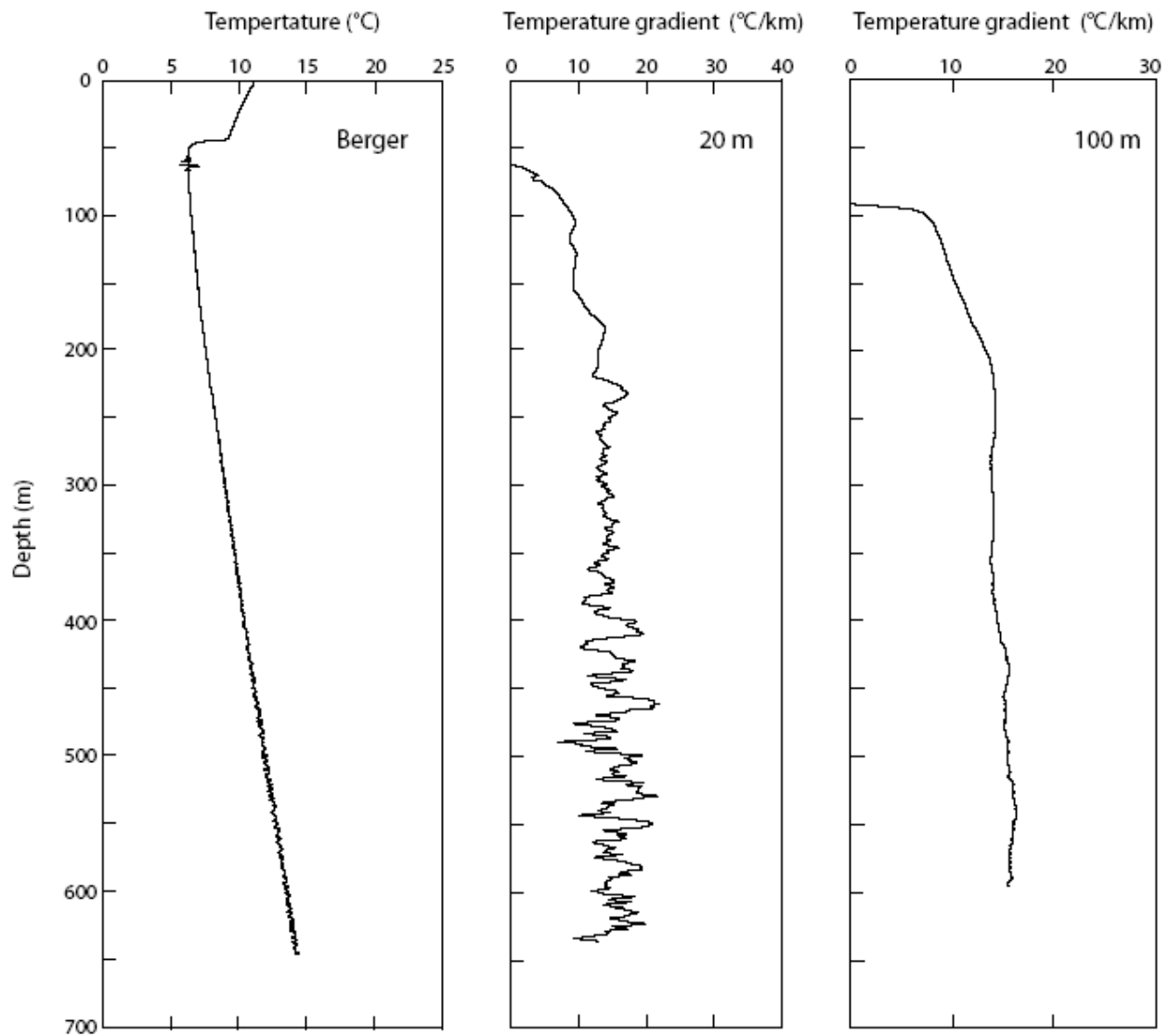
Figure C3. Temperature unfiltered and mean interval temperature gradients as indicated for borehole Berger, Skedsmo.
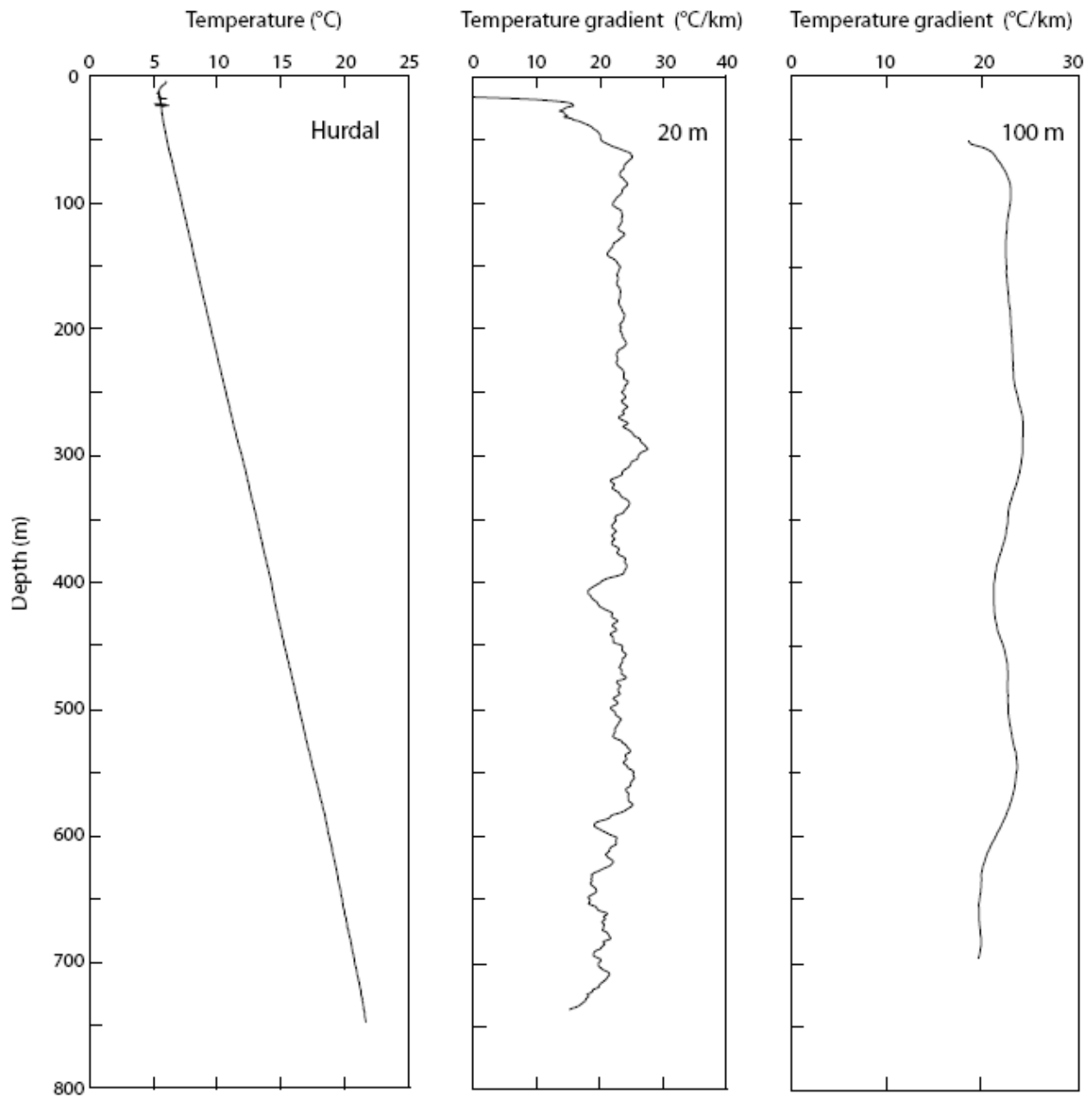
Figure C4. Temperature unfiltered and mean interval temperature gradients as indicated for borehole Hurdal.
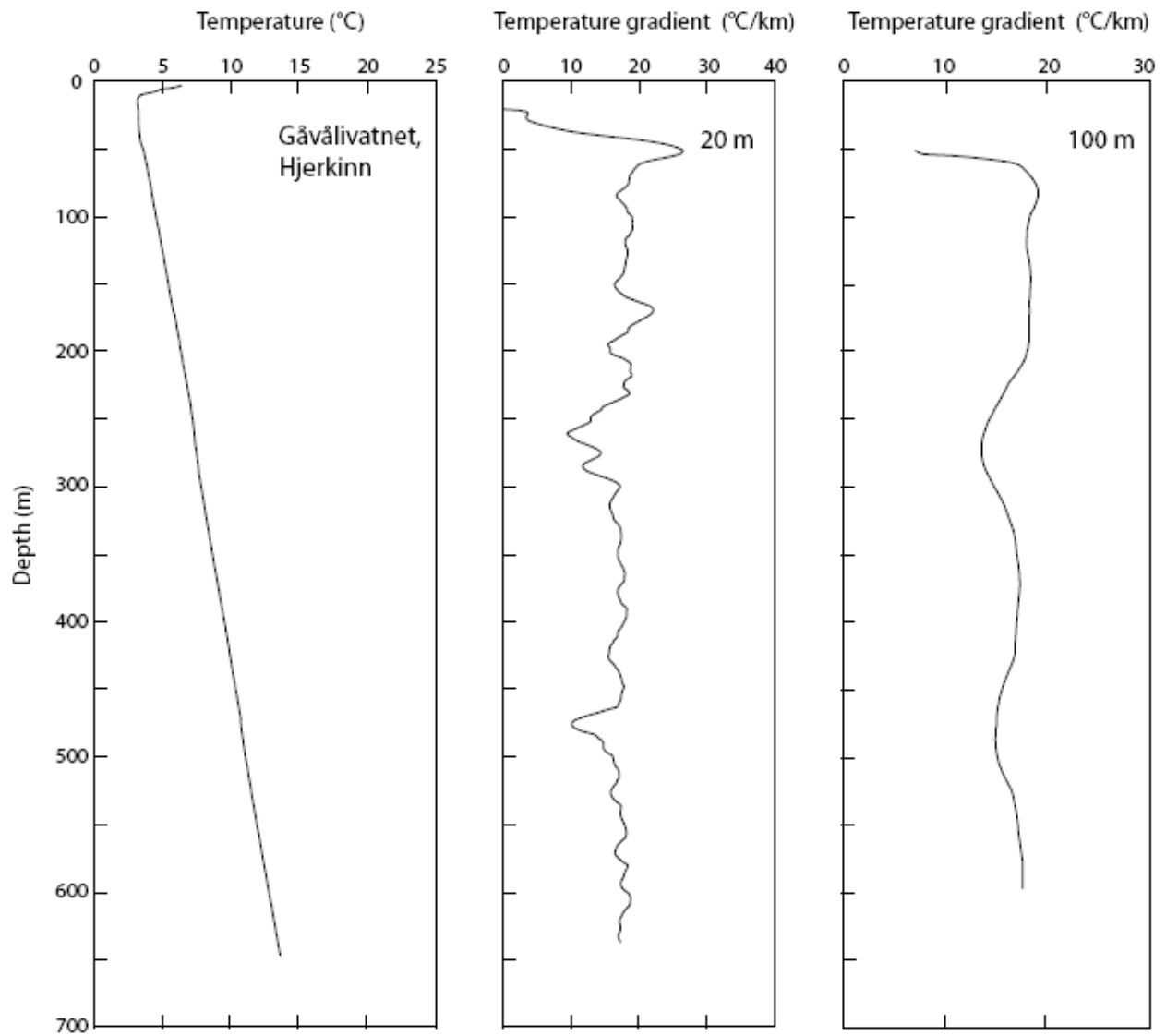
Figure C5. Temperature unfiltered and mean interval temperature gradients as indicated for borehole Gåvålivatnet, Hjerkinn.

Figure C6. Temperature unfiltered and mean interval temperature gradients as indicated for borehole Løkken.

Figure C7. Temperature unfiltered and mean interval temperature gradients as indicated for borehole Kjøsnesbogen, Aure.
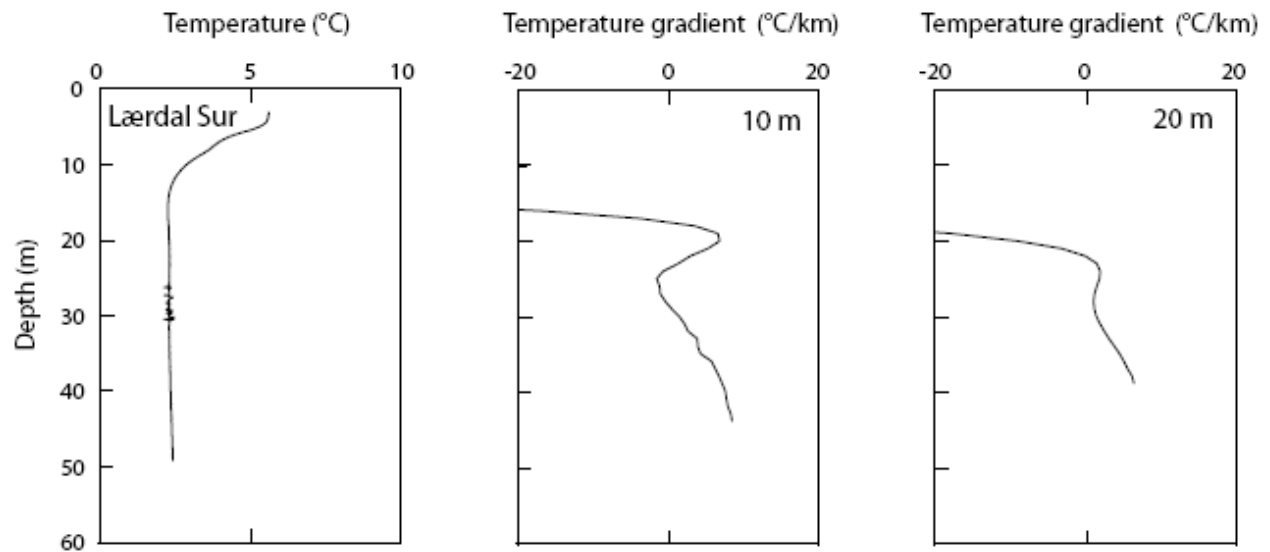

Figure C8. Temperature unfiltered and mean interval temperature gradients as indicated for borehole Lærdal surface.
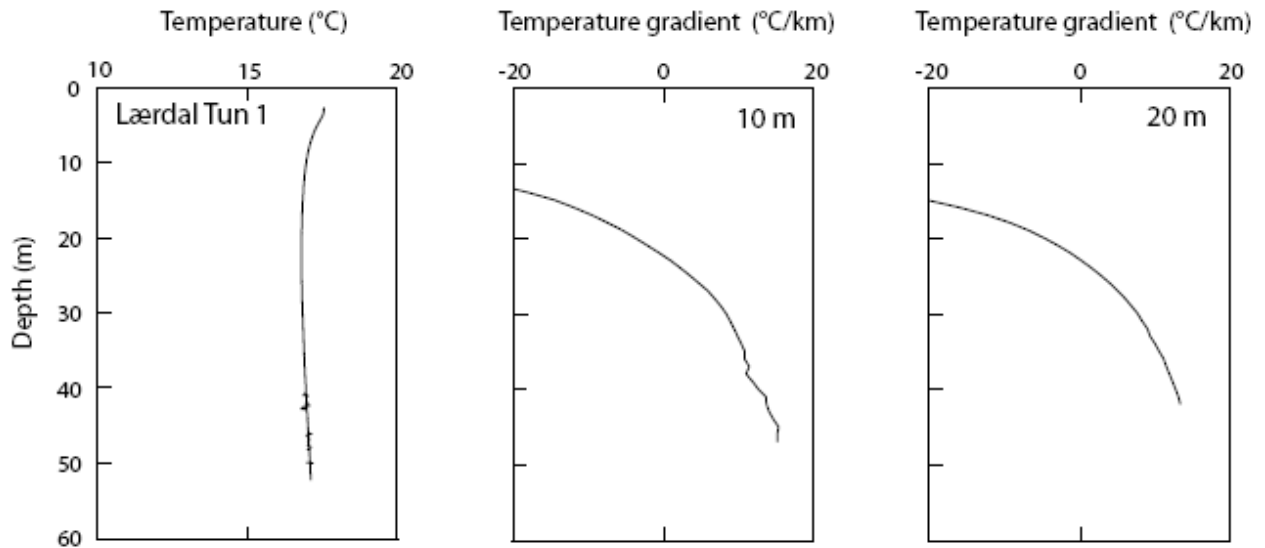
Figure C9. Temperature unfiltered and mean interval temperature gradients as indicated for borehole Lærdal tunnel 1.
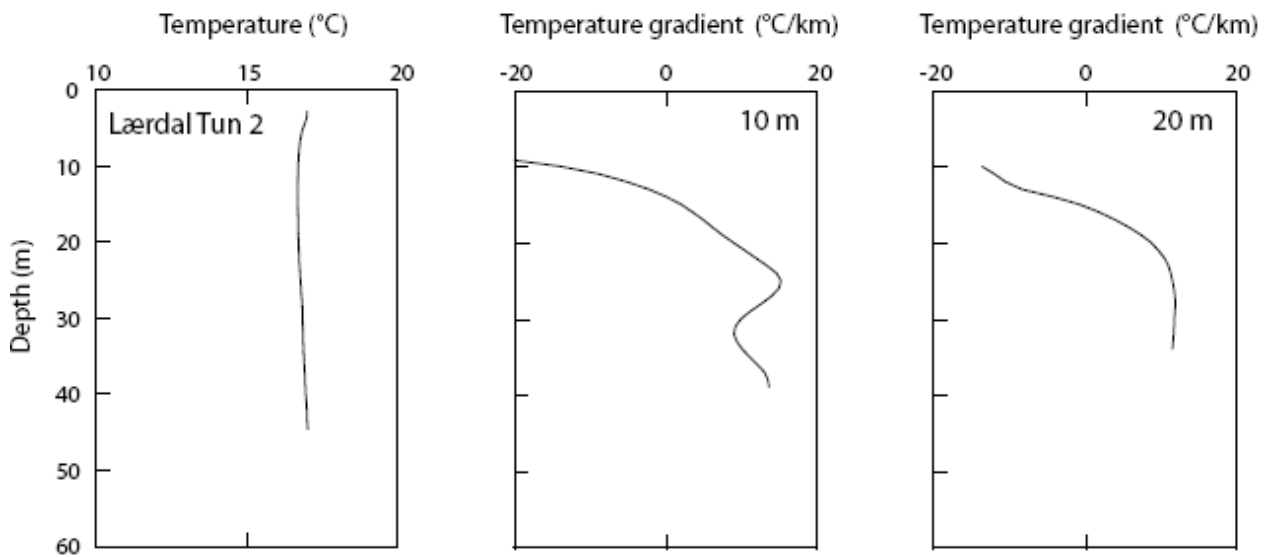

Figure C10. Temperature unfiltered and mean interval temperature gradients as indicated for borehole Lærdal tunnel 2.